AD-A045 951 VOUGHT CORP DALLAS TEX F/G 20/4
INVESTIGATION OF A VARIABLE CAMBER WING DESIGN.(U)
MAY 77 T D BEATTY, W B BROOKS, L D ROBINSON N62269-76-C-0361
UNCLASSIFIED 2-53300/7R-5977 NADC-76114-30 NL

1 OF 2
ADA 045951

Unclassified

SECURITY CLASSIFICATION OF THIS PAGE (When Data Entered)

REPORT DOCUMENTATION PAGE	READ INSTRUCTIONS BEFORE COMPLETING FORM
1. REPORT NUMBER: NADC-76114-30	2. GOVT ACCESSION NO. / 3. RECIPIENT'S CATALOG NUMBER
4. TITLE (and Subtitle): INVESTIGATION OF A VARIABLE CAMBER WING DESIGN,	5. TYPE OF REPORT & PERIOD COVERED: ~~JULY 1976 TO MAY 1977~~ FINAL REPORT, Jul 76-May 77,
	6. PERFORMING ORG. REPORT NUMBER: 2-53300/7R-5977
7. AUTHOR(s): T. D. Beatty, W. B. Brooks, L. D. Robinson	8. CONTRACT OR GRANT NUMBER(s): N62269-76-C-0361
9. PERFORMING ORGANIZATION NAME AND ADDRESS: VOUGHT CORPORATION, P. O. BOX 5907, DALLAS, TEXAS 75222	10. PROGRAM ELEMENT, PROJECT, TASK AREA & WORK UNIT NUMBERS: 62241N; F41421; WF41-421-203
11. CONTROLLING OFFICE NAME AND ADDRESS: NAVAL AIR SYSTEMS COMMAND (320D), DEPARTMENT OF THE NAVY, WASHINGTON, D. C. 20361	12. REPORT DATE: May 1977 / 13. NUMBER OF PAGES: ~~178~~ 188
14. MONITORING AGENCY NAME & ADDRESS (if different from Controlling Office): NAVAL AIR DEVELOPMENT CENTER (3015), WARMINSTER, PA. 18974	15. SECURITY CLASS. (of this report): UNCLASSIFIED / 15a. DECLASSIFICATION/DOWNGRADING SCHEDULE

16. DISTRIBUTION STATEMENT (of this Report)

Approved for Public Release; Distribution Unlimited

DDC RECEIVED OCT 28 1977 B

17. DISTRIBUTION STATEMENT (of the abstract entered in Block 20, if different from Report)

18. SUPPLEMENTARY NOTES

19. KEY WORDS (Continue on reverse side if necessary and identify by block number)

VARIABLE CAMBER WING DESIGN
TRANSONIC BUFFET FREE AIRCRAFT PERFORMANCE

20. ABSTRACT (Continue on reverse side if necessary and identify by block number)

The principal objective of this NASC sponsored investigation involved definition of the buffet free transonic maneuvering benefits derivable from an innovative skewed hingeline variable camber wing design concept. These benefits have been established from comparisons of the predicted performance obtainable with this camber concept with those of conventional uncambered and fixed camber wing designs in a common aircraft application. The aircraft configuration considered in these performance comparisons was selected as

DD FORM 1 JAN 73 1473 EDITION OF 1 NOV 65 IS OBSOLETE S/N 0102-014-6601

Unclassified

SECURITY CLASSIFICATION OF THIS PAGE (When Data Entered)

392990

representative of an advanced lightweight fighter aircraft.

Wing aerodynamic characteristics for the differing aircraft configurations were established from analysis of experimental data available from prior test programs. Analytical methods were utilized to aid in the analysis required to evaluate the influence of Reynolds number and test installation interference effects upon the experimental results.

For the aircraft configuration of this study program, it was found that substantial improvements to buffet-free performance could be attained from implementation of this camber concept. For subsonic flight conditions the maximum buffet free performance was attained with a camber scheduling which also yielded minimum drag. At transonic conditions, however, greatest improvements in buffet free performance was achieved only with wing camber configurations producing aircraft drag levels above the minimum.

SUMMARY

The potential improvements in aircraft transonic buffet free performance derivable from an innovative variable camber wing design previously developed at Vought were investigated in this study program. This wing design concept involves use of multi-segmented leading and trailing edge flaps having skewed hingelines to provide variations in wing camber. The potential benefits obtainable from this design concept were established from comparative maneuvering performance data for an aircraft configuration incorporating this wing configuration, a conventional uncambered wing configuration and a fixed wing camber configuration. The aircraft configuration considered in these performance comparisons was selected as representative of an advanced supersonic lightweight fighter aircraft.

Wing aerodynamic forces and conditions for onset of wing buffet for the individual aircraft configurations were established from analysis of experimental data available from prior wind tunnel test programs. Analytical methods were utilized to investigate the influence of Reynolds number effects and test installation interferences upon the experimental data.

Results from this program show that substantial improvements to the buffet free performance of the aircraft configuration considered in these investigations can be attained from implementation of this camber concept. For 0.6 Mach number flight conditions, the wing camber variation yielding minimum trimmed flight drag also produced the maximum buffet free lift. At 0.9 Mach number conditions, however, greatest improvement in aircraft buffet free sustained load factors and turn radius was achieved with wing camber configurations producing aircraft drag levels above the minimum. Aircraft buffet free load factor and turn radius improvements were found to be only slightly reduced by representative increases in aircraft weight associated with incorporation of the variable camber capability.

TABLE OF CONTENTS

Section		Title	Page
		SUMMARY	
		LIST OF ILLUSTRATIONS	vi
		LIST OF TABLES	xi
1.0		INTRODUCTION	1
2.0		WING ANALYSIS	11
	2.1	Buffet Boundary Definition	11
	2.2	Reynolds Number Effects	25
	2.3	Tunnel Interference Investigations	64
3.0		AIRCRAFT APPLICATION STUDIES	102
	3.1	Aircraft Configuration Definition	102
	3.2	Configuration Aerodynamic Characteristics	103
	3.3	Aircraft Perfromance Comparisons	114
4.0		CONCLUSIONS AND RECOMMENDATIONS	136
5.0		REFERENCES	139
		APPENDIX A PLOTTED WIND TUNNEL FORCE DATA	A-1
		APPENDIX B PREDICTED AIRCRAFT LIFT AND DRAG CHARACTERISTICS	B-1

LIST OF ILLUSTRATIONS

Figure	Title	Page
1	Variable Camber Wing Design Concept	4
2	Semi-Span Wing-Body Configuration During NASA Langley Test Series	6
3	Cross-Sectional Area Distribution of NASA Langley Wing-Body Test Configuration	7
4	Comparison of Satisfactory and Unsatisfactory Wing Root Bending Moment Data	14
5	Comparison of Pitching Moment Breaks and Wing Bending Divergence	17
6	Comparison of Pitching Moment Breaks and Wing Bending Divergence	18
7	Comparison of Pitching Moment Breaks and Wing Bending Divergence	19
8	Comparison of Pitching Moment Breaks and Wing Bending Divergence	20
9	Comparison of Pitching Moment Breaks and Wing Bending Divergence	21
10	Comparison of Pitching Moment Breaks and Wing Bending Divergence	22
11	Comparison of Experimental and Calculated Pressure Distributions for Configuration LO/TO at M=.6, $\alpha=3.949^{o}$, $\eta=.4$	28
12	Comparison of Experimental and Calculated Pressure Distributions for Configuration LO/TO at M=.6, $\alpha=5.946^{o}$, $\eta=.4$	29
13	Comparison of Experimental and Calculated Pressure Distributions for Configuration LO/TO, M=.6, $\alpha=1.951^{o}$, $\eta=0.85$	30
14	Comparison of Experimental and Calculated Pressure Distributions for Configuration L6/TO, M=.6, $\alpha=4^{o}$, $\eta=.4$	32
15	Comparison of Experimental and Calculated Pressure Distributions for Configuration L6/TO, M=.6, $\alpha=5.984^{o}$, $\eta=.7$	33

LIST OF ILLUSTRATIONS (Continued)

Figure	Title	Page
16	Comparison of Experimental and Calculated Pressure Distributions for Configuration L6/T15, M=.6, $\alpha=6.026^{o}$, $\eta=.4$	34
17	Comparison of Experimental and Calculated Pressure Distributions for Configuration L6/T15, M=.6, $\alpha=6.026^{o}$, $\eta=.7$	35
18	Comparison of Experimental and Calculated Pressure Distributions for Configuration L0/T0, M=.9, $\alpha=6^{o}$, $\eta=.56$	39
19	Comparison of Experimental and Calculated Pressure Distributions for Configuration L0/T0, M=.9, $\alpha=6^{o}$, $\eta=.85$	40
20	Comparison of Experimental and Calculated Pressure Distributions for Configuration L6/T0, M=.9, $\alpha=4^{o}$, $\eta=.56$	41
21	Comparison of Experimental and Calculated Pressure Distributions for Configuration L6/T0, M=.9, $\alpha=4^{o}$, $\eta=.85$	42
22	Comparison of Experimental and Calculated Pressure Distributions for Configuration L6/T1, M=.9, $\alpha=3^{o}$, $\eta=.54$	43
23	Comparison of Experimental and Calculated Pressure Distributions for Configuration L6/T1, M=.9, $\alpha=3^{o}$, $\eta=.8108$	44
24	Reynolds Number Effect on Displacement Thickness for Configuration L0/T0 at M=.6 and .9	47
25	Reynolds Number Effect on Shape Factor for Configuration L0/T0 at M=.6 and .9	49
26	Reynolds Number Effect on Displacement Thickness for Configuration L6/T0 at M=.6 and .9	50
27	Reynolds Number Effect on Shape Factor for Configuration L6/T0 at M=.6 and .9	51
28	Reynolds Number Effect on Displacement Thickness for Configuration L6/T15, M=.6, $\alpha=6^{o}$	52

LIST OF ILLUSTRATIONS (Continued)

Figure	Title	Page
29	Reynolds Number Effect on Shape Factor for Configuration L6/T15, M=.6, $\alpha=6^{o}$	52
30	Reynolds Number Effect on Displacement Thickness for Configuration L6/T1, M=.9, $\alpha=3^{o}$	54
31	Reynolds Number Effect on Shape Factor for Configuration L6/T1, M=.9, $\alpha=3^{o}$	54
32	Effect of Reynolds Number on Parasite Drag for Configuration L0/T0, M=.6 and .9	57
33	Effect of Transition Location and Reynolds Number on the Chordwise Distribution of Displacement Thickness for Configuration L0/T0, M=.6, $\alpha=4^{o}$	58
34	Effect of Reynolds Number on Parasite Drag for Configuration L6/T0, M=.6 and .9	61
35	Effect of Reynolds Number on Parasite Drag for Configuration L6/T15, M=.6	62
36	Effect of Reynolds Number on Parasite Drag for Configuration L6/T1, M=.9	62
37	Predicted Drag Variation with Reynolds Number	63
38	Potential Flow Predicted Body Interference Effect on Lift	65
39	Potential Flow Predicted Body Interference Effect on Drag	66
40	Potential Flow Predicted Body Interference Effect on Pitching Moment	67
41	Comparison Between Prediction and Experimental Lift Coefficient	75
42	Comparison of Tip Pressure Distributions with and without Body Effects, Configuration L6/T11	79
43	Comparison of Tip Pressure Distributions with and without Body Effects, Configuration L6/T11	80
44	Effect of Body Interference on Angle for Buffet Onset	83

LIST OF ILLUSTRATIONS (Continued)

Figure	Title	Page
45	Effect of Body Interference on Angle for Buffet Onset	84
46	Effect of Body Interference on Angle for Buffet Onset	85
47	Effect of Body Interference on Angle for Buffet Onset	86
48	Effect of Body Interference on Angle for Buffet Onset	87
49	Effect of Body Interference on Angle for Buffet Onset	88
50	Body Interference Effect on Lift	91
51	Body Interference Effect on Drag	92
52	Body Interference Effect on Pitching Moment	94
53	Body Interference Effect on Drag at Fixed Wing Lift	97
54	Body Interference Effect on Pitching Moment at Fixed Wing Lift	98
55	Estimated Drag Polar Uncertainties	101
56	Camber Influence Upon Aircraft Drag Characteristics, M=0.6	116
57	Analysis Aircraft Trimmed Aerodynamics, M=0.6	117
58	Camber Influence Upon Aircraft Drag Characteristics, M=0.9	119
59	Camber Influence Upon Aircraft Buffet Free Drag Characteristics, M=0.9	121
60	Analysis Aircraft Trimmed Aerodynamics, M=0.9	122
61	Maximum Sustained Buffet Free Load Factor, M=0.6	125
62	Maximum Sustained Buffet Free Load Factor, M=0.9	126
63	Minimum Equilibrium Buffet Free Turn Radius, M=0.6	127

LIST OF ILLUSTRATIONS (Continued)

Figure	Title	Page
64	Minimum Equilibrium Buffet Free Turn Radius, M=0.9 . . .	128
65	Effect of Camber on Sustained Maneuver Thrust Requirements, M=0.6	130
66	Effect of Camber on Sustained Maneuver Thrust Requirements, M=0.9	131
67	Effect of Variable Camber System Weight on Thrust Required, M=0.6	133
68	Effect of Variable Camber System Weight on Thrust Required, M=0.9, h=20,000 ft	134
69	Effect of Variable Camber System Weight on Thrust Required, M=0.9, h=30,000 ft	135

LIST OF TABLES

Table	Title	Page
1	Variable Camber Semispan Wing High Speed Wind Tunnel Model Characteristics	5
2	Wing Camber Configurations Investigated in NASA-Langley Test Series	8
3	Predicted Buffet Onset From Pitching Moment Characteristics.	24
4	Body Interference Effects on Angle of Attack For Buffet Onset	89
5	Analysis Aircraft Physical Characteristics	104
6	Predicted Isolated Fuselage/Vertical Tail Aerodynamic Characteristics	113
7	Predicted Horizontal Tail Aerodynamic Characteristics. .	113

1.0 INTRODUCTION

As mission requirements for military aircraft have advanced primary emphasis has been placed on such design considerations as those imposed by takeoff or landing; subsonic cruise, loiter or maneuvering; and supersonic dash or maneuvering. Wings designed to comply with these requirements necessarily involve compromises due to the conflicting parameters which affect subsonic and supersonic performance. Additionally, mission profiles specified for past aircraft designs often have not included transonic maneuvering requirements. In such instances the design compromise process may not specifically address transonic performance and the resulting aircraft may have little or no transonic maneuvering capability. Achievement of significant combat advantages in advanced fighter aircraft dictates that highly manuverable buffet-free transonic flight be included as a major design goal, particularly since well designed supersonic aircraft have the thrust potential for high levels of sustained transonic maneuverability. Attainment of this goal, however, requires improved wing designs yielding greater efficiency at transonic conditions than that offered by existing designs.

The elevated angles of attack required for maneuvering along with the mixed flow field characteristic at high subsonic flight conditions have a strong impact upon the efficiency of wings designed for supersonic flight. Such wings typically involve small leading edge radii and thin sections which are susceptible to leading edge type flow separations. The local supersonic regions that are embedded in the predominately subsonic wing flow field usually are terminated by shock waves. The location and strength of such shock waves can produce localized pressure gradients of sufficient severity to induce flow separations and thereby reduce wing efficiency. Minimization, if not the complete elimination, of such types of flow separation is the major problem which must be overcome to achieve the performance improvements desired in advanced wing designs.

The objective of this program has been the definition of the potential improvements in aircraft transonic buffet free performance that are derivable from a variable camber wing concept developed at Vought. These improvements have been established from performance predictions for an aircraft configuration incorporating this wing design and two more conventional wing configurations; one representing an uncambered wing and the other a wing with fixed leading edge camber representative of conical camber. The general arrangement of the aircraft considered in this program is representative of configurations developed in Vought's in-house lightweight fighter design studies. Experimental results from wind tunnel tests conducted prior to this study program have provided the principal source of information required in defining the aerodynamic characteristics of the individual configuration components.

Background

Significant effort has been expended in the past, both by governmental agencies and private industry, in wing research and development programs to define techniques for achieving improved wing performance over broader ranges of flight conditions. This research has resulted in such operational aircraft design features as variable wing sweep, variable wing/stabilizer incidence and high lift systems to improve off-design performance. In recent years, research investigating the use of variable wing camber to improve transonic performance has been included as part of Vought's inhouse advanced wing design studies. Various techniques of applying variable camber technology to wing configurations representative of those required for supersonic aircraft have been evaluated in these investigations. Results from this research identified the desirability of the uniform wing leading edge loading offered by the concept of conical wing camber and the increased aft loading characteristics of the supercritical airfoil sections developed by the NASA. As a consequence of these considerations, a concept for incorporation of variable wing camber in advanced

wing designs was developed at Vought. This concept involves the use of multi-segment leading and trailing edge flap segments having skewed hinge lines as illustrated in Figure 1. The skew of the camber segment hinge lines provides a spanwise variation of leading edge camber similar to conical camber and allows the wing trailing edge to be more highly loaded without introducing excessive changes in wing pitching moment characteristics.

During 1972, a cooperative program involving Vought and the NASA was established to obtain aerodynamic data for this variable camber wing design concept. In this program Vought provided the model, NASA Ames Research Center (ARC) provided analytical assistance in selecting test configurations and wind tunnel tests were performed by the NASA Langley Research Center (LRC). During 1974, a semi-span wing model incorporating eight individually deflectable camber flap segments was tested in the LRC 8-foot transonic wind tunnel. In this test series, the wing model was installed in the tunnel using a non-metric body as a support fairing. Geometric features of this wing model along with the wind tunnel test instrumentation are defined in Table 1. Figures 2 and 3 illustrate the physical arrangement of the wing-body configuration during the LRC test series. Twelve different wing camber configurations were investigated in this test program. The individual designations for these configurations along with the respective hinge line deflections are defined in Table 2. These configuration designations have been retained in subsequent discussions of this report to distinguish individual wing camber distributions. Results from the LRC test program are documented in Reference 1 and have been reproduced in this report only as required. Analysis of these results have shown that significant improvements in wing performance can be achieved by proper variations of wing camber. As a consequence of this result, the present studies were initiated to determine the extent to which these wing improvements are reflected in aircraft performance characteristics.

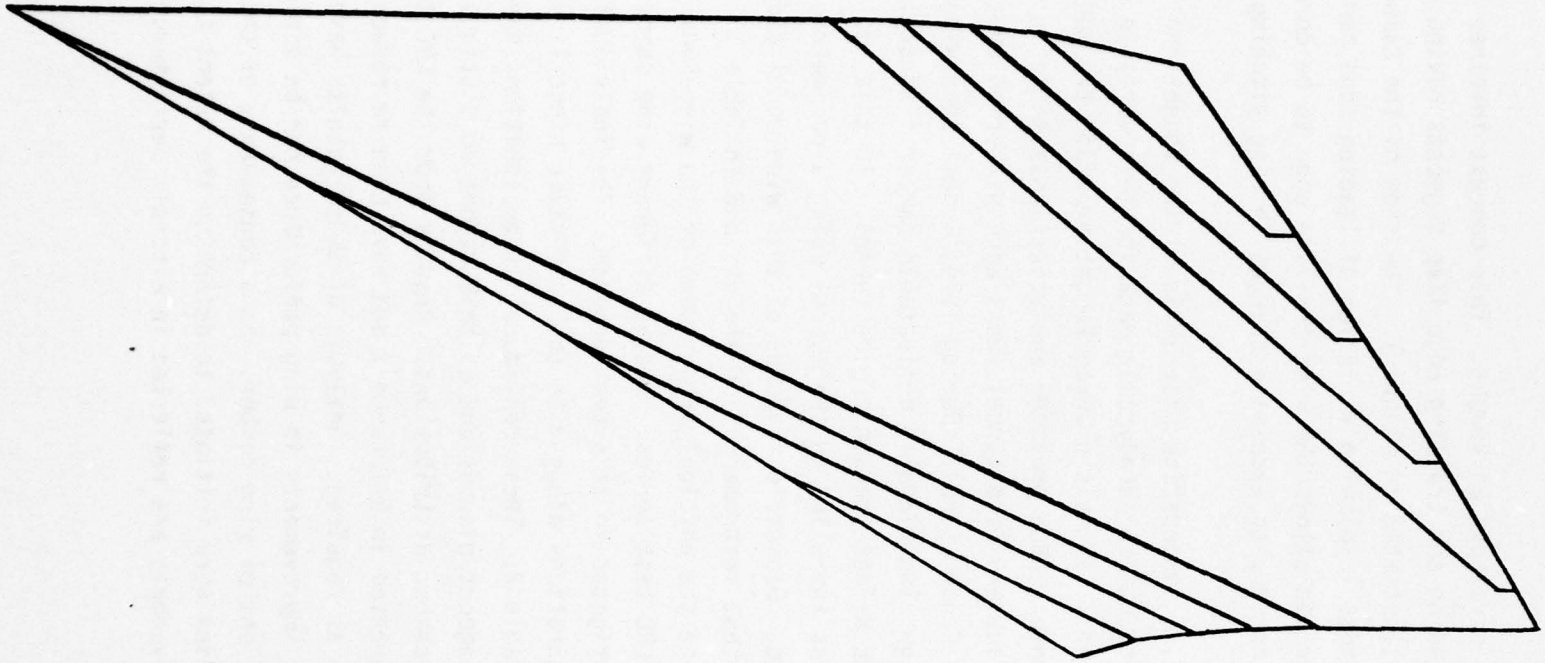

FIGURE 1 VARIABLE CAMBER WING DESIGN CONCEPT

TABLE 1

VARIABLE CAMBER SEMISPAN WING HIGH SPEED
WIND TUNNEL MODEL CHARACTERISTICS

WING GEOMETRY	
Area, Sq. In.	928.4
Semispan, In.	42.0
Aspect Ratio	3.8
Sweep Angle, Leading Edge, Deg.	35.0
Trailing Edge, Deg.	14.0
Taper Ratio	0.4
Root Chord, In.	31.6
Tip Chord, In.	12.6
Airfoil Section, Uncambered	
(1) Wing Root	NACA 65A005
(2) Wing Tip	NACA 65A004
CAMBER PANEL GEOMETRY	
Leading Edge Panels	
Max. Deflection, Deg.	± 12.0 Typ.
Hingeline Sweep, Deg.	40.9 Typ.
Chord @ Wing Tip, In.	1.74 Typ.
Trailing Edge Panels	
Max. Deflection, Deg.	± 12.0 Typ.
Hingeline Sweep, Deg.	25.4 Typ.
Chord @ Wing Root, In.	
Panel No. 5	1.89
Panel No. 6	1.89
Panel No. 7	1.89
Panel No. 8	3.79

WING INSTRUMENTATION

(1) 267 Pressure Taps

(2) Wing Root Bending Moment Strain Gage @ 0.15 b/2

(3) Wing Tip Accelerometer @ 0.8 b/2

(4) Five Component External Strain Gage Balance

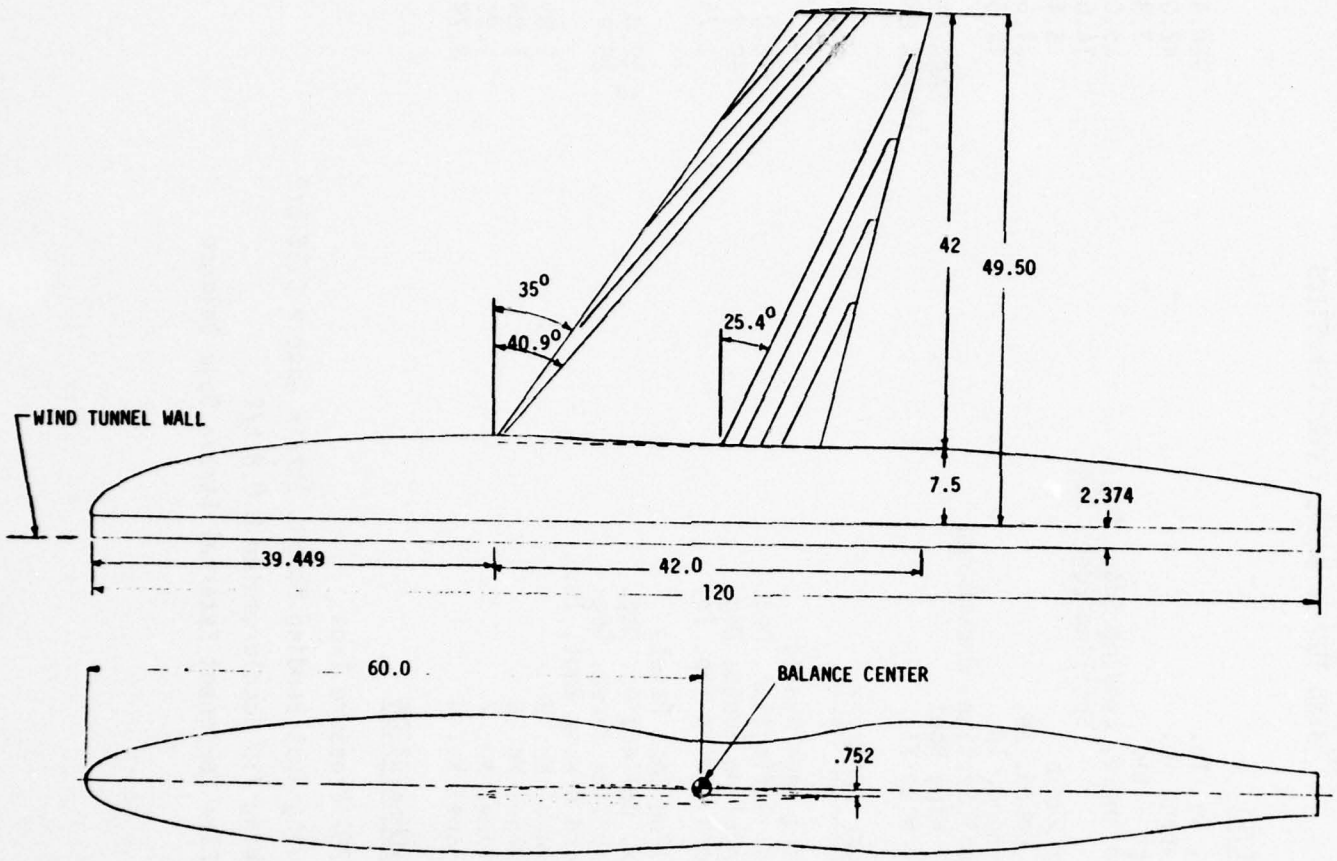

FIGURE 2 SEMI-SPAN WING BODY CONFIGURATION DURING NASA LANGLEY TEST SERIES

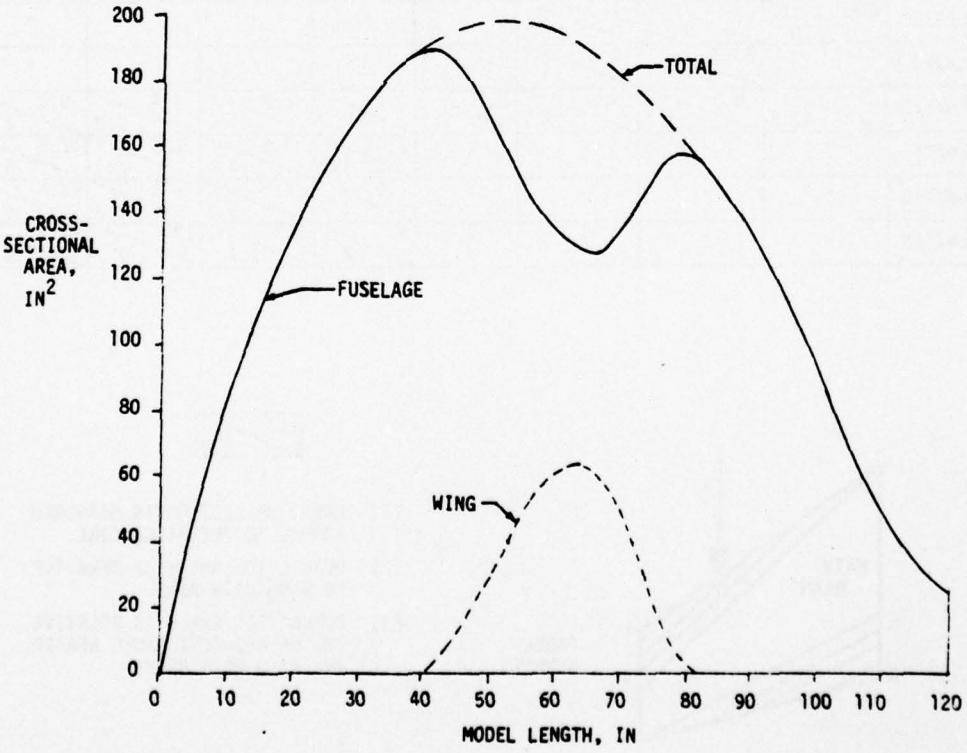

FIGURE 3 CROSS-SECTIONAL AREA DISTRIBUTION OF NASA LANGLEY WING-BODY TEST CONFIGURATION

TABLE 2 WING CAMBER CONFIGURATIONS INVESTIGATED IN NASA LANGLEY TEST SERIES

CONFIG	PANEL DEFLECTION IN DEGREES FOR PANEL NUMBERS							
	1	2	3	4	5	6	7	8
L0/T0	0 / 0	0 / 0	0 / 0	0 / 0	0 / 0	0 / 0	0 / 0	0 / 0
L5/T0	14.9 / 9.1	5.8 / 3.2	2.6 / 1.8	.8 / .8	"	"	"	"
L6/T0	21.6 / 13.1	8.5 / 4.7	3.8 / 2.7	1.1 / 1.1	"	"	"	"
L29/T0	7.7 / 0	7.7 / 0	7.7 / 7.7	0 / 0	"	"	"	"
L25/T0	12.6 / 0	12.6 / 8.7	3.9 / 3.9	0 / 0	"	"	"	"
L24/T0	16.1 / 4.6	11.5 / 4.6	6.9 / 4.5	2.4 / 2.4	"	"	"	"
L28/T0	24 / 0	24 / 12	12 / 12	0 / 0	"	"	"	"
L8/T0	27.9 / 7.6	20.3 / 8	12.3 / 8.2	4.1 / 4.1	"	"	"	"
L6/T11	21.6 / 13.1	8.5 / 4.7	3.8 / 2.7	1.1 / 1.1	.7 / .7	2.2 / 1.5	4.4 / 2.2	6.5 / 2.1
L6/T1	"	"	"	"	1.1 / 1.1	3.5 / 2.4	6.2 / 2.7	12.5 / 6.3
L6/T10	"	"	"	"	1.6 / 1.6	4.8 / 3.2	9.1 / 4.3	18.5 / 9.4
L6/T15	"	"	"	"	4 / 4	11 / 7	18 / 7	27 / 9

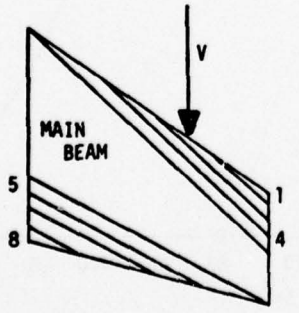

(2) / (3)

(1) PANEL DEFLECTION IS MEASURED NORMAL TO THE HINGE LINE.

(2) DEFLECTION ANGLE IS RELATIVE TO WING MAIN BEAM.

(3) DEFLECTION ANGLE IS RELATIVE TO THE ADJACENT PANEL NEARER THE WING MAIN BEAM.

Technical Approach

The basic approach taken in this study involved use of existing experimental data to predict the aerodynamic characteristics of the variable camber wing in free flight. To this end, program studies involved performance of two major tasks; (1) determination of wing inflight aerodynamics based upon the LRC wind tunnel test results and (2) determination of aircraft transonic buffet free performance benefits derivable from the Vought variable camber wing concept. The first task necessitated analyses of wind tunnel test interferences; particularly those induced by the non-metric body which was used as a wing support fairing during the LRC test series. Since flight Reynolds numbers were not simulated in the wind tunnel, the initial task included investigations to define experimental force data corrections necessary to account for Reynolds numbers effects. Viscous analyses were also included in these studies to assure that the conditions corresponding to onset of wing buffet established from the test results were representative of those expected in flight.

The second program task required development of comparative performance data for a representative advanced aircraft configuration incorporating the variable camber wing design as well as two more conventional wing designs. Since the program objective was definition of variable camber wing benefits rather than developing an aircraft design, the aircraft configuration considered in this program was established from the Vought lightweight fighter design program. Trimmed, buffet free, flight aerodynamics for these three aircraft configurations were developed by combining the corrected LRC wind tunnel data with fuselage and stabilizing surface aerodynamic characteristics obtained from wind tunnel tests conducted as part of Vought's inhouse advanced aircraft design studies. Configuration lift and drag characteristics established in this manner were used in defining the variable camber wing improvements to aircraft buffet free load factor, buffet free turn radius, and thrust requirements for sustained maneuvers at altitudes of 20,000 and 30,000 feet and Mach numbers of 0.6 and 0.9.

Specific details of the individual studies required by this program approach are presented along with the study results in the following report sections.

2.0 WING ANALYSES

Techniques employed and results from program studies to define wing inflight aerodynamic characteristics based upon the LRC wind tunnel tests conducted using the Vought semi-span wing model are identified in this report section. Buffet boundaries for each of the experimentally investigated wing camber distributions are defined in Section 2.1. Reynolds number effects upon the wing force and buffet characteristics are defined in Section 2.2. Results from the program investigations of tunnel interferences are contained in Section 2.3.

2.1 Buffet Boundary Definition

Flight buffet is a dynamic aircraft behavior resulting from unsteady aerodynamic forces induced by flow separations. Because buffet is assumed independent of the local structural deformations, buffet onset predictions are often based on the dynamic response and force measurements obtained using "rigid" wind tunnel models. Such methods, as will be discussed in later paragraphs of this report section, were used in the current studies.

While the aerodynamic forces inducing buffet may be independent of local structural deformations, wind tunnel model and aircraft dynamic response is strongly dependent on structural characteristics. For tunnel measurements to be indicative of flight characteristics, the tunnel buffet force frequency spectra must have a similar relation to the tunnel model as the flight buffet force frequency spectra have to the aircraft. Such correspondence cannot be fully established for the Vought variable wing since this entails development of a detailed full scale wing design. One area where previous tests have shown fair correspondence is in the point of buffet onset. Past experience indicates that two conditions are required for reasonable correlation between wind tunnel and free flight buffet onset conditions. First, the wing must respond to buffet in a single mode, whose reduced frequency is approximately the same as that of the "rigid" wind tunnel model. Secondly, the flow separation which induces the onset of buffet must be essentially independent of Reynolds number.

Mabey, Reference 2, has indicated that the structural response condition is normally satisfied for wings of moderate sweep and sufficiently high aspect ratio. The wing bending loads for the Vought variable camber wing are expected to be carried by the main beam with the leading and trailing camber flap systems contributing little to the wing stiffness. Thus, in spite of the moderate wing aspect ratios characteristic of advanced aircraft designs, the variable camber wing is expected to respond structurally like a much higher aspect ratio wing and satisfy the Reference 2 criteria for reduced frequency; product of wing chord and response frequency. The natural frequency of the Vought semi-span model first bending mode is 25 Hertz. As a consequence the ratio of model reduced frequency to that typical of an aircraft wing is within the bounds for good correlation indicated in Reference 2.

In general, since wing boundary layer separation is not independent of Reynolds number, good correlation between flight and tunnel conditions for initial flow separation are assured only when careful efforts have been made to match boundary layer characteristics in the region of separation. There are two types of flow separation, however, which exhibit little sensitivity to Reynolds number. These include the leading edge type laminar separations often encountered with relatively thin wings and the shock induced separations that are encountered at transonic conditions. Supersonic wave drag characteristics are a prime consideration in the selection of thickness distributions for wings designed to satisfy supersonic flight requirements. Similar considerations were included in the selection of the Vought variable camber wing thickness distribution. Consequently, the leading edge is relatively thin and for low Mach numbers initial flow separations are expected to be of the leading edge variety. Pearcey, Osborne, and Haines, Reference 3, have studied the similarity between tunnel shock induced separations and those encountered on full scale vehicles. In those studies, the conclusion was drawn that good correlations between flight and tunnel shock induced separation characteristics can be achieved provided that wind tunnel model flow separations of the trailing edge type do not occur downstream of the shock induced separation. Investigations of the wing boundary layer characteristics, discussed in Section

2.2, were included in the present program studies to define the degree to which the experimentally defined buffet onset conditions can be expected to simulate the free flight circumstances.

Experimental Buffet Onset Predictions

Measurements included in the LRC wind tunnel test series for use in evaluating wing buffet characteristics included wing trailing edge pressures, wing tip acceleration, and wing root bending moment. Trailing edge pressures provide an effective means for identifying buffet onset for trailing edge type separations in two dimensional flow but the uncertainties introduced by choice of the spanwise location for data analysis precludes use of this type measurement for three dimensional phenomena without other means of confirmation. Since the wing root bending moment and tip acceleration test measurements indicated similar characteristics, subsequent discussions of the experimental buffet measurements are restricted to root bending moment.

Buffet measurement procedures during the LRC test series were modeled after those developed by Ray and Taylor, Reference 4. In this method the primary measurement is the model structural response (specifically the first symmetric wing bending mode) as indicated by levels of root mean squared (RMS) wing root bending moment. Unfortunately satisfactory wing root bending moment data were not obtained for all configurations tested. The type problems encountered with several of the configurations are illustrated by the comparison of wing root bending moment data taken at Mach number 0.6 for configurations L5/T0 and L6/T15 shown in Figure 4. The measurements for configuration L5/T0 illustrate a satisfactory set of data. The rms wing root bending moment is well behaved and has a clearly defined divergence at about 5.7 degrees angle of attack. Test results for configuration L6/T15, however, are not satisfactory. The most apparent deficiency is the reversal in wing root bending moment between 7 and 8 degrees. This reversal is an unexpected and certainly questionable variation with increasing angle of attack. Interpretation of such test results is further complicated by the limited number of data points. With only three data points

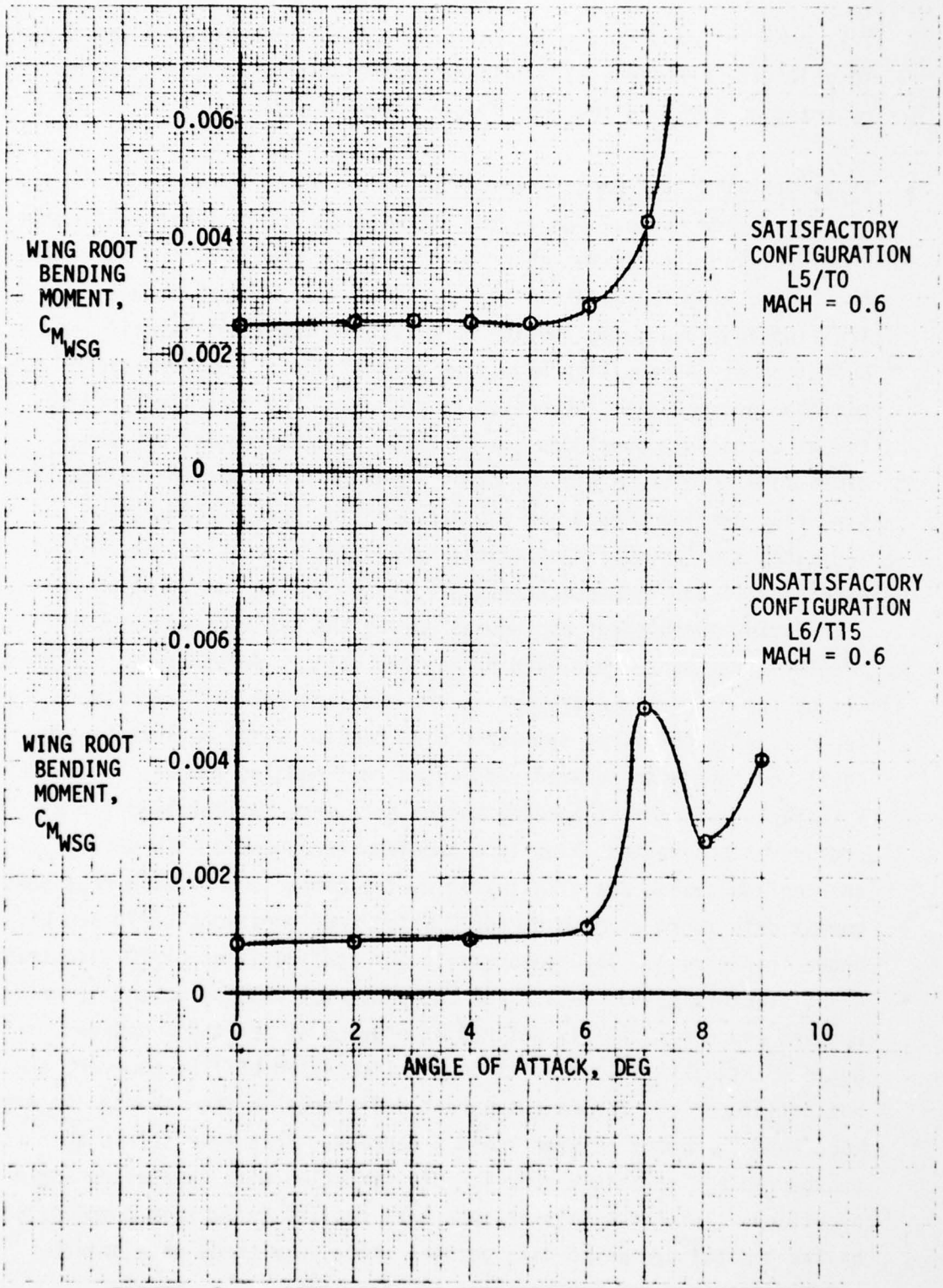

FIGURE 4 COMPARISON OF SATISFACTORY AND UNSATISFACTORY WING ROOT BENDING MOMENT DATA

available in the critical 5-8 degree range, accurate determination of the proper curve shape and, consequently, the angle of attack for root bending moment divergence is not possible.

The comparisons of Ray and Taylor and, more specifically, those of Hollingsworth and Cohen, Reference 5, underline the importance and even necessity of using a single buffet indicator for configuration comparisons. In a comparative test of eight different forms of buffet instrumentation, Hollingsworth and Cohen found only limited agreement between the buffet onset indications of the various methods. The disagreement between the different methods of measurement for a given configuration was often considerably greater than the variation found when the same method was used to indicate buffet onset for different configurations. The general trend of buffet onset with changes in either configuration or conditions was the same, however, when any single one of the methods was used exclusively to indicate the onset of buffet. Since the rms root bending moment could not be used for all configurations, it was necessary to substitute one of the other available force or moment measurements as the indicator of buffet onset.

Ray and Taylor included correlations between various force and moment variations and wing root bending moment divergence in their study. They concluded that the axial force coefficient was the most sensitive static component to the onset of buffeting. Their use of the axial force coefficient, however, required computation of the theoretical variation of the axial force with angle of attack. Even in their own report, Ray and Taylor made this computation only for an untwisted and uncambered wing. For the present wing, which is both twisted and cambered, the uncertainty as to the proper fraction of leading edge suction that could be theoretically expected was too great to allow the required theoretical variation to be accurately computed.

Of the remaining static force components surveyed by Ray and Taylor, the pitching moment coefficient appeared to be the most promising buffet onset indicator. The comparisons of Reference 4 indicate that, for an uncambered and untwisted wing, discontinuities (i.e., breaks) in the pitching moment characteristics tended to give

high (unconservative) buffet onset indications relative to that indicated by the wing root bending moment divergence. For cambered sections (Ray and Taylor did not test twisted wing configurations) the correlation between the pitching moment breaks and the wing root bending moment divergence was better. Satisfactory measurements of both root bending and pitching moments are available from the LRC test series for configurations L0/T0, L5/T0, and L6/T11 at both 0.6 and 0.9 Mach number. The angles of attack corresponding to the onset of wing buffet indicated by these two differing measurements are compared in Figures 5 through 10. These comparisons are consistent with the previous observations of Ray and Taylor. The pitching moment for configuration L0/T0 does indeed break at a somewhat higher angle of attack than the angle for wing root bending moment divergence; however, data for the cambered wings, configurations L5/T0 and L6/T11, show better agreement between the two buffet indicators. The trend of buffet onset with configuration change was consistent between the two methods. Consequently the breaks in wing pitching moment characteristics are considered to provide a reliable indication of the variation in the buffet onset angle of attack for the wing camber configurations in the LRC test series and were used in this study to predict the wing buffet onset angle of attack.

Figures 4 through 10 illustrate a data characteristic that was consistently observed for all of the LRC test wing camber configurations. The variation of the rms wing root bending moment with angle of attack changes significantly as the Mach number is increased from 0.6 to 0.9. At 0.6 Mach number a single well defined divergence is generally observed. At the higher Mach number, however, the rms wing root bending moment appears to suddenly change to a higher "plateau" at the angle of attack corresponding to the break in pitching moment curve. As the angle of attack increases further, the rms moment first remains almost constant for about 2 degrees and then diverges in the expected fashion. An examination of the experimental data of Ray and Taylor suggests that a similar change in the basic curve shape occurred in the results of Reference 4 as well. The final divergence in the rms bending moment curve occurs at an angle of attack that is roughly in agreement with

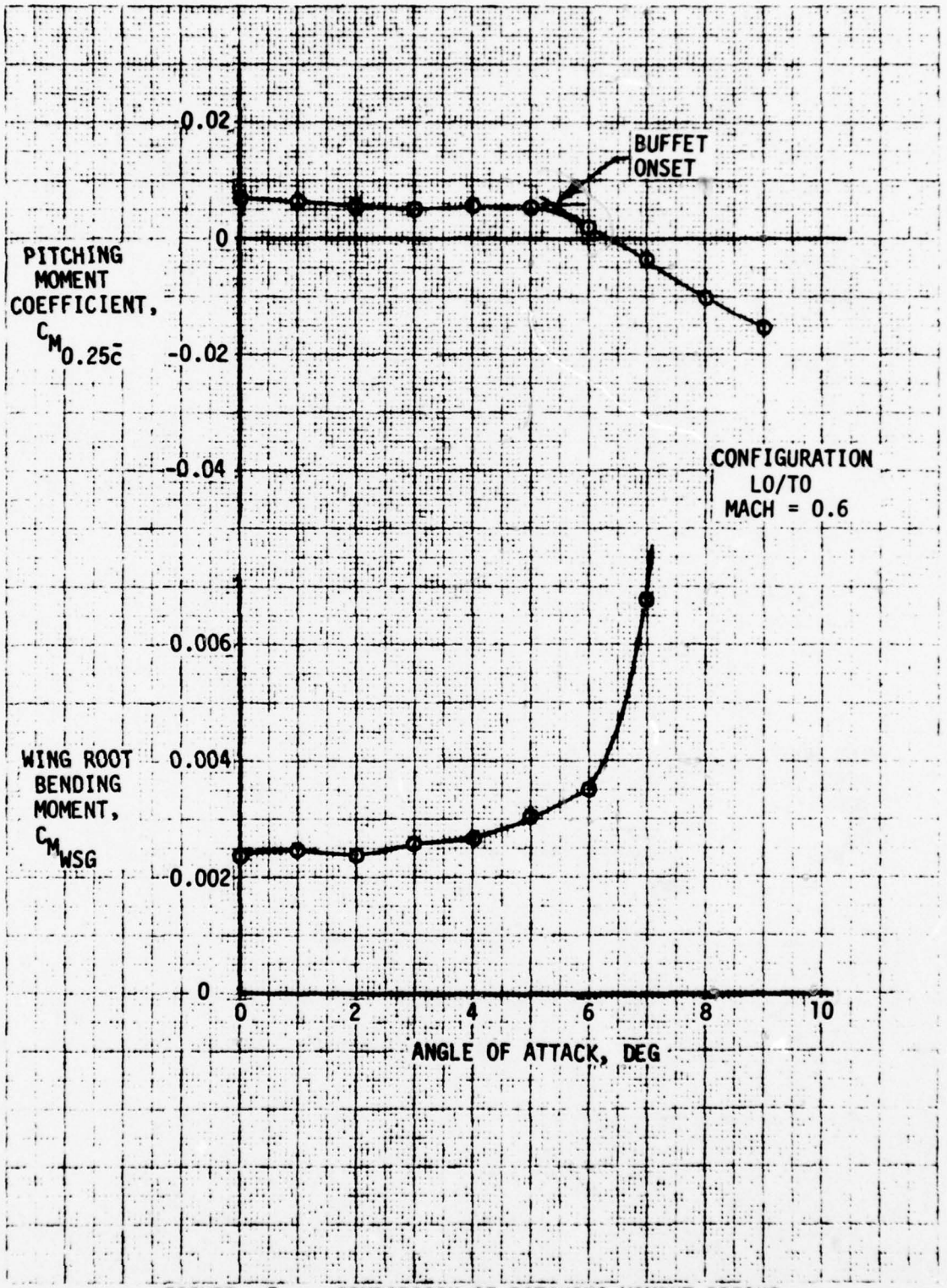

FIGURE 5 COMPARISON OF PITCHING MOMENT BREAKS AND WING BENDING DIVERGENCE

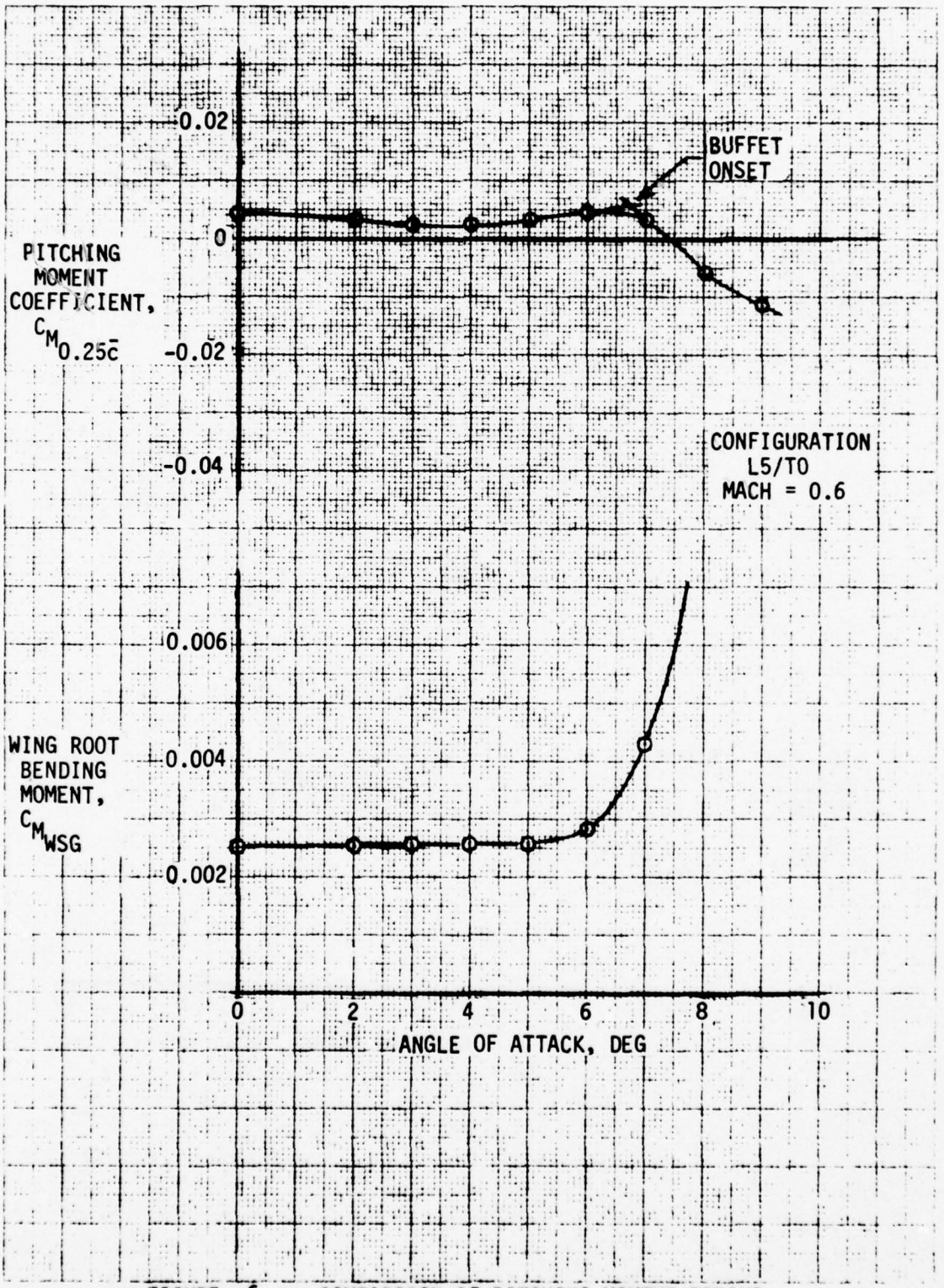

FIGURE 6 COMPARISON OF PITCHING MOMENT BREAKS AND WING BENDING DIVERGENCE

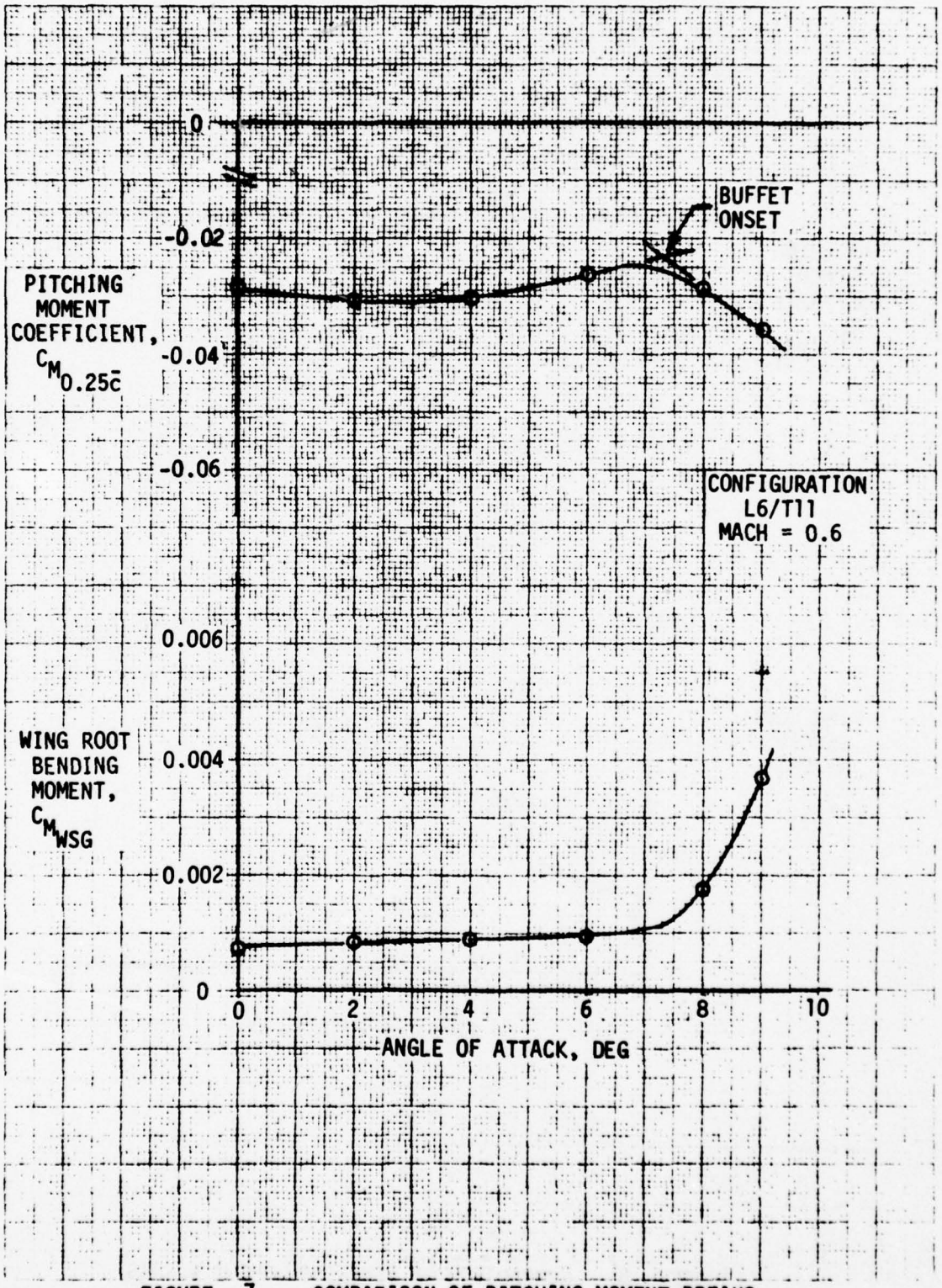

FIGURE 7 COMPARISON OF PITCHING MOMENT BREAKS AND WING BENDING DIVERGENCE

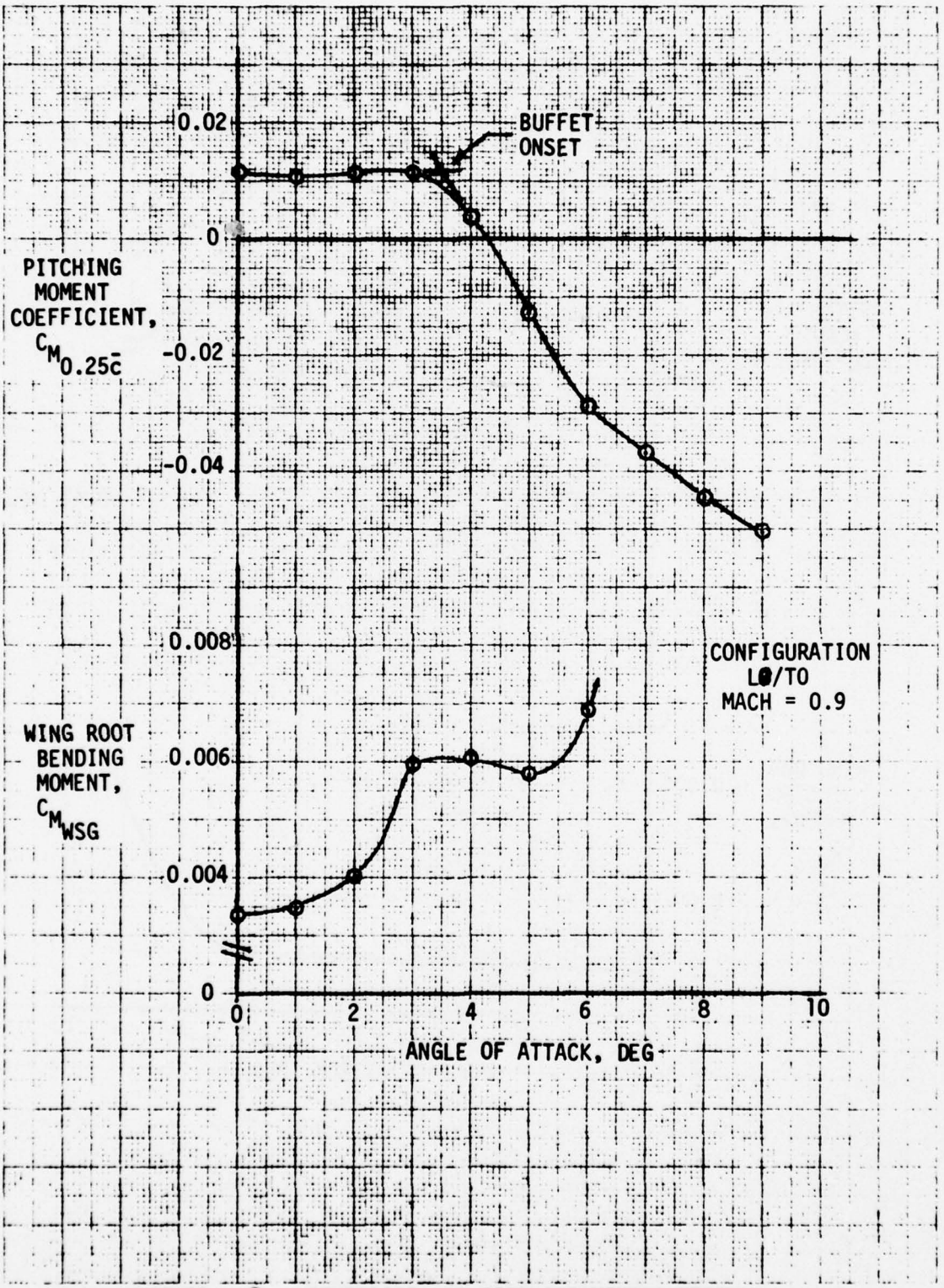

FIGURE 8 COMPARISON OF PITCHING MOMENT BREAKS AND WING BENDING DIVERGENCE

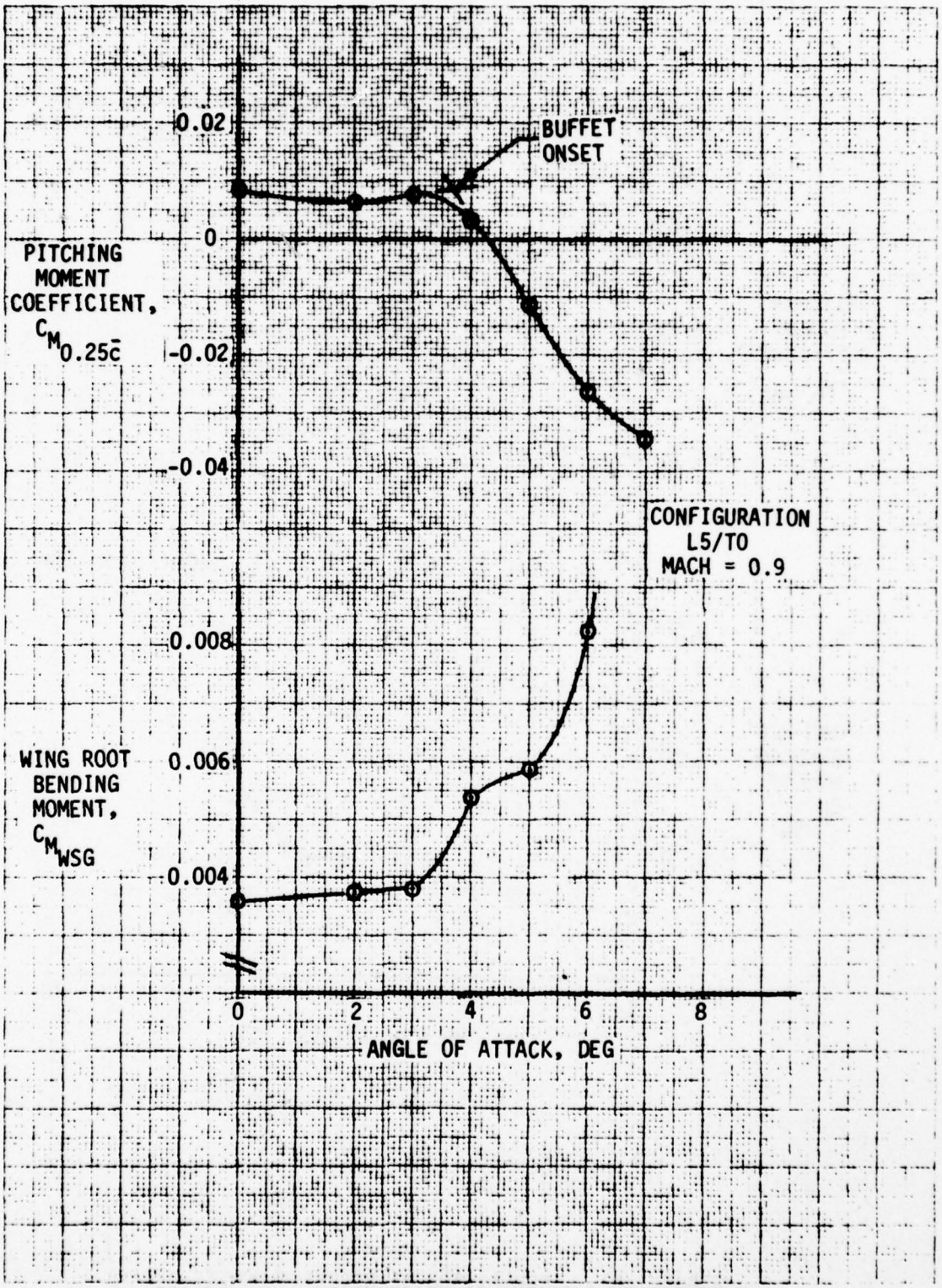

FIGURE 9 COMPARISON OF PITCHING MOMENT BREAKS AND WING BENDING DIVERGENCE

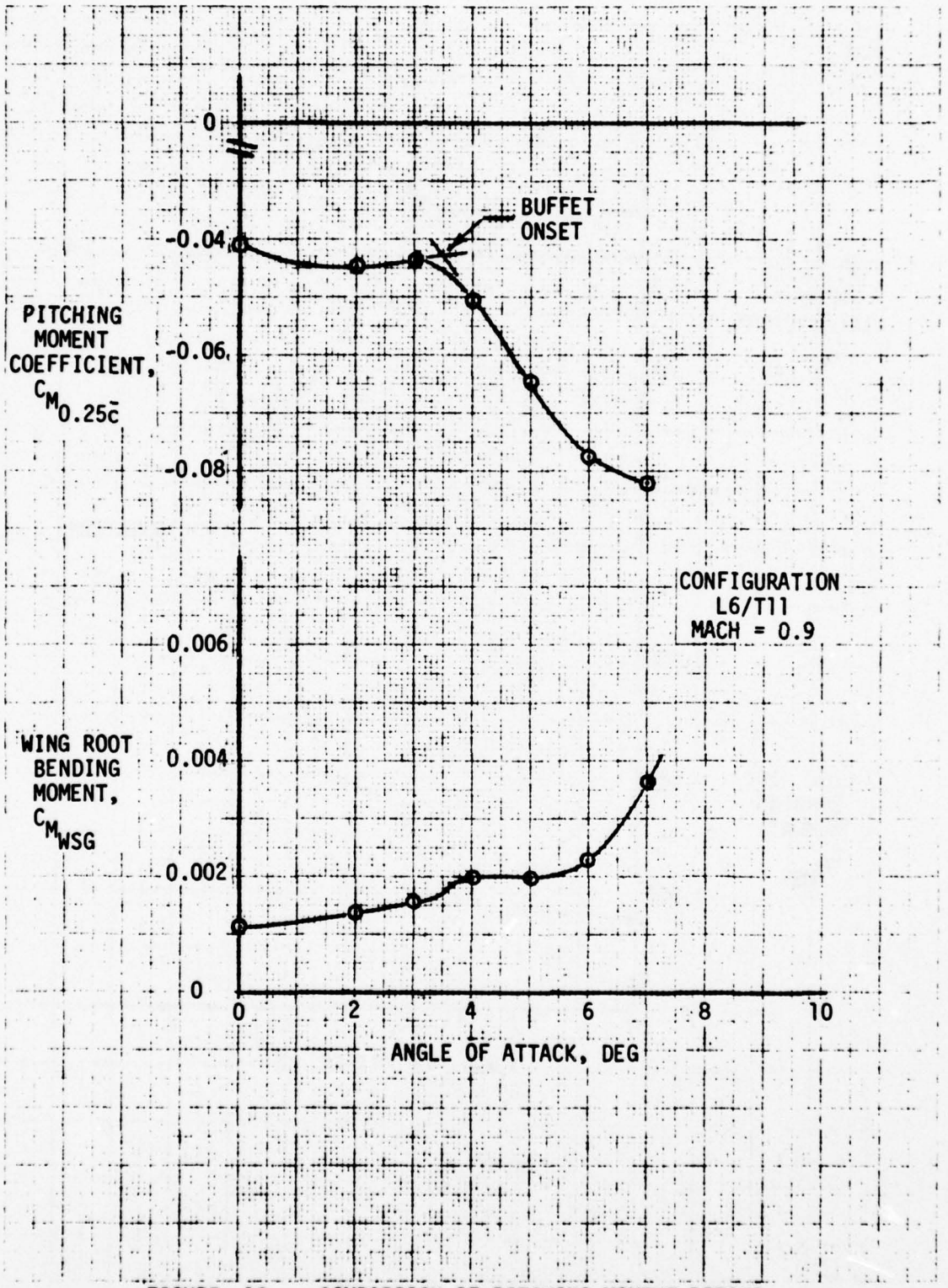

FIGURE 10 COMPARISON OF PITCHING MOMENT BREAKS AND WING BENDING DIVERGENCE

that predicted by a simple continuation of the 0.6 Mach number results. This change in the wing root bending moment characteristics between 0.6 and 0.9 Mach number indicates that the flow separation precipitating buffet onset is different for these two flow conditions.

Wing buffet onset angles of attack and lift coefficients obtained from analyses of the pitching moment characteristics for each of the camber configurations investigated in the LRC test series are presented in Table 3. These results show that, at 0.6 Mach number, changes in leading edge camber can produce an increase in the angle of attack for buffet onset. This type of camber effect indicates that the flow separations at this Mach number are of the leading edge type and more specifically, since the maximum camber change occurs near the tip, the initial separations must also occur on the outboard portion of the wing. Experimental wing pressure distributions obtained at this Mach number exhibit characteristics consistent with these conclusions. At 0.9 Mach number conditions, results from the wing pitching moment analyses indicate that changes in leading edge camber had little influence on the buffet onset angle of attack. Trailing edge camber variations also had little effect on the angle of attack for buffet onset at both 0.6 and 0.9 Mach number. Indeed the observed effect of trailing edge camber variations is a reduction in the buffet onset angle of attack with increases in trailing edge camber (see Table 2 for relative camber comparisons). Experimental wing pressure obtained at 0.9 Mach number indicate the shock waves in the wing flow field are of greatest strength in the mid to outboard portion of the wing. If the wing buffet characteristics at this Mach number are produced by a shock induced type separation, as indicated by the wing pressures, then the results in Table 3 indicate the initial separation occurs on the outer wing in the region least affected by trailing camber variations.

TABLE 3

PREDICTED BUFFET ONSET FROM PITCHING MOMENT CHARACTERISTICS

CONFIGURATION		MACH NUMBER			
		0.6		0.9	
		ANGLE OF ATTACK, DEG	LIFT COEFFICIENT	ANGLE OF ATTACK, DEG	LIFT COEFFICIENT
LEADING EDGE CAMBER VARIATION	L0/T0	5.4	0.39	3.5	0.31
	L5/T0	6.7	0.48	3.6	0.31
	L6/T0	7.3	0.52	3.7	0.32
	L29/T0	7.5	0.53	3.5	0.30
	L25/T0	8.1	0.56	3.5	0.30
	L24/T0	7.8	0.55	4.0	0.34
	L28/T0	7.3	0.53	4.2	0.37
	L8/T0	-	-	4.1	0.34
TRAILING EDGE CAMBER VARIATION	L6/T0	7.3	0.52	3.7	0.32
	L6/T11	7.3	0.63	3.4	0.43
	L6/T1	7.0	0.67	3.4	0.51
	L6/T10	6.7	0.71	3.2	0.56
	L6/T15	6.4	0.85	2.7	0.63

2.2 Reynolds Number Effects

Prior to use of the wing aerodynamic characteristics determined from the LRC wind tunnel tests in the aircraft application studies of this program, an assessment of the effects of Reynolds number differences between wind tunnel and flight must be considered. The primary effect of Reynolds number variations are reflected in changes in wing boundary layer transition location, turbulent boundary layer growth and initial turbulent boundary layer separation. When significant variations in wing boundary layer characteristics are incurred by differences in tunnel and flight Reynolds numbers, wing force and buffet onset characteristics can be appreciably altered. Changes in wing lift and pitching moment characteristics result from the effective airfoil geometry modification caused by the addition of the streamline displacement thickness, δ^*, which alters the wing pressure distribution. Drag is directly influenced by the Reynolds number effects on local skin friction and the extent of laminar flow and indirectly by the change in effective airfoil geometry which alters the pressure drag component.

The impact of wind tunnel and flight Reynolds number differences upon wing buffet onset characteristics is strongly dependent on the type of flow separation encountered. As indicated in Section 2.1, laminar boundary layer separations and to a major extent shock induced flow separations are independent of Reynolds number variations. Turbulent boundary layer separations of the trailing edge type are, however, sensitive to Reynolds number variations.

Evaluation of Reynolds number effects upon the LRC wind tunnel test results included in the present program studies involved analytical predictions of the boundary layer characteristics for representative wing camber distributions at both tunnel conditions and flight altitudes of 20,000 and 30,000 feet. As will be shown the changes in wing boundary layer displacement thickness due to the Reynolds number differences were small enough to be ignored. Consequently, Reynolds number corrections to the experimental lift and pitching moment data were not necessary. Similarly, the types of flow separation predicted in these boundary layer analyses indicated that the experimentally defined buffet onset conditions are not sensitive to Reynolds number differences. The analytical

techniques employed in reaching these conclusions consisted of two three-dimensional potential flow methods, a two-dimensional boundary layer method and a method for predicting sectional drag characteristics. The following paragraphs provide a discussion of the investigation techniques employed, analysis results, and the experimental drag data corrections developed for use in the subsequent aircraft application studies.

Predicted Wing Pressure Distributions

The potential flow techniques used in this program to provide the pressure distributions necessary for investigations of wing boundary layer characteristics were the Hess method, References 6 and 7, and the Bailey-Ballhaus method, References 8 and 9. The Hess method, which is applicable to wing-body configurations, provided the pressure predictions at 0.6 Mach number. Due to the unavailability of a similar method applicable to wing-body configurations at supercritical flow conditions involving embedded shock waves, the isolated wing coding of Reference 9 was utilized for pressure predictions at 0.9 Mach number.

The Hess method is explained thoroughly in References 6 and 7 and, thus, a detailed description is not presented in this report; only a discussion of the applicability to the present study. The method as described in Reference 6 solves the incompressible potential flow problem, however, the version utilized in this study contained a modification which incorporated a Gothert compressibility correction. One of the prime considerations involved in use of this program concerns definition of the proper geometric modeling of the configuration under consideration. The method provides an "exact" solution of the potential flow equation providing the number of panel elements used in the geometric model is essentially infinite. In practice, however, an infinite number of elements is impossible to attain due to limitations of computer storage capability and execution times. Therefore the proper utilization of the Hess method requires that a geometric model be developed which adequately represents the desired configuration without exceeding the above computer constraints. The skewed hingelines for the Vought variable camber wing leading and trailing edge flap segments introduce a

further constraint upon the geometric model options since element lines must be included which coincide with these hingelines. As will be shown, the variable camber wing geometric model developed for use in the Hess program adequately represented the wing from the leading edge to approximately the 75% chord line. Aft of this chord line, however, experimental and predicted pressure comparisons indicate that the representation may have been degraded by the limited number of chordwise elements. The agreement between experimental and predicted pressures for the wing camber distributions included in the boundary layer investigations is discussed in the following paragraphs.

Figure 11 presents a comparison of Hess Predictions to wind tunnel data for the LO/TO wing camber configuration at approximately the wing mid-span station (η=.40), and an angle of attack of 3.95 degrees. This figure, which is typical of the low angle cases, illustrates the above comments quite well. When the angle of attack is increased above approximately 5 degrees for this particular case, some viscous phenomena appear at the upper surface leading edge which alters the leading edge pressures. Since the Hess routine is strictly potential flow, the calculations begin to diverge from the wind tunnel data as shown in Figure 12. However, for this configuration, the buffet onset angle of attack is approximately 5 degrees, so the primary region of interest is adequately calculated by the Hess program. Another comparison of experimental data to calculated results for this wing camber configuration at a spanwise station, η=.85, is shown in Figure 13 indicating results similar to those of Figure 11.

The comparisons presented in Figures 11 through 13 are typical of the results obtained from the Hess program for the uncambered wing configuration. As a consequence of the relatively good correlation, the Hess geometric model was considered to provide an adequate representation of the wing leading edge pressures which would allow realistic predictions of the laminar boundary layer characteristics. As was noted earlier and as shown in these figures, discrepancies between calculated and experimental pressures are more severe in the vicinity of the wing trailing edge. These differences were considered to be sufficiently small that the

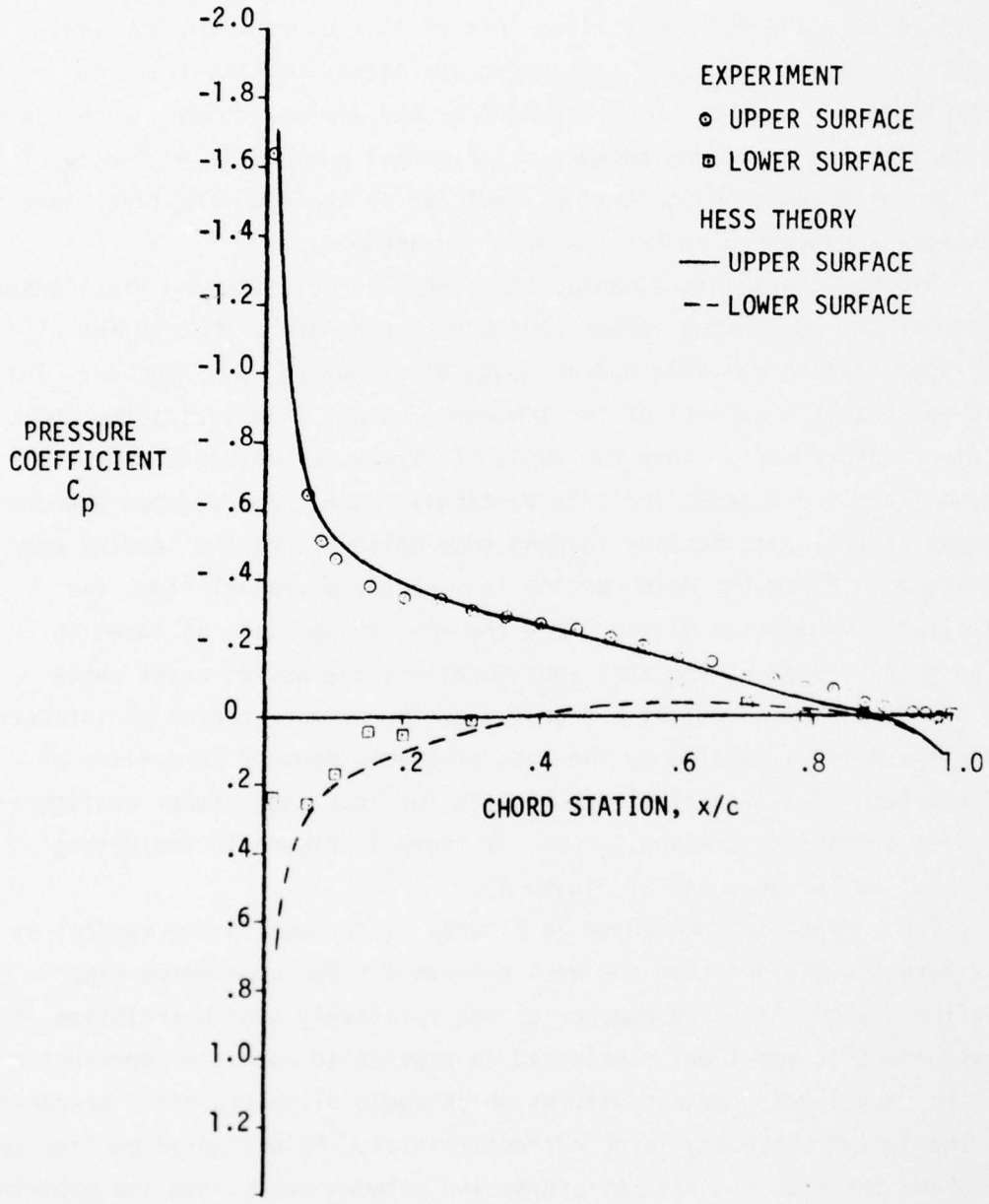

FIGURE 11 COMPARISON OF EXPERIMENTAL AND CALCULATED PRESSURE DISTRIBUTIONS FOR CONFIGURATION LO/TO AT M=.6, α=3.949, n=.4

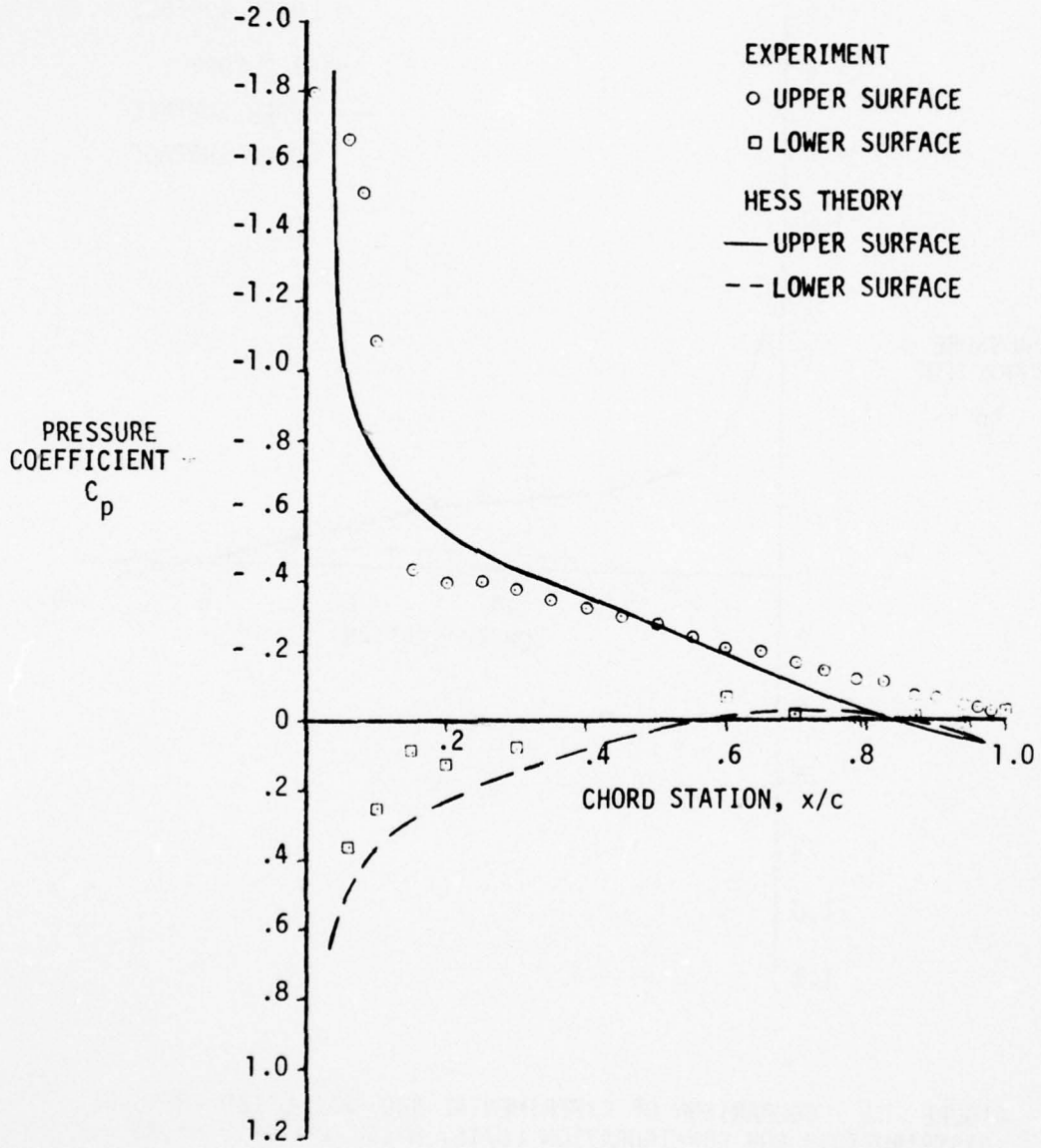

FIGURE 12 COMPARISON OF EXPERIMENTAL AND CALCULATED PRESSURE DISTRIBUTIONS FOR CONFIGURATION LO/TO, M=.6, α=5.946, n=.4

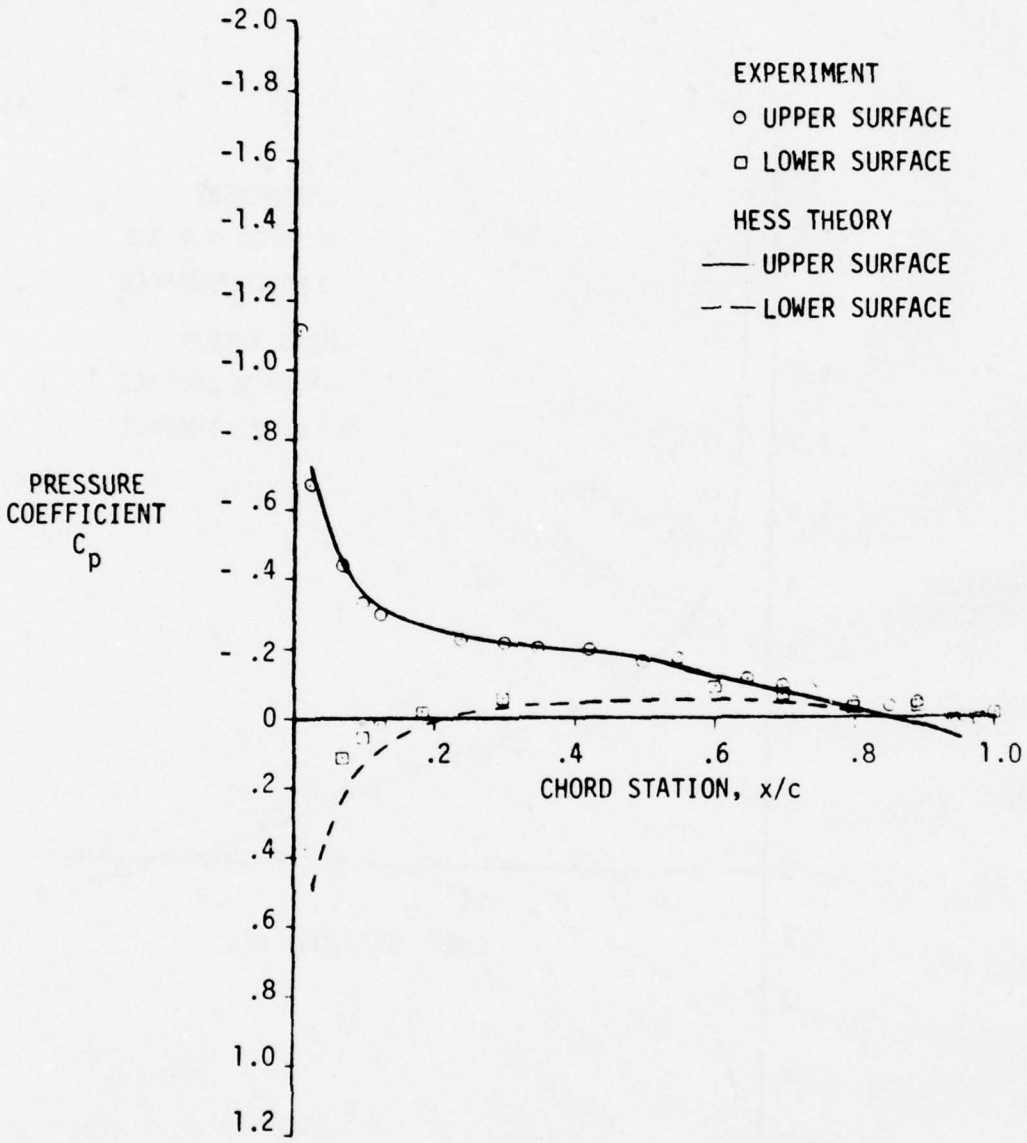

FIGURE 13 COMPARISON OF EXPERIMENTAL AND CALCULATED PRESSURE DISTRIBUTIONS FOR CONFIGURATION LO/TO, M=.6, α=1.951, n=.85

predicted incremental changes in wing boundary layer characteristics due to Reynolds number variations would not be substantially altered.

Figure 14 presents a comparison of experimental pressure data and analytical predictions for a wing configuration involving leading edge camber, configuration L6/T0. Differences between experimental results and calculations in the vicinity of the upper surface leading edge are illustrated in this figure which were not observed in the previous comparisons. This disagreement is attributed to be at least partly the result of the requirement for the geometric model panel edges to coincide with the camber segment hinge lines. This requirement produces a degraded leading edge representation at this span station. For other span stations better correlations between the experimental and predicted pressures are obtained near the leading edge as illustrated in Figure 15. Even at this more outboard span station, however, the calculated pressures deviate from experiment in the immediate vicinity of the leading edge; possibly again due to the geometric model used in the Hess method finite element problem formulation. Conversely, the limited number of experimental pressures in the leading edge region does not permit a firm exclusion of the possibility that viscous effects are the source of the observed pressure differences.

Predicted and calculated pressure comparisons for the final wing camber configuration (L6/T15) considered in evaluating Reynolds number effects are presented in Figures 16 and 17. This configuration involves both leading and trailing edge wing camber. Differences are noted in both the leading and trailing regions for this configuration and angle of attack. The discrepancies for the outboard wing station (η=0.7) leading edge pressures are most certainly the result of a viscous phenomena so limited agreement is expected in this region. Although perhaps not as obvious, viscous effects in all likelihood are the primary cause of the leading edge pressure differences observed for the more inboard wing station, Figure 16. In the trailing edge region the calculated pressure deviations from experimental may again be due in part to the geometric model but the experimental trailing edge measurements also indicate that a flow separation has occurred at both wing

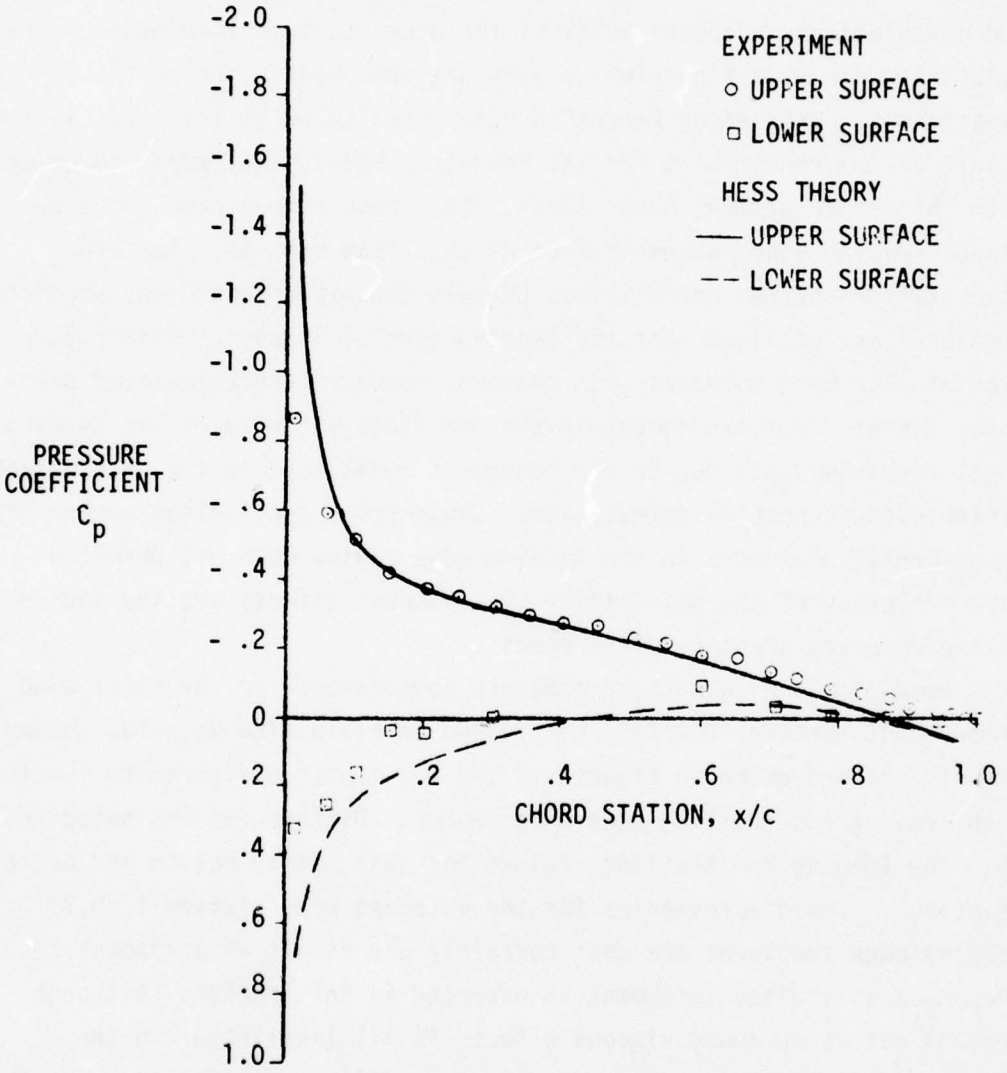

FIGURE 14 COMPARISON OF EXPERIMENTAL AND CALCULATED PRESSURE DISTRIBUTIONS FOR CONFIGURATION L6/T0, M=.6, $\alpha=4^{o}$, n=.4

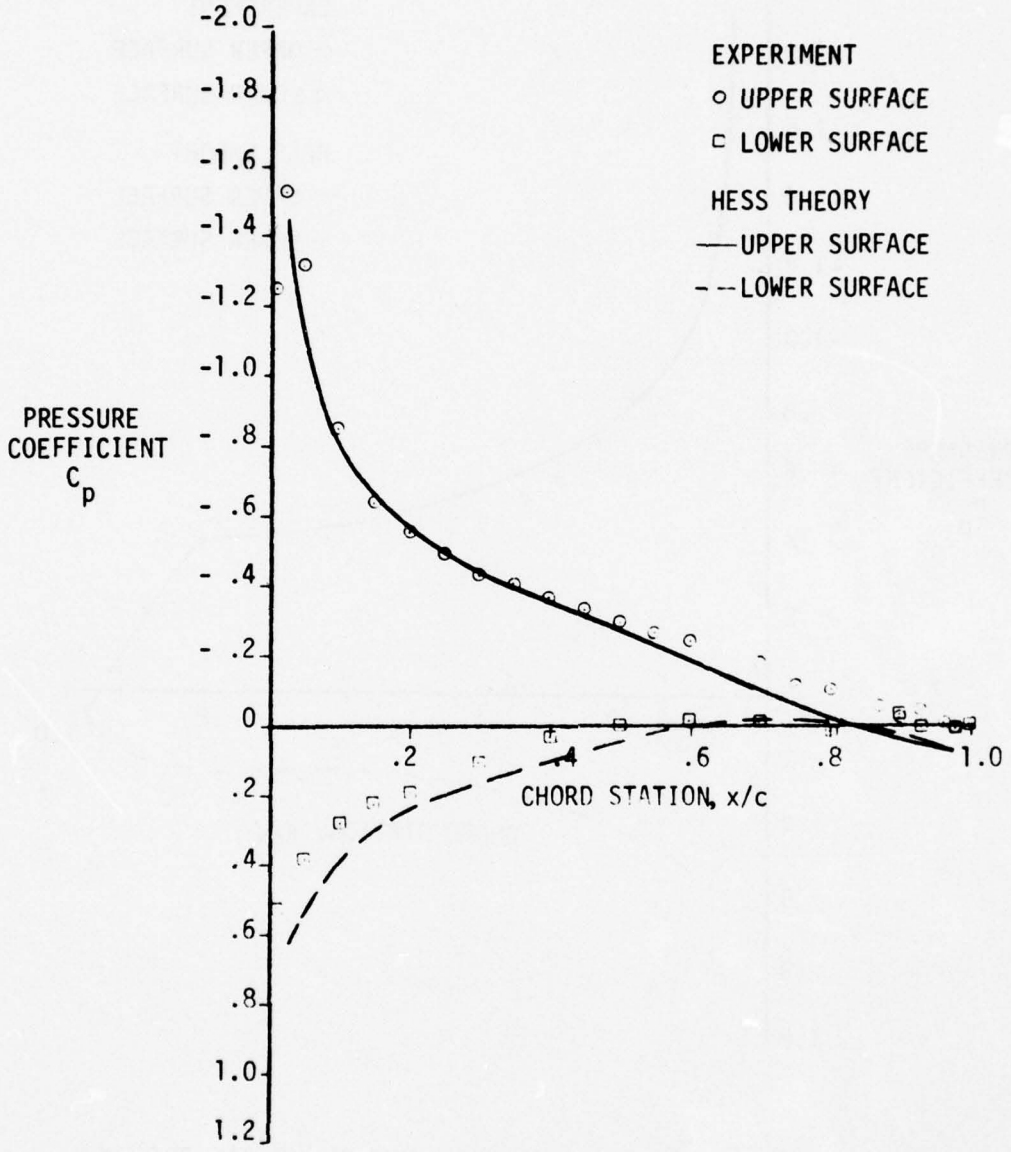

FIGURE 15 COMPARISON OF EXPERIMENTAL AND CALCULATED PRESSURE DISTRIBUTIONS FOR CONFIGURATION L6/TO, M=.6, α=5.984°, n=.7

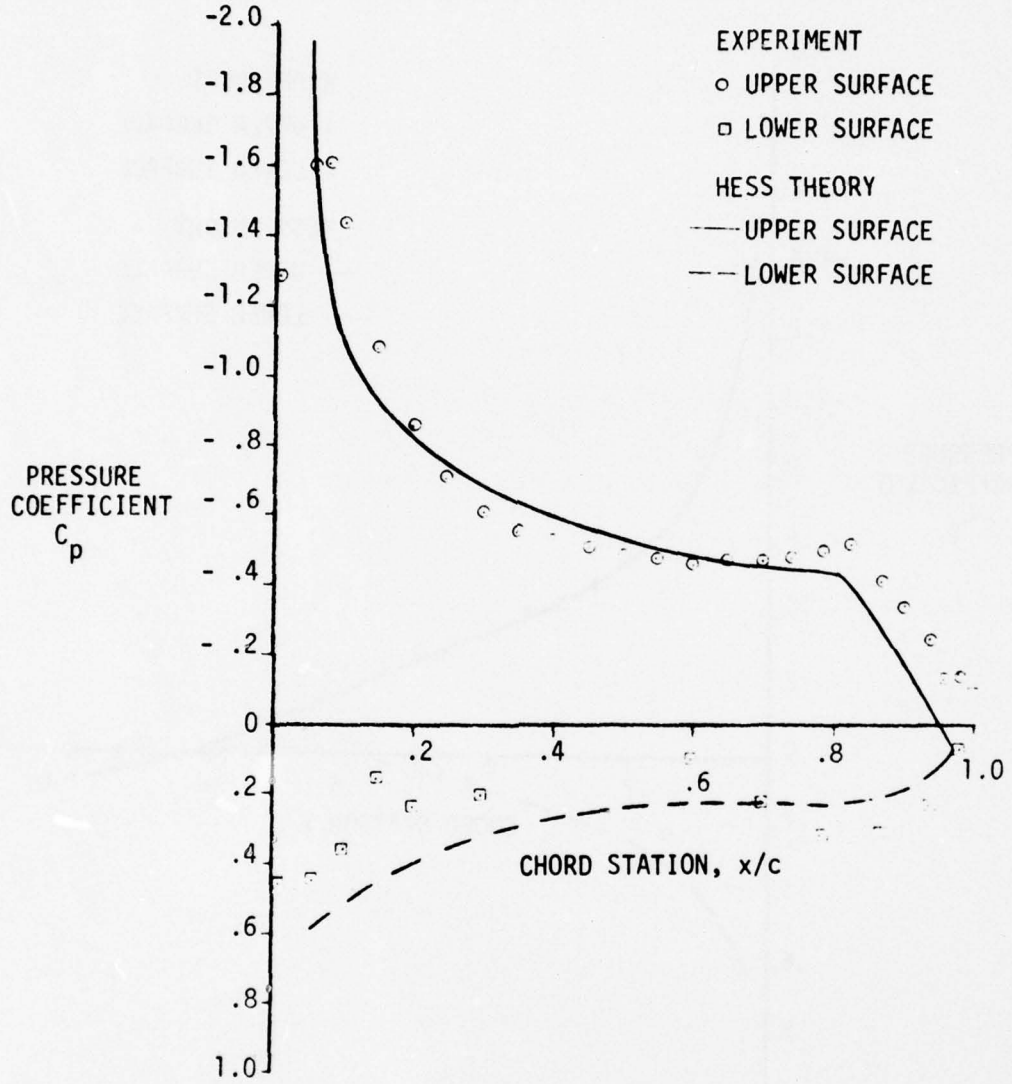

FIGURE 16 COMPARISON OF EXPERIMENTAL AND CALCULATED PRESSURE DISTRIBUTIONS FOR CONFIGURATION L6/T15, M=.6, α=6.026°, n=.4

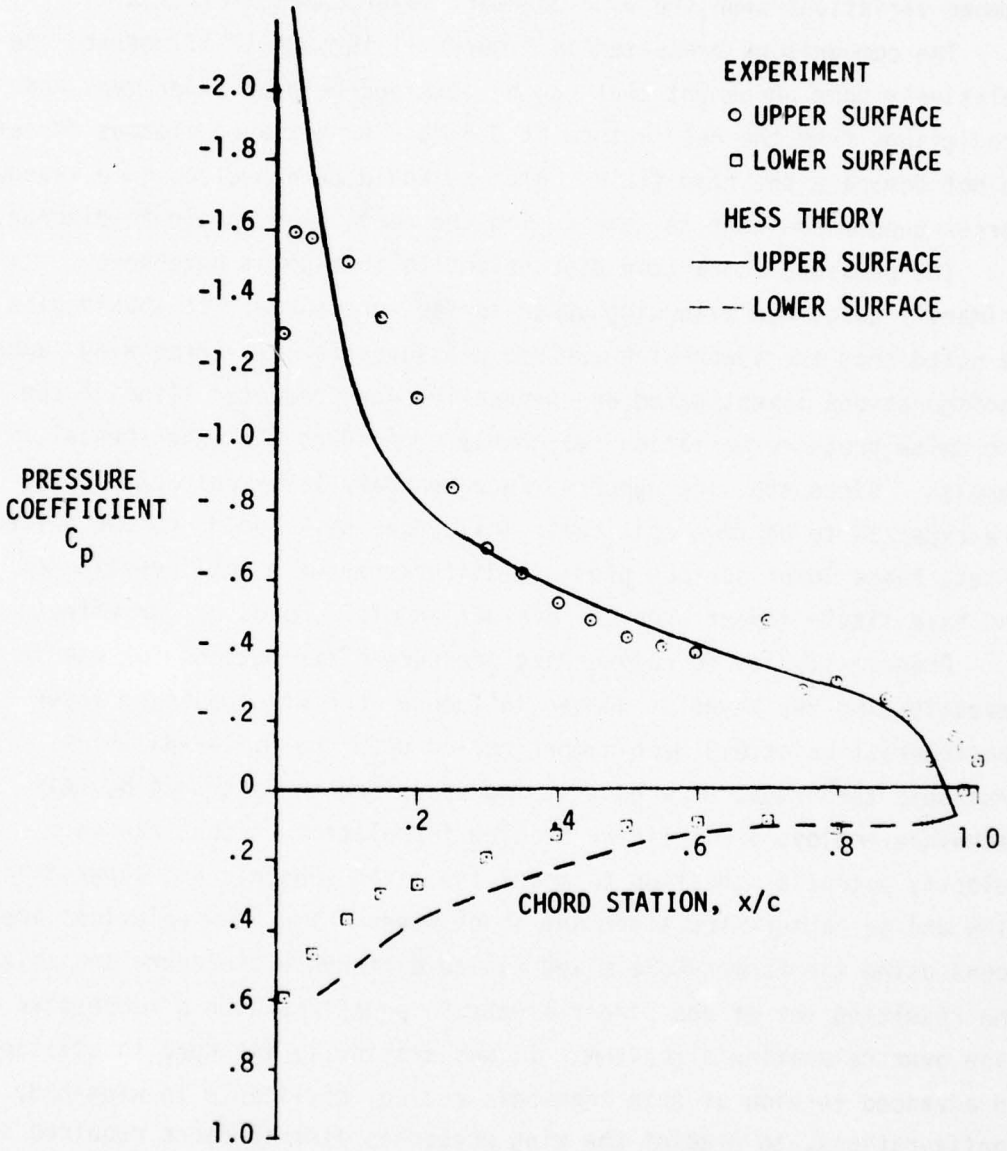

FIGURE 17 COMPARISON OF EXPERIMENTAL AND CALCULATED PRESSURE DISTRIBUTIONS FOR CONFIGURATION L6/T15, M=.6, α=6.026°, n=.7

stations. In either circumstance, since the calculated pressure gradients are representative of that from the experimental results, the predicted pressure should permit a valid assessment of the effect of Reynolds number variations upon the wing boundary layer characteristics.

The comparisons presented in Figures 11 through 17 illustrate the relatively good agreement that can be obtained between experiment and predictions from the Hess method at 0.6 Mach number when viscous forces do not dominate the flow field. Also as would be expected, once viscous forces become dominant in some region the comparisons begin to diverge.

The pressure comparison discussions to this point have been primarily concerned with wing upper surface pressures. It should also be noted that the lower wing surface pressures for all three wing camber configurations investigated are generally over predicted although the chordwise pressure variation reasonably reproduces the experimental results. Since the wing upper surface boundary layer characteristics are expected to be more critically influenced by Reynolds number differences, these lower surface pressure differences were not investigated and have little impact upon the evaluation of Reynolds number effects.

Program studies to define wing pressure distributions for use in investigating the Reynolds number influence upon wing boundary layer characteristics at 0.9 Mach number relied upon the Bailey-Ballhaus transonic technique, Reference 9. As described in Reference 8, this technique employs a non-linear problem formulation of the transonic velocity potential equation to model the mixed subsonic and supersonic flow and to capture the attendant shock waves. The flow solutions are found using the Murman-Cole mixed finite difference procedure and solving the resulting set of non-linear algebraic equations with a successive line over relaxation algorithm. It was originally intended to utilize an advanced version of this transonic coding, applicable to wing-body configurations, to predict the wing pressures distributions required in investigating Reynolds number effects. Since this program, which is being developed by NASA Ames, was not available in the time frame required by these studies, the isolated wing prediction coding was utilized. As a consequence, good correlation between predictions and experimental pressures were not expected and indeed not obtained. Direct comparisons

of the predicted isolated wing and experimental wing-body configuration pressure data are presented in Figures 18 through 23 to illustrate these differences. Figures 18 and 19 provide comparisons for wing camber configuration L0/T0 at an angle of attack of 6 degrees. Since this angle of attack is beyond the experimentally defined buffet onset angle of attack (see Table 3), the high loading shown near the leading edge is not expected to be attained in flight due to viscous effects. For the more inboard span station, the theoretical calculations reasonably reproduce the shock wave location at approximately the wing mid-chord station. On the outboard station, viscous effects obviously dominate the flow from leading to trailing edge and consequently little agreement is observed in the upper wing surface pressures. Also the lower wing surface pressures differ from predicted in a manner similar to that noted for the 0.6 Mach number pressure comparisons.

Experimental and calculated wing pressures for a leading edge camber configuration, L6/T0, are shown in Figures 20 and 21 for an angle of attack of 4 degrees. Differences between the experimental and calculated results in this comparison are not as severe as those noted for the uncambered wing, Figures 18 and 19. Indeed, for this lower angle of attack which is near the experimentally defined buffet onset angle, viscous and/or body interference effects should be reduced and the observed effects are to be expected.

A final 0.9 Mach number comparison of predicted isolated wing and experimental wing-body configuration pressures for a combined leading and trailing edge camber configuration, L6/T1, is shown in Figures 22 and 23. For this case, where the angle of attack is below that predicted for buffet onset, differences are still evident between the calculated and experimental pressures. These comparisons, as well as others obtained in this study, suggest that the Bailey-Ballhaus transonic potential flow solution method yields a predicted shock wave location which is consistently farther aft on the wing than indicated by the experimental results. Also the experimental results shown in Figure 22 suggest the presence of one or more shock waves on the forward portion of the wing which are not reproduced in the theoretical predictions.

As a consequence of the noted differences between the 0.9 Mach number experimental and predicted wing pressures, the question of the validity of using these predictions in evaluating Reynolds number effects for the present studies as well as the adequacy of this theoretical method must be addressed. First, since this method is purely a potential flow technique differences due to viscous effects are to be expected. Secondly, since this method is based upon the assumption of small disturbances, differences between predicted and experimental pressures in regions where this assumption is violated, such as near the wing leading edge, are also understandable. Thirdly, the limited agreement between predicted and experimental shock wave locations may be the result of the fact that this method obtains solutions to the flow field at specific points which are defined by a user supplied computational grid. Consequently the possibility exists that improved correlations of the shock wave positions may be achievable with a computational grid different from that used in the studies of this program. Verification of this possibility, which may entail development of a specific computational grid for each individual camber configuration, was judged beyond the scope of the present investigations. Also, these theoretical predictions did not reproduce the forward shock waves suggested by the experimental results, Figure 22. This deficiency may also be related to the input computational grid or may possibly be the result of a body effect which is not represented in the analytical method. These comments, however, do not necessarily negate the usefulness of the predicted wing pressures in evaluating the Reynolds number effects upon results from the LRC test series. There are reasonable similarities between the analytical and experimental chordwise pressure variations. Use of pressures should provide reasonably valid evaluations of the type of flow separation expected for both tunnel and free flight conditions as well as valid indications of the effect of differences between tunnel and flight Reynolds numbers upon the wing boundary layer characteristics. This rationale has been the basis for using the predicted isolated wing pressures in the wing boundary layer investigations discussed in the following section.

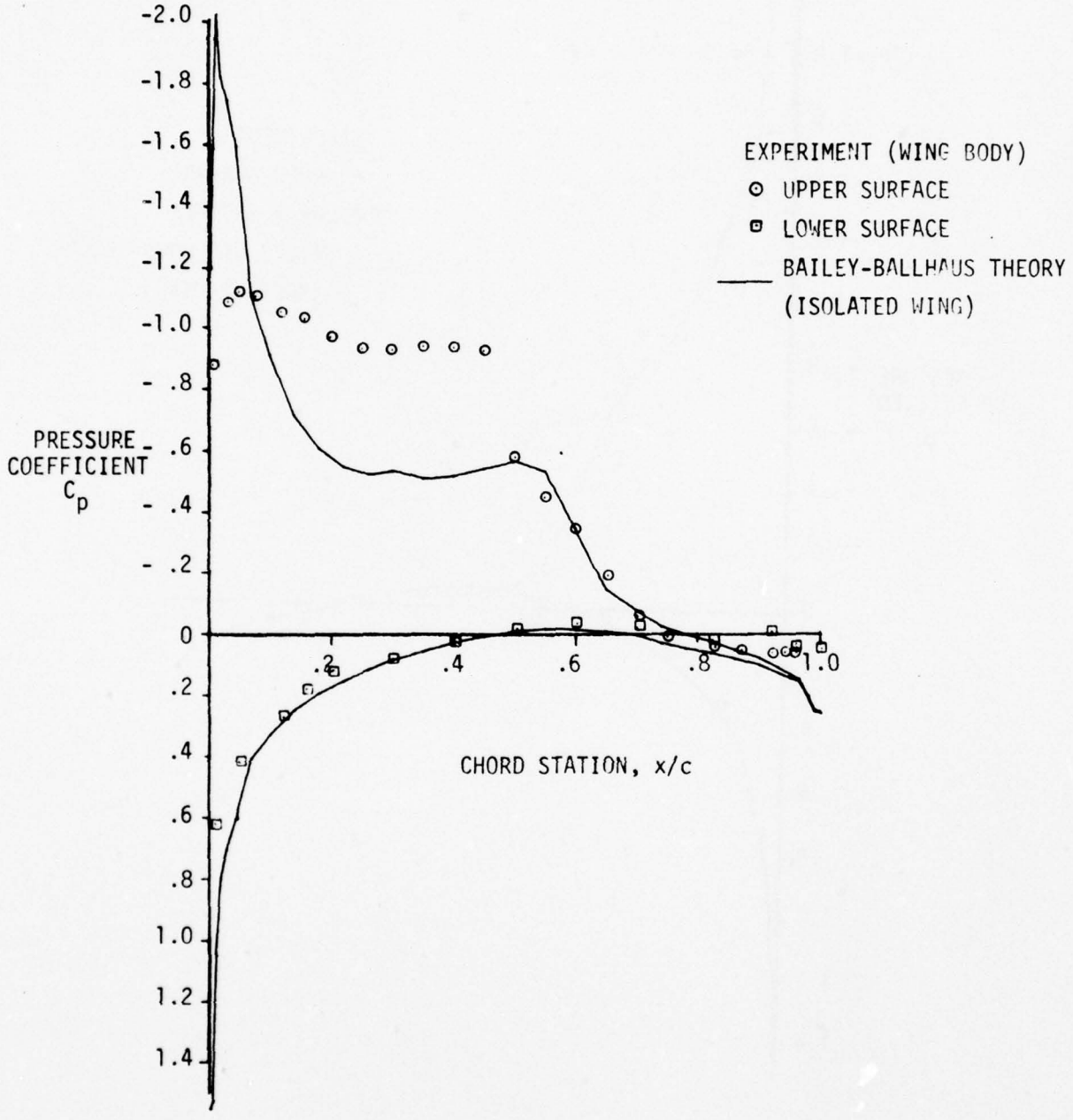

FIGURE 18 COMPARISON OF EXPERIMENTAL AND CALCULATED PRESSURE DISTRIBUTIONS FOR CONFIGURATION LO/TO, M=.9, $\alpha=6^{0}$, $\eta=.56$

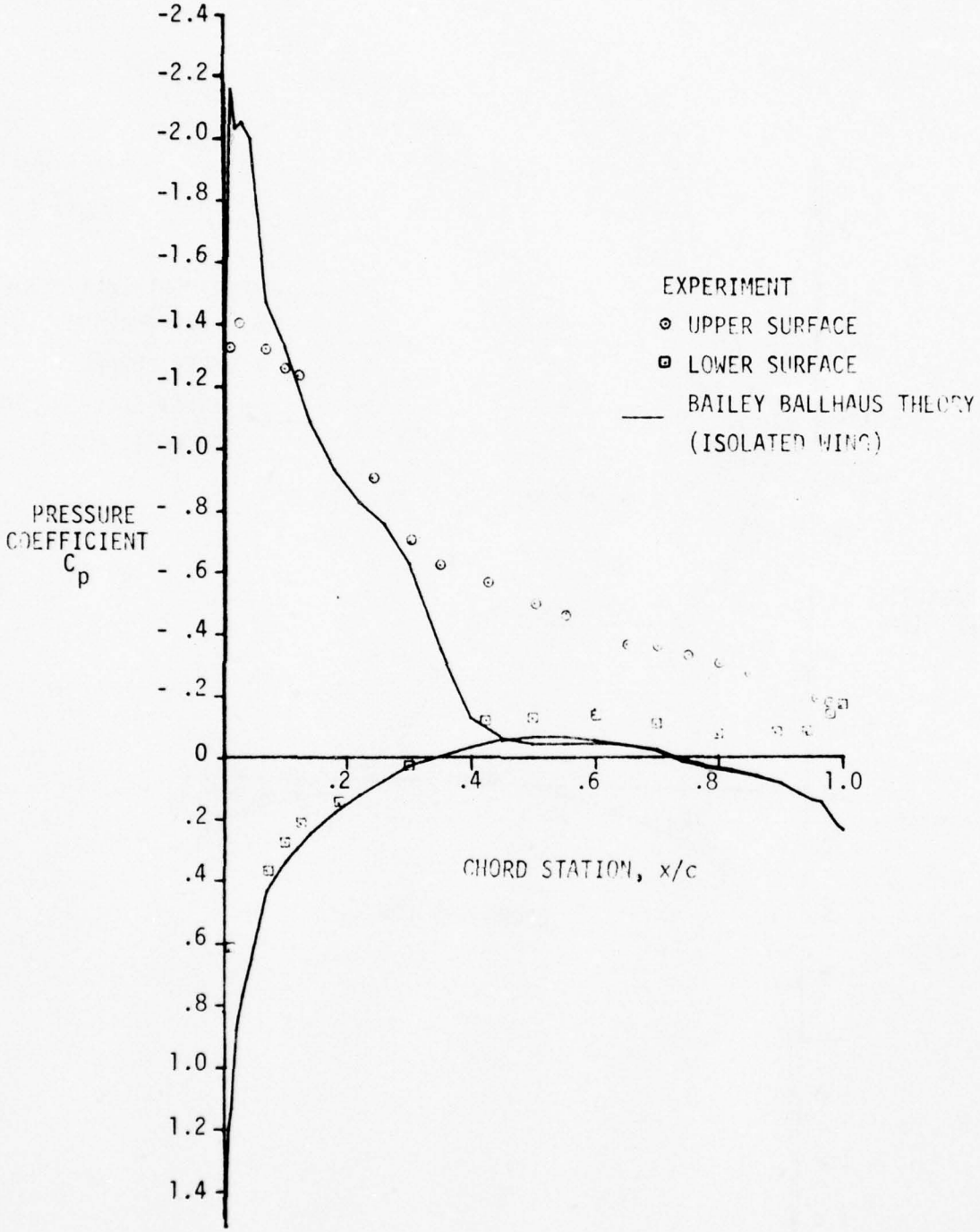

FIGURE 19 COMPARISON OF EXPERIMENTAL AND CALCULATED PRESSURE DISTRIBUTIONS FOR CONFIGURATION LO/TO, M=.9, $\alpha=6^{o}$, $\eta=.85$

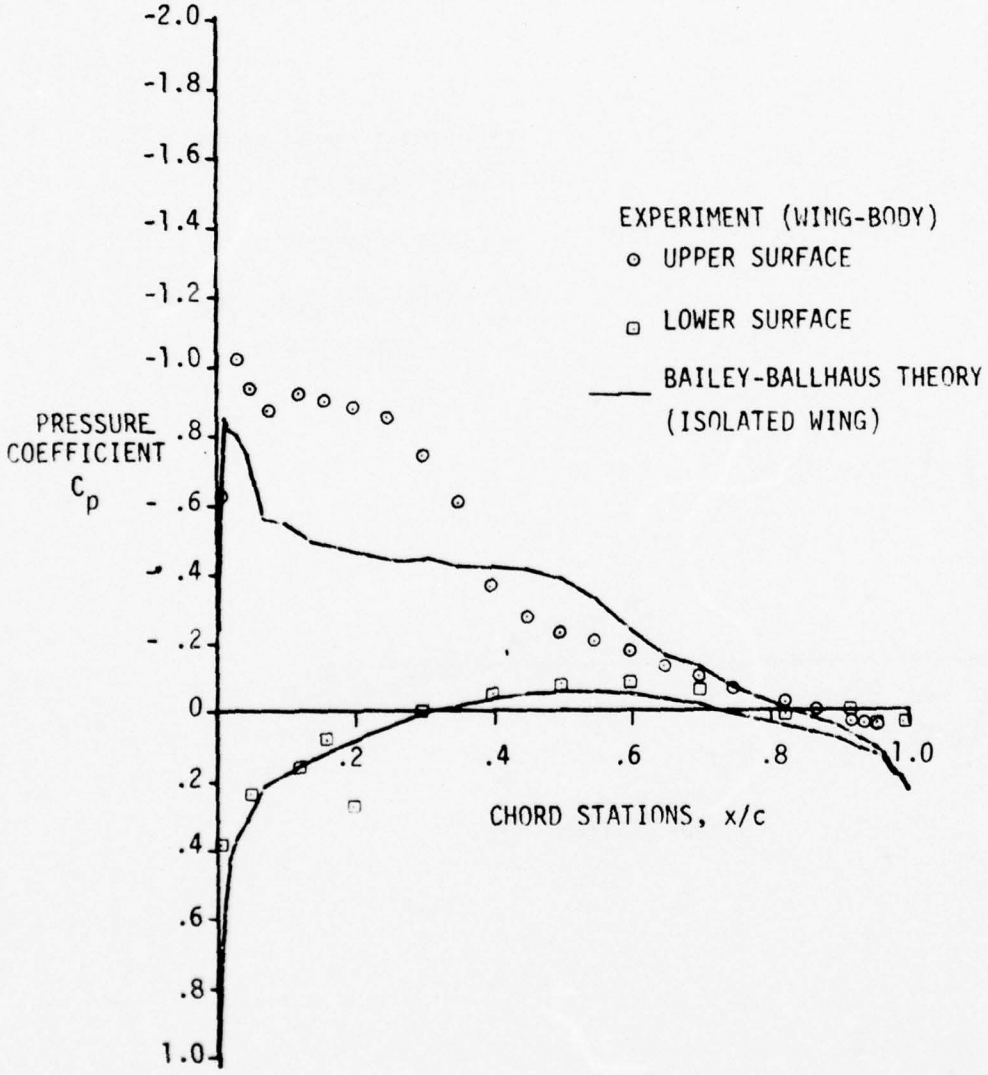

FIGURE 20 COMPARISON OF EXPERIMENTAL AND CALCULATED PRESSURE DISTRIBUTIONS FOR CONFIGURATION L6/TO, M=.9, $\alpha=4^{o}$, $\eta=.56$

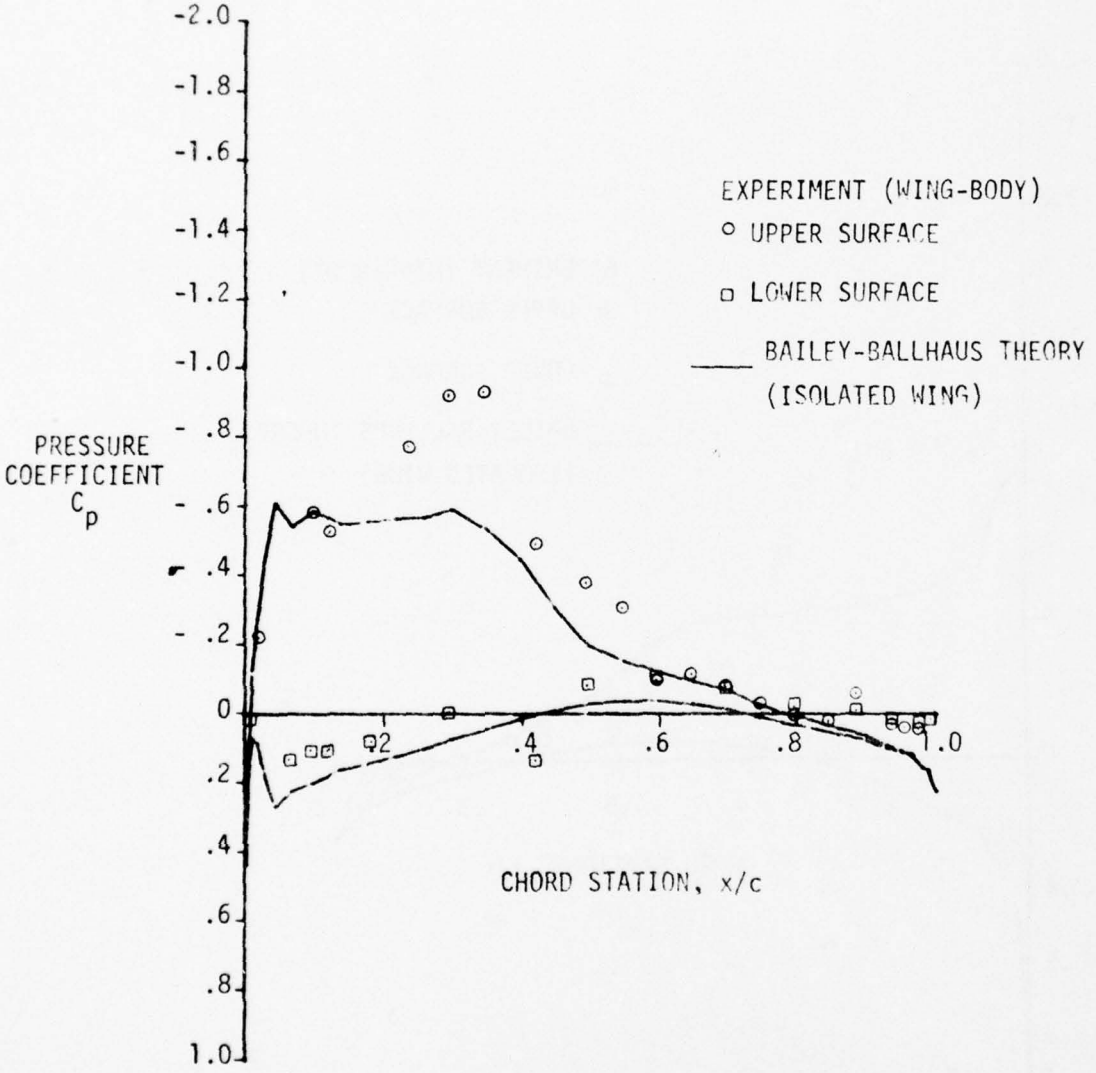

FIGURE 21 COMPARISON OF EXPERIMENTAL AND CALCULATED PRESSURE DISTRIBUTIONS FOR CONFIGURATION L6/TO, M=.9, α=4°, η=.85

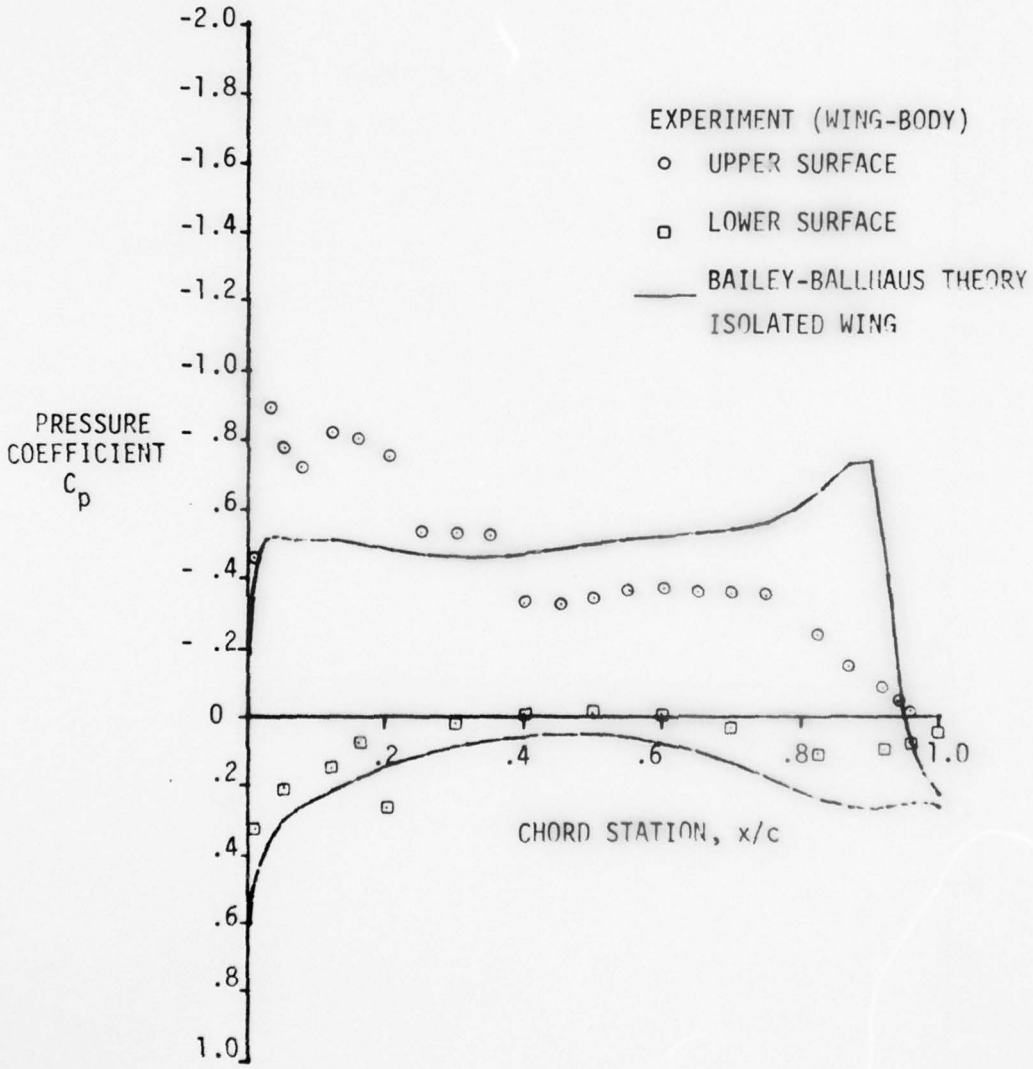

FIGURE 22 COMPARISON OF EXPERIMENTAL AND CALCULATED PRESSURE DISTRIBUTIONS FOR CONFIGURATION L6/T1, M=.9, $\alpha=3^{o}$, $\eta=.54$

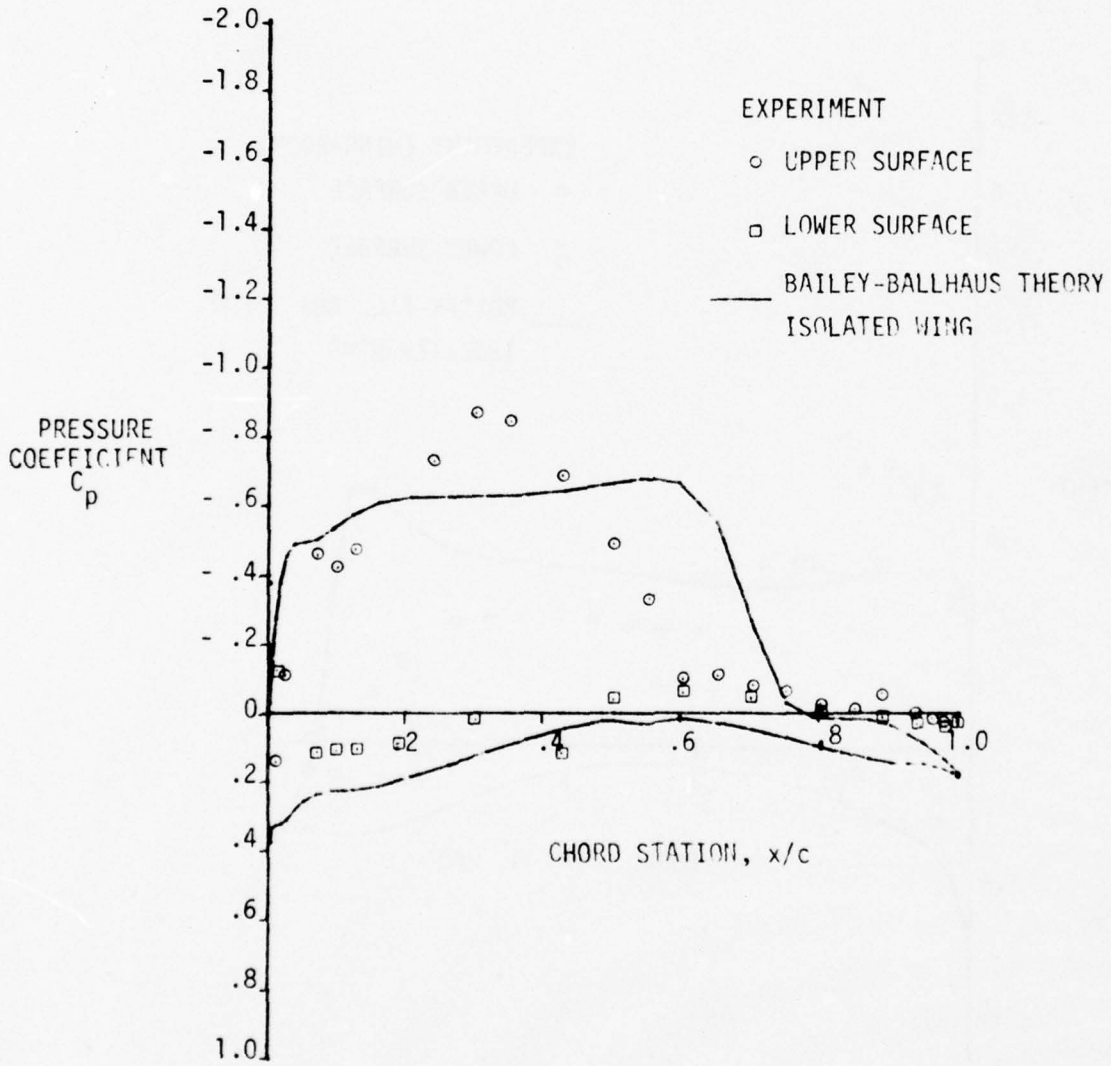

FIGURE 23 COMPARISON OF EXPERIMENTAL AND CALCULATED PRESSURE DISTRIBUTIONS FOR CONFIGURATION L6/T1, M=.9, $\alpha=3^{o}$, $\eta=.8108$

Predicted Boundary Layer Characteristics

The boundary layer technique used in this study, Reference 10, solves the boundary layer equations using an integral approach in both the laminar and turbulent regions. The separation location for the laminar region is determined by the wall shear stress, τ_ω, becoming negative. In the turbulent case, separation is predicted when the boundary layer form factor, H, attains a value of 2.8. Transition from laminar to turbulent flow is determined using the method of Schlichting-Ulrich-Granville. In addition, if separation is predicted prior to transition, the flow can be forced to transition to turbulent flow at this point. This latter option was used throughout the investigations of this study in order to ascertain whether the flow if reattached would again separate in the turbulent region.

The boundary layer analysis was performed for streamwise sections at several spanwise stations. It is realized that this "strip analysis" is not an exact solution to the three-dimensional boundary layer problem, in that cross flow components are ignored. However, since no compressible solution to the three dimensional boundary layer problem exists, this strip analysis, which gives at least a first order approximation to the boundary layer solution, was used.

This boundary layer analysis method was used in conjunction with the potential flow pressures predicted by the Hess method for a Mach number of 0.6 without difficulty. When the technique was employed using the 0.9 Mach number pressure predictions from the Bailey-Ballhaus potential flow solution, a minor problem was encountered. The method of Reference 10, due to limitations in the basic formulation of the Cohen and Reshotko laminar boundary layer solution method, fails for very large or extensive favorable pressure gradients like those predicted from the transonic flow solution. This problem was circumvented in these studies by fixing the transition location earlier than would normally have been done. The errors introduced in defining the effects of Reynolds number variations upon wing force and boundary layer characteristics using this approach were considered justifiably small since the difference between expected transition and that prescribed was only a few percent of wing chord.

Typical results from the boundary layer analyses are presented in Figures 24 through 31 for four different wing camber configurations and Reynolds numbers corresponding to the wind tunnel tests and flight altitudes of 20,000 and 30,000 feet. Figure 24 presents results for configuration LO/TO, the uncambered wing configuration, at Mach numbers of 0.6 and 0.9 and angles of attack of 6 and 4 degrees, respectively. These angles of attack were chosen for discussion because they are near the experimentally defined angles for buffet onset.

Figure 24a shows the trailing edge boundary layer displacement thickness variation with Reynolds number for both upper and lower wing surfaces as a function of wing span station. In the analysis for tunnel conditions, the boundary layer transition was fixed at 5 percent chord for both surfaces since the test data were obtained with transition fixed on the model at this location. The flight Reynolds number investigations were initially performed allowing for free transition on both wing surfaces. Little difference is noted in the upper surface trailing edge displacement thickness due to these transition differences because the analytical transition location for all Reynolds numbers was established by a laminar separation occurring in the first 5 percent of wing chord. The lower surface wing trailing edge displacement thicknesses shown in Figure 24a indicate significant variation due to the differences in flight and tunnel Reynolds numbers. This effect occurs because the lower surface pressure gradients are favorable for most of the wing chord which results in the transition location for the flight Reynolds number cases being predicted well aft on the airfoil section. Thus, the region of laminar flow was predominant in the flight Reynolds number cases giving displacement thicknesses which are small compared to the tunnel Reynolds number case with transition fixed near the leading edge. The actual free flight transition location would be expected near the leading edge due to the influence of surface roughness, which is not considered in the Reference 10 analysis technique. The impact of this analysis result will be addressed later when the effects of Reynolds number on drag is discussed. For the 0.9 Mach number conditions presented in Figure 24b, this effect is not observed since transition

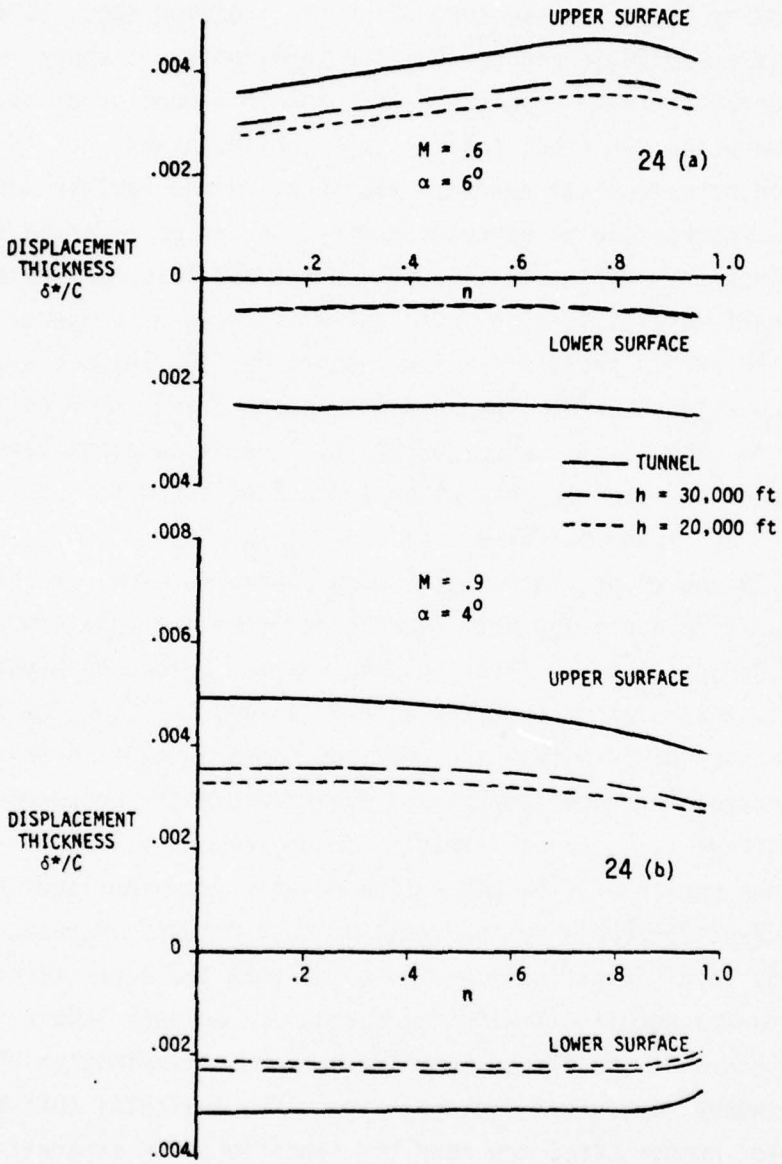

FIGURE 24 REYNOLDS NUMBER EFFECT ON DISPLACEMENT THICKNESS FOR CONFIGURATION LO/TO AT M=.6 AND .9

was fixed on the lower surface for all Reynolds numbers. Therefore the Figure 24b results are considered to reflect a more valid prediction of the effect of Reynolds number on the trailing edge displacement thickness for this configuration.

The boundary layer form factor, H, at the trailing edge, is presented for configuration L0/T0 in Figure 25. The form factor is shown to be essentially invarient with Reynolds number for this configuration. No turbulent separation was predicted for this configuration, but laminar separation did occur for all spanwise stations. Since laminar separation is relatively insensitive to Reynolds number, it can be inferred from this result that the prediction of buffet onset for this configuration using the tunnel results is also invarient with Reynolds number.

Figures 26 and 27 present similar results for the leading edge camber configuration, L6/T0. The Reynolds number effects for L6/T0 are essentially the same as discussed for L0/T0. The discussions regarding transition location, laminar separation and buffet onset for L0/T0, for both upper and lower surfaces also apply to L6/T0.

Figures 28 amd 29 provide similar wing boundary layer predictions for a configuration involving both leading and trailing edge camber, L6/T15, at 0.6 Mach number. These results show an effect of Reynolds number variation similar to that for configurations L0/T0 and L6/T0 but this configuration differs from the previous cases in that for this configuration trailing edge separations are predicted to occur on the upper wing surface from approximately 50 to 85 percent of the wing semispan. This region of flow separation results from the large adverse pressure gradients produced by the trailing edge camber. Results from these boundary layer investigations indicated that the separations occur only at the tunnel conditions with the turbulent boundary layer remaining attached at the flight Reynolds numbers. Examination of the predicted boundary layer form factors, Figure 29, indicates that the flight Reynolds number cases are near the conditions for separation. The boundary layer predictions for this configuration also indicate that laminar separations occur near the leading edge of this configuration which contributes to the tendency of turbulent separation as well as onset of wing buffet.

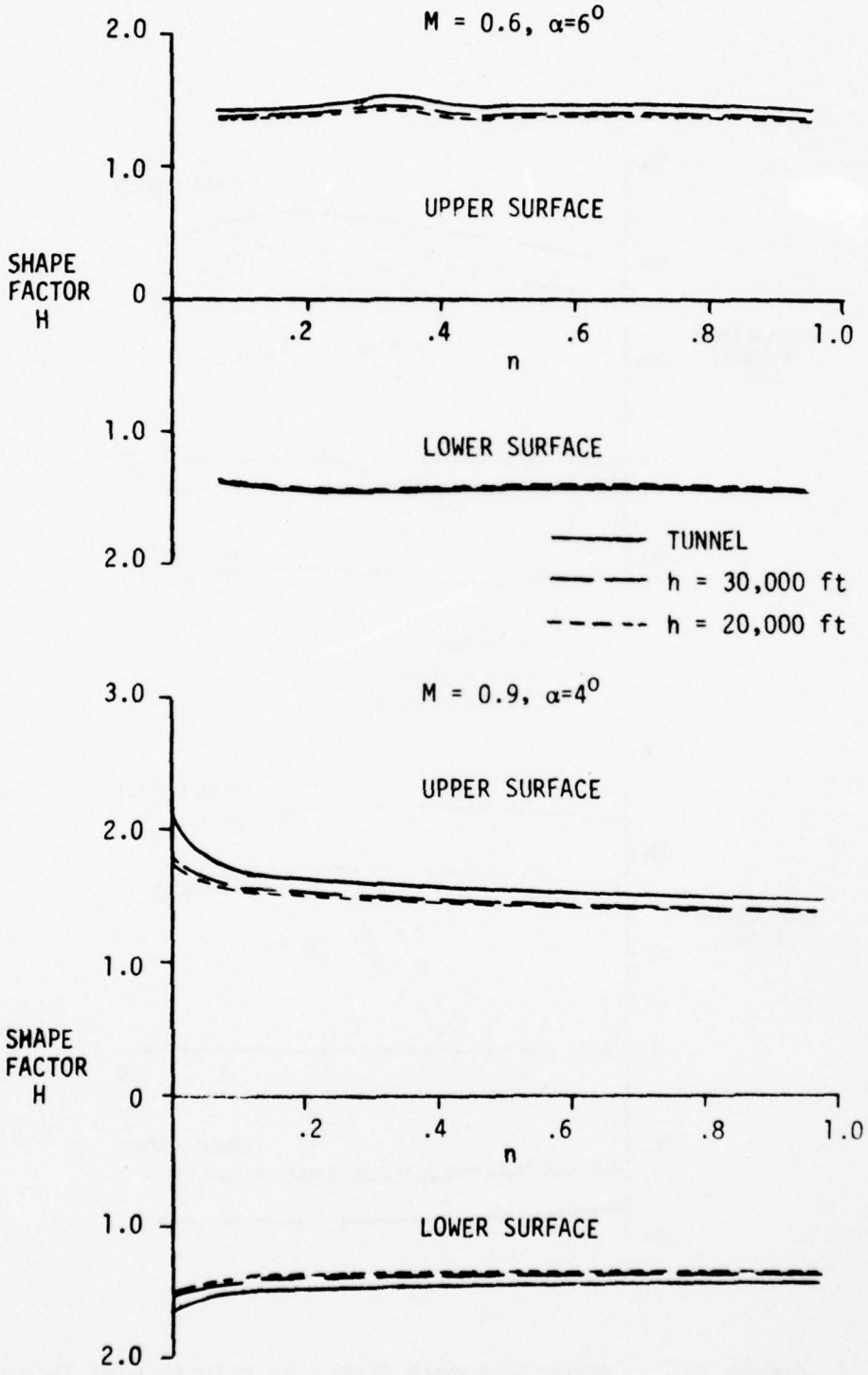

FIGURE 25 REYNOLDS NUMBER EFFECT ON SHAPE FACTOR FOR CONFIGURATION LOTO AT M=.6 AND .9

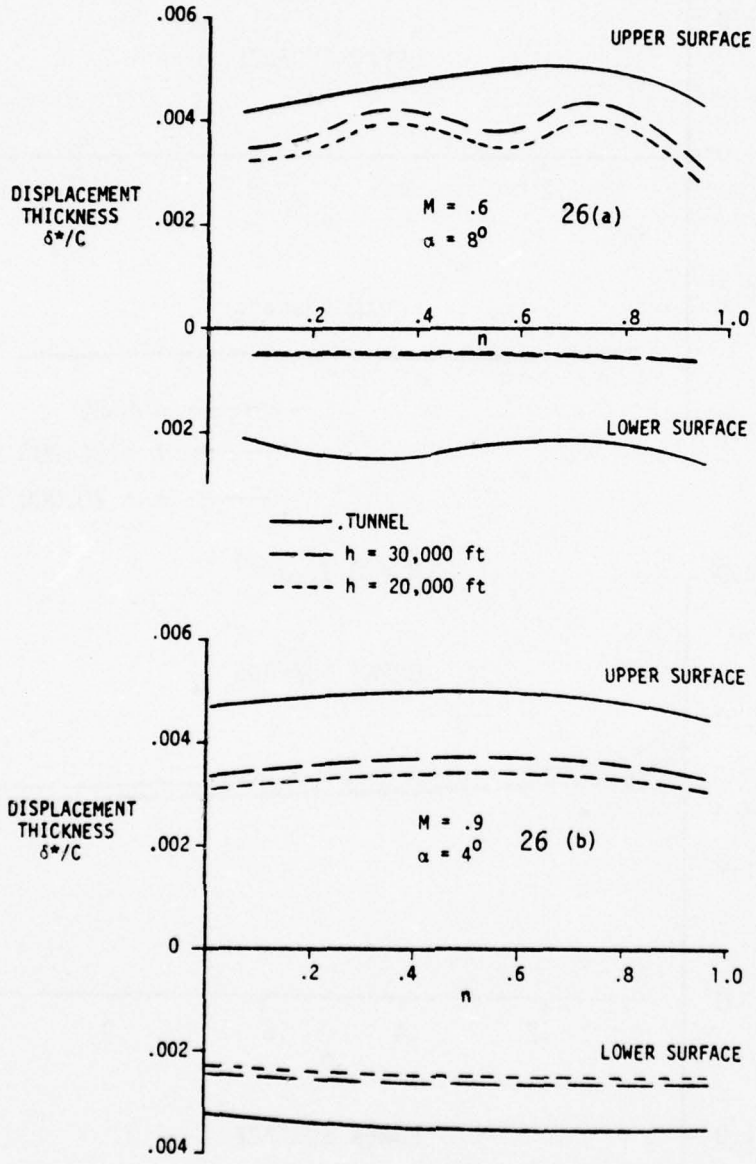

FIGURE 26 REYNOLDS NUMBER EFFECT ON DISPLACEMENT THICKNESS FOR CONFIGURATION L6/TO AT M=.6 AND .9

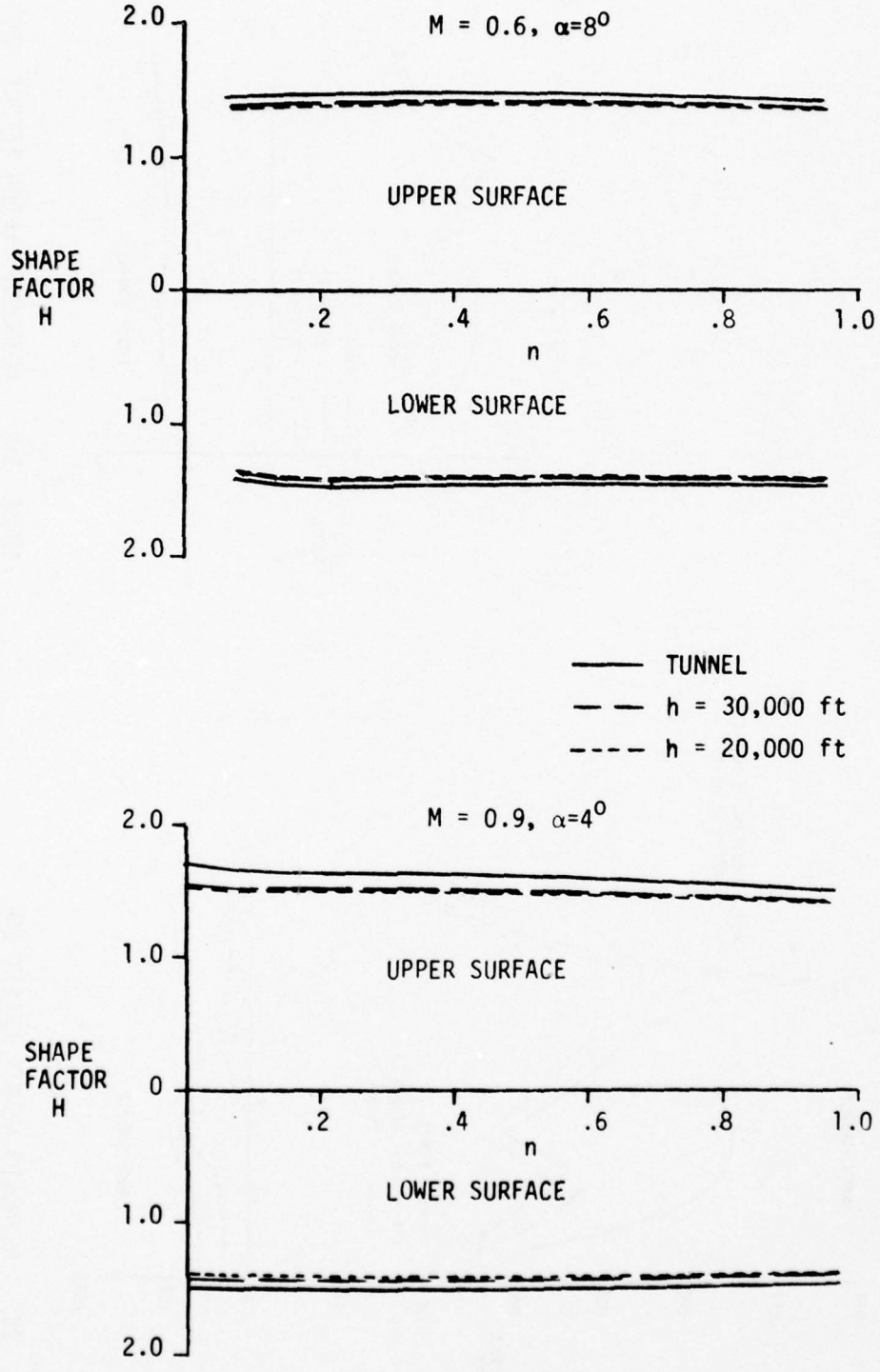

FIGURE 27 REYNOLDS NUMBER EFFECT ON SHAPE FACTOR FOR CONFIGURATION L6TO at M=.6 and .9

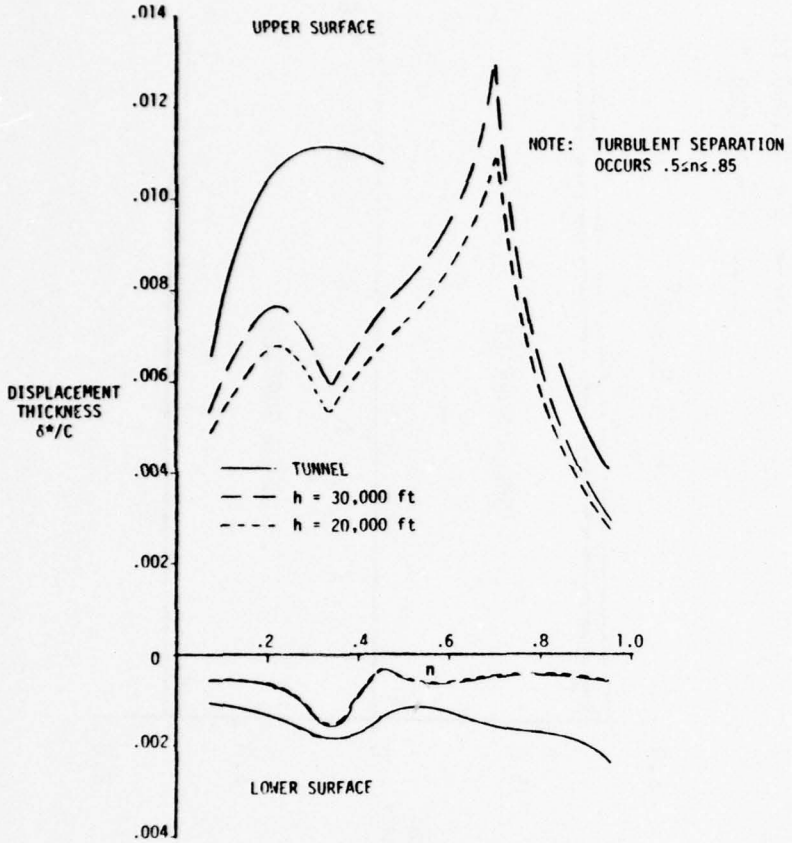

FIGURE 28 REYNOLDS NUMBER EFFECT ON DISPLACEMENT THICKNESS FOR CONFIGURATION L6/T15, M=.6, $\alpha=6^{o}$

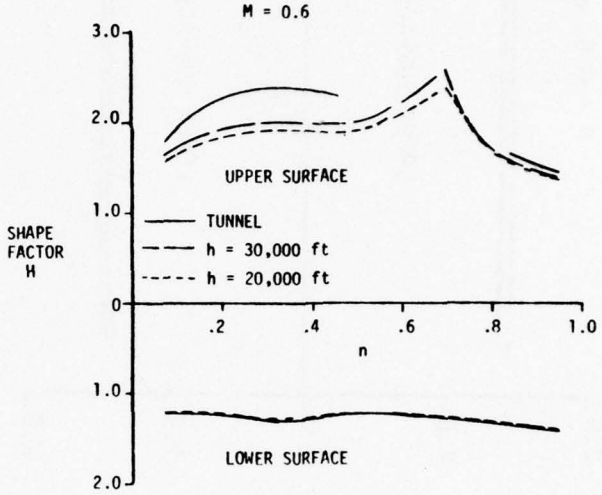

FIGURE 29 REYNOLDS NUMBER EFFECT ON SHAPE FACTOR FOR CONFIGURATION L6T15, M= .6, $\alpha=6^{o}$

Figures 30 and 31 illustrate the boundary layer characteristics for a combined leading and trailing edge wing camber configuration, L6/T1, at 0.9 Mach number. Analysis of this configuration is further complicated by the presence of shock waves in the flow field. The shock waves, present at this angle of attack for most of the configuration spanwise stations, vary in intensity and location. The analysis methods of Reference 10 are not strictly applicable to shock wave/boundary layer interaction. In the analysis for this study, the shock waves were treated as relatively sharp increases in pressure but the pressure rise was forced to occur over a finite chordwise length. This approach while not theoretically correct, does provide an indication of the boundary layer characteristics. The flow separations indicated in Figures 30 and 31, which are typical of the results obtained for this configuration, occur at chordwise locations corresponding to the pressure rise associated with the wing shock waves. Variations in Reynolds number representative of the tunnel and free flight conditions had negligible effect upon the position of initial flow separations.

The boundary layer analysis results discussed above, even with the noted analysis deficiencies and assumptions, do allow an assessment of the Reynolds number effects upon the wing camber configurations considered in this study. Considering first the effects of Reynolds number upon the effective wing geometry, the maximum change to wing thickness as indicated by the total trailing edge displacement thickness is shown to be less than approximately one percent of the chord for all span stations. The relative change in wing thickness due to differences in tunnel and flight Reynolds numbers is on the order of 0.5 percent of the wing chord or less. Such small variations in the effective wing geometry can be expected to produce negligible changes in the wing pressure distributions. Consequently, for this study, the effects of tunnel and flight Reynolds number differences upon the wing lift and pitching moment prior to flow separation can be neglected and the tunnel test results can be used without Reynolds number corrections. The initial flow separations identified in these boundary layer investigations were of either the leading edge or shock induced type. Thus, the boundary layer investigation results support the conclusions obtained from analysis of test

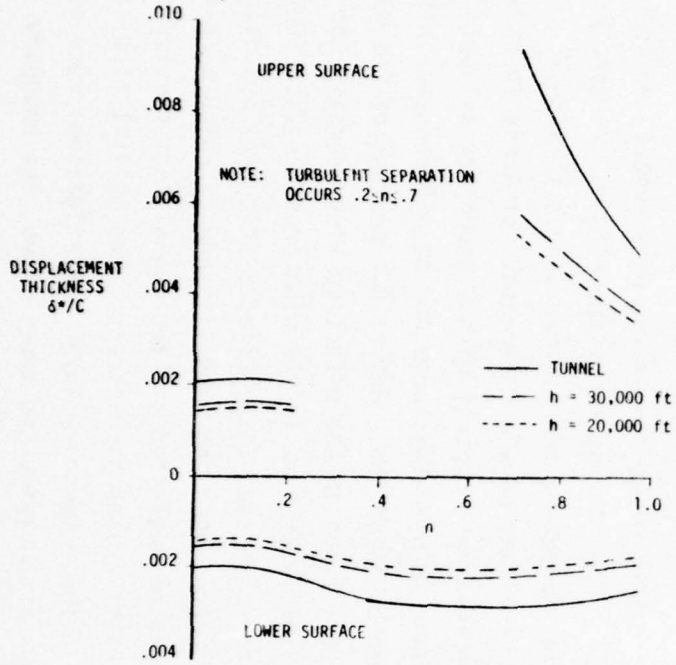

FIGURE 30 REYNOLDS NUMBER EFFECT ON DISPLACEMENT THICKNESS FOR CONFIGURATION L6/T1, M= .9, $\alpha=3^{o}$

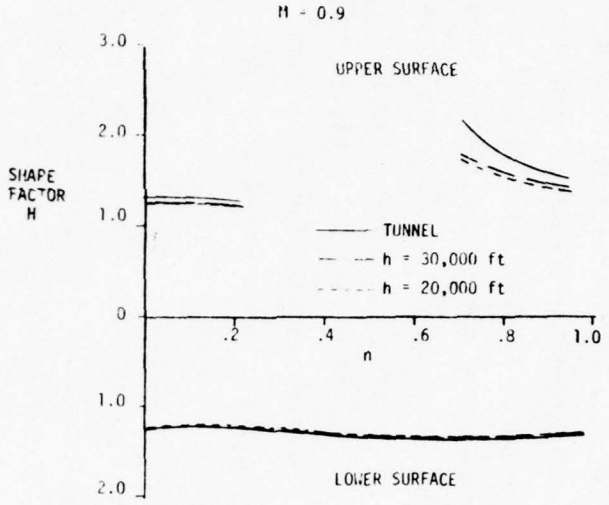

FIGURE 31 REYNOLDS NUMBER EFFECT ON SHAPE FACTOR FOR CONFIGURATION L6/T1, M=.9, $\alpha=3^{o}$

results concerning the type of flow separations which induced the onset of wing buffet. Based upon this agreement, the wind tunnel test results for buffet onset should be a valid indication of the wing characteristics at free flight altitudes of 20,000 and 30,000 feet.

Experimental Data Corrections

Results from the wing boundary layer investigations were utilized to aid in defining the necessary corrections to the LRC wind tunnel test results to account for the tunnel and flight Reynolds number differences. As discussed above, no corrections to the wing lift and pitching moment data were considered necessary due to the small effect of the Reynolds number differences upon the boundary layer displacement thickness. Thus, only the experimental drag data required correction. In particular, since the induced drag is a function of span only, no correction is required to the wing induced drag, C_{D_i}. The necessary corrections to drag are strictly applicable to the profile drag coefficient, or in this study, the experimental value of drag at zero lift, C_{D_o}, was modified.

Predictions of the profile drag for the configurations included in the wing boundary layer investigations were obtained by calculating the sectional profile drags, c_{d_p}, and then performing a spanwise integration. The sectional profile drag predictions were accomplished using a procedure based upon that developed by Squire and Young. The Squire-Young technique for incompressible flow relates the boundary layer trailing edge momentum thickness, $\theta_{T.E.}$, shape factor, $H_{T.E.}$, and velocity ratio, $(U/U_\infty)_{T.E.}$, to the momentum thickness far downstream, θ_∞. For incompressible conditions, the sectional profile drag is obtained from the relationship;

$$c_{d_p} = 2\theta_\infty$$

Profile drag predictions based upon this approach have been shown, Reference 11, to agree very well with experimentally determined drag values. Profile drag predictions for this study were obtained by using Stewartson's transformations to modify the Squire-Young approach to

include the effects of compressibility. The resulting compressible form of the Squire-Young relationship is given by:

$$c_{d_p} = 2f_{re_{T.E.}}^{.789}\left[1 + .2M_\infty^2\right]^{.76}\left[\frac{M_{e_{T.E.}}}{M_\infty}\right]^{\frac{H_{T.E.}+3}{2}}\frac{1}{R_N}$$

where:

$f_{re_{T.E.}}$ = Boundary layer growth parameter as computed by the McNalley program, Reference 10

$M_{e_{T.E.}}$ = Mach number at the outer edge of the boundary layer at the trailing edge

R_N = Free stream Reynolds number $\frac{U_\infty C}{\nu}$; C = Airfoil chord

M_∞ = Free stream Mach number

This equation was used to determine the wing profile drag as a function of angle of attack and Reynolds number for each of the configurations included in the boundary layer investigations. Figure 32 presents predicted results for configuration LO/TO at 0.6 and 0.9 Mach number respectively. The results shown in Figure 32a indicate a much larger decrease in drag between tunnel and flight Reynolds number than is shown in Figure 32b. This difference is a result of the lower surface transition location as discussed earlier. Figure 33 illustrates the chordwise distribution of displacement thickness as a function of Reynolds number and transition location. The lower surface values at 20,000 ft altitude for free transition show that transition occurred at approximately eighty to ninety percent chord depending on the spanwise location. If this transition location is fixed near the leading edge, the displacement thickness increases considerably as shown in Figure 33. In Figure 32a, the lower surface transition location determined by the boundary layer program was fairly well aft on the airfoil, while in Figure 32b the transition location was fixed at 7% on the lower surface. Since the transition on both surfaces in flight will normally be near the leading edge due to surface roughness, calculations were performed for an angle of attack of 4 degrees at 0.6 Mach number with transition fixed on the lower surface. These calculations showed a drag reduction

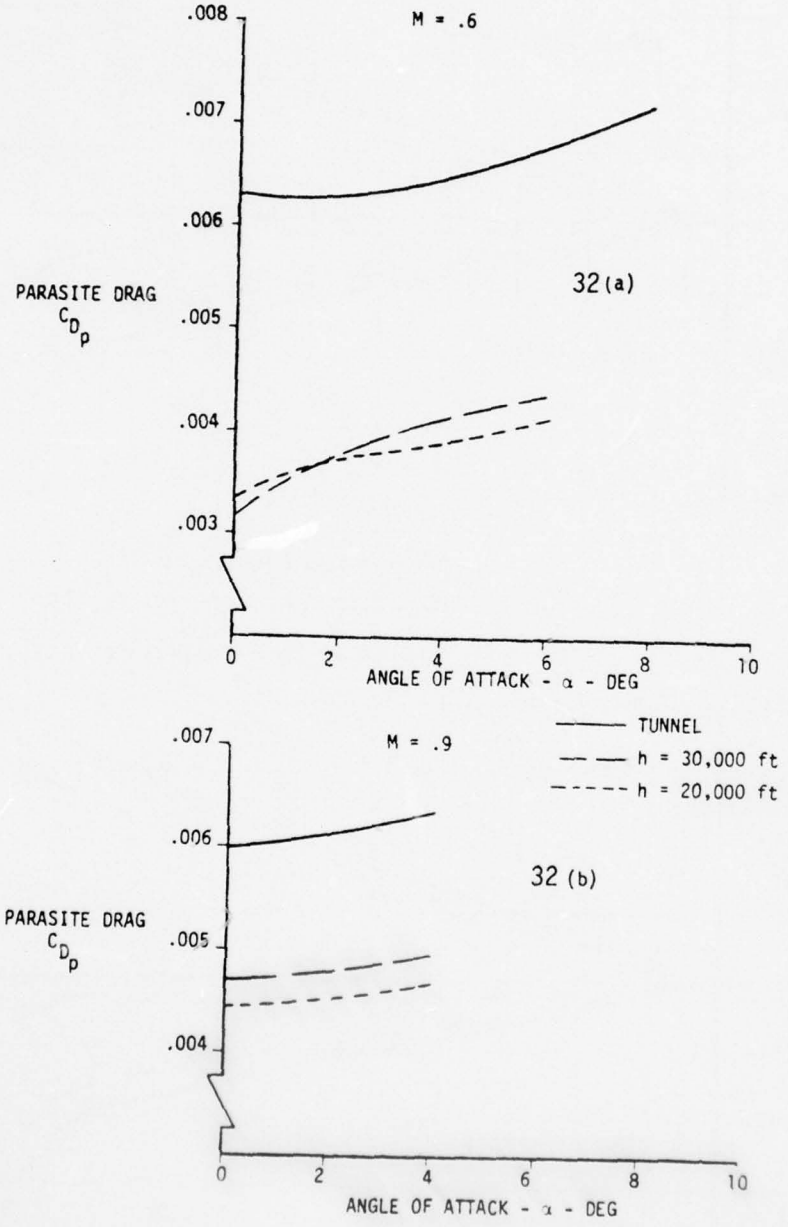

FIGURE 32 EFFECT OF REYNOLDS NUMBER ON PARASITE DRAG FOR CONFIGURATION LO/TO, M=.6 AND .9

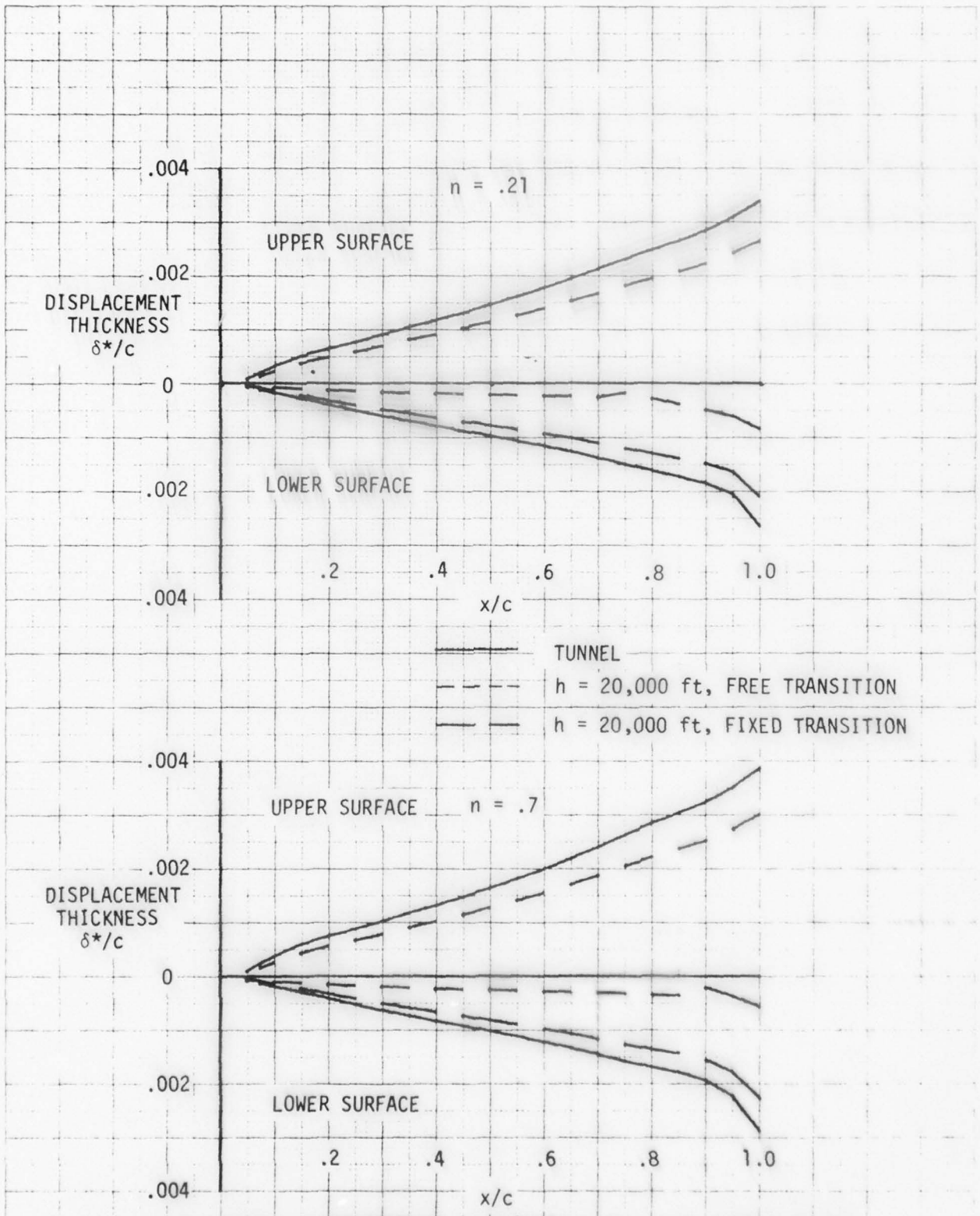

FIGURE 33 EFFECT OF TRANSITION LOCATION AND REYNOLDS NUMBER ON THE CHORDWISE DISTRIBUTION OF DISPLACEMENT THICKNESS FOR CONFIG. LO/TO, M=.6, $\alpha=4^{o}$

similar to that shown in Figure 32b for the 0.9 Mach number condition. Additional comparisons of calculated parasite drag are presented in Figures 34 through 36, for the cambered wing configurations. Figure 34 shows the results obtained for L6/T0 at 0.6 and 0.9 Mach number which are similar to the results for L0/T0. Figure 35 presents the results for L6/T15 at 0.6 Mach number which shows the same large differences in drag due to excessive laminar flow on the lower surface. Figure 36 shows the calculated values for L6/T1 at 0.9 Mach number which show less Reynolds number effect since transition is fixed on both surfaces for all Reynolds numbers.

Profile drag predictions shown in these figures indicate the drag variation with angle of attack is not significantly altered by Reynolds number variation. Consequently, experimental data corrections established for zero angle of attack should also be representative of the necessary corrections at other angles. The Reynolds number variation of predicted wing profile drag is plotted in Figure 37. Data for the 0.6 Mach number flight conditions have been adjusted to simulate an earlier transition on the lower wing surface. Flat plate skin friction drag coefficients for fully turbulent incompressible flow, i.e., M=0, and skin friction coefficients for 5 percent laminar flow at 0.6 and 0.9 Mach number are also shown in Figure 37 for reference. Experimental zero angle of attack drag measurements at 0.8 Mach number for the uncambered wing are observed to fall between the 0.6 and 0.9 Mach number flat plate drag estimates. This indicates that the wind tunnel data vary with Mach number in a manner similar to a flat plate. The other camber cases while yielding higher levels of profile drag than that for a flat plate exhibit the same trend with Reynolds number. Thus, the technique for predicting the wing sectional profile drag and integrating over the wing span appears to yield reasonable estimates of the parasite drag.

Results presented in Figure 37 were used in this study to define corrections to LRC wind tunnel test drag data to account for tunnel and flight Reynolds number differences. Since the predicted results indicate little variation in the profile drag due to wing camber variations a single correction applicable to all test configurations was established at 0.6 and 0.9 Mach number, respectively. Since the data presented in

Figure 37 are normalized by the exposed wing area and the aircraft performance studies were performed using coefficients normalized by the theoretical wing area (i.e., including wing area submerged in the fuselage), drag corrections developed from Figure 37 were further modified by the following relationship.

$$\Delta C_{DP_{R_N}} = \Delta C_{DP_{exp}} \left(\frac{S_{W_{Exposed}}}{S_{W_{Theoretical}}}\right)$$

The specific values for the drag corrections established from these analyses are:

$$\Delta C_{DP_{R_N}} = -.0008 \quad \text{at} \quad M=0.6$$

$$\Delta C_{DP_{R_N}} = -.0011 \quad \text{at} \quad M=0.9$$

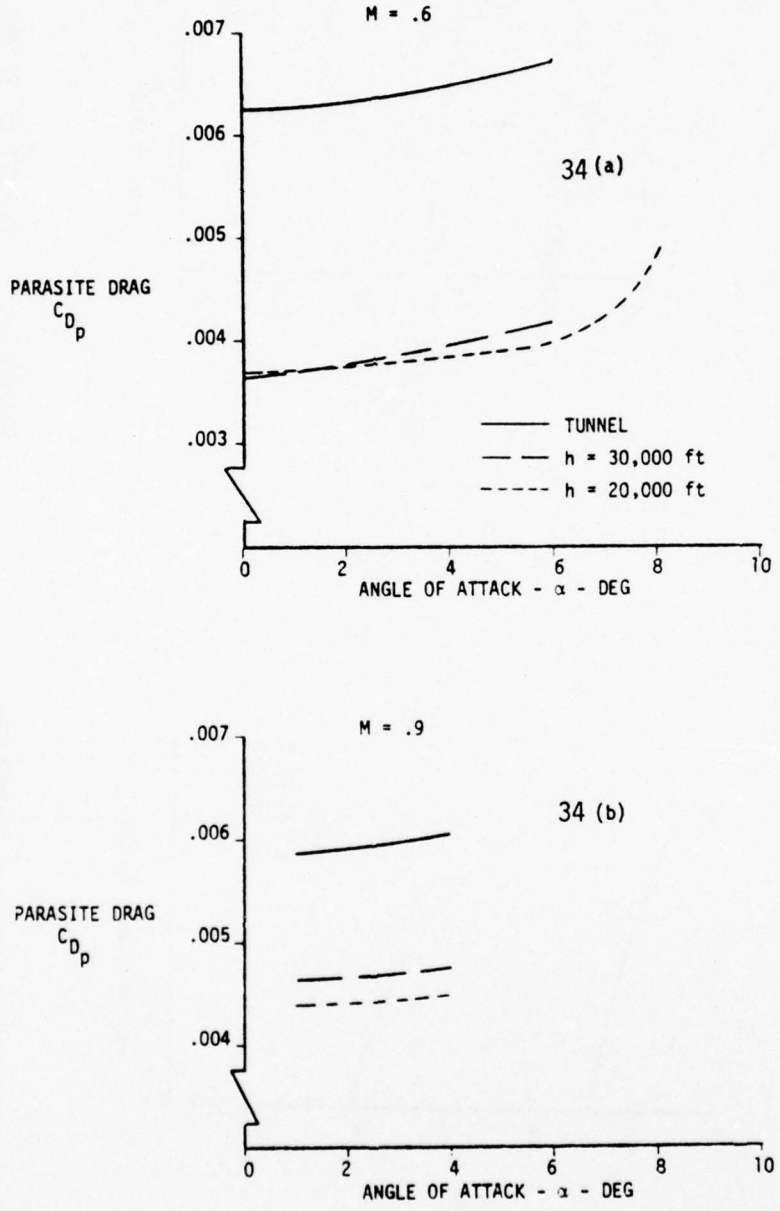

FIGURE 34 EFFECT OF REYNOLDS NUMBER ON PARASITE DRAG FOR CONFIGURATION L6/TO, M = .6 and .9

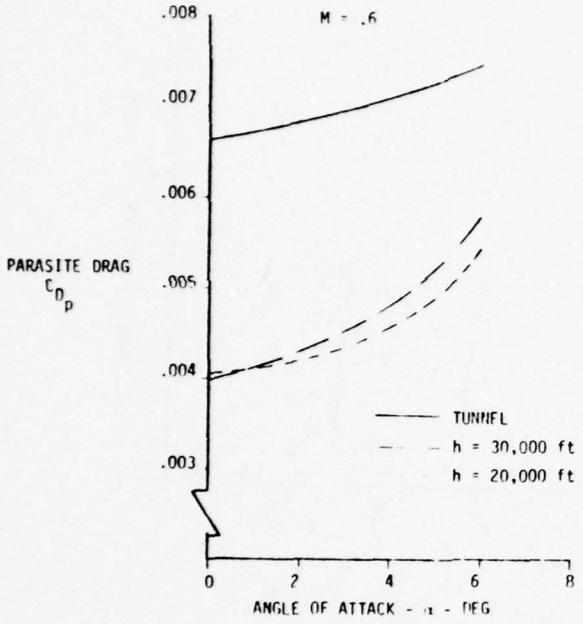

FIGURE 35 EFFECT OF REYNOLDS NUMBER ON PARASITE DRAG FOR CONFIGURATION L6/T15, M=.6

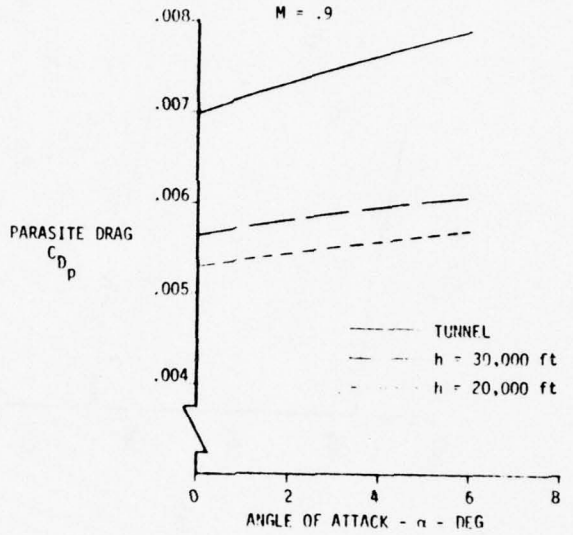

FIGURE 36 EFFECT OF REYNOLDS NUMBER ON PARASITE DRAG FOR CONFIGURATION L6/T1, M=.9

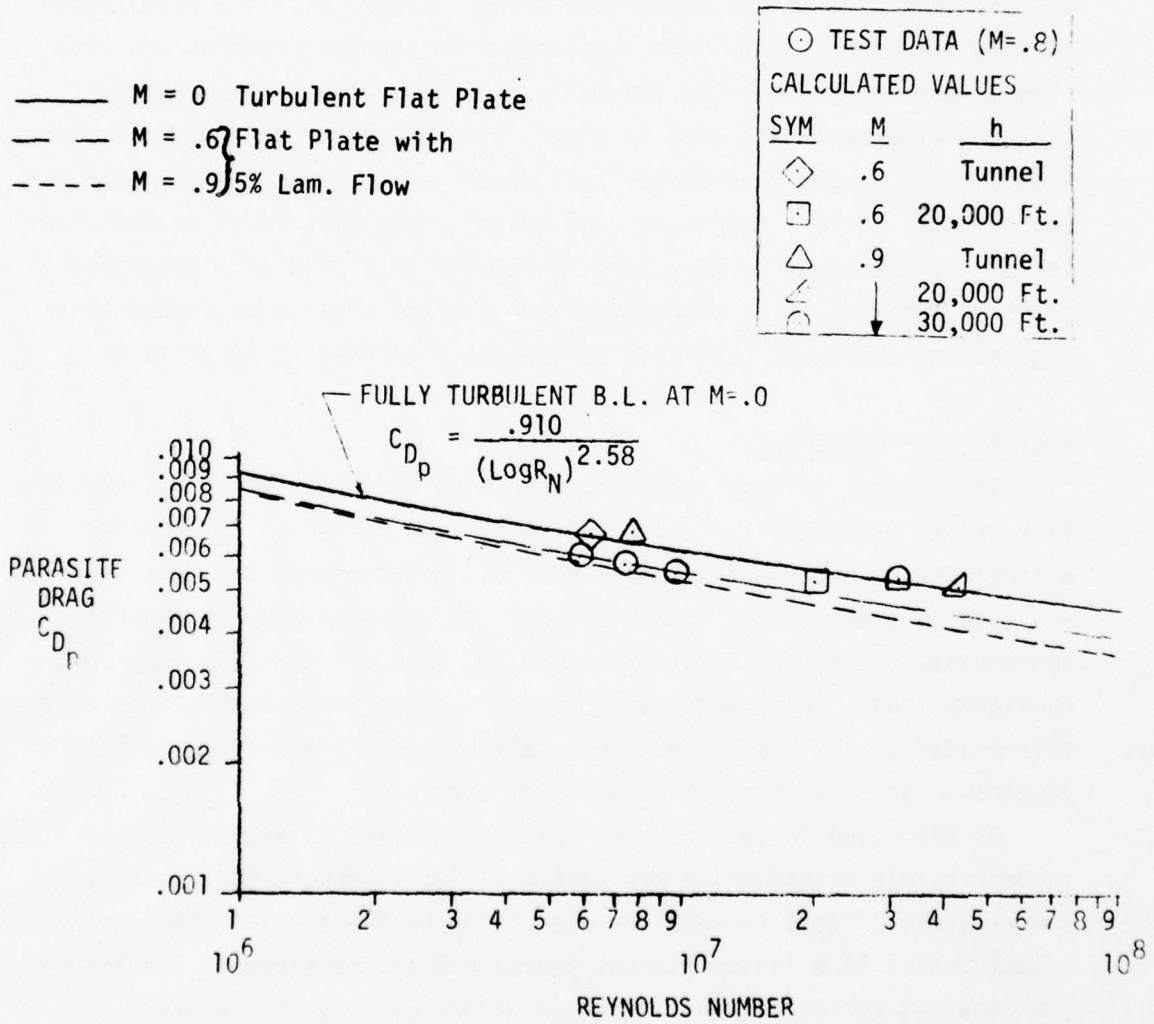

FIGURE 37 PREDICTED DRAG VARIATION WITH REYNOLDS NUMBER

2.3 Tunnel Interference Investigations

Wing-body and isolated wing configurations were examined in these program studies to determine the effect of tunnel interferences upon the wing performance characteristics during the LRC test series. Emphasis during these studies was placed upon identifying the effects of the LRC test non-metric body wing support fairing. The examinations of this program consisted of both analytical predictions and comparisons of the analytical predictions with experimental results. Potential flow methods were used in the analytical investigations with the predictions at subsonic Mach numbers being obtained from the Hess routine and from slender body theory for the transonic flow conditions. Experimental isolated wing test data used in these interference studies were obtained from a prior Vought wind tunnel test conducted in the NASA Ames Research Center (ARC) 14 foot transonic wing tunnel. The wing model in this test series was identical to that used in the LRC test program. Comparison plots of the wing force characteristics for the three wing camber configurations common to both test series are presented in Appendix A.

Analytical Predictions

The non-metric body influence upon wing performance during the LRC test series was predicted using potential flow methods. In order to estimate these interference effects at 0.6 Mach number, the Hess routine was used to predict both wing alone and the LRC wing-body configuration aerodynamic characteristics for the L0/T0, L6/T0, and L6/T15 wing camber configurations. Incremental differences between these predictions were interpreted as the body interference effect and are presented in Figures 38 through 40 as a function of angle of attack.

As discussed in Section 2.2, the Hess routine is essentially an incompressible method which has been modified at Vought to incorporate compressible effects through the use of the Goethert rule. The computational method is a finite element approach with the elements located on the physical surface. Non-lifting solutions converge to an exact solution as the number of computational elements becomes infinite. The lifting problem, however, is more complicated in that the wake location

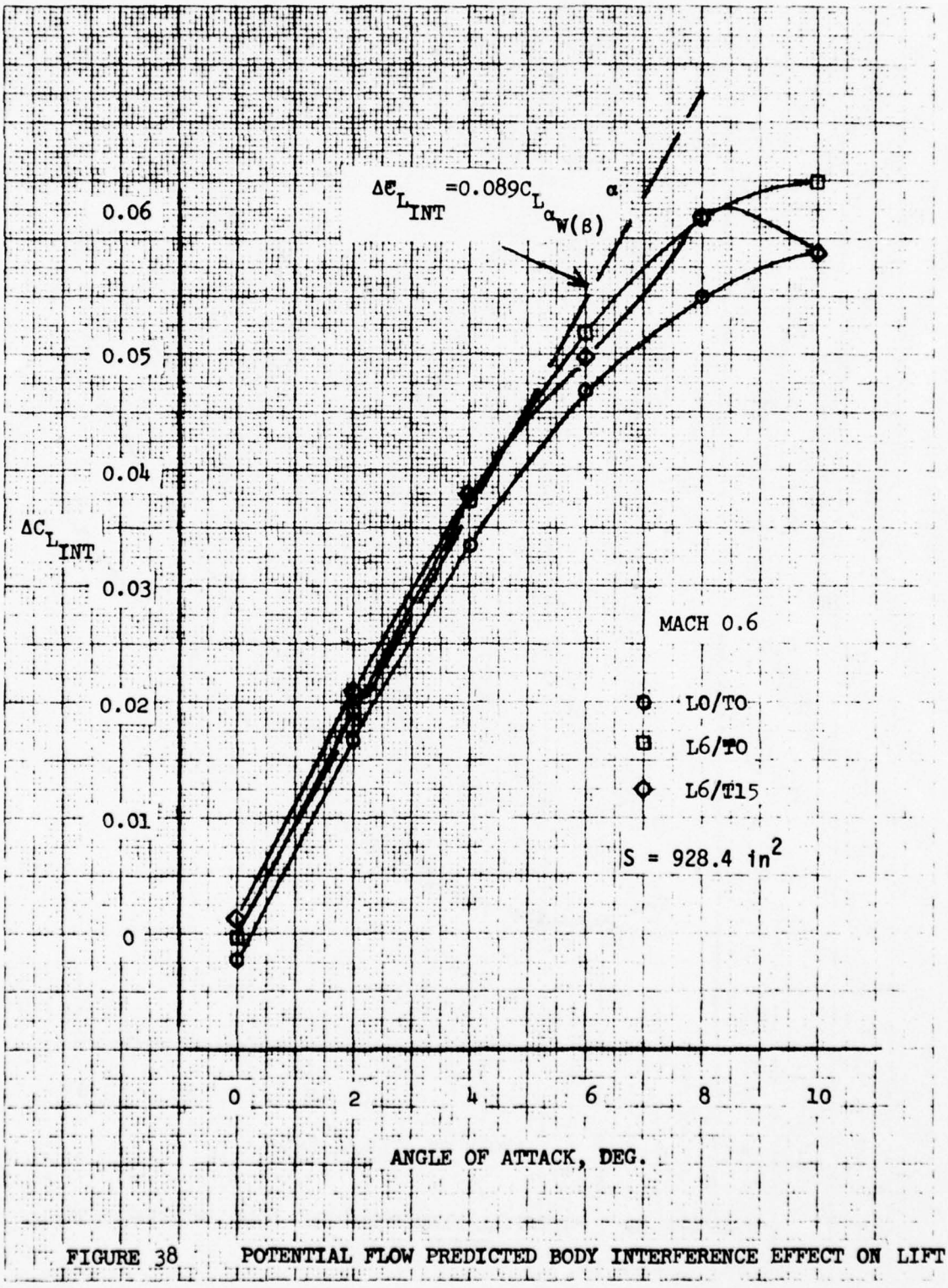

FIGURE 38 POTENTIAL FLOW PREDICTED BODY INTERFERENCE EFFECT ON LIFT

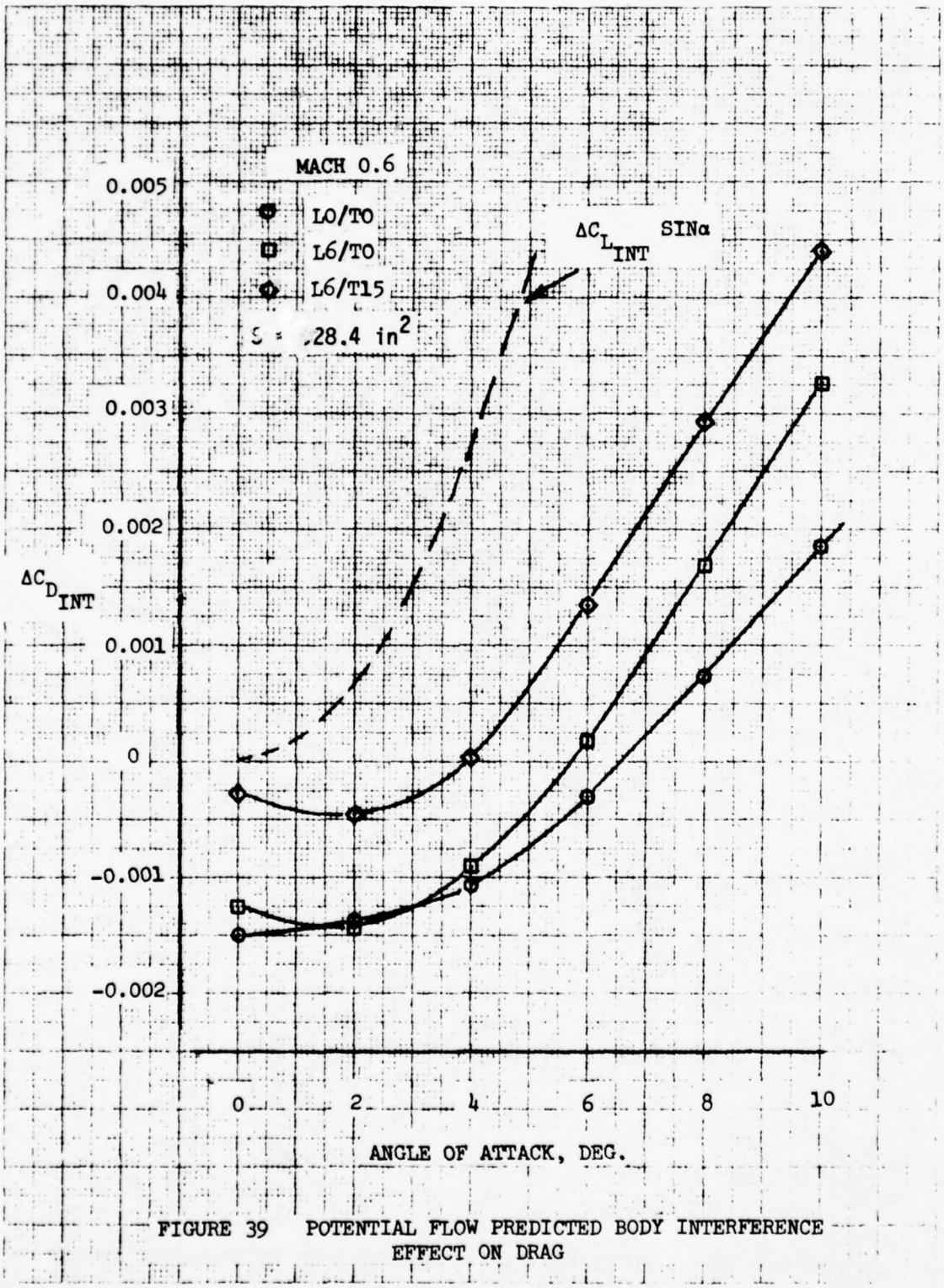

FIGURE 39 POTENTIAL FLOW PREDICTED BODY INTERFERENCE EFFECT ON DRAG

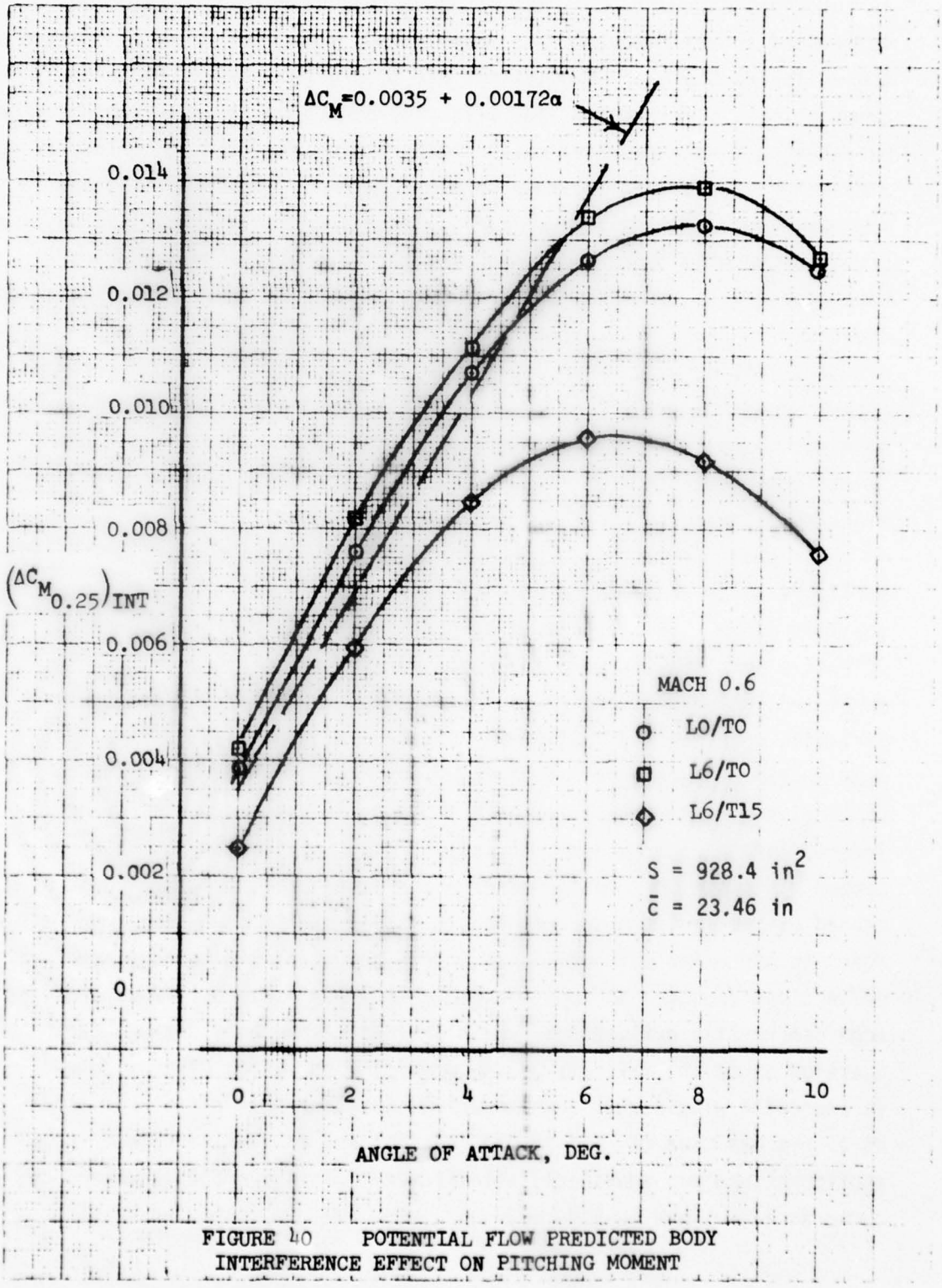

FIGURE 40 POTENTIAL FLOW PREDICTED BODY INTERFERENCE EFFECT ON PITCHING MOMENT

is not known a priori. In theory the wake location and shape could be determined in the course of the solution but the techniques for correctly accomplishing the wake computations are beyond the present state of computational development. The Hess program avoids this wake computation by assuming a wake geometry which trails behind the lifting surface along a bisector of the trailing edge or along an input direction. Errors in the wake geometry should have little effect upon isolated wing aerodynamics provided the wing sweep and angle of attack are not large. Since the wake geometry is dependent upon the lift developed, wake geometry assumptions may be of significance in predicting the flow field around the body aft of a lifting wing which would also influence the body interference effects upon the wing. For the computations of this study, the wing wake was approximated by the bisector of the trailing edge since investigations to identify the effect and/or best wake geometry assumptions were beyond the scope of the present program.

The predicted effect of the LRC test body upon wing lift presented in Figure 38 is shown to be predominantly an increase in the slope of the lift curve. This effect is to be expected due to the increase in effective span for the wing body configuration. The tendency of the predicted incremental interference lift to have less than a linear variation with angle of attack may be a reflection of the wake geometry used in the computations rather than an accurate reflection of the physical body interference. A small change in the body interference induced lift is observed to occur as a result of changes in the wing camber distribution. This predicted characteristic is suspected to be caused by the finite number of panels used in the computational geometric model to approximate the LRC body. The fact that leading edge camber flap deflections produced as much change in the body induced lift as trailing edge camber flap deflections, which are nearer the body, raises the question as to the validity of the predicted variation of body interference with wing camber configuration. Because this effect was small no effort was made to resolve the question and an average effect for all configurations was considered satisfactory. This average interference curve is also shown in Figure 38.

The effects of body interference upon wing drag are illustrated in Figure 39. These effects can be separated roughly into two parts. The first is an apparent drag reduction at zero angle of attack which is strongly dependent on the wing camber configuration. The test body included an asymmetric area ruling which produced crossflow velocities of differing sign at the wing leading and trailing edges near the body. The net effect of this flow field change results in a wing thrust at zero angle of attack. As indicated in Figure 39, the body induced wing thrust was not altered significantly by changes in the wing leading edge camber geometry since these changes in geometry are concentrated near the wing tip. Trailing edge camber variations which are concentrated nearer the body would be expected to influence the body induced crossflow effects near the trailing edge and thus strongly influence the predicted wing thrust. Results shown in Figure 39 are consistent with this expected effect.

All potential flow drag computations suffer from the absence of viscous effects which, near zero lift, must be the dominant contributor to the wing drag force. The very body induced velocity field which produces the apparent wing thrust also affects the wing boundary layer and resulting skin friction drag. Thus, the magnitude of the predicted configuration effects upon the interference drag increments must be considered as suspect unless verified by experiment. The correlation of these predicted effects with experiment are included in discussions presented later in this section.

An additional observation concerning the interference drag increments shown in Figure 39 should be mentioned. The predicted wing thrust results from the body influence upon the wing. A related effect, not addressed here, would be the wing influence upon the body which must be a drag. The net result of the combined wing-body interferences is not necessarily a reduction in drag at zero lift for the overall vehicle in comparison to the sum of the drags for the individual isolated configuration components.

The second observed body interference effect upon the wing drag is an approximate quadratic angle of attack variation of the incremental

drag. The incremental wing drag expected from the body induced incremental change in wing lift has been included in Figure 39 for comparison with the Hess routine predictions. This comparison shows that the Hess routine predicts an increase in wing drag of lower magnitude than that predicted based upon the body induced increase in wing lift. The lower drag prediction results from the attendant effective increase in wing span for the wing-body configuration. The fact that a different angle of attack variation of the incremental drag was obtained for the three different wing camber configurations must be regarded with some suspicion.

Due to the low thickness ratio of the Vought variable camber wing, drag computations are quite sensitive to the finite element analysis approach. Because of machine storage and cost factors, definite limits exist as to the number of geometric elements which can be included in the computations. In particular, the wing leading edge is difficult to reproduce with sufficient accuracy to correctly model the leading edge suction effects and, therefore, the efficiency of lifting wings is rarely accurately predicted from integration of surface pressures. Consequently further efforts to define the change in the body induced wing drag variation with angle of attack for different wing camber configurations was not considered warranted and the current analysis results were used to establish an average body induced drag angle of attack variation for all configurations.

Predicted body interference effects upon wing pitching moment characteristics, Figure 40, show that the general effect of the body influence induces a positive increment in the wing pitching moments referenced to 25 percent of the mean geometric chord. These predictions show that the change in wing pitching moment is relatively insensitive to variations in leading edge camber but is sensitive to the amount of wing trailing edge camber. As expected from the linear nature of the body influence upon wing lift, the initial incremental pitching moment exhibits a linear angle of attack variation. Deviations from a linear variation at the higher angles of attack result from an apparent aft shift in the wing-body center of pressure.

Classical pitching moment predictions based upon potential theory, neglecting the wake effects, only vary with twice the angle of attack.

Consequently, without the wake effects, little deviation from a linear pitching moment variation is expected in the 0 to 10 degree range of angle of attack. The apparent aft shift of the wing-body center of pressure observed from the Hess computations suggests that the interference effect is associated with a wing wake interaction with the body. As previously indicated such interactions may involve some error due to the assumed wake geometry. Consequently, the predicted interference results shown in Figure 40 may be increasingly in error as angle of attack increases. Consistent with the approach used in both the interference lift and drag studies, the body effects upon pitching moment were considered to be a camber configuration dependent effect at zero angle of attack and an effect at angle of attack which is independent of the wing camber distribution. The variation of the average body induced pitching moment with angle of attack developed in this manner is also illustrated in Figure 40. As will be shown later, the predicted configuration dependent body effect at zero angle of attack did not correlate with experimental results, thus, further studies to quantify the moment increment variation with trailing edge camber were not pursued.

The method of Pitts, Nielson and Kaattari, Reference 12, was used in these interference studies to estimate the LRC body influence upon the wing characteristics at 0.9 Mach number. Consistent with the methods of Reference 10, the incremental wing lift induced by the body is given by:

$$\Delta C_{L_{INT}} = C_{L_\alpha}[K_{W(B)}-1]\alpha + C_{L_o}[k_{W(B)}-1]$$

where C_{L_α} is the exposed wing lift curve slope
C_{L_o} is the exposed wing lift at zero angle of attack
α is the angle of attack
$K_{W(B)}$, $k_{W(B)}$ are interference factors defined in Reference 12.

This equation indicates the same general interference effects as obtained from the Hess method at 0.6 Mach number. The last term is a configuration dependent effect at zero angle of attack which is small because the interference factor $k_{W(B)}$ is approximately equal to 1.0 regardless of

the wing-body configuration. Since C_{L_α} is independent of wing camber distribution, according to lifting surface theory, the angle of attack dependent term is also independent of wing camber configuration.

Using the method of Reference 12 to express the total lift of the LRC test wing-body configuration in terms of the exposed wing lift and the classical induced drag relation to wing lift and downwash, the body induced incremental wing drag is defined by

$$\Delta C_{D_{INT}} = (C_{D_{i\,W}}) \frac{C_{L_\alpha}\left[\frac{K_{WB}b^2e_W}{K_{W(B)}(b+r)^2e_{W(B)}} - 1\right]\alpha + C_{L_o}\left[\frac{k_{WB}b^2e_W}{(b+r)^2e_{WB}} - 1\right]}{C_{L_\alpha}\,\alpha + C_{L_o}}$$

where b is the exposed wing semi-span

r is the body radius

e_{WB} is the lift efficiency of the wing-body system

e_W is the lift efficiency of the isolated wing

$(C_{D_{i\,W}})$ is the induced drag of the isolated wing

K_{WB} and k_{WB} are total interference factors defined in Reference 12.

Reference 12 does not provide information required to define the lift efficiency ratio required in this equation. The general body effect, obtained from cross flow analysis methods, is a reduction in lift over the body with the loss in lift at the body centerline proportional to the ratio of the body radius to wing semi-span. Thus, to a first order approximation, the total loss in lift is proportional to the square of the ratio of body radius to wing semi-span; i.e.,

$$\frac{e_{WB}}{e_W} \sim 1 - \left(\frac{r}{r+b}\right)^2$$

The form of the expression defining body effects upon wing drag indicates that the body influence is linearly dependent upon the isolated wing induced drag provided the wing camber distribution induces only small values of lift at zero angle of attack. The formulation of body effects

in terms of the isolated wing induced drag was used in the present studies because of the expected variation of wing efficiency with angle of attack and this form permits use of experimental data which include this variation.

Reference 12 also contains slender body estimates of wing-body configuration pitching moments; however, for the present analyses a simplified form of those results was developed. This approach was based upon the slender body theory considerations which permit the lift due to angle of attack of a wing-body system to be expressed solely in terms of the ratio of body radius to wing semi-span. With the assumption of a constant body radius, the wing pitching moment about the wing apex can be expressed in integral form in terms of the axial rate of change of the ratio of body radius and wing span. The solution of this integral equation for a delta wing, assuming body lift independent of axial distance, was used to estimate the aerodynamic center of the wing in the presence of the body in terms of the isolated wing aerodynamic center. This estimate of wing aerodynamic center along with the previously indicated lift relationship allows the body interference upon wing pitching moment to be expressed in terms of isolated wing characteristics;

$$(\Delta C_{M_\alpha})_{INT} = \left(\frac{3}{4}\left[\frac{r}{s} + \left(\frac{r}{s}\right)^2\right] \frac{(x_{ac})_w}{c_R} - \left[K_{W(B)} - 1\right] \frac{x_R}{c_R} \right) C_{L_\alpha}$$

where s is the total wing-body system span, r+b

$(x_{ac})_w$ is the isolated wing aerodynamic center relative to the wing apex

x_R is the moment reference point relative to the wing apex

c_R is the moment coefficient reference length.

It should be noted that this form of the slender body theory predictions does not yield an indication of the body effect on pitching moments at zero angle of attack and implies that the body interference upon pitching moment varies linearly with angle of attack. As a consequence, of the

limited correlation of this predicted effect with experimental results discussed in subsequent paragraphs further refinement of this approach to include effects at zero angle of attack was not considered justified.

Experimental Results

Test data for three wing camber configurations investigated in both the LRC test series and an isolated wing test series conducted in the NASA Ames Research Center (ARC) 14-foot transonic wind tunnel were analyzed during these program studies to verify and/or supplement the prediction of the body interference effects during the LRC tests. Force data for these wing configurations are included in Appendix A. Since these tests were performed in different facilities the question of general tunnel interferences was also addressed.

Goethert, Reference 13, suggests that data obtained in a good transonic tunnel would be essentially free of tunnel interference provided that the blockage is less than one percent and the wing span is less than half the tunnel width. The Vought variable camber wing installation in the ARC transonic tunnel amply satisfies these criteria. Some peculiarities, however, have been noted in the ARC test results which are discussed below. The wing-body installation during the LRC test series violated both of the general requirements for interference free test results in that the blockage was approximately 1.4 percent and the wing-body span was approximately 60 percent of the tunnel width. Consequently closer examination of the blockage and span to width ratio effects for this installation were required and are also discussed in later paragraphs of this report section.

Examination of the lift characteristics for configuration LO/TO at 0.6 Mach number shows that some unexpected effects were present in the ARC isolated wing test results. Isolated wing experimental results are compared with predictions from the Hess routine in Figure 41. Examination of the predicted and experimental lift curves indicate expected variations except for the experimental lift at zero angle of attack. Since this wing configuration was symmetric, no lift would be expected at zero angle of attack. Thus, the validity of this non-zero

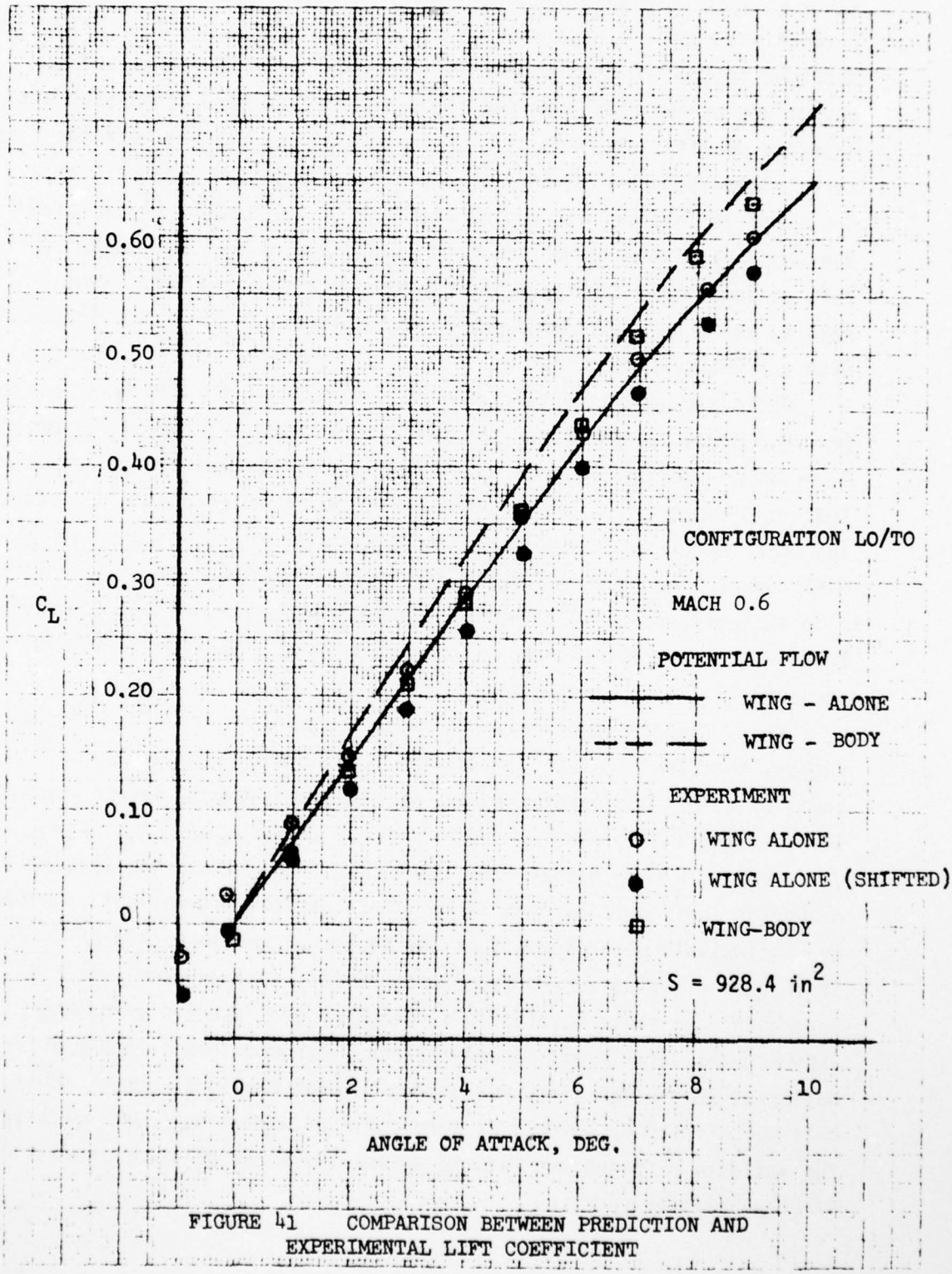

FIGURE 41 COMPARISON BETWEEN PREDICTION AND EXPERIMENTAL LIFT COEFFICIENT

value of lift is highly questionable. A similar comparison between predictions from the Hess routine and data for configuration LO/TO obtained in the LRC test series is also shown in this figure. This comparison of the wing lift indicates a variation more consistent with expected results. The potential flow predictions overestimate the lift curve slope at both high and low angles of attack and underestimates the slope at intermediate angles where vortex lift might be expected. The presence of the non-metric body did produce a non-zero value of lift at zero angle of attack in both the predicted and experimental results but the magnitude is small in comparison to the value indicated from the ARC test results.

The angle of attack for zero lift observed in the ARC test results ($\alpha \approx 0.5$ deg.) is considered too large to attribute to tunnel asymmetries. Also, since precautions were taken during the ARC test series to insure that wing camber flap deflections were within a tolerance of 0.1 degrees, the observed effect is too large to be attributable to wing camber differences. As shown in Figure 41, however, application of a constant lift increment to the ARC test data produces the same relative correlation between the experimental and predicted isolated wing results as was observed in the LRC test data.

While the zero angle of attack measurements for configuration LO/TO suggest that the ARC test results may be in error by a constant lift or angle of attack increment, results for the leading edge camber configuration, L5/TO, indicate a different error magnitude as well as an error variation with Mach number. Because of this result and the limited number of configurations available for comparison, it was not possible to conclusively determine either the source of the suspected error or if the error varied during the course of this test program. As a consequence of these observations, other program studies using the experimental data to define body effects, assumed that a random error may exist in the ARC force measurements which precludes use of these data to define body effects at zero angle of attack but does not affect the validity of using the data to define the angle of attack variation of body interferences.

Reference 14 contains recommended model size limits for testing at 0.95 Mach number in the LRC 8 foot transonic tunnel. These limits restrict wing area to 288 square inches, wing span to 50 inches, model length to 60 inches and total tunnel blockage to 0.5 percent of the test section area. This model length restriction is not considered applicable to the LRC variable camber wing test series because of the nature of the wall mount used. The recommended blockage limits would be expected to increase due to the reductions in test Mach number. Also, the wing area and span limitations, which are related, are strongly dependent upon the lift levels expected during testing.

Goethert, Reference 13, indicates that the tunnel wall interference effects, which are related to ratio of wing span and tunnel width, are definable in terms of a correction to the effective wing angle of attack;

$$\Delta\alpha = -\frac{\delta A_W}{8 A_T} C_L$$

where A_W is the wing area
A_T is the tunnel cross-sectional area
δ is a tunnel correction factor.

One function of the slots in a perforated transonic tunnel is to reduce the value of δ and permit testing of larger models than would otherwise be possible. For a wing of small span in a circular slotted tunnel with 11 percent open area, Goethert predicts a value for δ of approximately -0.25. Using this value for the 8-foot tunnel correction factor along with the appropriate wing and tunnel areas results in a predicted angle of attack correction due to wall interference effects during the LRC test series of less than 5 percent of the wing induced angle of attack. Since the experimental wing buffet onset lift coefficient at 0.9 Mach number was less than 0.65 the magnitude of the downwash correction is predicted to be less than 0.15 degrees. Corrections of this magnitude would have a negligible effect upon the pertinent LRC test results.

As the wing span to tunnel width ratio increases, tunnel wall interferences may exceed the above estimate at the wing tip. An additional evaluation of the tunnel wall effects can be obtained from comparisons

of wing pressures measured in the LRC and ARC tests. Body interferences included in the LRC data have been predicted to involve effects of two types; the body induced upwash and the increased wing vortex span. Of these two effects only the increased vortex span should be significant at the wing tip where wall effects would be the greatest. The effect of the increased vortex span is predicted to cause a reduction of approximately 0.7 degrees in the induced angle of attack at the wing tip for a lift coefficient of 0.63. Figures 42 and 43 present the chordwise pressure distributions obtained at the 0.85 and 0.95 span stations of configuration L6/T11 for a Mach number of 0.9. At this angle of attack condition, the isolated wing produced a lift coefficient of 0.63. Wing pressures from the LRC test series included in these figures were obtained at an angle of attack of 5.01 degrees. The agreement between these wing pressure distributions indicates that the wing tip was at approximately the same effective angle of attack. Consequently, the downwash angle at the wing tip for the isolated wing test conditions was approximately 0.91 degrees larger than that for the LRC wing-body configuration. In view of the previously discussed 0.5 degree angle of attack uncertainty in the ARC test results, this experimental downwash difference agrees with the predicted vortex span effects. Based upon these observations, the span to tunnel width ratio of the LRC test was judged to be sufficiently small to permit use of the test data without tunnel wall downwash corrections.

Data presented in Reference 13 indicate that limits upon model size due to blockage considerations can be increased by a factor of four if the test Mach number is reduced from 0.95 to 0.90. Therefore, the Reference 14 recommended model blockage at 0.95 Mach number would correspond to approximately 2.1% at 0.90 Mach number. Since the model blockage at zero angle of attack during the LRC test series was approximately 1.4%, blockage effects upon the test results should not be significant at low angles of attack.

Barnwell, Reference 15, indicates that one effect of slotted tunnel walls is a reduction of the extent of the sonic region at transonic conditions. This effect becomes significant when the sonic region would be expected to extend beyond the tunnel walls. Thus, tunnel blockage

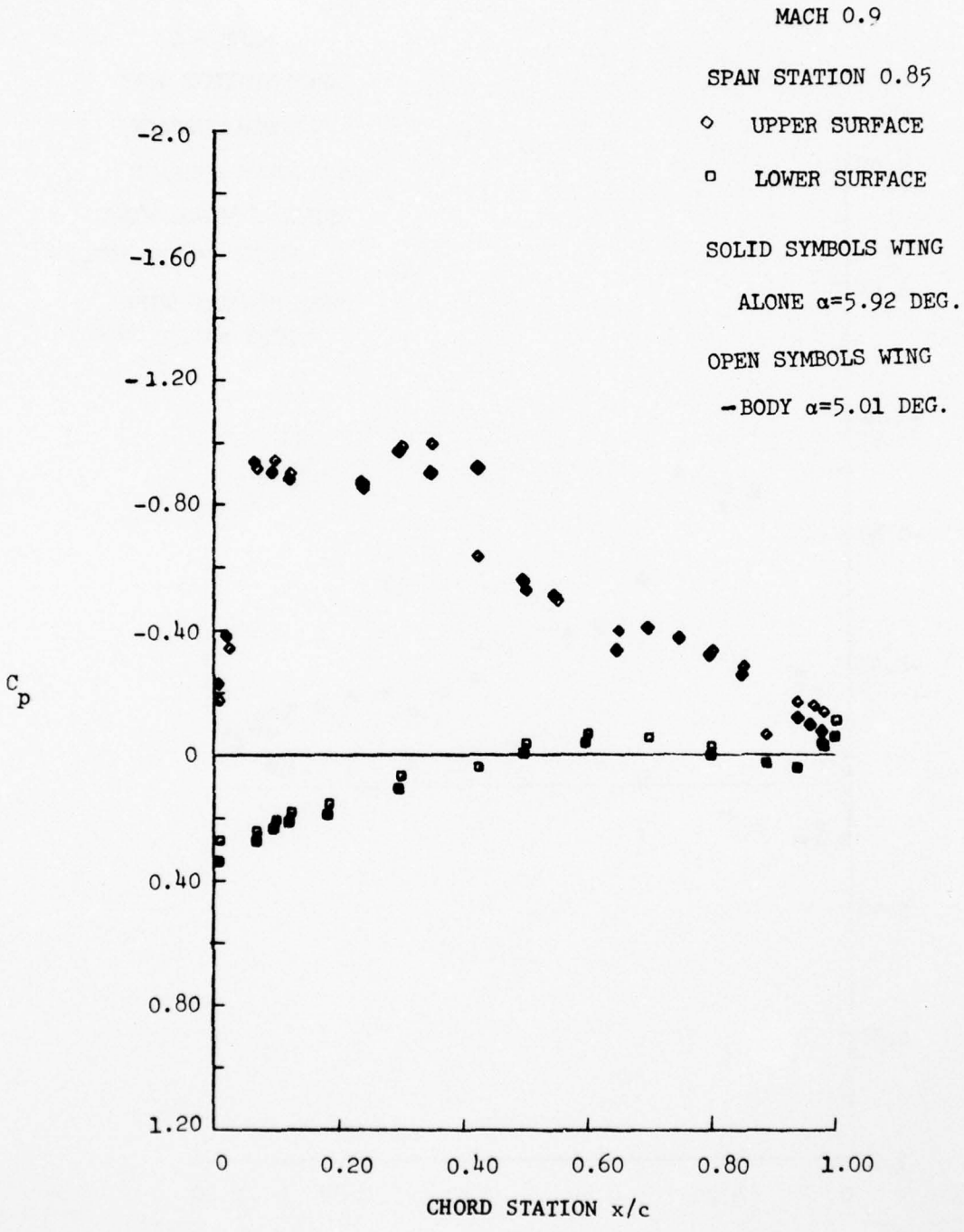

FIGURE 42 COMPARISON OF TIP PRESSURE DISTRIBUTIONS WITH AND WITHOUT BODY EFFECTS, CONFIGURATION L6/T11

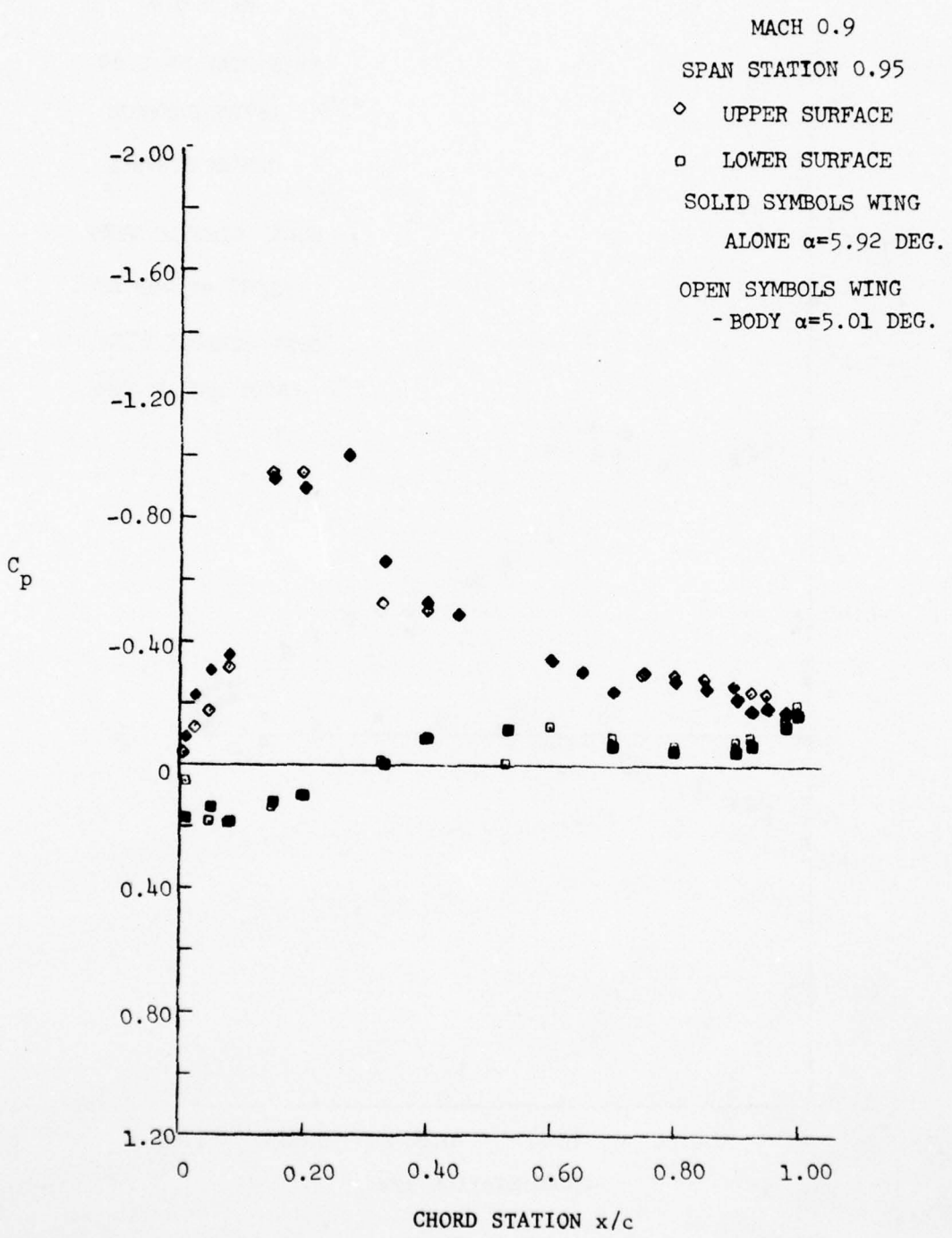

FIGURE 43 COMPARISON OF TIP PRESSURE DISTRIBUTIONS WITH AND WITHOUT BODY EFFECTS, CONFIGURATION L6/T11

effects should become significant for model angles of attack that are sufficient to produce a sonic region which extends to the tunnel wall. Results from the Bailey-Ballhaus transonic coding, Reference 9, have been used in these studies to define the level of wing lift for which tunnel blockage becomes significant. Predicted flow field characteristics for configuration L6/T11 at angles of attack of 0, 2, and 4 degrees and a Mach number of 0.9 have been analyzed to define the extent of the wing sonic region as a function of wing lift. These predictions indicate that the height of the sonic line is approximately proportional to wing lift coefficient; with the height of 29.78 inches corresponding to a coefficient of 0.436. Since the test section of the LRC tunnel is actually 7.1 feet in height, the analytical results indicate blockage effects would begin to be significant at a lift coefficient of 0.624. This level of wing lift is above that for buffet onset for all configurations investigated in the LRC test series except configuration L6/T15.

Based upon the results presented in the preceding paragraphs, data obtained in the LRC wind tunnel test program are judged as free from general tunnel interferences and, thus, data corrections for such effects are not required for the aircraft application studies of this program.

Body Effects Upon Wing Buffet Onset

Analyses of camber configuration influences upon wing buffet onset angles of attack discussed in Section 2.1 indicate flow separations on the outboard portion of the wing are the primary source of initial wing buffet. This region of the wing is least affected by the upwash generated by the non-metric body. Consequently, the principal body influence upon wing buffet results from the increase in configuration span which causes a reduction in the downwash in the tip region of the wing-body configuration relative to an isolated wing. Thus, for buffet onset to occur at the same effective wing tip angle of attack, buffet onset for the isolated wing would be expected at a higher geometric angle of attack but lower wing lift coefficient.

Wing pitching moment characteristics were used in the manner described in Section 2.1 to assess the body influence upon wing buffet

onset. Wing pitching moment variations with angle of attack for the camber configurations common to the LRC wing-body and ARC isolated wing test series and Mach numbers of 0.6 and 0.9 are shown in Figures 44 through 49. These results show that the body influence produces a positive increment in the wing pitching moment and, prior to buffet, alters the pitching moment rate of change with angle of attack. After buffet onset, however, the body has little effect upon the moment rate of change with angle of attack. The change in body influence before and after buffet onset allows the wing-body configuration pitching moment breaks to be more accurately defined than for the isolated wing configurations. The relatively gentle change in the pitching moment characteristics causes some increased uncertainty in the buffet onset angles of attack for the isolated wing configurations.

Table 4 provides a comparison of the experimentally defined buffet onset angles of attack for the wing-body and wing alone configurations. The expected tendency for the isolated wing buffet onset to occur at higher angles of attack is suggested by these data. The theoretical change in downwash at buffet onset is estimated to be less than 0.5 degrees and, thus, is of the order of magnitude of the experimental differences. The apparent data scatter, however, precludes a firm definition of this angle of attack trend.

The aircraft configuration considered in the studies of this program and described in Section 3.1 has a body radius to wing semi-span ratio only 27 percent less than the LRC test configuration. Thus, the changes in the wing tip induced angle of attack and hence changes in the body influence upon the angle for buffet onset would be significantly less than the differences shown in Table 4 and, therefore, within the inherent uncertainty in the buffet onset determination. Consequently, the buffet onset angles of attack established from the LRC test results have been used without correction in the aircraft application studies of this program.

Comparison of Predicted and Experimental Body Interferences

If, as suggested in previous discussions, the ARC isolated wing test data include a random angle of attack error, then corrections for this

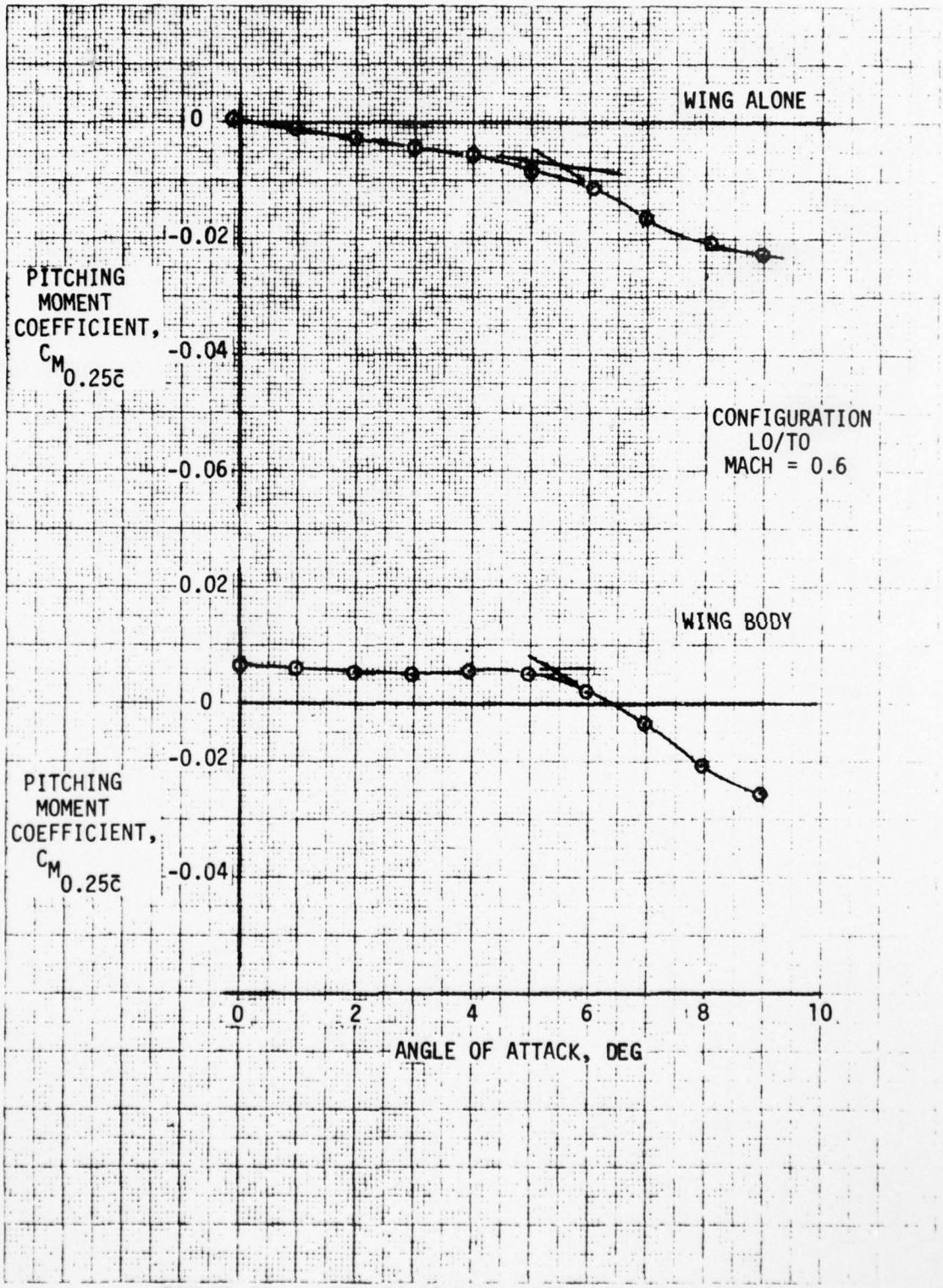

FIGURE 44 EFFECT OF BODY INTERFERENCE ON ANGLE FOR BUFFET ONSET

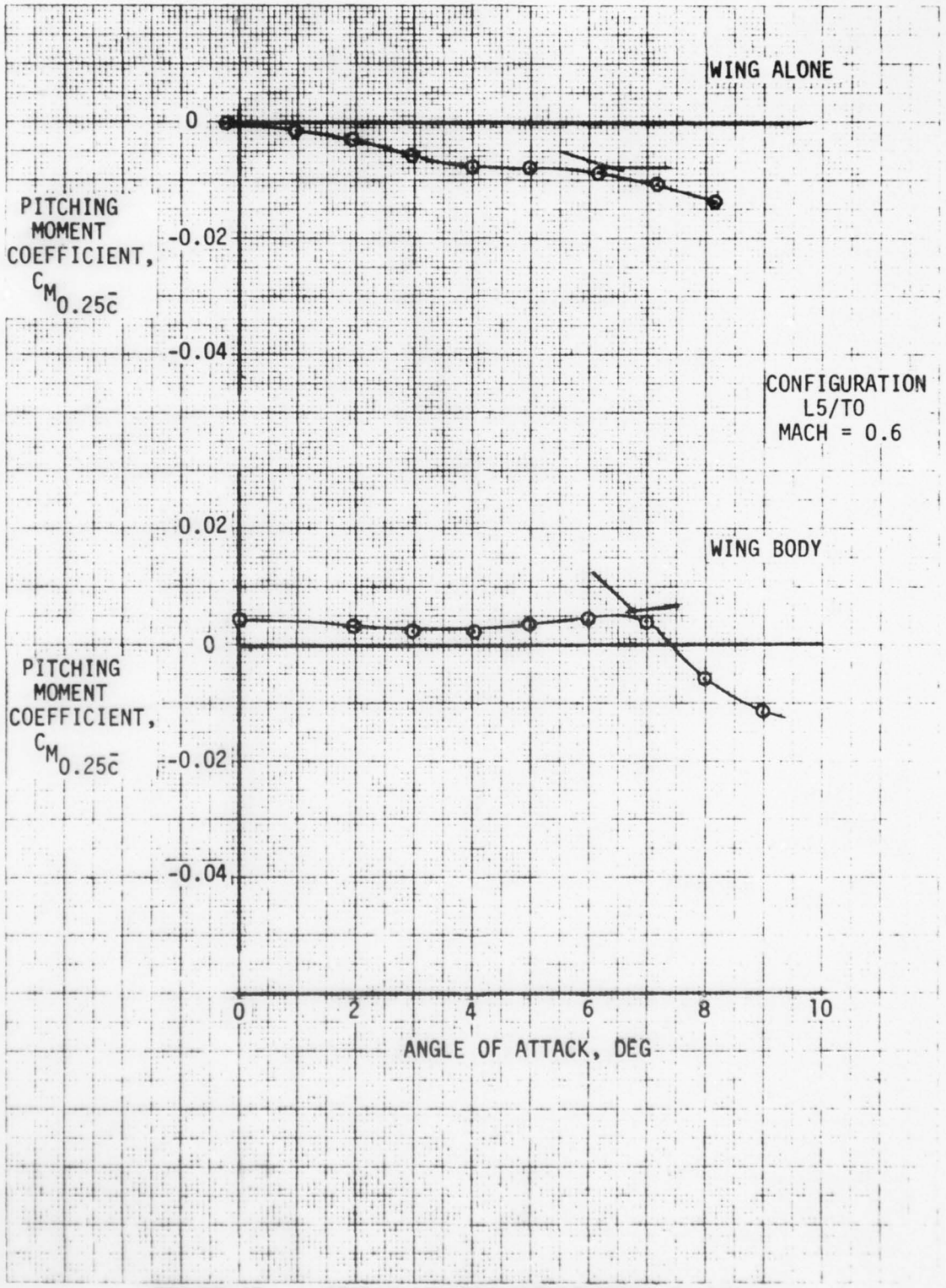

FIGURE 45 EFFECT OF BODY INTERFERENCE ON ANGLE FOR BUFFET ONSET

AD-A045 951 VOUGHT CORP DALLAS TEX F/G 20/4

INVESTIGATION OF A VARIABLE CAMBER WING DESIGN.(U)

MAY 77 T D BEATTY, W B BROOKS, L D ROBINSON N62269-76-C-0361

UNCLASSIFIED 2-53300/7R-5977 NADC-76114-30 NL

2 OF 2 ADA 045951

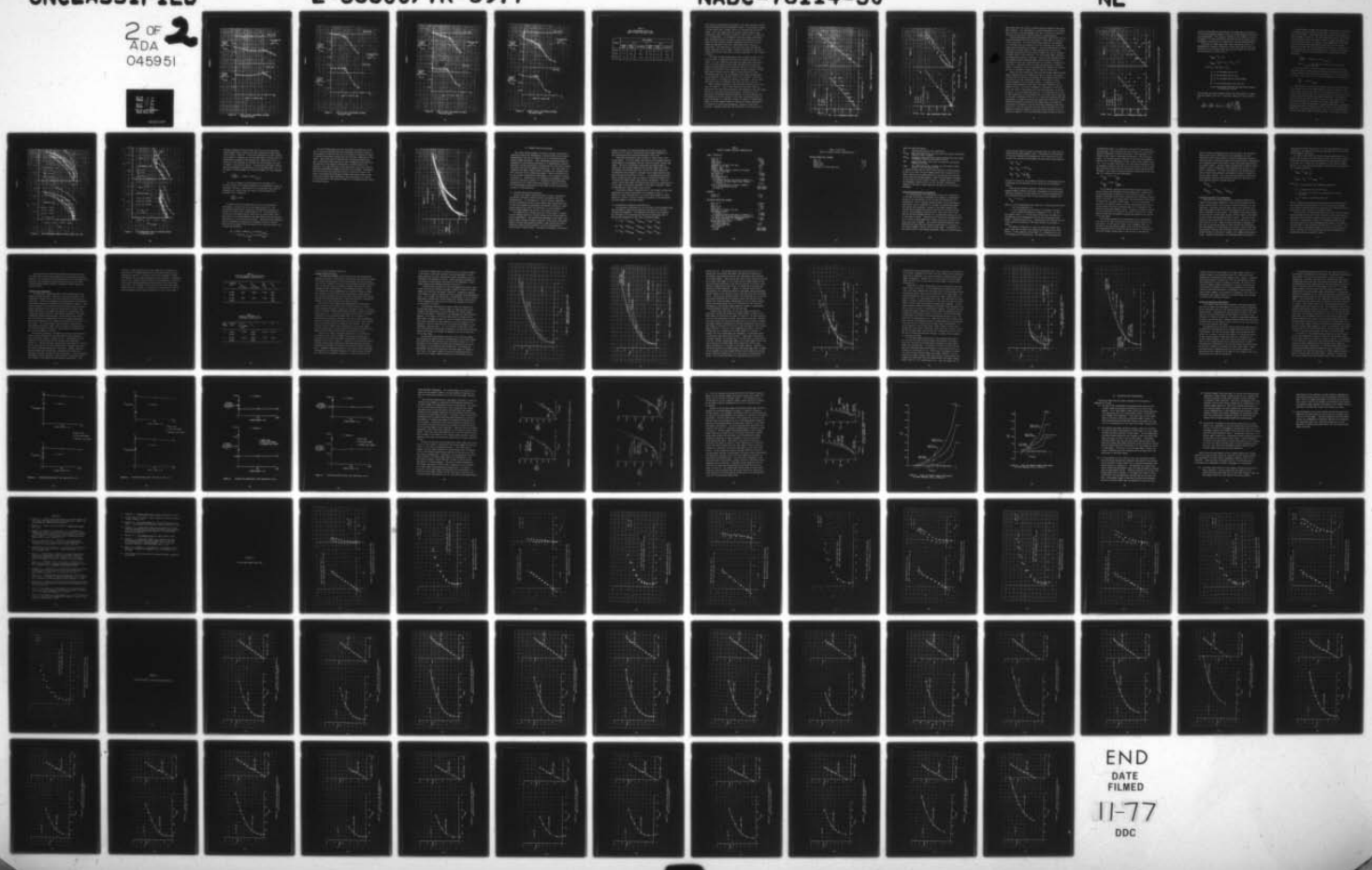

END

DATE FILMED

11-77

DDC

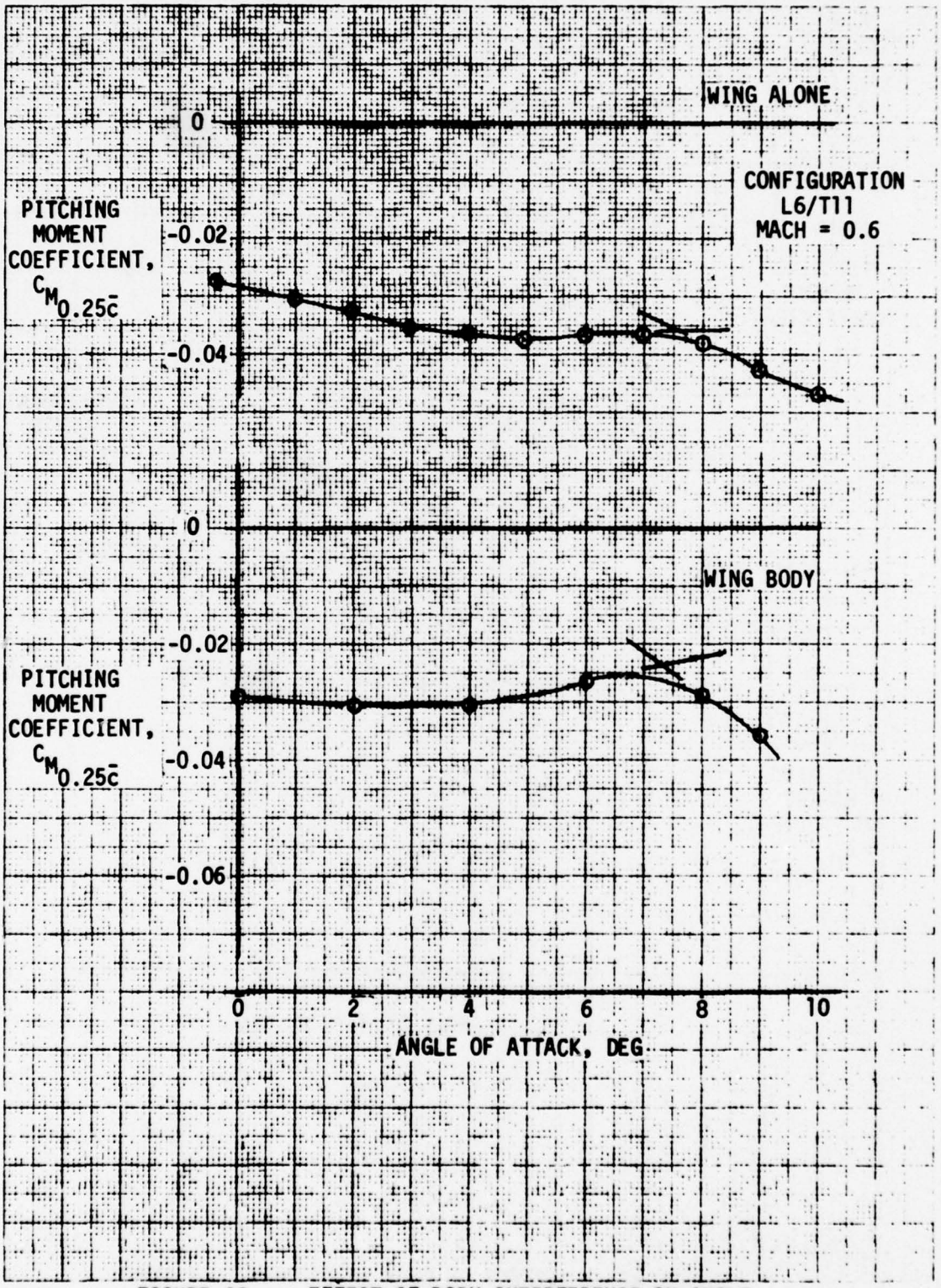

FIGURE 46 EFFECT OF BODY INTERFERENCE ON ANGLE FOR BUFFET ONSET

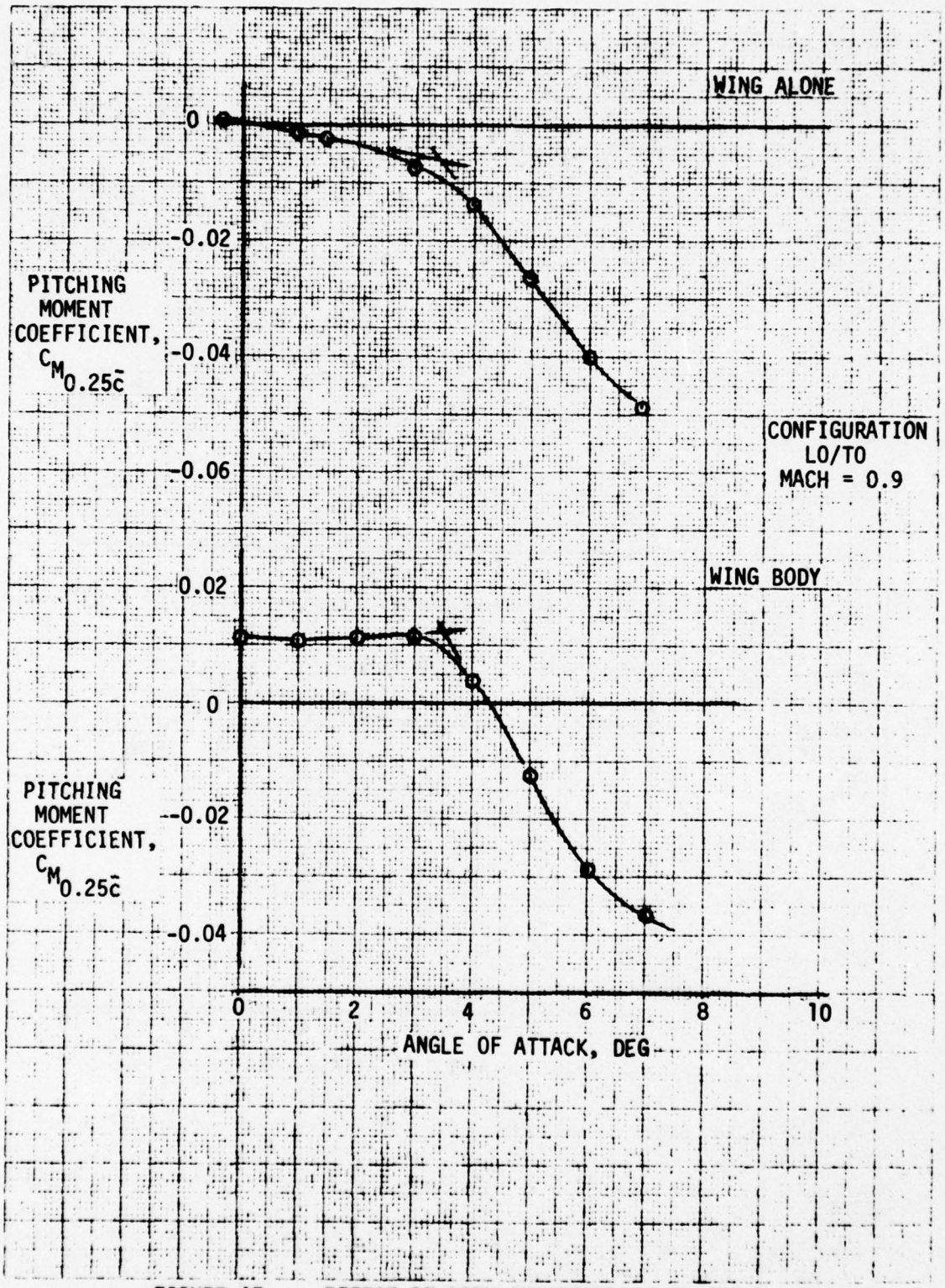

FIGURE 47 EFFECT OF BODY INTERFERENCE ON ANGLE FOR BUFFET ONSET

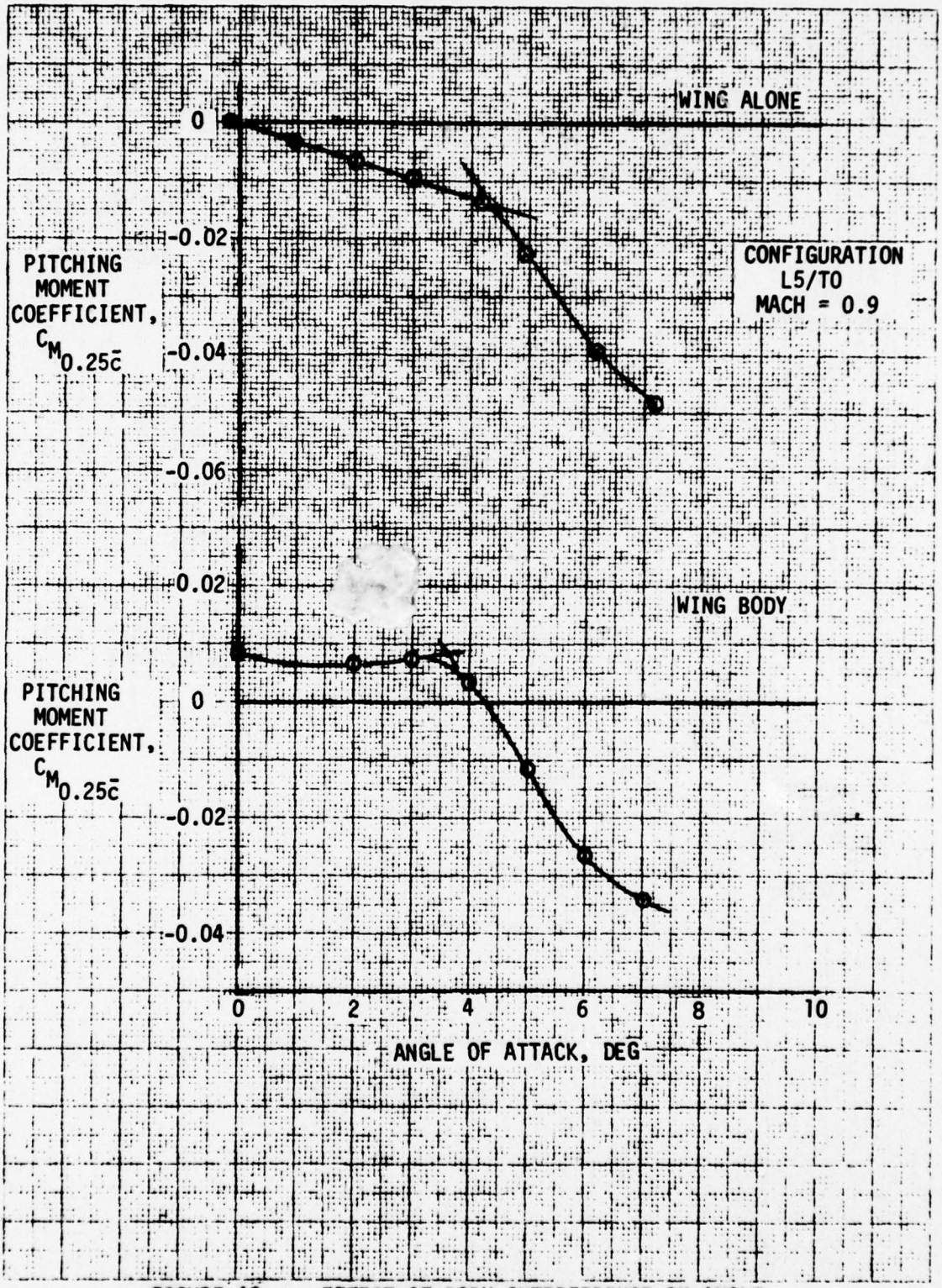

FIGURE 48 EFFECT OF BODY INTERFERENCE ON ANGLE FOR BUFFET ONSET

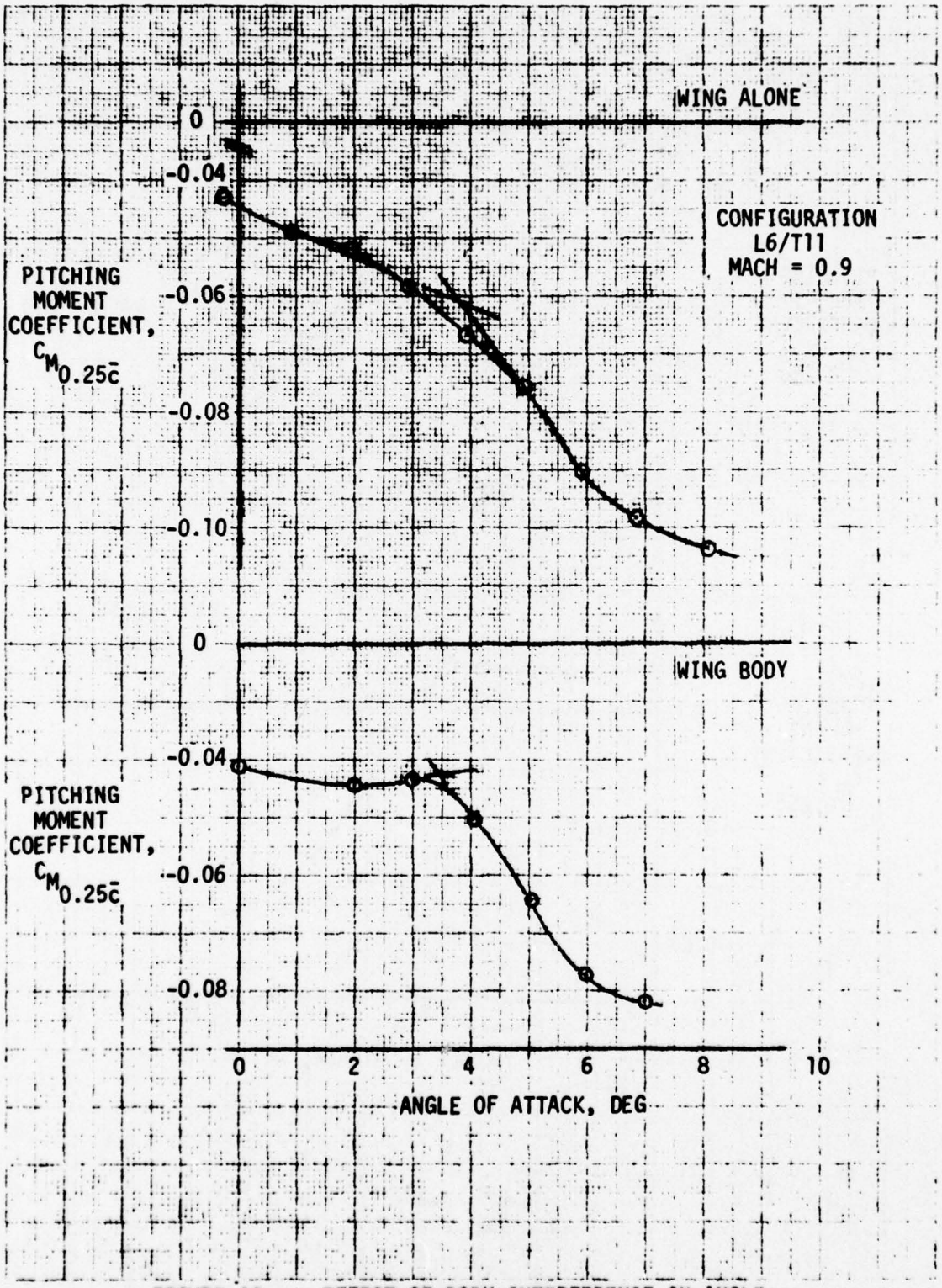

FIGURE 49 EFFECT OF BODY INTERFERENCE ON ANGLE FOR BUFFET ONSET

TABLE 4

BODY INTERFERENCE EFFECTS ON
ANGLE OF ATTACK FOR BUFFET ONSET

CONFIG	MACH NUMBER					
	0.6			0.9		
	WING-BODY	WING ALONE	DIFFERENCE	WING-BODY	WING ALONE	DIFFERENCE
LO/TO	5.4	5.5	-0.1	3.5	3.4	+0.1
L5/TO	6.7	6.4	+0.3	3.6	4.3	-0.7
L6/T11	7.3	7.6	-0.3	3.4	3.8	-0.4

error would be required before estimates of the body interference effects could be obtained from the experimental results. Unfortunately, however, no single coefficient is known a priori for configurations involving camber. Thus, the random error must remain unknown; however, body interference trends with angle of attack or other similar variables can still be determined. The incremental difference between experimental body interference effects at angle of attack and the effects at zero angle of attack should be directly comparable with predictions even though the magnitude of the total interference effect cannot be established. Such comparisons of the wing lift, drag, and pitching moment characteristics are shown in Figures 50 through 52. Note that induced wing drag has been used in the drag comparisons in lieu of angle of attack.

The effect of body interference on the variation of wing lift with angle of attack is observed from Figure 50 to exhibit the predicted trends. It is of interest to note that the slender body theory predictions at 0.9 Mach number exhibit better agreement with experimental results than the predictions from the Hess routine at 0.6 Mach number; however no explanation of this observation has been attempted. Slender body theory indicates that the angle of attack variation of body interference upon wing lift is dominated by the effective body radius to wing semi-span ratio and that little or no variation in the interference effect is introduced by changes in wing camber. The available experimental data are reasonably consistent with this conclusion.

Body interference effects on the wing drag variation with lift are shown in Figure 51. Since viscous effects are obviously involved, appreciable variations between potential flow predictions and experimental results are to be expected and are observed. The potential flow predictions do reproduce the trends observed in the experimental data. As expected, due to the increase in wing span, the principal effect of body interference is a reduction in drag. The effect of leading edge camber at 0.9 Mach number appears to improve the leading edge behavior at low angles of attack and consequently, produces a larger drag reduction. Somewhat surprising, the same effect is not evident at 0.6

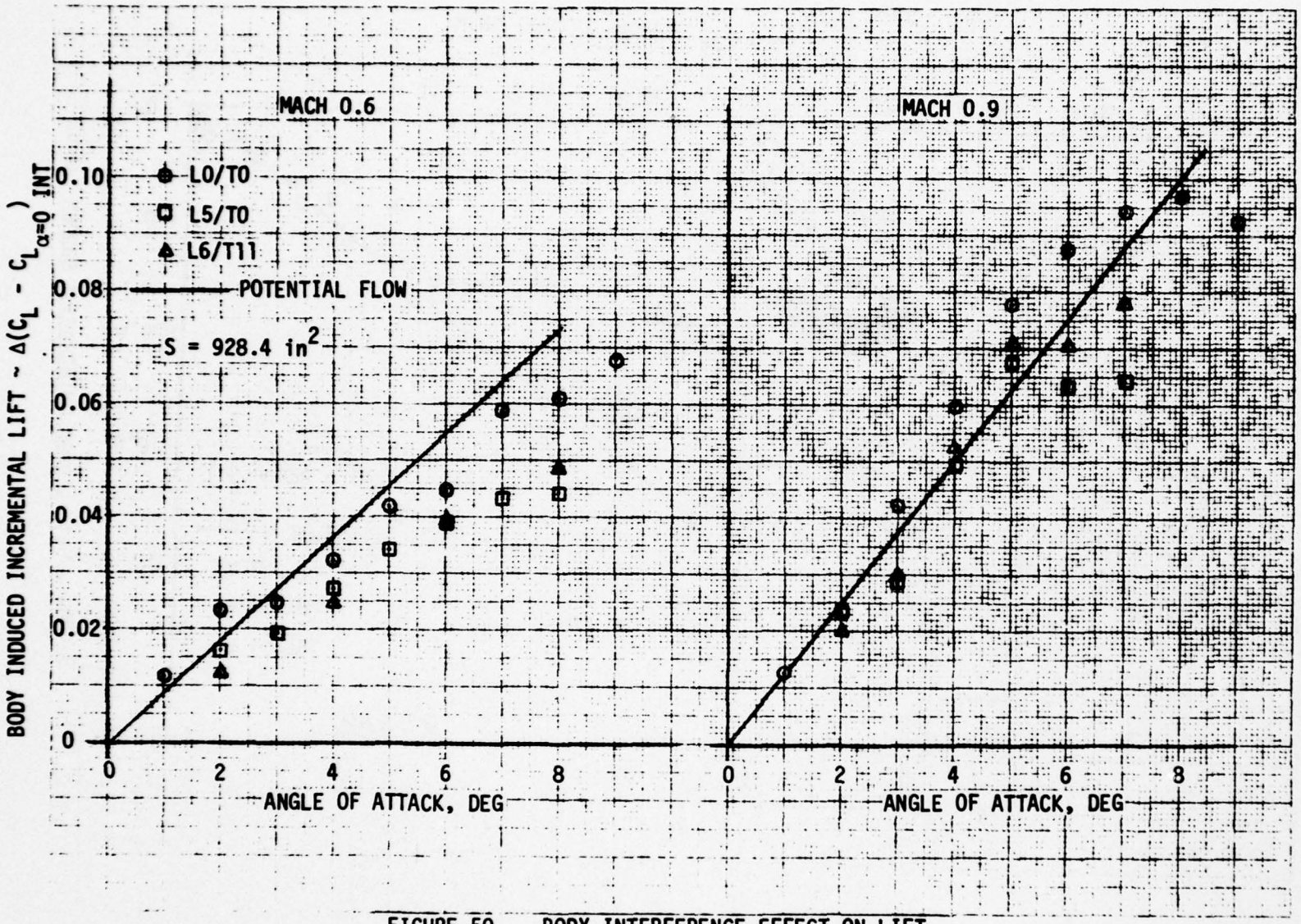

FIGURE 50 BODY INTERFERENCE EFFECT ON LIFT

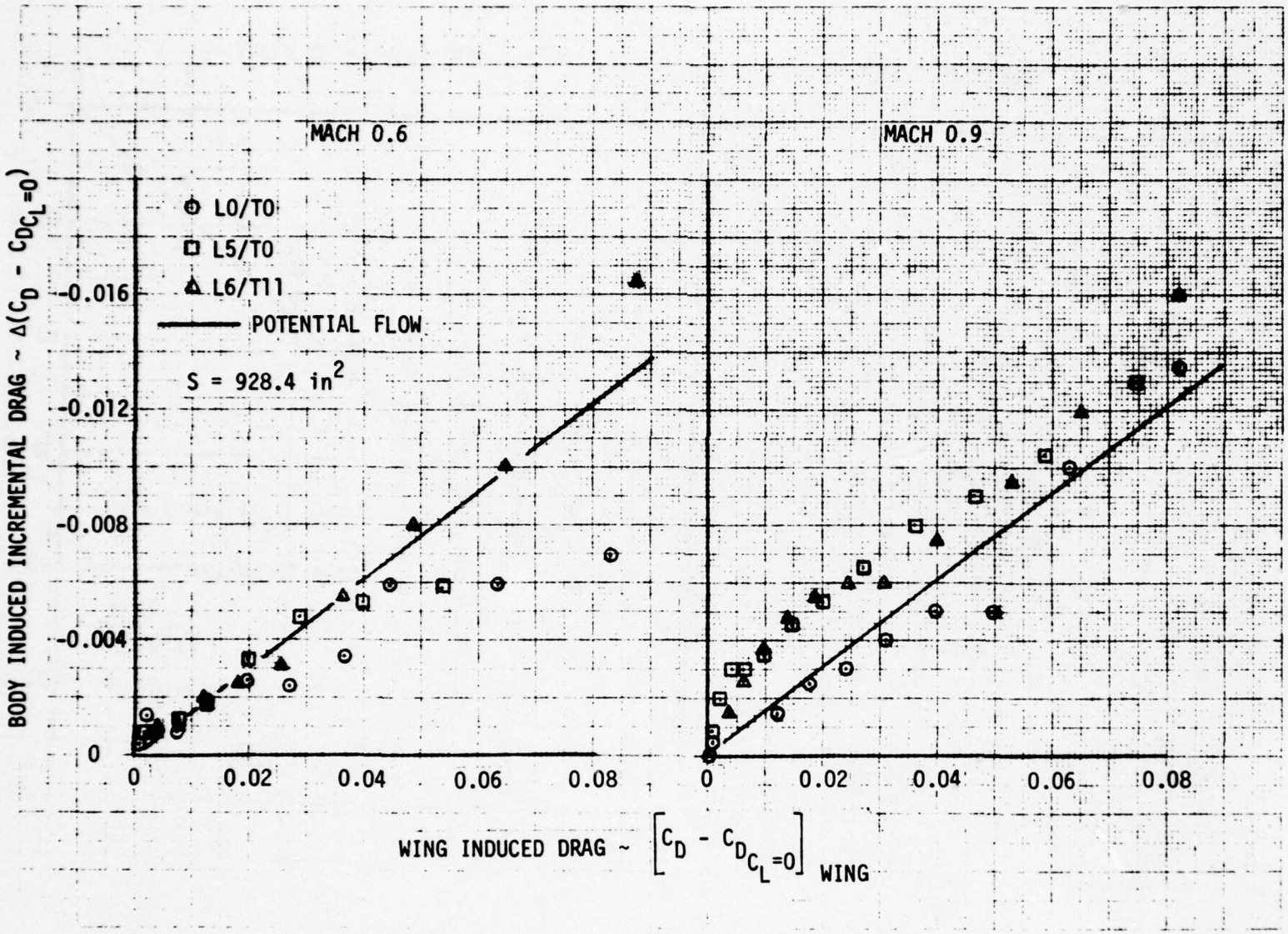

FIGURE 51 BODY INTERFERENCE EFFECT ON DRAG

Mach number where this type of influence would be expected to have been more prevalent. Such improvements in leading edge behavior are probably due to control of viscous phenomena and, thus, failure of the potential solutions to reproduce the observed effects is understandable.

Correlation between predicted and experimental body effects upon the wing pitching moment variation with angle of attack shown in Figure 52 is less conclusive. For the 0.6 Mach number condition, the agreement is on the same order as observed in the lift comparisons for angles of attack below approximately six degrees. Since the experimentally defined conditions for buffet onset for these configurations (see Table 4) correspond approximately to this angle of attack, the lack of agreement at higher angles is not surprising. For the 0.9 Mach number condition, considerable data scatter is observed. It may be that reasonable agreement between predicted and experimental results would be obtained at low angles of attack but insufficient data are available to support this conclusion. Since buffet onset for these configurations at 0.9 Mach number is estimated to occur at approximately four degrees, the scatter and lack of agreement at higher angles is again not surprising.

Except for some reservations concerning the 0.9 Mach number pitching moment characteristics, the comparisons shown in Figures 50 through 52 indicate that the potential flow methods yield reasonable predictions of the variations of body interference effects with angle of attack. Similar agreement was not obtained, however, in comparisons of the predicted and experimental total body interference effect at specific angles of attack. This lack of agreement is suspected to be at least partly the result of the previously discussed uncertainties in the ARC test data. As was observed from Figure 41, the suspected errors in the 0.6 Mach number wing lift measurements are of the same order of magnitude as the total interference effect for lift coefficients below buffet onset. Consequently, it cannot be conclusively stated that corrections for body interference based on the potential flow predictions will reduce the uncertainty in estimates of aircraft performance compared to that which would exist if the LRC test data were used without consideration of the geometric differences between the test body and the analysis aircraft. Conversely, however, if all the differences between the ARC and LRC test

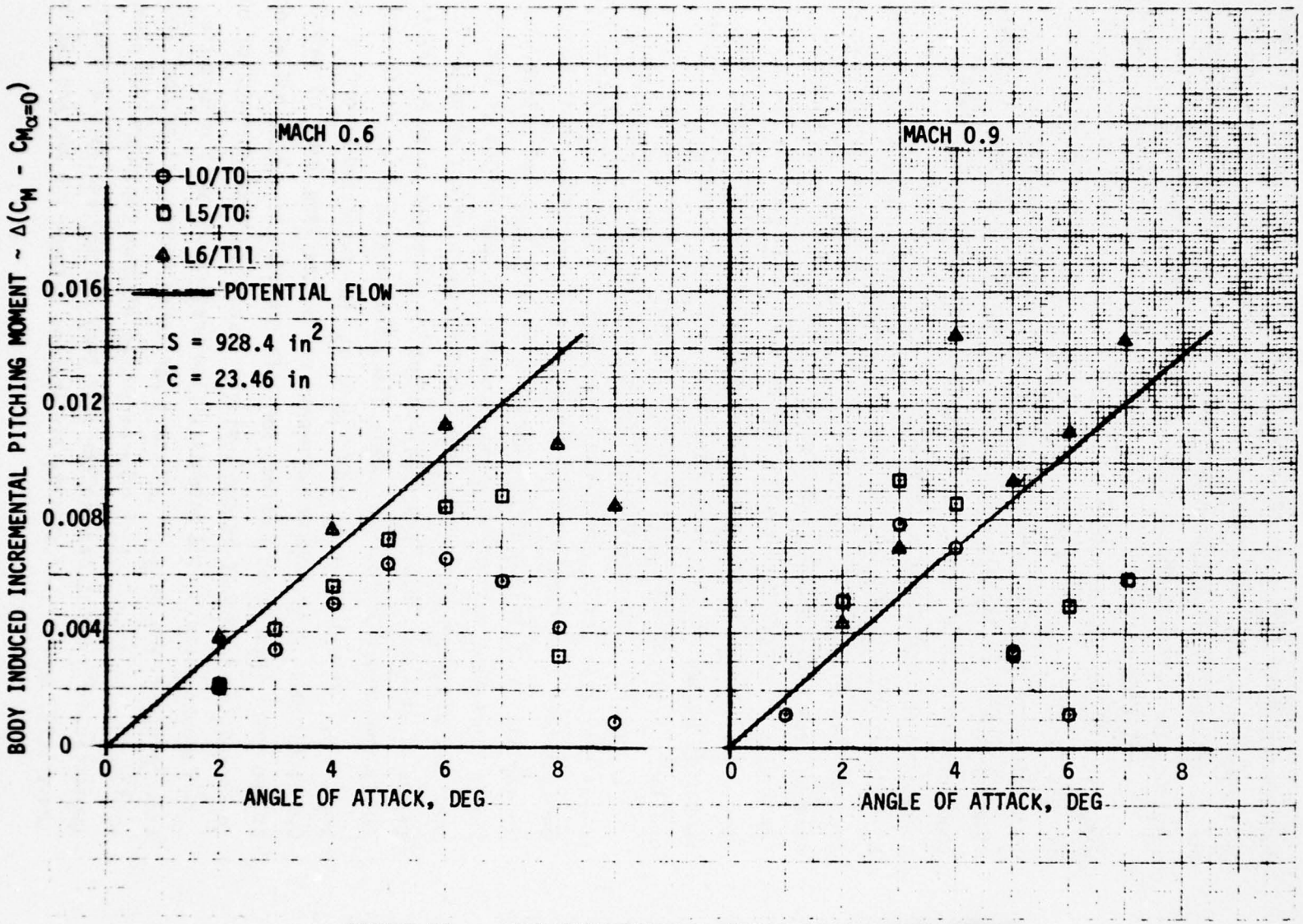

FIGURE 52 BODY INTERFERENCE EFFECT ON PITCHING MOMENT

results are attributed to body effects, then bounds upon the uncertainty in aircraft performance estimates caused by the body geometric differences can be established. Investigations included in these studies to define the impact of the body interference uncertainties upon estimated aircraft aerodynamic characteristics are summarized in the following paragraphs.

According to slender body theory, body interference effects are predominantly a function of the ratio of body radius and wing semi-span. Using this ratio, the body effects upon aircraft trimmed lift and drag can be expressed in function form as;

$$C_{L_{TRIM}} = C_{L_u} + C_{L_T}$$

$$C_{D_{TRIM}} = C_{D_u}(r/s,\ C_{L_u}) + K(C_{L_T} - k)^2$$

where $C_{L_T} = \frac{\bar{c}}{x_T}\ C_{M_u}(r/s,\ C_{L_u})$

C_{L_u} is the untrimmed vehicle lift

C_{D_u} is the untrimmed vehicle drag

C_{M_u} is the untrimmed vehicle pitching moment

$\frac{x_T}{c}$ is the non-dimensional tail lever arm

K and k are constants defining the relationship between lift and drag of the tail

Solving these functional relations permits the total change in trimmed drag with respect to r/s for a fixed total vehicle lift to be expressed as;

$$\frac{dC_D}{d(r/s)} = \frac{\partial C_{D_u}}{\partial(r/s)} + \left[2K(C_{L_T} - k) - \frac{\partial C_{D_u}}{\partial C_{L_u}}\right] \frac{\frac{\bar{c}}{x_T}\ \frac{\partial C_{M_u}}{\partial(r/s)}}{1 + \frac{\bar{c}}{x_T}\ \frac{\partial C_{M_u}}{\partial C_{L_u}}}$$

Drag differences between the wing camber configurations investigated in the ARC and LRC test series are presented in Figure 53 for both 0.6 and 0.9 Mach number. Predictions based upon potential flow computations are also shown in Figure 53. The Hess routine was used for the 0.6 Mach number predictions and as previously indicated slender body theory was used at 0.9 Mach number. The potential flow computations yield reasonable predictions of the experimental trends but do not accurately reproduce the magnitude of the experimental differences. Note that, for all configurations, the body influence causes a reduction in wing drag. The change in drag for a fixed untrimmed lift can be bounded by the expression;

$$\left| \frac{C_{D_u}}{(r/s)} \right| \leq \left| 0.0223 + 0.2128 \, (C_{L_{w(B)}})^2 \right|$$

where $C_{L_{w(B)}}$ is the wing lift coefficient in the presence of the body.

Since wing drag can always be bounded by the product of lift and effective angle of attack, expressing the angle of attack as the ratio of the untrimmed lift to the minimum experimental lift curve slope allows the change in drag with lift for a fixed body geometry to be bounded by;

$$\frac{\partial C_{D_u}}{\partial C_{L_u}} \leq 0.3810 \left| C_{L_{w(B)}} \right|$$

The differences in wing pitching moments obtained in the ARC and LRC test programs at 0.6 and 0.9 Mach number are shown in Figure 54. These results again show that body effects are not altered by changes in wing leading edge camber but that trailing edge camber variations have a strong influence upon the magnitude of the body interference. As indicated previously only the angle of attack variation of body interference on wing pitching moment was estimated using slender body theory. This variation is relatively insensitive to camber configuration, consequently only the prediction for configuration LO/TO is shown in the 0.9 Mach number comparisons. This predicted variation is seen to be in good agreement with the experimental angle of attack variation. Since the Hess routine

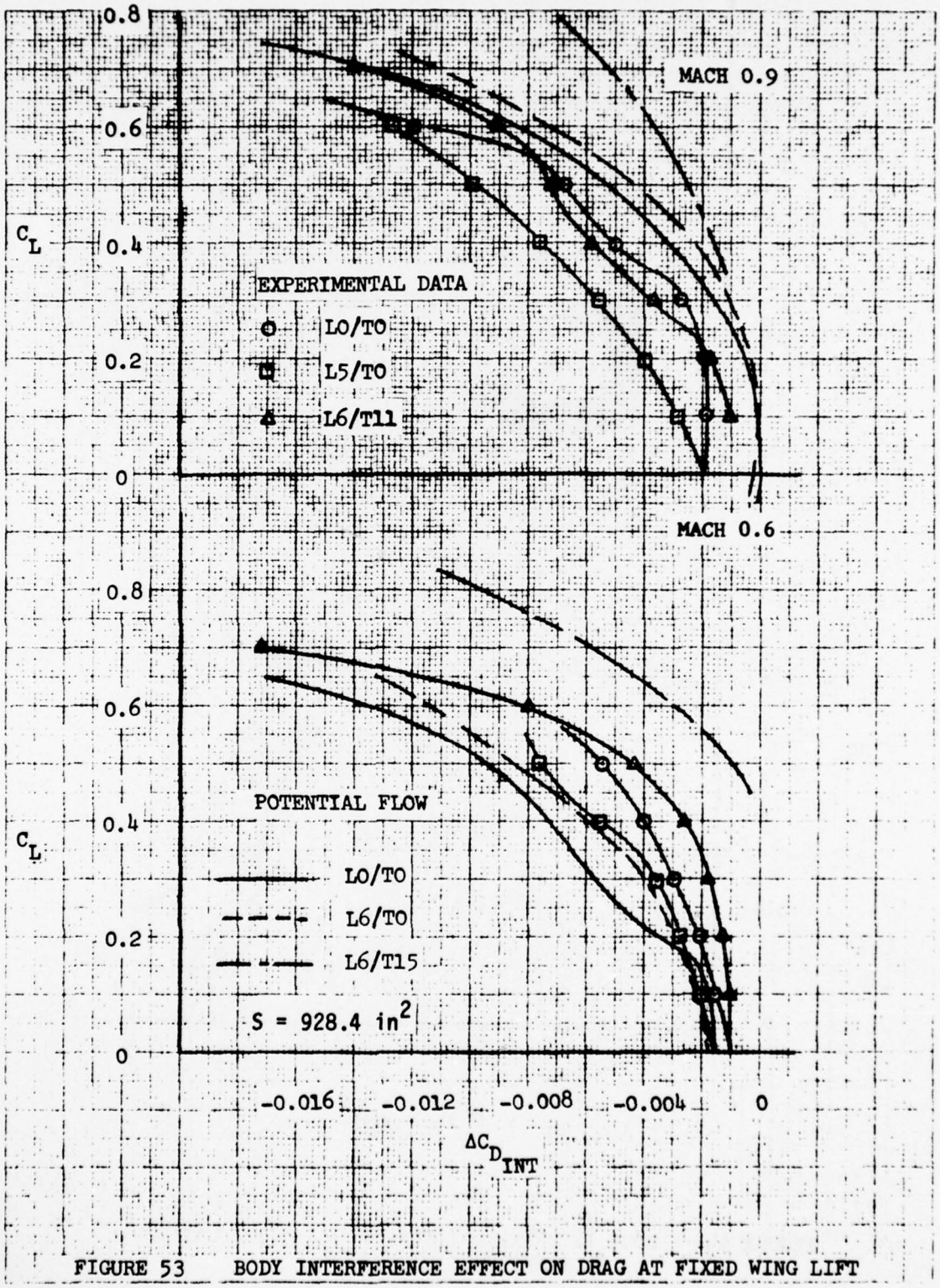

FIGURE 53 BODY INTERFERENCE EFFECT ON DRAG AT FIXED WING LIFT

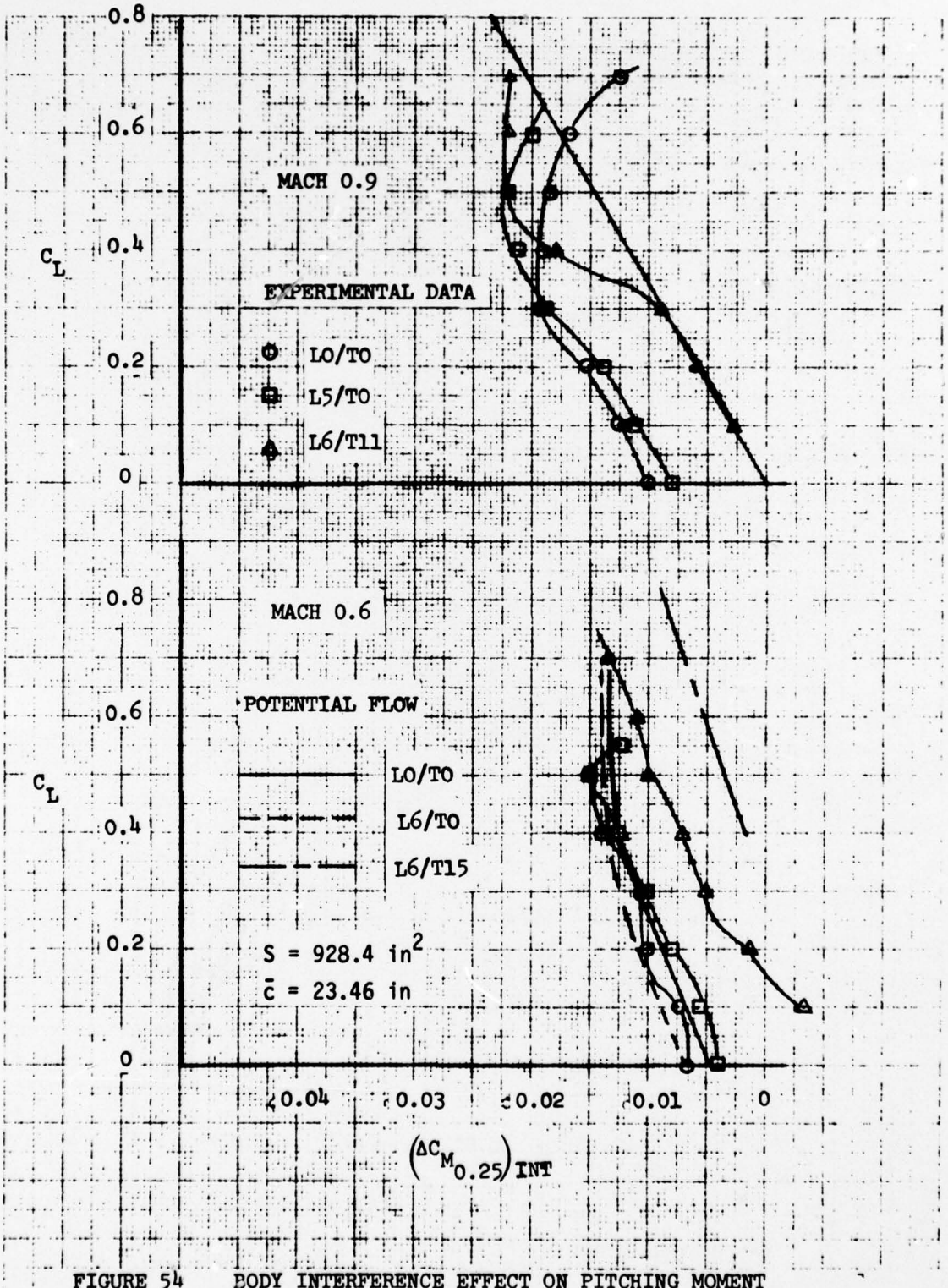

FIGURE 54 BODY INTERFERENCE EFFECT ON PITCHING MOMENT AT FIXED WING LIFT

provides estimates of the total body effect on wing pitching moment, three separate camber configurations were examined at 0.6 Mach number and are shown in Figure 54. Predictions obtained from the Hess program do not appear to reproduce the trailing edge camber influence since the experimental incremental pitching moment for configuration L6/T11 is almost half that predicted for configuration L6/T15 whereas the amount of camber is less than one quarter. Assuming body interference effects upon pitching moment are proportional to trailing edge camber, the rate of change in pitching moment for constant untrimmed lift can be bounded by;

$$\left|\frac{\partial C_{M_u}}{\partial (r/s)}\right| \leq 0.0792 + 0.182 \left|C_{L_{w(B)}}\right|$$

The rate of change of pitching moment with untrimmed lift is directly related to the distance between the wing aerodynamic center and the moment reference. Examinations of the experimental wing stability characteristics indicate that the change in pitching moment with untrimmed lift is bounded by;

$$\left|\frac{\partial C_{M_u}}{\partial C_{L_u}}\right| \leq 0.0414$$

The body radius to wing semi-span ratio for the configuration investigated in the LRC test series was approximately 0.15. The corresponding dimension for the aircraft configuration considered in Section 3.1 of this report is approximately 0.11. The uncertainties in the LRC body interference effects along with this smaller body radius would result in an overestimation of the body effects upon the wing drag characteristics in the aircraft application. Using the aircraft geometric and tail aerodynamic characteristics presented in Section 3 and the above derivative bounds yields the expression for the error bound on the aircraft drag estimates:

$$\delta C_D \leq 0.0008 + 0.0044 \left|C_{L_T}\right| + 0.0010 \left|C_{L_{w(B)}}\right| + 0.0120 \left|C_{L_T}\, C_{L_{w(B)}}\right| + 0.0128 \left|C_{L_{w(B)}}\right|^2$$

Aircraft trimmed drag polars for wing camber configurations L0/T0, L6/T11, and L6/T15 obtained using the procedures discussed in Section 3 are presented in Figure 55 with this error bound to illustrate the impact of the body interference uncertainties upon the basic comparisons of this report. While these results show that the interference uncertainties have a significant effect upon the aircraft trimmed drag characteristics, the ordering of wing camber configurations to minimize drag is not affected. This same conclusion is also applicable to the other aircraft maneuvering performance parameters desired in this program. Consequently, while the aircraft drag predictions may be in error by as much as 10%, buffet free maneuvering performance estimates obtained by using the LRC test results without body interference corrections would still provide a valid indication of the potential benefits of the Vought variable camber wing design concept.

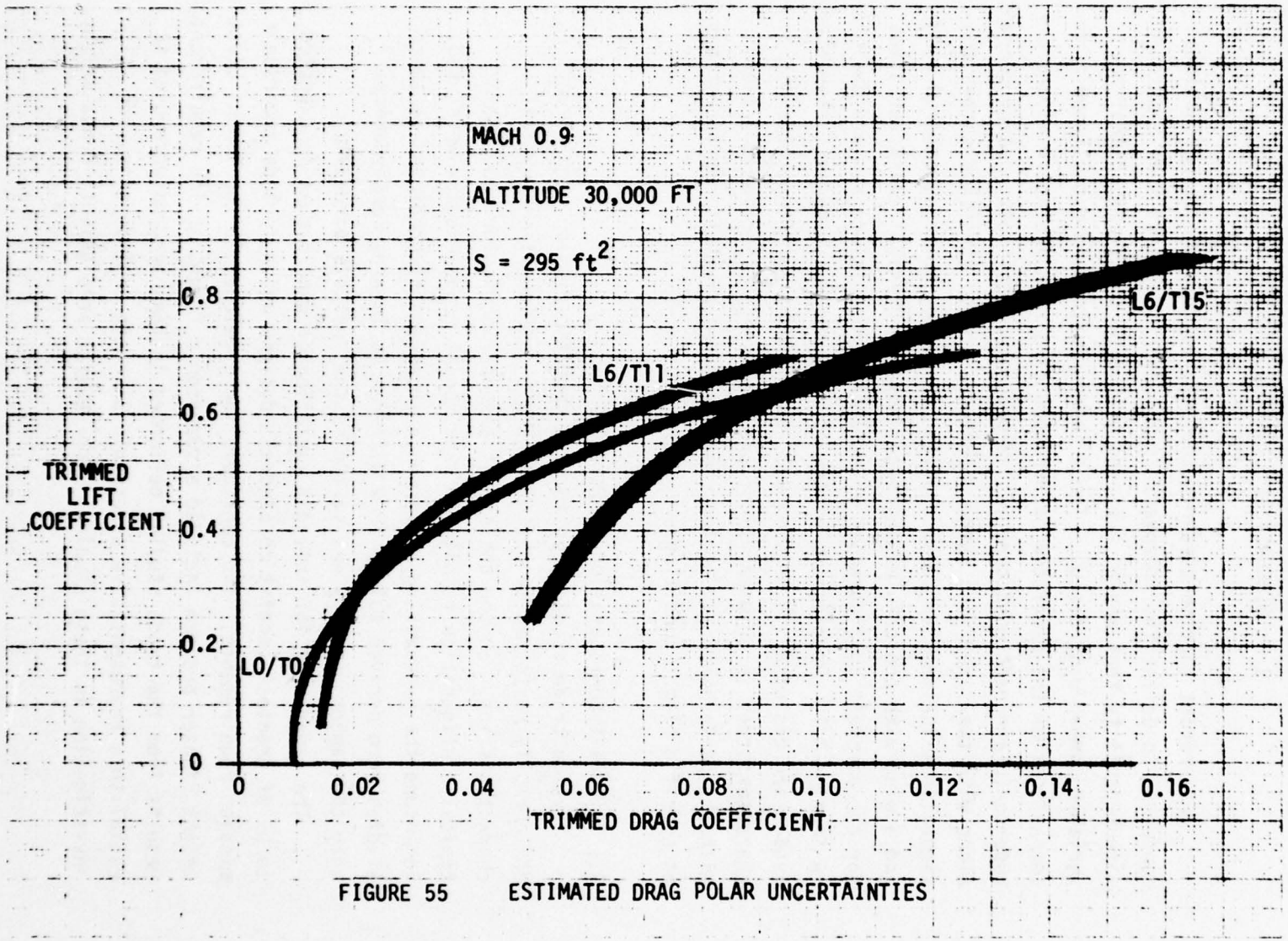

FIGURE 55 ESTIMATED DRAG POLAR UNCERTAINTIES

3.0 AIRCRAFT APPLICATION STUDIES

This report section presents the results from the investigations conducted to define the improvements in aircraft buffet free transonic maneuverability that may be achieved by use of the skewed hingeline variable camber wing design. These improvements were established from comparisons of the predicted performance of a representative advanced supersonic aircraft configuration incorporating this wing design concept along with two fixed wing camber configurations. The fixed camber configurations included in these studies correspond to an uncambered wing and a wing with conical leading edge camber. Physical characteristics for the aircraft configuration investigated in this program are defined in Section 3.1. Predictions of the configuration aerodymamic characteristics are discussed in Section 3.2 Estimated aircraft aerodynamic characteristics in trimmed flight are discussed in Section 3.3 along with the performance predictions for the three aircraft configurations at specific flight conditions.

3.1 Aircraft Configuration Definitions

Design trade studies considering specific mission requirements are normally performed to define aircraft configuration physical characteristics. In the absence of a specific mission requirement typical configuration results of past Vought trade studies were used. To insure the maneuvering performance improvements predicted in these studies were derived solely from differences in wing aerodynamics, only the camber geometry was varied in the analysis aircraft.

The capability for inflight variation of wing camber is expected to be of greatest benefit to aircraft designs which include supersonic mission requirements. The configuration developed in the Vought Lightweight Fighter program included a supersonic flight design requirement. Results from the trade studies performed in that program were used to establish a representative supersonic aircraft configuration for investigation in these studies. The general arrangement, gross weight,

center of gravity, tail area and volume coefficient and wing area defined for this analysis configuration were assumed independent of wing configuration and associated aerodynamic differences.

Three wing configurations were included in these aircraft application studies. Two of the camber distributions were assumed fixed and corresponded to an uncambered wing and a wing with conical leading edge camber. The third configuration represented the skewed hingeline leading and trailing edge segmented flap variable camber wing concept. The exposed wing planform and airfoil sections for these three wing configurations were assumed to correspond to the Vought semi-span wing model characteristics defined in Table 1. The uncambered wing configuration, termed the basic wing, was used as a baseline configuration to illustrate the camber effects upon transonic performance. The fixed conical leading edge camber configuration was chosen to be representative of the camber distributions developed in the Vought Lightweight Fighter and Advanced Navy Fighter design trade studies.

The pertinent physical characteristics of the aircraft configuration established for these investigations are presented in Table 5. In addition to these characteristics, an aircraft gross weight of 15,000 pounds and a center of gravity located at 24 percent of the theoretical wing mean geometric chord were assumed.

3.2 Configuration Aerodynamic Characteristics

The aerodynamic characteristics for the three aircraft configurations were developed by combining the predicted contribution of the major configuration components. The components considered in this approach are indicated by the following basic analytical expressions used in defining the configuration lift, drag, and pitching moment.

$$C_L = C_{L_{BV}} + \Delta C_{L_{B(W)_{\alpha\neq 0}}} + \Delta C_{L_{B(W)_{\alpha=0}}} + C_{L_{W(B)}} + C_{L_{T_{(WB)}}}$$

$$C_M = C_{M_{BV}} + \Delta C_{M_{B(W)_{\alpha\neq 0}}} + \Delta C_{M_{B(W)_{\alpha=0}}} + C_{M_{W(B)}} + C_{M_{T_{(WB)}}}$$

$$C_D = C_{D_{BV}} + \Delta C_{D_{B(W)_{\alpha\neq 0}}} + \Delta C_{D_{B(W)_{\alpha=0}}} + C_{D_{W(B)}} + C_{D_{T_{(WB)}}}$$

TABLE 5

ANALYSIS AIRCRAFT PHYSICAL CHARACTERISTICS

Wing - Theoretical	
Area, sq. ft.	295.0
Span, ft.	34.585
Aspect Ratio	4.055
Taper Ratio	.3723
Sweepback of 1/4 chord line, deg.	30.43
Geometric twist, deg.	0.0
Dihedral, deg.	0.0
Geometric wing incidence, relative to fuselage reference line, deg.	0.0
Root chord, ft.	12.4335
Tip chord, ft.	4.62917
Mean geometric chord	
(1) Length, ft.	9.1258
(2) Spanwise location from plane of symmetry, ft.	7.3297
(3) Location of leading edge of MGC, fuselage station, ft.	23.6751
Airfoil section parallel to plane of symmetry	
(1) At wing-fuselage junction	NACA 65A005
(2) Wing tip	NACA 65A004
Fuselage	
Length, ft.	44.83
Width, ft.	3.80
Horizontal Stabilizer, Exposed	
Area, sq. ft.	44.2679
Span, ft.	11.92
Aspect ratio	3.2097
Taper ratio	.1921
Sweepback of 1/4 chord line, deg.	45
Mean geometric chord	
(1) Length, ft.	4.28242
(2) Spanwise location from plane of symmetry, ft.	4.20674
Tail length from 25 percent theoretical wing MGC to 25 percent horizontal tail exposed MGC, ft.	12.8958
Tail volume coefficient (L_T = 12.8958)	.212
Maximum Deflections, deg.	
(1) Leading edge up	6.75
(2) Leading edge down	26.5
Airfoil section	
(1) Root	NACA 65A005
(2) Tip	NACA 65A004

TABLE 5 (Continued)

ANALYSIS AIRCRAFT PHYSICAL CHARACTERISTICS

Vertical Stabilizer, Exposed

Area, ft.	87.23
Span, ft.	10.77
Aspect ratio	1.33
Taper ratio	.30
Sweepback of leading edge, deg.	50

where the subscripts denote

BV	Isolated body-vertical tail coefficients
$B(W)_{\alpha \neq 0}$	Body coefficient values resulting from wing induced interference loading at angle of attack
$B(W)_{\alpha=0}$	Incremental body coefficient values resulting from wing induced interference loading at zero angle of attack
W(B)	Exposed wing panel coefficients including the interference induced by the body
$T_{(WB)}$	Tail coefficient values including the interference loading induced by both the wing and body

It should be noted that the coefficients indicated in these equations as well as all other force and moment coefficients discussed in this report section are non-dimensionalized by the analysis aircraft theoretical wing area and mean geometric chord with the moments referenced to the analysis aircraft center of gravity. Methods used to estimate the aerodynamic characteristics for the individual configuration components indicated in these equations are detailed in the following paragraphs.

Predicted Fuselage-Vertical Aerodynamics

As indicated above, the fuselage and vertical tail contribution to the total configuration aerodynamics was assumed to be composed of two parts; the contribution of the isolated fuselage/vertical tail configuration and the fuselage loading induced by wing interferences. Experimental results, Reference 16, obtained from design development wind tunnel tests conducted in support of the Vought Advanced Navy Aircraft design program were used to establish the isolated fuselage/vertical tail aerodynamic characteristics. These test results show that the isolated fuselage/vertical tail configuration produces no lift at zero angle of attack. These data also indicate the fuselage/vertical tail lift and pitching moment vary linearly with angle of attack for angles less than 10 degrees. The isolated fuselage aerodynamic center predicted from these data was located at approximately 11 percent of the fuselage length at both 0.6 and 0.9 Mach number. Consequently, for the present studies, the fuselage aerodynamic center was located forward

of the aircraft center of gravity a distance equal to 2.3196 times the theoretical wing mean geometric chord. Examinations of the Reference 16 test data indicate the fuselage/vertical tail contribution to the aircraft lift, drag and pitching moment are analytically represented by:

$$C_{L_{BV}} = C_{L_{\alpha_{BV}}} \alpha$$

$$C_{M_{BV}} = C_{D_{O_{BV}}} + 2.3196\ C_{L_{BV}}$$

$$C_{D_{BV}} = C_{D_{O_{BV}}} + C_{L_{BV}}^{2} \frac{\delta C_D}{\delta C_{L_{BV}}} 2$$

The specific values for the parameters indicated in these equations were established from the Reference 16 test results and are presented in Table 6.

Since the test results contained in Reference 16 were obtained at Reynolds numbers different from those corresponding to the free flight conditions considered in these studies, the isolated fuselage/vertical tail configuration drag at zero lift was analytically estimated from:

$$C_{D_{O_{BV}}} = 1.1\ C_1\ C_f$$

where C_f is the incompressible flat plate skin friction drag coefficient for fully turbulent flow

C_1 is the compressibility correction for turbulent flat plate skin friction drag defined in Reference 18. [$C_1 = 1\text{-}0.9M^2$]

The constant factor, 1.1, in this drag estimation was included as an approximation of the fuselage/vertical tail base and pressure drag effects. Predicted values of $C_{D_{O_{BV}}}$ obtained using this relation for the flight conditions considered in these studies are presented in Table 6.

The methods of Reference 12, which are based upon slender body theory, were used to predict the fuselage lift induced by wing interference. In this approach, the fuselage lift is proportional to the lift produced by the isolated wing. The constant of proportionality,

(interference factor), is a function of the ratio of body radius and wing semi-span. Wing influences upon the fuselage lift characteristics defined in Reference 12 involve two effects: the interference lift induced at zero angle of attack,and the additional lift at non-zero angles. As discussed earlier, Reference 12 also provides estimates of the wing lift in the presence of a body in terms of the isolated wing lift. Thus, by proper substitution, the wing induced fuselage lift can be expressed in terms of the wing lift in the presence of the fuselage. This substitution along with the interference factors determined from Reference 12 were used to establish analytical expressions of the fuselage lift induced by the wing interference:

$$\Delta C_{L_{B(W)}}\Big|_{\alpha=0} = 0.117 \; C_{L_{W(B)}}\Big|_{\alpha=0}$$

$$\Delta C_{L_{B(W)}}\Big|_{\alpha\neq 0} = 0.1422 \; \frac{\delta C_{L_{W(B)}}}{\delta \alpha} \; \alpha$$

The incremental fuselage pitching moments induced by wing interference effects were determined from the computed lift increments and the predicted center of pressure of the interference loading. The methods of Reference 20 were used to establish the interference loading center of pressure. This method defines the interference loading center of pressure as a function of Mach number. For the 0.6 Mach number condition, the predicted center of pressure was located forward of the aircraft center of gravity a distance equal to 17.21 percent of the theoretical wing mean geometric chord. The center of pressure location was also predicted to be forward of the center of gravity at 0.9 Mach number although the corresponding distance was reduced to 14.5 percent of the mean chord.

The fuselage incremental drag induced by the wing interference also involves an effect at zero angle of attack and an effect at non-zero angles. At zero angle of attack, this incremental drag is a function of the wing induced changes in the fuselage pressures and the corresponding local surface inclination relative to the body axis. Since the fuselage surface slopes in the vicinity of the wing for

typical aircraft configurations are relatively small, the incremental drag at zero angle of attack would also be expected to be small. Prediction of this effect requires a detailed configuration geometric definition which is beyond the scope of the present studies, consequently, the incremental drag at zero angle of attack was assumed negligible for the present studies. The wing induced fuselage drag at angle of attack, however, involves a component of the induced normal force that is not small or neglectable. For these investigations, the induced drag at angle of attack was estimated as the product of the wing induced lift and the angle of attack. Thus, the total contribution of the wing induced fuselage loading to the analysis aircraft drag characteristics were predicted from the following relations:

$$\Delta C_{D_{B(W)}}\Big|_{\alpha=0} = 0$$

$$\Delta C_{D_{B(W)}}\Big|_{\alpha\neq 0} = \left[\Delta C_{L_{W(B)}}\Big|_{\alpha=0} + \Delta C_{L_{W(B)}}\Big|_{\alpha\neq 0} \right] \alpha$$

Predicted Horizontal Tail Aerodynamics

Wind tunnel test results obtained for the Vought Advanced Navy Fighter design program, Reference 17, were used to establish the aerodynamic characteristics of the analysis aircraft horizontal tail configuration. The aspect ratio and taper ratio of the horizontal tail model investigated in that test series correspond to the tail configuration considered in these studies. The geometric relationship between the wing and tail of this model, however, differs from the relationship for the aircraft configuration defined in Table 5. The ratio of the model tail area and wing area in the test was 0.13 and the tail volume coefficient was o.1733. Empirical charts contained in Reference 20 were used to evaluate the effect of these configuration differences upon the downwash at the horizontal tail location. Results from these investigations indicate these differences would induce less than one percent variation in the rate of change in tail downwash with angle of attack. Downwash differences of this magnitude would be expected to

have negligible effect upon the tail lift and drag characteristics and, consequently, the Reference 16 test data have been used in these studies without downwash corrections.

In order to facilitate the aircraft balance computations of this program, the horizontal tail contribution to the total aircraft configuration drag and pitching moment characteristics were desired in terms of the tail lift. Analysis of the Reference 17 test results indicate the tail lift, drag, and pitching moment characteristics are related by the following expressions:

$$C_{M_{T(WB)}} = C_{L_{T(WB)}} \frac{l_T}{\bar{c}}$$

$$C_{D_{T(WB)}} = C_{D_{O_T}} + K_1 \left[C_{L_{T(WB)}} - K_2\right]^2$$

where $\frac{l_T}{\bar{c}}$ is the horizontal tail aerodynamic moment arm

K_1 is a measure of the tail efficiency

K_2 is the tail lift coefficient corresponding to minimum tail drag

$C_{D_{O_T}}$ is the tail minimum drag coefficient

The tail induced drag characteristics indicated by the above equation were established from experimental results involving four different tail incidence settings and wing configurations with camber distributions comparable to those included in the present studies.

The horizontal tail aerodynamic moment arm differs from the geometric distance between the aircraft center of gravity and the predicted tail aerodynamic center location primarily due to the inclination of the tail lift vector. The analysis aircraft tail aerodynamic moment arm was predicted assuming an aircraft aerodynamic and geometric tail moment arm ratio equal to that defined by the Reference 17 test results. The values of the tail aerodynamic moment arm as well as the constants, K_1 and K_2, relating tail lift and drag predicted from the Reference 16 experimental data are presented in Table 7.

The horizontal tail minimum drag coefficient was predicted from flat plate skin friction drag estimates using the relation previously defined in the discussion of the fuselage/vertical tail drag predictions. Horizontal tail minimum drag coefficients predicted for the flight altitude and Mach number conditions considered in these studies are listed in Table 7.

Predicted Wing Aerodynamics

The experimental results obtained from wind tunnel tests of the Vought semi-span wing model, Reference 1, were used to establish the aerodynamic characteristics of the three analysis aircraft wing configurations. The basic (uncambered) wing characteristics were estimated from the data obtained for configuration L0/T0 defined in Table 2. Test results obtained for configuration L6/T0 were used to define the aerodynamic characteristics for the wing configuration involving fixed leading edge camber. The camber distribution of configuration L6/T0 closely approximates the conical distributions developed in the Vought Lightweight Fighter and Advanced Navy Fighter design trade studies. This distribution also approximates the conical camber distribution defined from Reference 19 for a design lift coefficient of 0.50 at 1.0 Mach number. The variable camber wing aerodynamic characteristics were developed assuming a camber variation capability compatible with the fixed wing camber configurations investigated in the Reference 1 test series and defined in Table 2.

As discussed previously, the Reference 1 tests of the Vought semi-span wing were conducted with the model mounted on the tunnel wall using a non-metric body as a support fairing. Investigations of the influence of this body upon the wing test data were discussed in Section 2.3. Results from these investigations have shown the influences of this body upon the wing force characteristics generally agree with the trends predicted from potential flow theory. However, the experimentally defined body induced force increments did not agree with magnitudes indicated from the analytical predictions. Also the available experimental results indicated a larger variation in the body effects with changes in wing camber than the analytical predictions. This

variation in body interference with wing camber was considered more significant to the present studies than the potential analysis errors discussed in Section 2.3 incurred by neglecting the geometric differences between the test body and analysis aircraft fuselage. Consequently, the wing lift, drag and pitching moment data from Reference 1 have been used in these aircraft application studies without body interference corrections. The incremental drag corrections due to Reynolds number effects, defined in Section 2.2, were used in conjunction with the test data to estimate the wing drag characteristics in full scale flight.

TABLE 6
PREDICTED ISOLATED FUSELAGE/VERTICAL
TAIL AERODYNAMIC CHARACTERISTICS

M	ALTITUDE FEET	$C_{L_{\alpha_{BV}}}$ per degree	$C_{M_{O_{BV}}}$ per degree	$\frac{\delta C_D}{\delta C_{L_{BV}}^2}$	$C_{D_{O_{BV}}}$
.6	20,000	.0019	-.00584	10.085	.0053
	30,000	"	"	"	.0057
.9	20,000	.0017	-.0066	8.3759	.0048
	30,000	"	"	"	.0048

TABLE 7
PREDICTED HORIZONTAL TAIL
AERODYNAMIC CHARACTERISTICS

MACH NUMBER	ALTITUDE FEET	$(l_T/\bar{c})$ AERO MOMENT ARM	$C_{D_{O_T}}$	K_1	K_2
.6	20,000	-1.2296	.00096	1.0098	.01335
	30,000	"	.00099	"	"
.9	20,000	-1.3847	.00083	1.1375	.01224
	30,000	"	.00087	"	"

3.3 Aircraft Perfromance Comparisons

Trimmed Flight Predictions

The predicted aerodynamic characteristics for the configuration components discussed in the previous section were used to define trimmed lift curves and drag polars for the three analysis aircraft configurations at Mach numbers of 0.6 and 0.9 and altitudes of 20,000 and 30,000 feet. For the basic wing and fixed wing camber configurations, these computations were accomplished in a straightforward manner. The tail lift required to trim was determined as a function of angle of attack from the basic equation defining the configuration pitching moments. This lift and associated tail drag were then combined with the wing and fuselage lift and drag predictions to establish the total configuration trimmed lift and drag variation with angle of attack.

Definition of the trimmed flight aerodynamics for the variable camber wing configuration was more complicated since the "optimum" camber schedule with angle of attack was not known a priori. For these studies "optimized" camber schedules were defined to satisfy two separate design objectives: (1) minimize configuration drag, and (2) minimize configuration drag maintaining buffet-free lift. Although it is recognized that structural, actuation, and various other considerations would also influence the camber scheduling in an actual aircraft design, such considerations were not included in these studies. Thus, two different camber schedules were considered for the variable camber aircraft configuration; one with and the other without consideration of camber influences upon the wing buffet onset angles of attack.

Both variable camber wing camber schedules were established by correlation of the aircraft trimmed lift and drag characteristics computed for each of the wing camber configurations investigated in Reference 1 and listed in Table 2. Trimmed lift curves and drag polars for these eleven camber configuration were developed using the same procedures as described for the basic and fixed wing camber configurations. Computed trimmed characteristics for these aircraft wing camber configurations for flight Mach numbers of 0.6 and 0.9 and an altitude of 30,000 feet are presented in Appendix B. Similar predictions for

an altitude of 20,000 feet are different only by a constant increment in the zero lift drag and, therefore, have not been shown. Buffet onset conditions for each aircraft/wing camber configuration are also indicated on the Appendix B figures. These conditions correspond to the angles of attack defined from analyses of the Reference 1 experimental data using the methods discussed in Section 2.1.

Trimmed flight drag polars for the wing camber distributions determined to satisfy the minimum drag camber schedule criteria at 0.6 Mach number and 30,000 feet are shown in Figure 56. As would be expected, this schedule is seen to originate with the uncambered wing configuration, L0/T0. At a trimmed lift coefficient of approximately 0.15, the leading edge camber configuration, L24/T0, becomes the "optimum" camber distribution subsequently transitioning to L6/T10 and eventually to L6/T15 at the higher lift levels.

The predicted characteristics shown in Figure 56 indicate the leading edge camber is an effective means for improving the aircraft trimmed flight performance at low to moderate lift levels; whereas trailing edge camber is indicated to be a detriment at these conditions. However, at the higher lift levels, these results indicate trailing edge camber is needed to reduce the aircraft trimmed flight drag levels. These same characteristics were observed in previous analyses of the Reference 1 wing test data and thus, are directly attributable to wing aerodynamic characteristics. It is of interest to note that, of the wing configurations investigated in Reference 1, the L24/T0 configuration camber distribution also yielded the greatest wing lift to drag ratio at this Mach number.

The drag polars developed for the basic wing, fixed wing camber and variable wing camber aircraft configurations at the 0.6 Mach number and 30,000 feet flight conditions are illustrated in Figure 57. The estimated aircraft trimmed lift coefficient corresponding to onset of wing buffet is also noted for each configuration. An interesting development from the investigations at this Mach number is implied in this figure. The camber schedule for minimum configuration drag is identical to the camber schedule predicted to yield minimum drag but

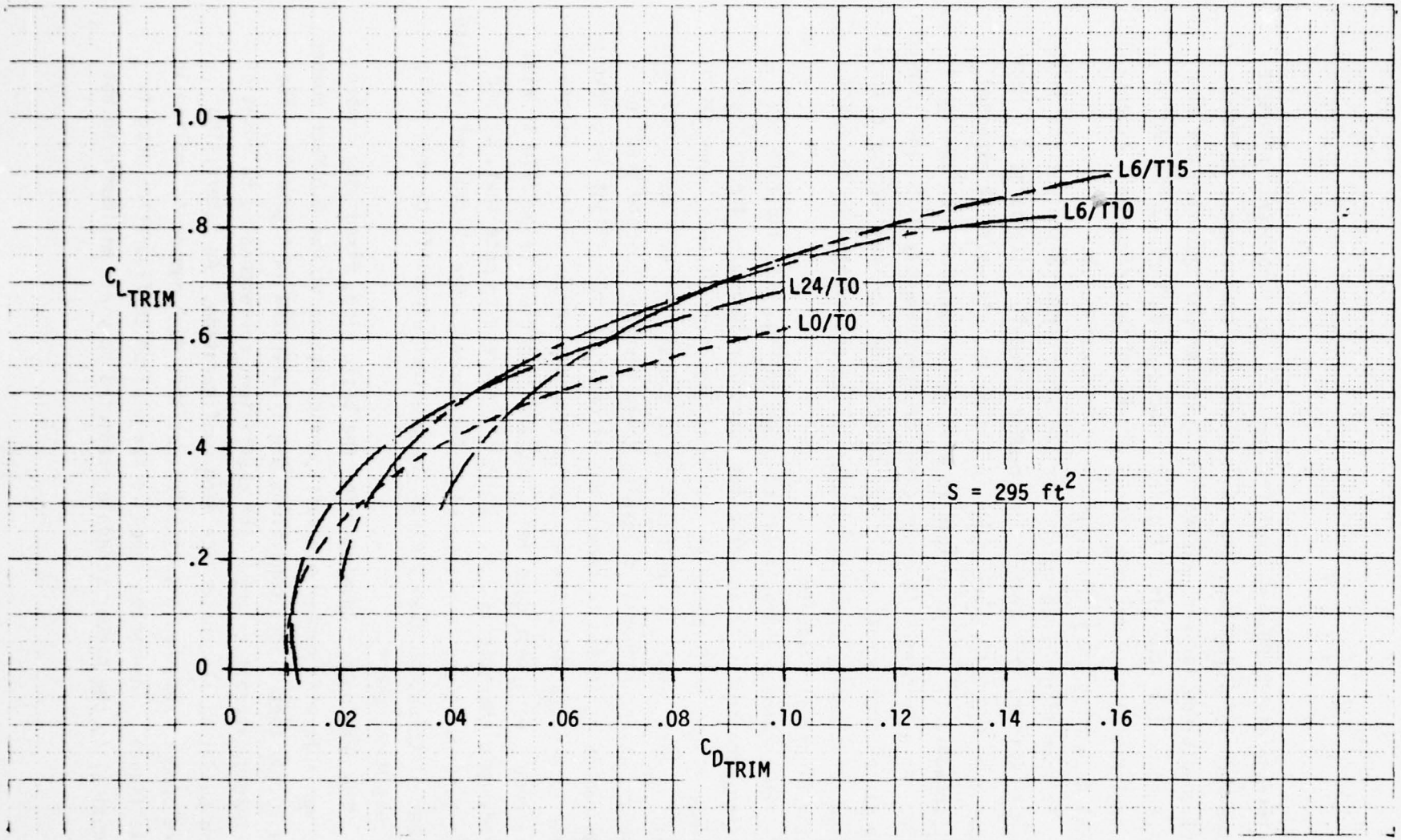

FIGURE 56 CAMBER INFLUENCE UPON AIRCRAFT DRAG CHARACTERISTICS, M=0.6

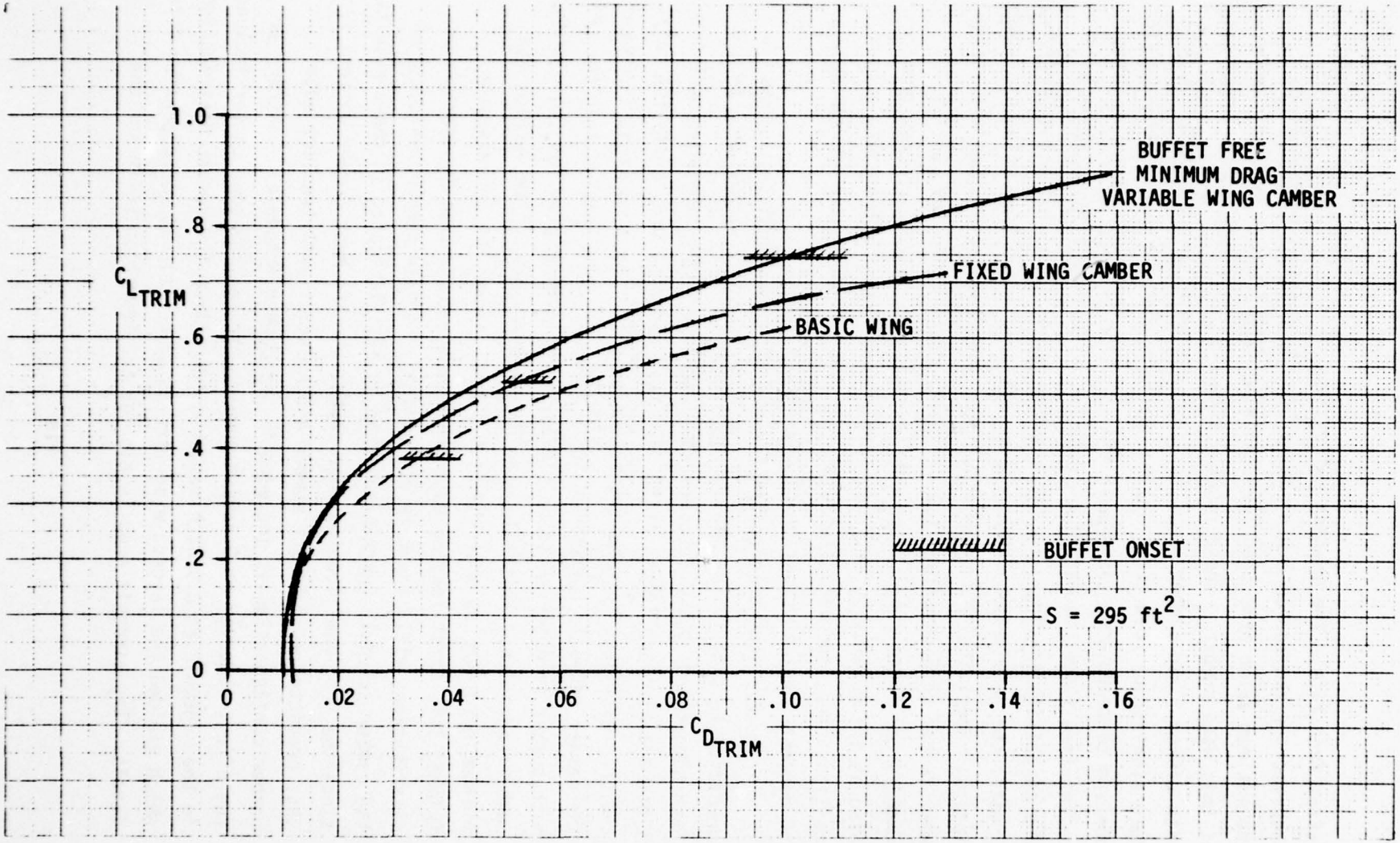

FIGURE 57 ANALYSIS AIRCRAFT TRIMMED AERODYNAMICS, M=0.6

buffet free lift. The maximum buffet free lift coefficient of 0.74 observed for the variable wing camber configuration corresponds to the maximum value predicted from the wing experimental data available at this Mach number. These results show that aircraft wing configurations with either fixed camber or an inflight variable camber capability produce significant reductions in the aircraft drag for lift levels corresponding to maneuvering flight as well as significantly increasing the buffet-free flight capability. However, as observed from Figure 57, the capability for inflight variation of wing camber induces appreciably greater changes in the analysis aircraft drag and buffet onset characteristics. Specifically, the buffet onset lift coefficient for the variable wing camber configuration is 95 percent greater than the basic wing whereas the fixed wing camber configuration is only 37 percent greater. Also at the maximum buffet free lift coefficient for the fixed wing configuration, the variable camber capability results in approximately 50 percent greater reduction of the aircraft drag.

Trimmed flight drag polars for the wing camber distributions predicted to satisfy the minimum drag camber schedule criteria at 0.9 Mach number and 30,000 feet are shown in Figure 58. The same configurations are also applicable at 20,000 feet since as previously indicated the drag estimates for the two altitudes differ by a constant increment. The camber schedule corresponding to minimum configuration drag for this Mach number is observed to be similar to that predicted for the 0.6 Mach number condition. Initially, the uncambered wing, L0/T0, yields the minimum drag but as observed at 0.6 Mach number for increases in trimmed lift first leading edge and subsequently, trailing edge camber distributions yield lower levels of drag. A Mach number influence on the camber schedule for minimum drag is also indicated in these results since the "optimum" leading edge camber at this Mach number differs from that predicted at 0.6 Mach number and an additional trailing edge camber configuration is included in the camber schedule. Contrary to the effect observed at 0.6 Mach number, the leading edge camber included in the schedule at 0.9 Mach number differs from the camber distribution which yielded the largest wing lift to drag ratio at corresponding lift levels. The aircraft drag levels for configuration L6/T0 and the

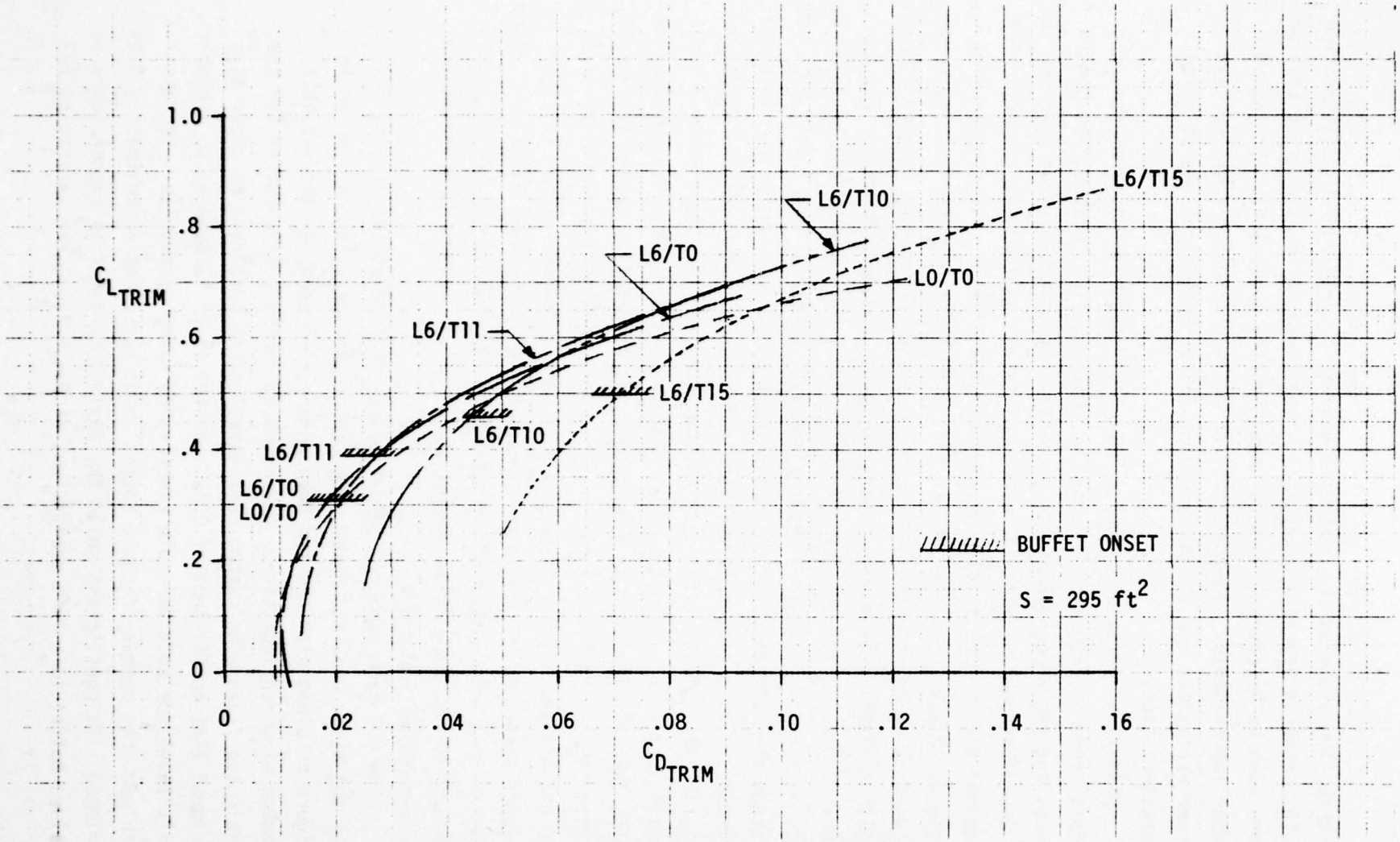

FIGURE 58 CAMBER INFLUENCE UPON AIRCRAFT DRAG CHARACTERISTICS, M=0.9

distribution yielding the maximum wing lift to drag ratio, configuration L5/T0, shown in Appendix B are small, and thus implies that wing test programs such as Reference 1 can be used directly to evaluate leading edge camber improvements. However, this is not the case for trailing edge camber variations due to the resulting large changes in wing pitching characteristics.

Conditions for onset of wing buffet are also indicated on the drag polars shown in Figure 58. As can be observed from these buffet conditions, the camber schedules for the buffet free lift-minimum drag and the minimum drag design criteria must be different at this Mach number. The required differences involve the variation of camber introduction with angle of attack. For the maximum buffet free lift, camber must be introduced in a manner to obtain increases in lift coefficient above 0.39 with angle of attack remaining constant at approximately 3 degrees. For the camber schedule minimizing configuration drag both camber and angle of attack vary up to an angle of approximately 7 degrees. The buffet free lift-minimum drag camber schedule at this Mach number was determined from the trimmed aircraft drag polars shown in Figure 59. The L0/T0 wing camber distributions yield buffet free minimum configuration drag up to a lift coefficient of approximately 0.31. Above this lift level, a camber schedule, and thus the trimmed drag polar, was developed from the results predicted for the four available trailing edge camber configurations. As can be observed, it was assumed that a camber schedule could be established which would yield a continuous buffet free drag variation. Since the trailing edge camber distributions for configurations L6/T11, L6/T1, and L6/T10 represent proportional increases in camber, this assumption is considered justified.

The 0.9 Mach number/30,000 feet altitude predicted drag polars for the basic wing and fixed wing camber configurations are shown in Figure 60 along with the two drag polars developed for the variable camber wing configuration. As indicated, initial wing buffet for the basic and fixed wing camber configurations is predicted to occur at a trimmed lift corfficient of 0.31. Buffet onset is delayed to a higher lift level for both variable camber wing camber schedules. For the minimum drag camber schedule buffet onset occurs at approximately 0.39 trimmed lift coefficient while the maximum buffet free camber schedule delays buffet to a lift coefficient of 0.5. Thus, the capability for

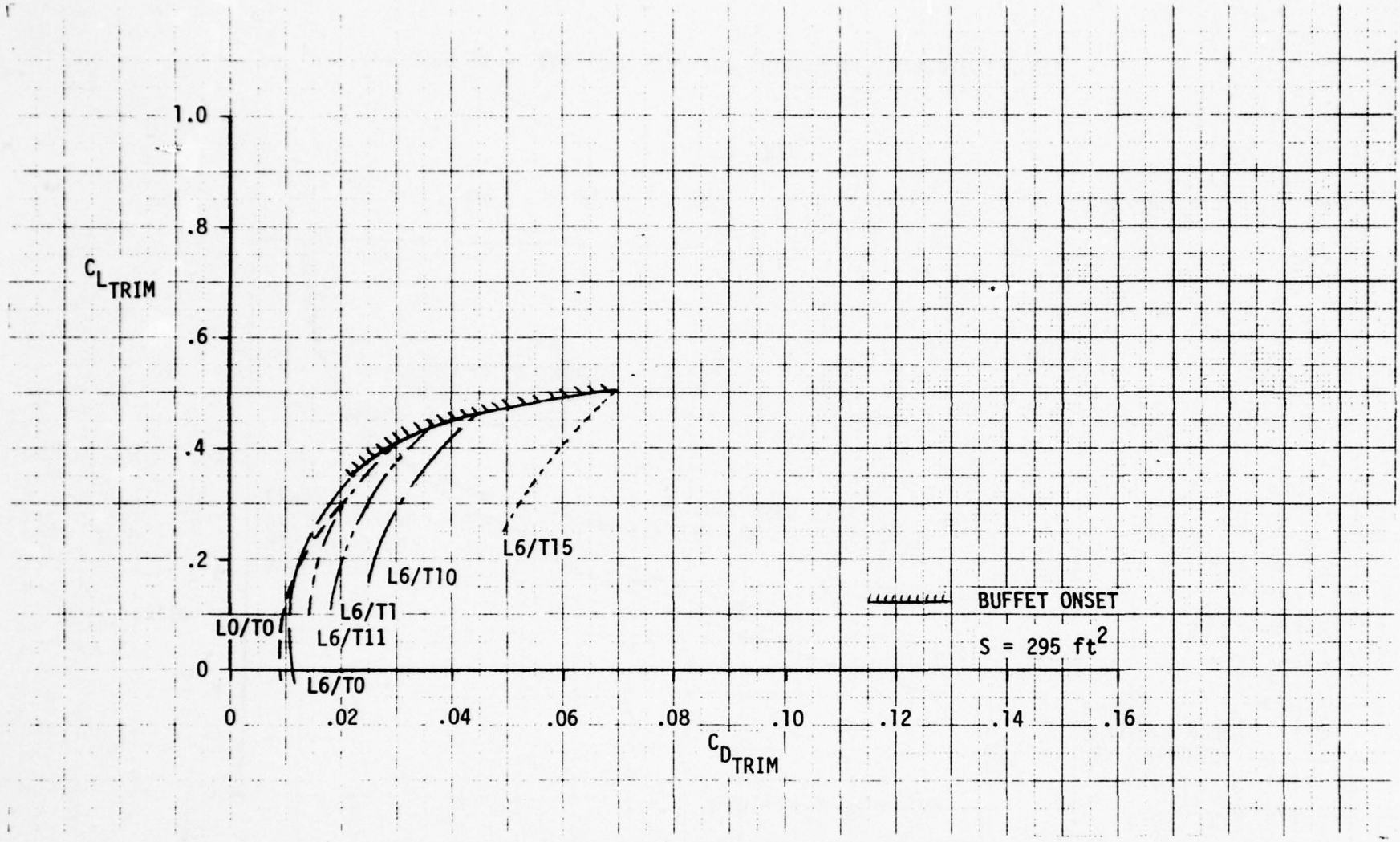

FIGURE 59 CAMBER INFLUENCE UPON AIRCRAFT BUFFET FREE DRAG CHARACTERISTICS, M=0.9

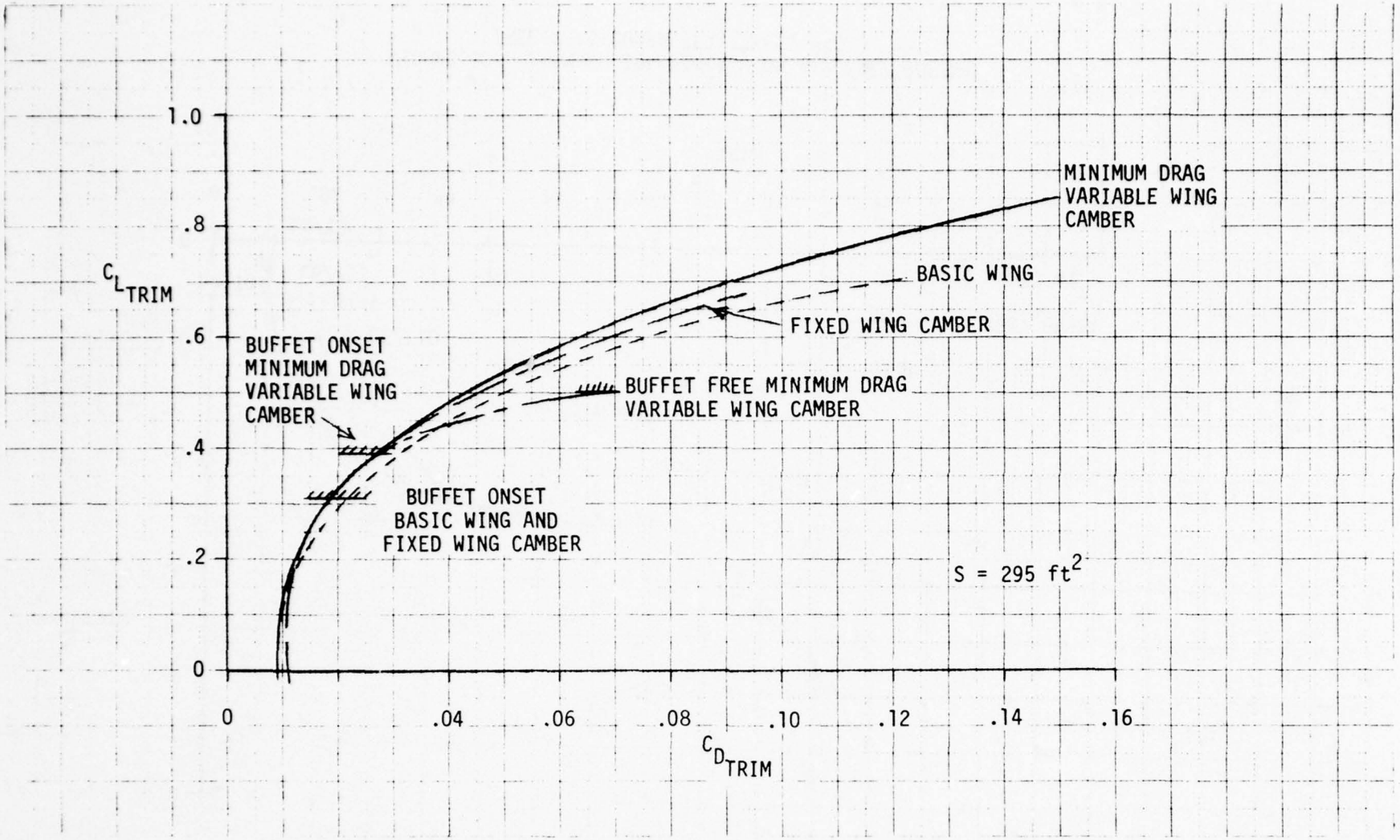

FIGURE 60 ANALYSIS AIRCRAFT TRIMMED AERODYNAMICS, M=0.9

inflight variation of wing camber at this Mach number provides a 25 percent increase in the wing buffet onset lift coefficient without degrading the configuration drag characteristics. However, to achieve the maximum increase in buffet free lift, the configuration trimmed drag characteristics must be allowed to increase. The choice of the particular camber schedule incorporated in an actual aircraft application would be expected to also include consideration of the buffet intensity variations once buffet is encountered. Data available for these studies, however, do not permit an assessment of this effect and consequently both camber schedules at this Mach number were included in the aircraft performance estimates.

Buffet Free Maneuvering Performance

The trimmed flight drag polars discussed in the above paragraphs were used to predict the improvements in aircraft buffet free maneuverability derivable from use of the skewed hingeline variable camber wing design concept. Performance data were predicted for each of the three analysis aircraft configurations at Mach numbers of 0.6 and 0.9 and altitudes of 20,000 and 30,000 feet. The specific performance parameters included in the studies were: maximun sustained buffet free load factor, minimum buffet free turn radius and the variation in the thrust required with aircraft sustained load factor.

Performance data for the basic wing and fixed wing camber aircraft configurations were developed using a common (baseline) gross weight of 15,000 pounds. Data for the variable camber wing configuration were defined for a range of aircraft gross weight to illustrate the effects of the necessary weight increase associated with incorporation of variable camber hardware. Preliminary design trade studies conducted prior to this program indicate the aircraft gross weight increase associated with incorporation of the variable camber wing design should be less than 5 percent of the baseline aircraft gross weight. Based upon these results, performance data for the variable camber wing configuration were computed for the baseline gross weight as well as for weight penalties of 500 and 1000 pounds.

The predicted maximum sustained buffet free load factors for the three analysis configurations at altitudes of 20,000 and 30,000 feet and Mach numbers of 0.6 and 0.9 are presented in Figures 61 and 62, respectively. Consistent with the results observed from the aircraft trimmed drag polars, both the fixed camber and variable camber wing configurations provide sustained buffet free load factors in excess of that for the basic wing at 0.6 Mach number, Figure 61. At 0.9 Mach number, however, aircraft buffet free load factors improvements are obtained only from the variable camber configuration. The sustained buffet free load factor for all three configurations are observed to be dependent upon Mach number with the higher values obtained at 0.9 Mach number. This characteristic is not unexpected since the predicted wing lift coefficients for buffet onset are reduced by less than 50 percent for changes in Mach number from 0.6 to 0.9 while dynamic pressure is increased by more than a factor of two. Past experience as well as the program investigations discussed in Section 2.2 indicate the configurations yielding improved buffet characteristics in the wind tunnel tests should also yield improved characteristics inflight. In this aircraft application, the improvements derived from the variable camber wing design correspond to an increase in buffet free sustained load factor of approximately 60 percent at both altitudes for a Mach number of 0.9. For the 0.6 Mach number conditions the potential improvements derivable from the variable camber capability result in approximately a 90 percent increase over the load factor predicted for the fixed wing camber configuration even with the associated increase in aircraft weight.

The benefits of the variable camber capability upon the aircraft buffet free minimum equilibrium turn radius for the two Mach numbers and altitude conditions are shown in Figures 63 and 64. Since maneuvering turn radius is a function of the sustained load factor, the configuration turn radius comparisons exhibit characteristics similar to sustained load factor comparisons. The variable camber wing configuration predicted buffet free equilibrium turn radius is predicted to be 40 percent less than the basic wing at 0.9 Mach number and approximately 60 percent less at 0.6 Mach number. Changes in altitude and the variable camber wing weight penalties have little influence upon

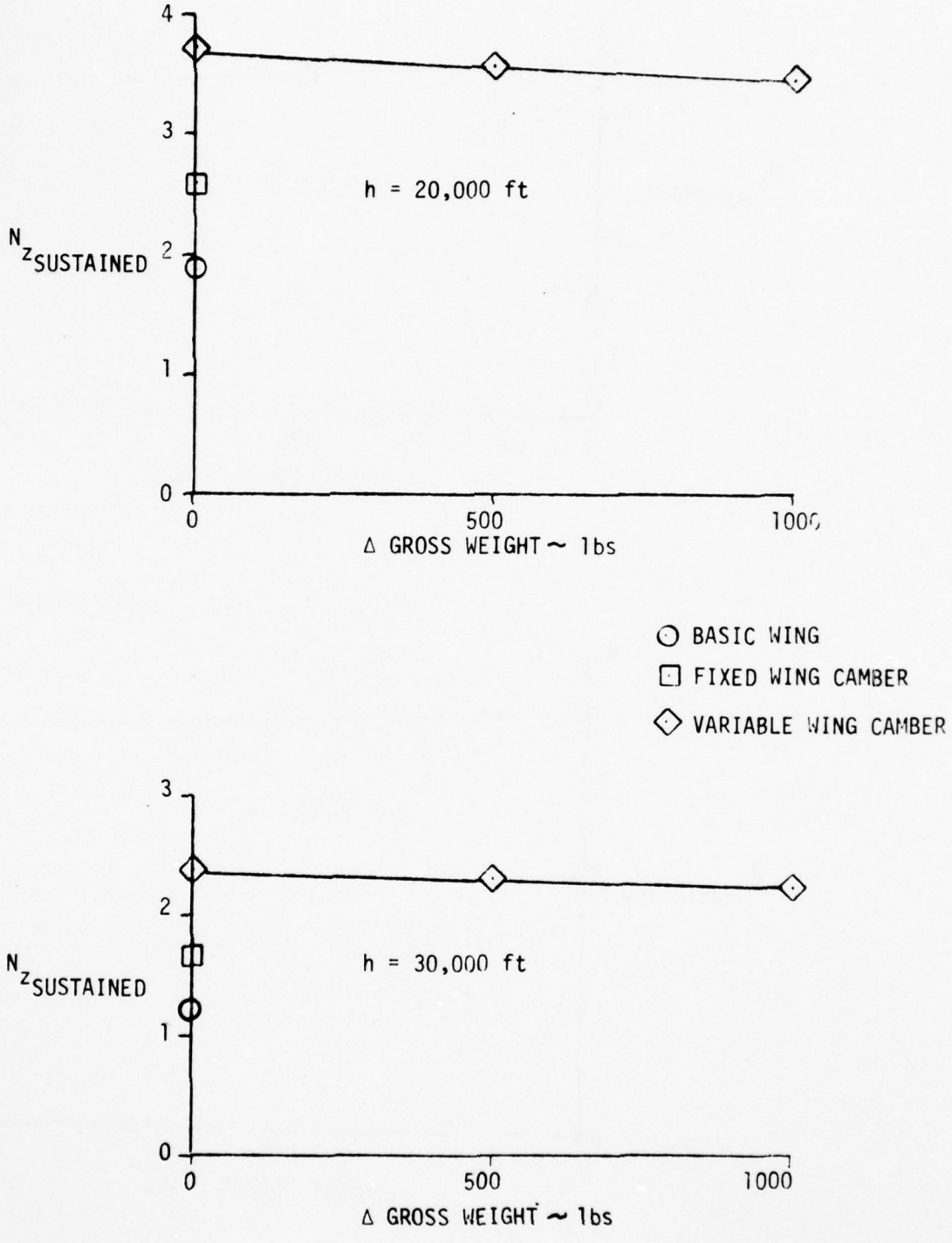

FIGURE 61 MAXIMUM SUSTAINED BUFFET FREE LOAD FACTOR, M=0.6

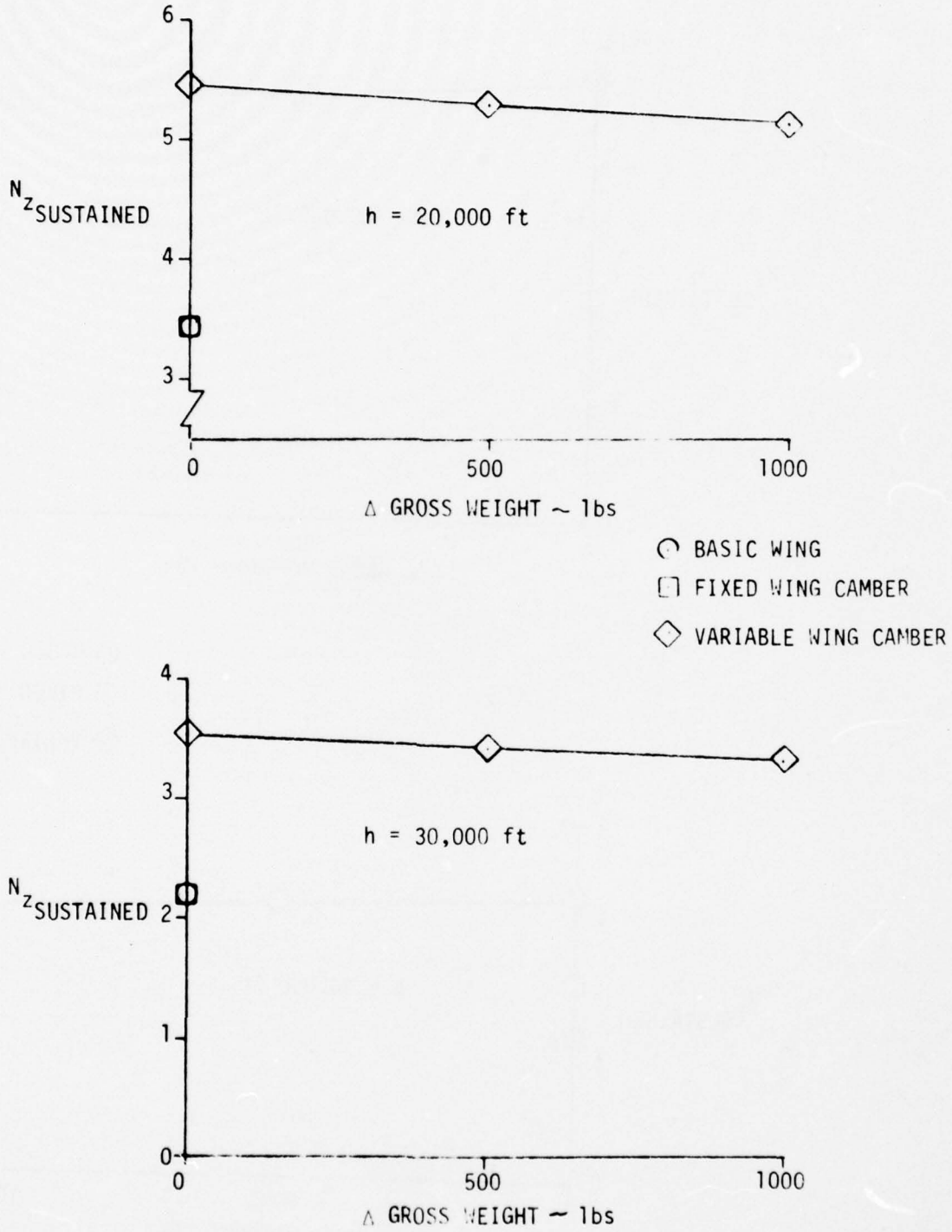

FIGURE 62 MAXIMUM SUSTAINED BUFFET FREE LOAD FACTOR, M=0.9

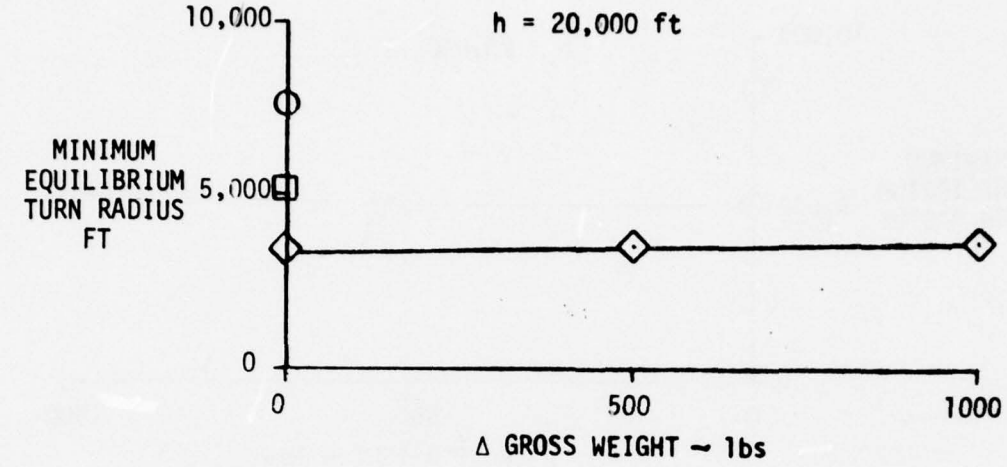

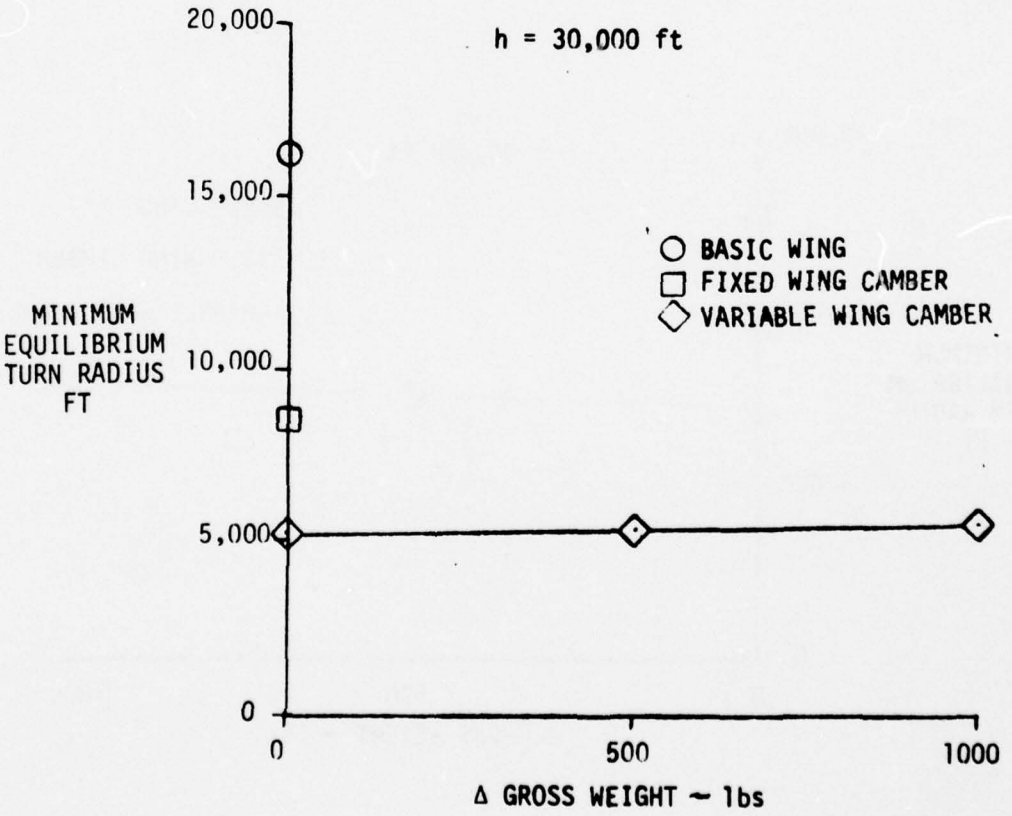

FIGURE 63 MINIMUM EQUILIBRIUM BUFFET FREE TURN RADIUS, M=0.6

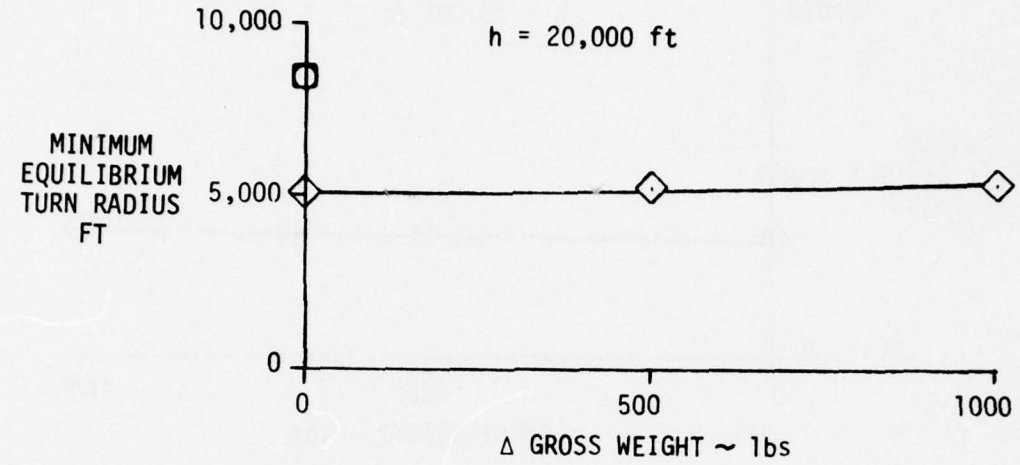

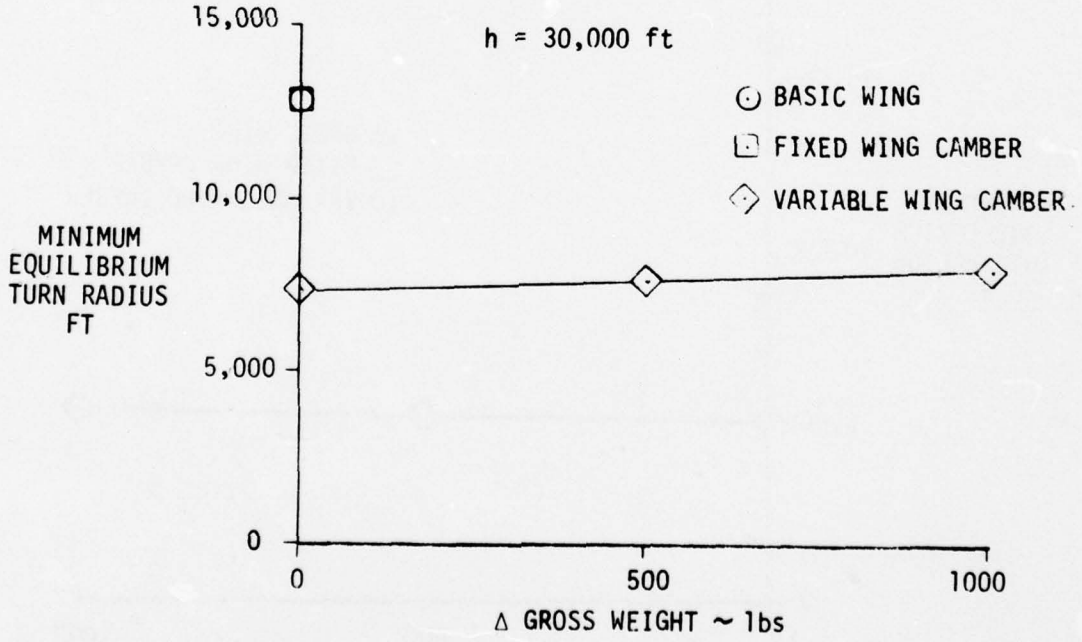

FIGURE 64 MINIMUM EQUILIBRIUM BUFFET FREE TURN RADIUS, M=0.9

these predicted improvements. At 0.6 Mach number, the predicted turn radius for the variable camber is also approximately 40 percent less than the corresponding prediction for the fixed wing camber configuration.

The sustained maneuverability improvements indicated in Figures 61 through 64 are primarily a reflection of the predicted increases in aircraft trimmed lift coefficient for onset of wing buffet. Variations in the aircraft drag characteristics have a negligibly small impact upon these results since the analysis aircraft thrust was assumed aligned with the fuselage centerline and the predicted aircraft angles of attack for buffet onset are small. Variations in the aircraft thrust requirements with sustained load factor were developed to illustrate the benefits of variable wing camber for maneuvering conditions prior to wing buffet. Predictions of the thrust required for variations of the aircraft sustained load factor are presented in Figures 65 and 66 for the two Mach number flight conditions. Predicted thrust requirements presented in these figures were computed for the baseline aircraft gross weight. While the thrust characteristics for a specific engine have not been included in the studies of this program, these estimated sustained maneuver thrust levels are within the capabilities of current technology engines.

As would be expected from the predicted 0.6 Mach number drag polars, Figure 57, less thrust is required for the variable camber wing configuration for all levels of sustained maneuvers. At 0.9 Mach number, however, the wing camber schedule for maximum buffet free lift imposes a thrust requirement exceeding that predicted for the basic and fixed wing camber configurations. Consequently, the maximum buffet free lift camber schedule at 0.9 Mach number requires the degradation of one performance parameter, thrust required, in order to obtain maximum improvement in another parameter. The camber schedule developed for the minimum drag design criteria offers a compromise to this tradeoff of variable camber wing performance characteristics. As noted on Figure 66, the variable camber configuration thrust requirements for the minimum drag camber schedule are less than those of the basic and fixed wing camber configurations for all load factors above approximately

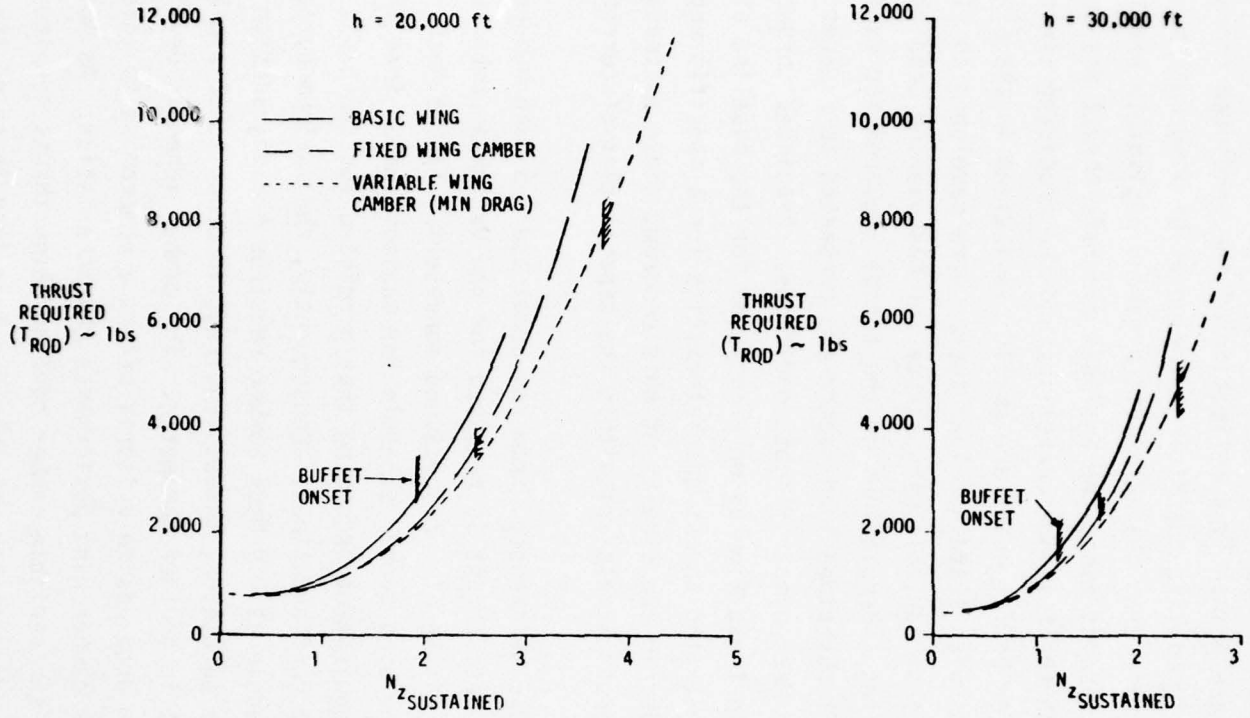

FIGURE 65 EFFECT OF CAMBER ON SUSTAINED MANEUVER THRUST REQUIREMENTS, M=0.6

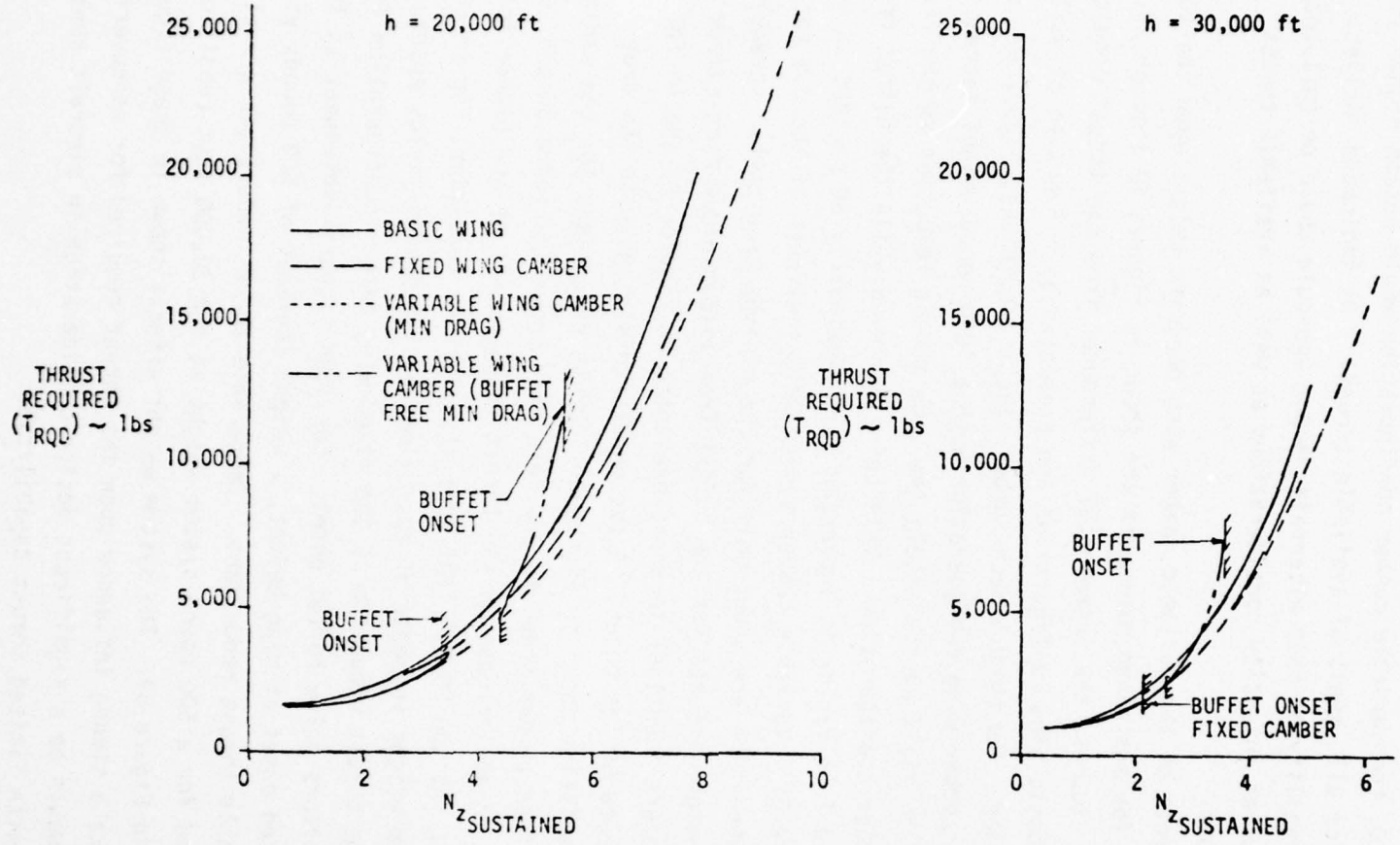

FIGURE 66 EFFECT OF CAMBER ON SUSTAINED MANEUVER THRUST REQUIREMENTS, M=0.9

2.8. Thus, by reducing the maximum buffet free load factor by approximately 1.0, the variable camber configuration would obtain higher load factors for all levels of available thrust. As indicated earlier, the desirability of this alternate camber schedule would be influenced by the buffet intensity considerations as well as available thrust limitations.

Effects of the variable camber wing hardware weight upon the thrust required for sustained maneuvers are shown in Figures 67 through 69. In these figures, the incremental differences from the thrust predictions for the basic wing configuration are presented as a function of sustained load factor. For the 0.6 Mach number flight conditions, Figure 67, the variable camber wing configuration with a 1000 pound weight increase is observed to yield approximately the same thrust reduction as the fixed wing camber configuration. This being achieved while the buffet free sustained load factor is increased by approximately 60 percent as shown in Figure 61. Variable camber system weight effects at the 0.9 Mach number condition are shown only for the minimum drag camber schedule. System weight effects for the buffet free lift-minimum drag camber schedule are identical to these presented in Figures 68 and 69 for loads below buffet onset. Above onset, consistent with the drag characteristics shown in Figure 60, thrust reductions for the maximum buffet free camber schedule are less than shown in Figure 60 and correspond to an increase in the thrust requirements at the higher load factors. At the 20,000 feet analysis altitude condition, Figure 68, a system weight increase of approximately 100 pounds yields approximately the same thrust reduction as the fixed wing camber configuration for load factors below buffet onset. For load factors subsequent to the predicted onset of wing buffet, a weight increase of 500 pounds yields comparable thrust reductions. Comparable thrust reductions are also observed for a 500 pound system weight at the 30,000 feet condition shown in Figure 69. The system weight effects shown in these figures indicate a strong influence upon the thrust required for maneuvering which would be a significant design consideration in aircraft applications with limited thrust capabilities.

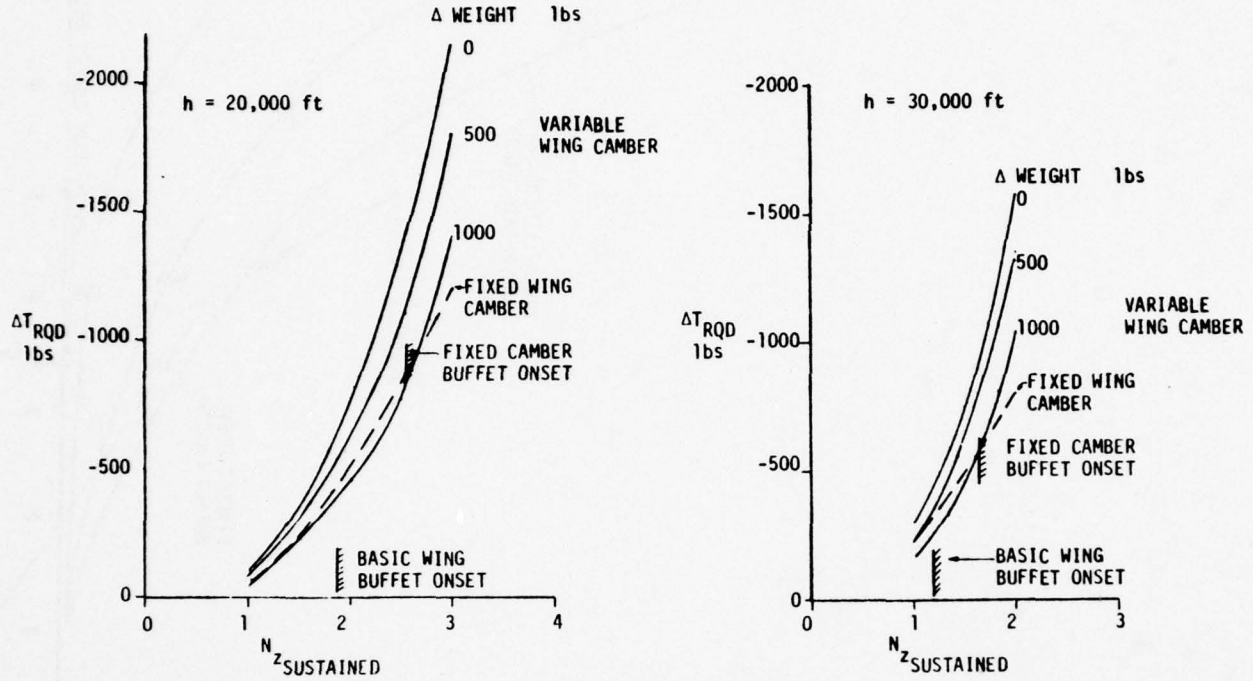

FIGURE 67 EFFECT OF VARIABLE CAMBER SYSTEM WEIGHT ON THRUST REQUIRED, M=0.6

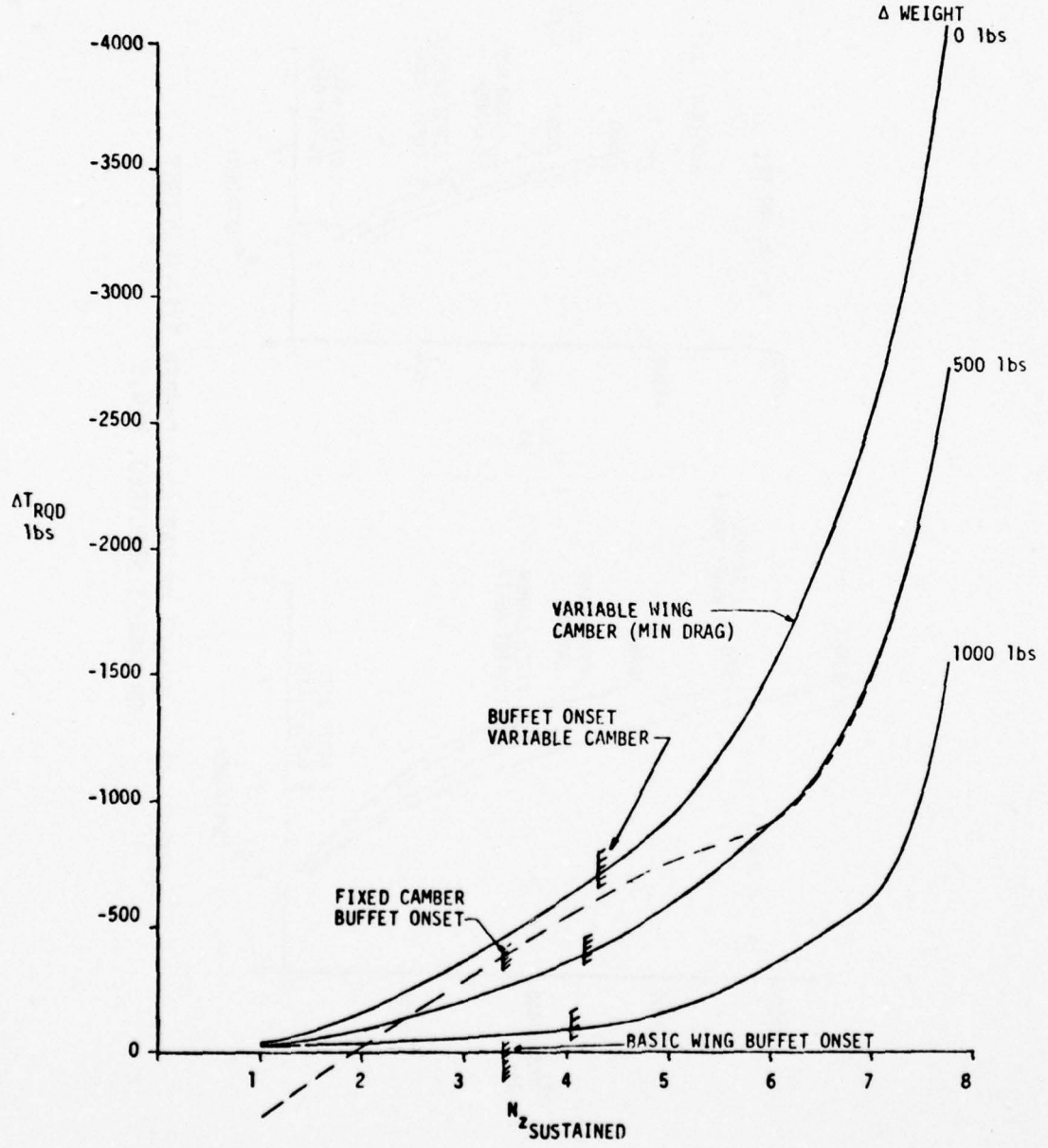

FIGURE 68 EFFECT OF VARIABLE CAMBER SYSTEM WEIGHT ON THRUST REQUIRED, M=0.9, h=20,000 ft

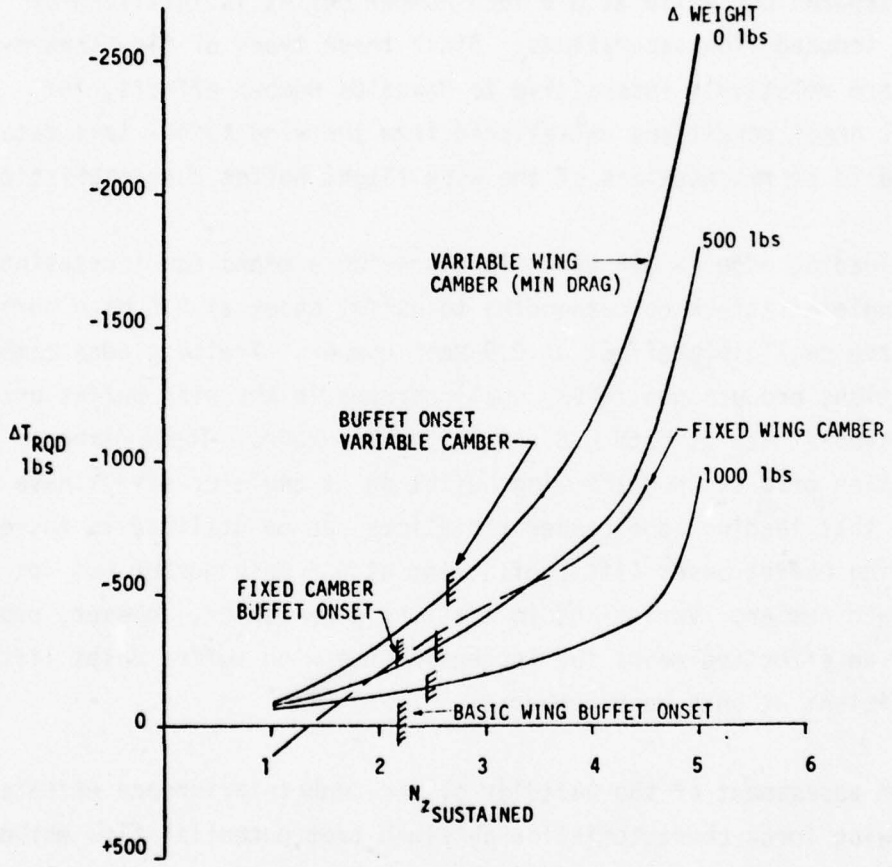

FIGURE 69 EFFECT OF VARIABLE CAMBER SYSTEM WEIGHT ON THRUST REQUIRED, M=0.9, h=30,000 ft

4.0 CONCLUSIONS AND RECOMMENDATIONS

Conclusions drawn from the studies conducted in this program are summarized as follows:

(1) The type of flow separations precipitating buffet onset for this variable camber wing design are different at 0.6 and 0.9 Mach numbers. At 0.6 Mach number, buffet results from leading edge type flow separations while at 0.9 Mach number buffet is initiated by shock induced flow separations. Since these types of flow separation are relatively insensitive to Reynolds number effects, the buffet onset conditions established from the wind tunnel test data are valid representations of the wing flight buffet characteristics.

(2) Wing leading edge camber variations provide a means for increasing the angle-of-attack corresponding to buffet onset at 0.6 Mach number but have negligible effect at 0.9 Mach number. Trailing edge camber variations produce negligibly small changes in the wing buffet onset angles-of-attack at both 0.6 and 0.9 mach number. These camber variation effects upon the wing buffet onset angle-of-attack have shown that leading edge camber variations can be utilized to increase the wing buffet onset lift coefficient at 0.6 Mach number but not at 0.9 Mach number. Variations in trailing edge camber, however, provides an effective means for increasing the wing buffet onset lift coefficient at both Mach numbers.

(3) A firm assessment of the validity of the body interference effects upon wing force characteristics obtained from potential flow methods was not possible in these studies due to suspected experimental data errors discussed in Section 2.3. The predicted body induced wing forces reflect the same general trend with angle-of-attack as observed from the experimental results. Predicted variations in the body interference effects due to changes in wing camber were found to differ significantly from the magnitudes indicated from the available test data. Body induced changes to the wing flow field were determined to have a negligible impact upon the conditions for onset of wing

(4) From the trimmed flight drag polars for the aircraft configurations considered in these studies, Figures 57 and 60, it is apparent that inflight variations of wing camber improves aircraft performance at transonic flight conditions. Even with a conservative 1000 pound estimate of the aircraft weight increase due to incorporation of the variable camber capability, buffet free sustained load factors 50 to 60 percent greater than those obtained for aircraft configurations with an uncambered and a fixed cambered wing were obtained. Consequently, aircraft with mission requirements for substantial buffet free lift coefficients at transonic speeds will derive the most benefit from the Vought variable camber wing design concept.

(5) The principal advantage of this variable camber wing at 0.9 Mach number is the improvement in the wing buffet onset lift coefficient. As shown in Figure 60, achievement of the greatest buffet free lift improvement requires that trimmed flight drag levels must be increased above the minimum obtainable levels. Consequently, definition of the optimum camber scheduling in a particular aircraft application requires consideration of the available thrust levels. Thrust requirements defined for the representative aircraft applications of this program are within the thrust to weight range of current technology engines and, thus, the buffet free performance benefits offered by this variable camber wing design should be obtainable.

Results from the investigations of this program indicate this variable camber wing design provides a means for improving aircraft transonic buffet free maneuverability without adverse aerodynamic effects at other flight conditions. Based upon these encouraging results, the following areas of investigation are recommended to further investigate this wing concept:

(1) The buffet onset analyses of this program, following the methods of Mabey, Reference 2, tacitly assume that the contours of lift coefficient versus Mach number for a given buffet intensity level are approximately parallel to the contours for onset of buffet.

Verification of this variation in buffet intensity subsequent to onset does not appear feasible with the presently available test data. Since in a combat environment, an aircraft can be expected to be flown at least to the maximum buffet intensity which permits satisfactory target tracking, verification of this buffet intensity variation is an area when further tests results are needed.

(2) Results obtained in this study indicate that the angle-of-attack conditions for buffet onset are not altered by wing camber variations at 0.9 Mach number. Additional analytical and experimental studies are recommended to investigate feasibility of increasing the wing buffet onset lift coefficient through use of lessor magnitudes of leading edge camber and/or full span trailing edge camber variations.

REFERENCES

1. Ferris, J. C., "Wind Tunnel Investigation of a Variable Camber and Twist Wing," NASA-Langley Research Center Report No. L-11357. (To be published as a NASA Technical Note 8475).

2. Mabey, D. G., "Beyond the Buffet Boundary," Aeronautical Journal, April 1973.

3. Pearcy, H. H., Osborne, J. and Haines, A. B., "The Interaction Between Local Effects at the Shock and Rear Separation - a Source of Significant Scale Effects In Wing Tunnel Tests on Airfoils and Wings," Paper No. 12, Fluid Dynamics Panel of AGARD Specialists' Meeting, Paris, France, September 1968.

4. Ray, E. J. and Taylor, R. T., "Buffet and Static Aerodynamic Characteristics of a Systematic Series of Wings Determined from a Subsonic Wind Tunnel Study," NASA TN D-5805, June 1970.

5. Hollingsworth, E. G. and Cohen, M., "Determination of F-4 Aircraft Transonic Buffet Characteristics," Journal of Aircraft, Vol. 8, No. 10, October 1971.

6. Hess, J. L.,"Calculation of Potential Flow About Arbitrary Three-Dimensional Lifting Bodies - Final Technical Report," McDonnell Douglas Report Number MDC 55679-01, October 1972. Done under Contract No. N00019-71-C-0524 for the Naval Air Systems Command.

7. Hess, J. L., and Smith, A. M. O,"Calculation of Potential Flow About Arbitrary Bodies", Progress in Aeronautical Sciences, edited by D. Kuchemann, Vol. 8, Pergamon Press, New York, 1966.

8. Ballhaus, W. F., and Bailey, F. R.,"Relaxation Methods for Transonic Flow About Wing-Cylinder Combinations and Lifting Swept Wings," Lecture Notes in Physics, Vol. 19, Spinger-Verlag, 1972.

9. Lores, M. E.,"A Numerical Method for Isolated Wing Transonic Flow Calculations - Final Report," Vought Technical Report No. 2-57110/4r-3190. Submitted to NASA Ames Research Center, November 15, 1974.

10. McNalley, W. D.,"Fortran Program for Calculating Compressible Laminar and Turbulent Boundary Layers in Arbitrary Pressure Gradients," NASA TN D-5681, May 1970.

11. Cebeci, T., Mosinskis, G. J., and Smith, A. M. O.,"Calculation of Viscous Drag of Two-Dimensional and Axisymmetric Bodies in Incompressible Flows," Journal of Aircraft, Vol. 9, 1972.

12. Pitts, W. C., Nielsen, J. N., and Kaattari, G. E., "Lift and Center of Pressure of Wing-Body-Tail Combinations at Subsonic, Transonic, and Supersonic Speeds," NACA TR 1307.

13. Goethert, H., Transonic Wind Tunnel Testing, Pergamon Press, 1961.

14. "A Description of the NASA - Langley Eight-Foot Transonic Pressure Tunnel," November 1973.

15. Barnwell, W., "Approximate Method for Calculating Transonic Flow About Li ting Wing-Body Configurations," NASA TR R-452, April 1976.

16. Zieglar, C. E., "Vought Wind Tunnel Test to Determine the Static Stability Characteristics on the ANA/V-526 Model in the Mach Range of 0.6 to 1.2," Vought Corporation Report No. 2-53710/5R-51152, HSWT Test 500, May 1975.

17. Hoerner, S. F., Fluid-Dynamic Drag, Published by Author, 1958.

18. Zeiglar, C. E., "Vought Wing Tunnel Test to Determine the Load Characteristics of Various Variable Camber Wings on the 0.04 Scale ANF/V523 Model in the Mach Range of 0.6 to 1.2," Vought Corporation Report No. 2-59710/4R-51008, July 1, 1974.

19. Boyd, J. W. , Migotsky, E., and Wetzel, B. E., "A Study of Conical Camber for Triangular and Sweptback Wings," NACA RMASSG19, Nov. 18, 1955.

20. "USAF Stability and Control DATCOM," McDonnell Douglas Corporation, revised 1968.

APPENDIX A

PLOTTED WIND TUNNEL FORCE DATA

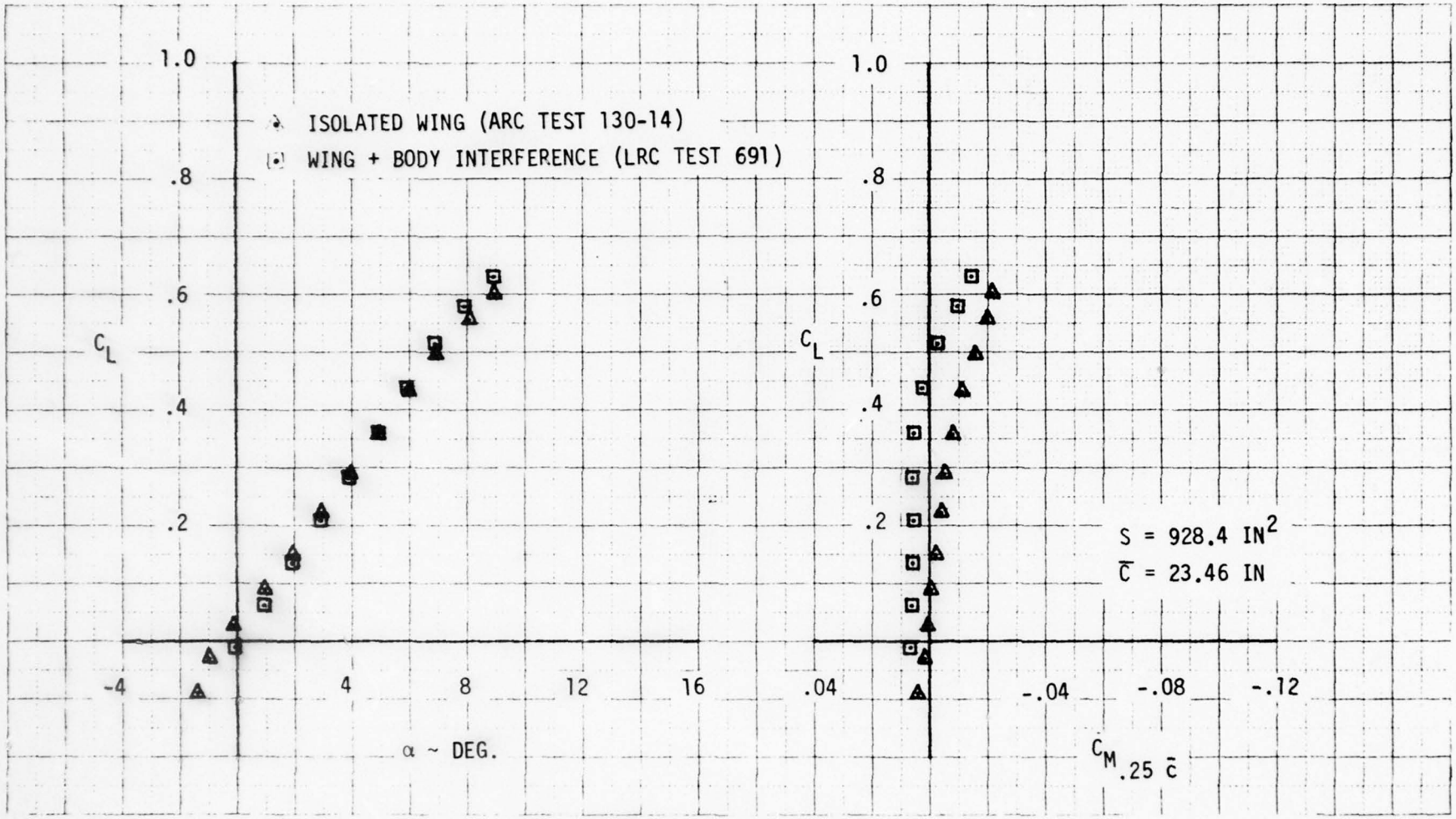

FIGURE A1 BODY INTERFERENCE EFFECT ON WING FORCE CHARACTERISTICS CONFIG. LO/TO, M = 0.6

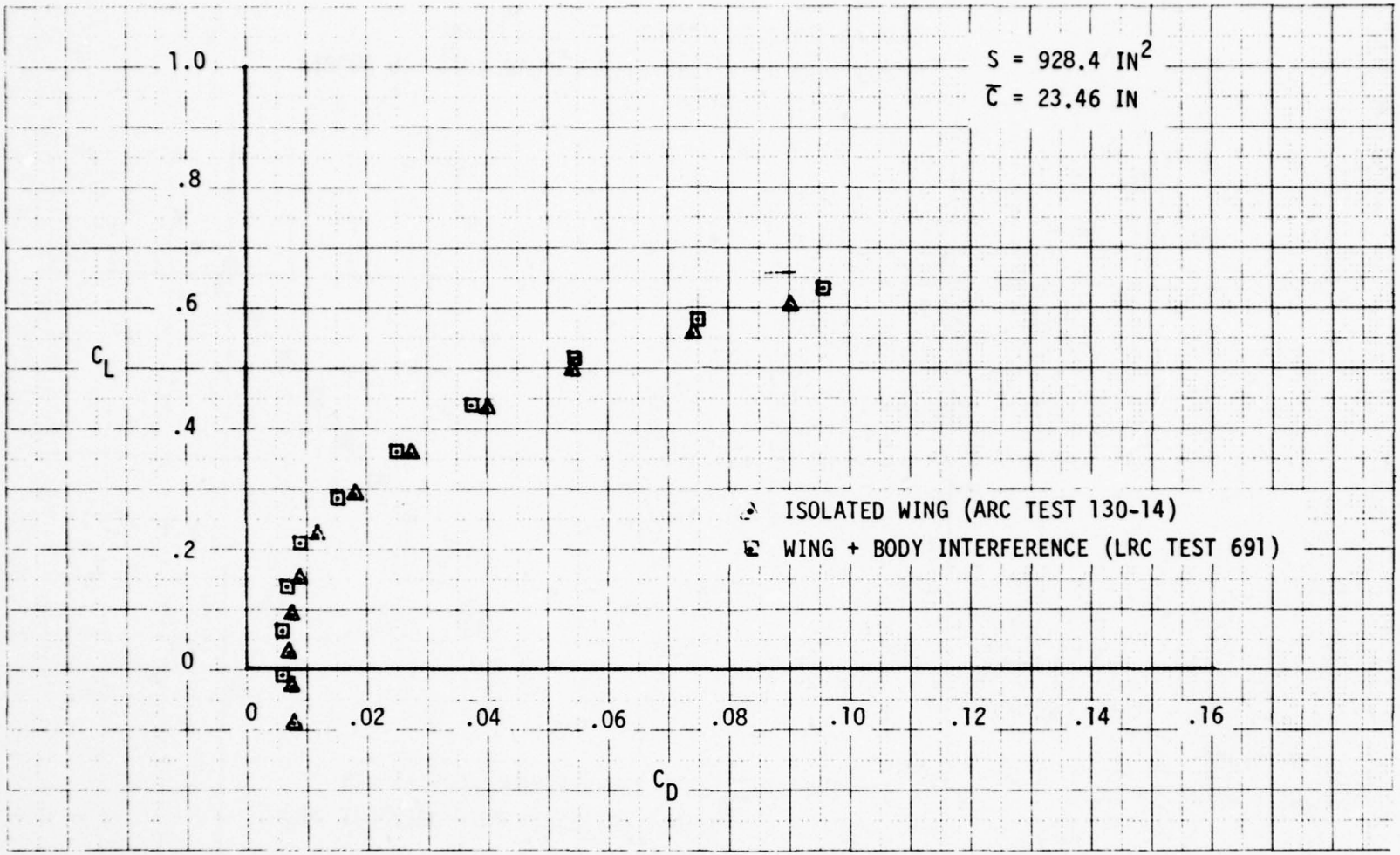

FIGURE A2 BODY INTERFERENCE EFFECT ON WING FORCE CHARACTERISTICS CONFIG. LO/TO, M = 0.6

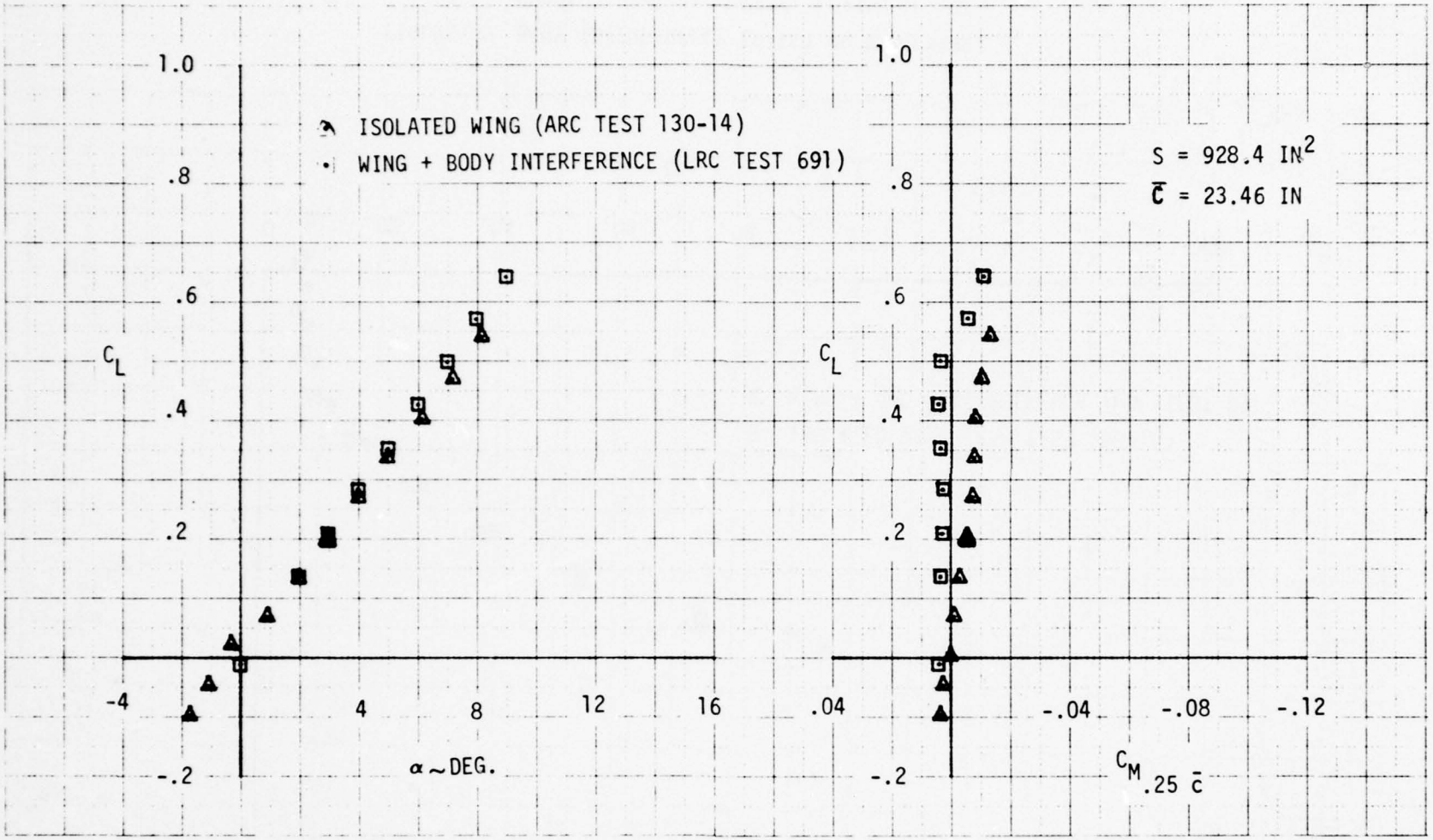

FIGURE A3 BODY INTERFERENCE EFFECT ON WING FORCE CHARACTERISTICS CONFIG. L5/TO, M = 0.6

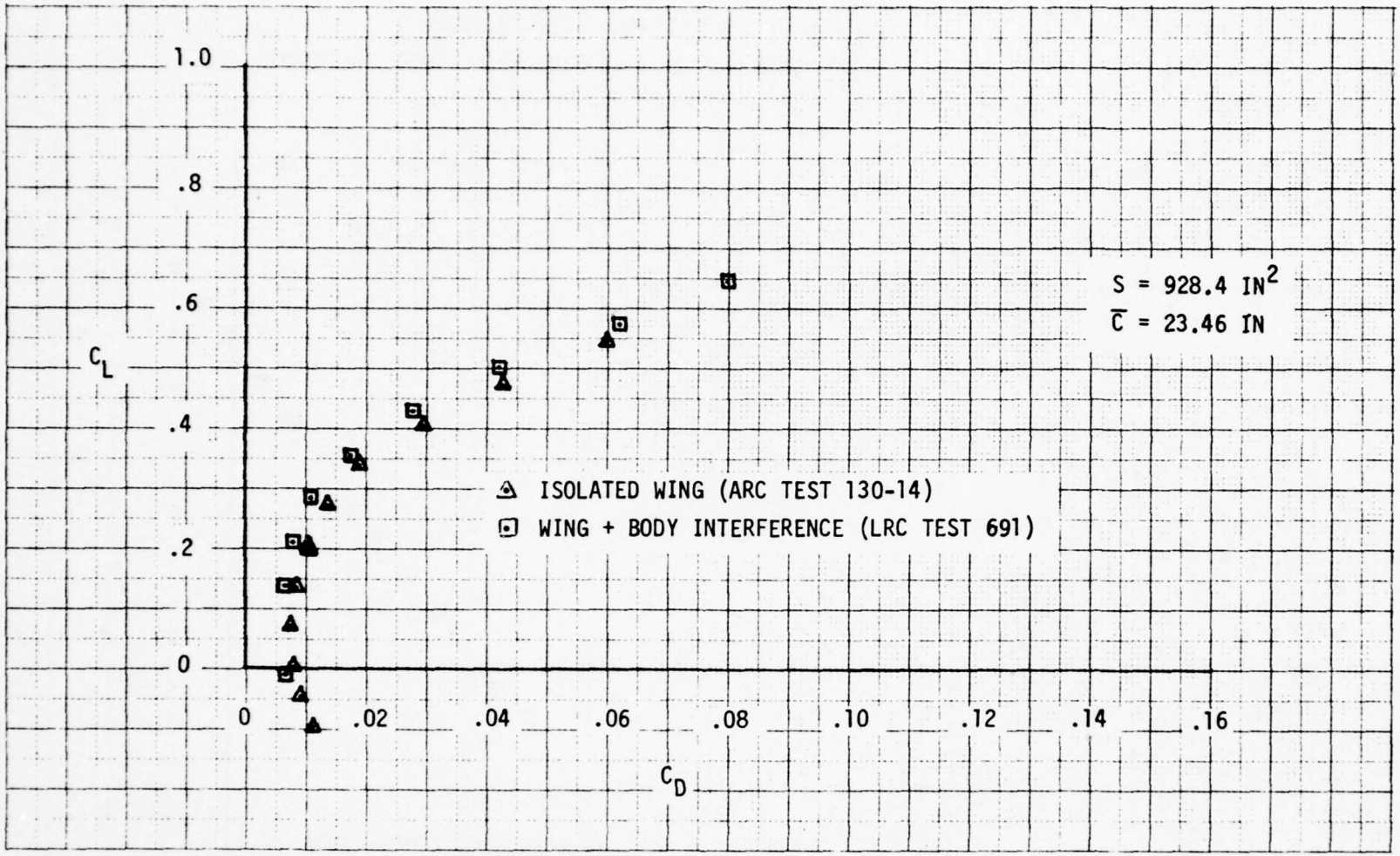

FIGURE A4 BODY INTERFERENCE EFFECT ON WING FORCE CHARACTERISTICS CONFIG. L5/TO, M = 0.6

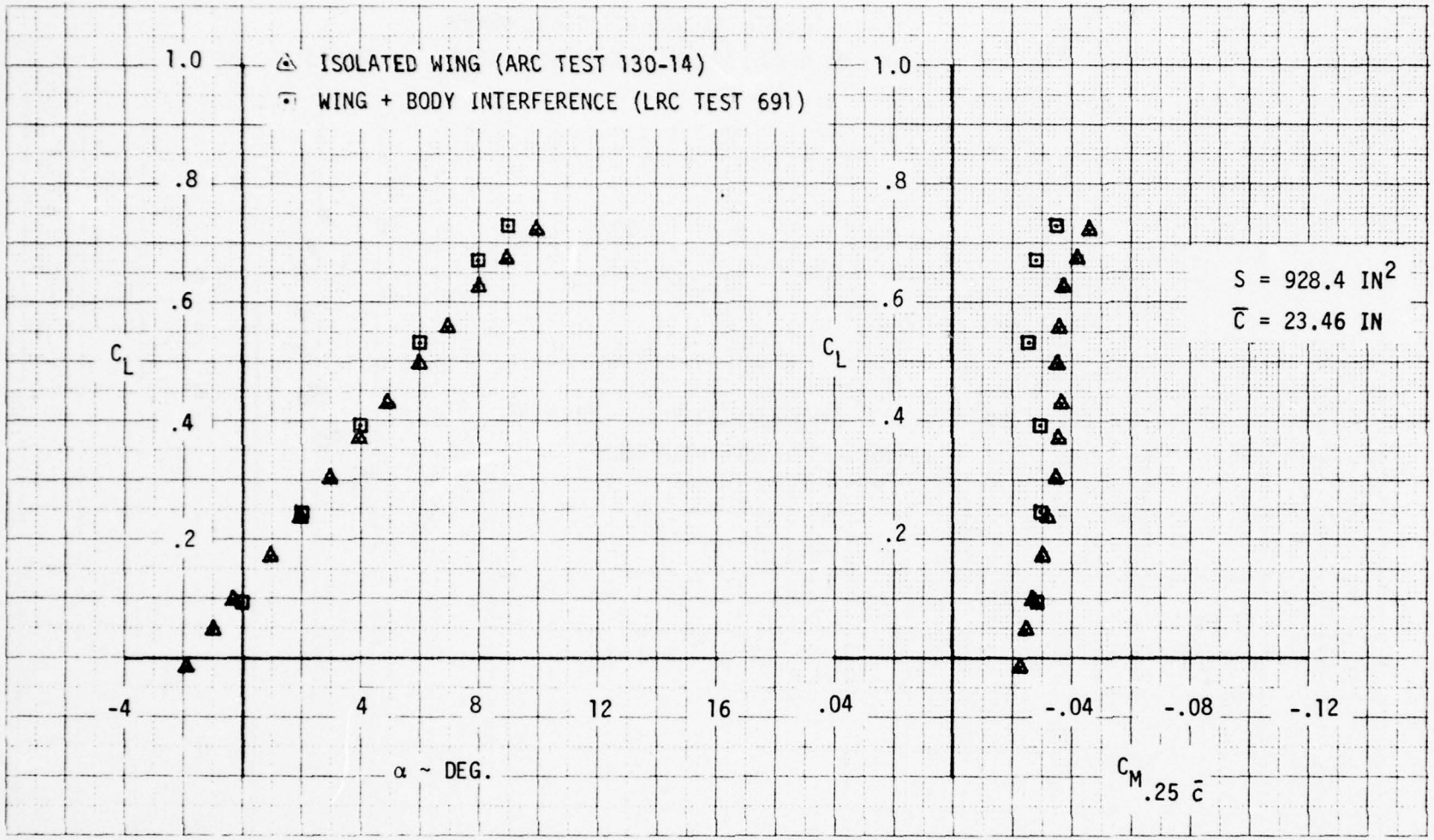

FIGURE A5 BODY INTERFERENCE EFFECT ON WING FORCE CHARACTERISTICS CONFIG. L6/T11, M = 0.6

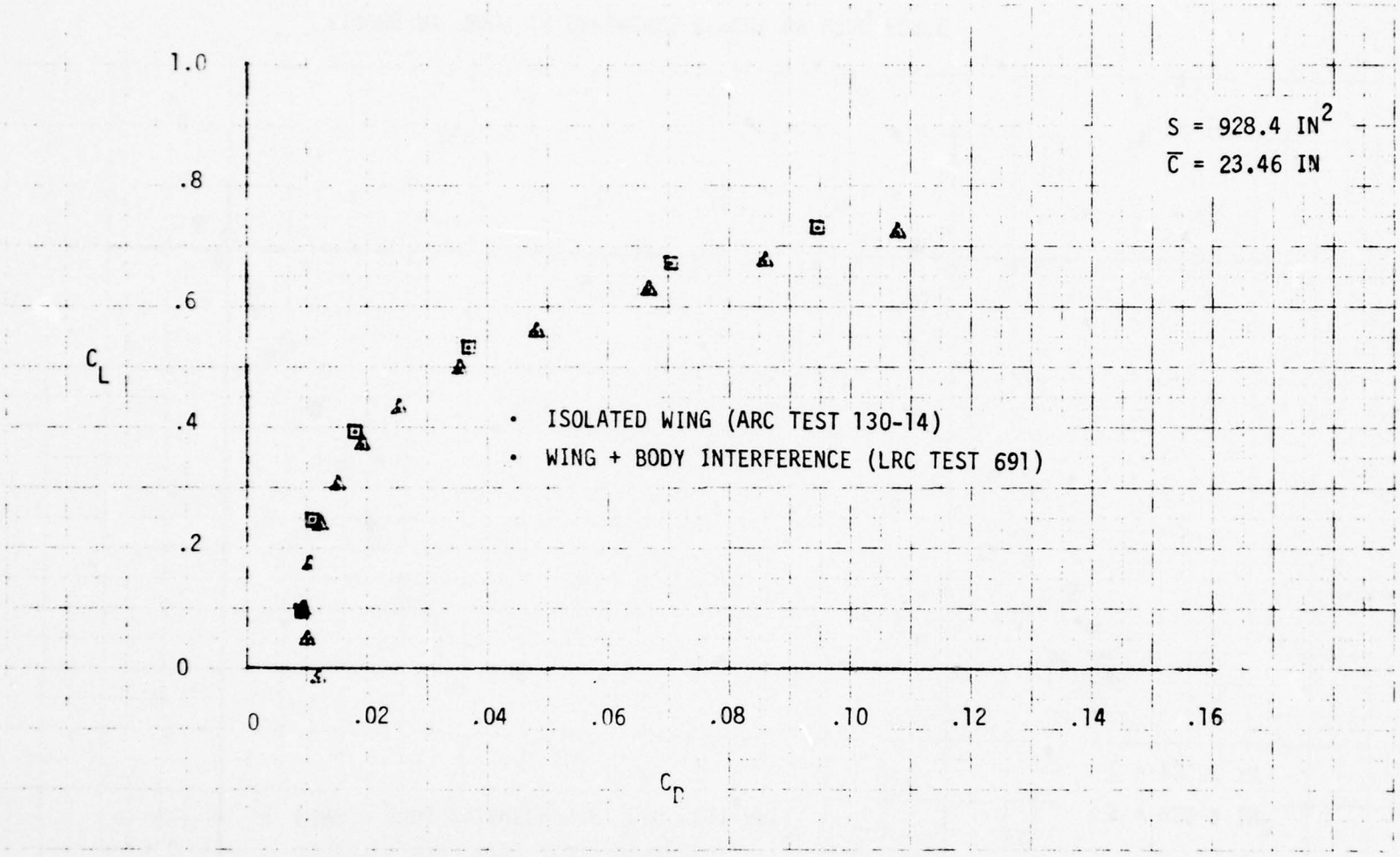

FIGURE A6 BODY INTERFERENCE EFFECT ON WING FORCE CHARACTERISTICS CONFIG. L6/T11, M = 0.6

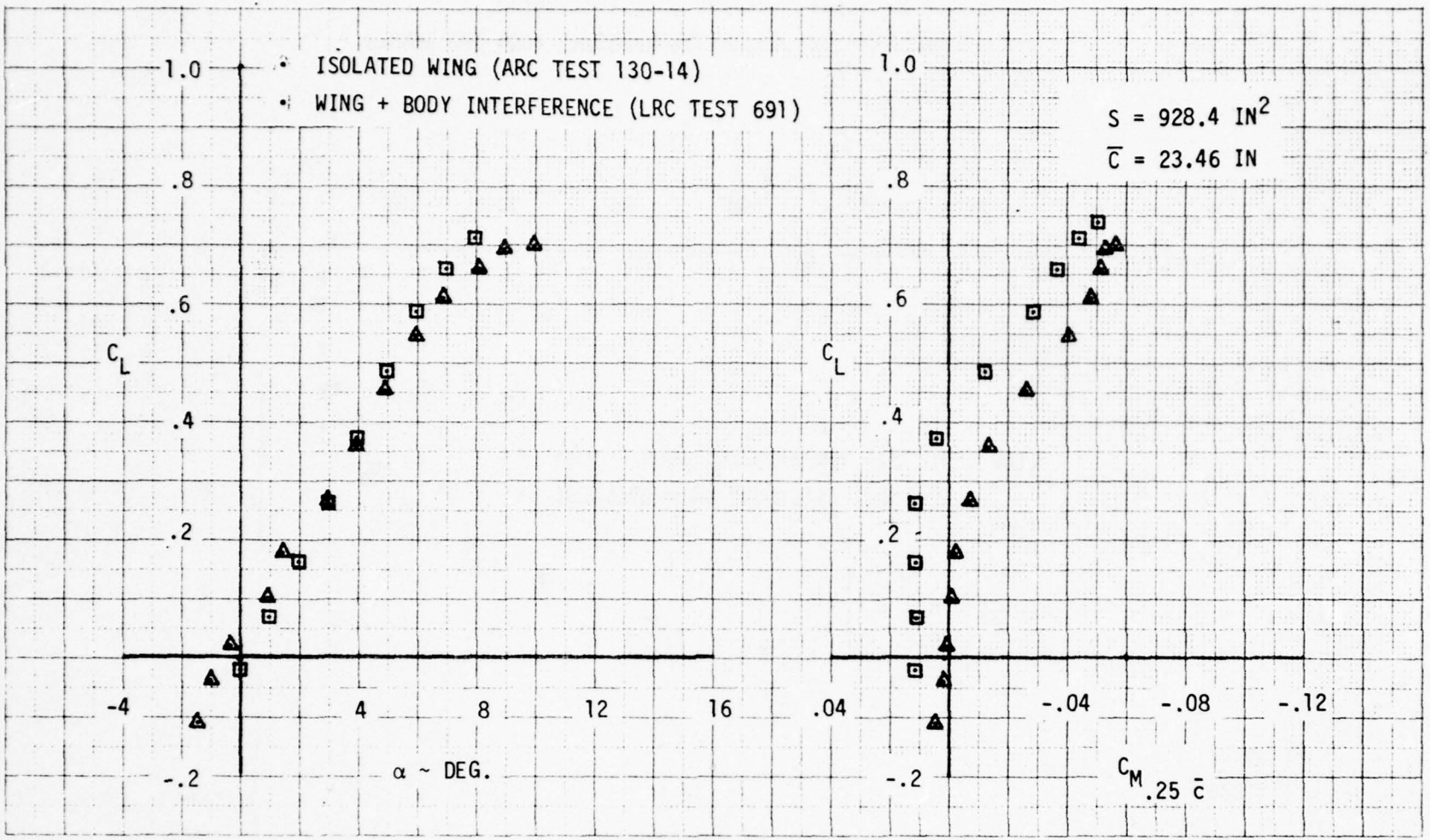

FIGURE A7 BODY INTERFERENCE EFFECT ON WING FORCE CHARACTERISTICS CONFIG. LO/TO, M = 0.9

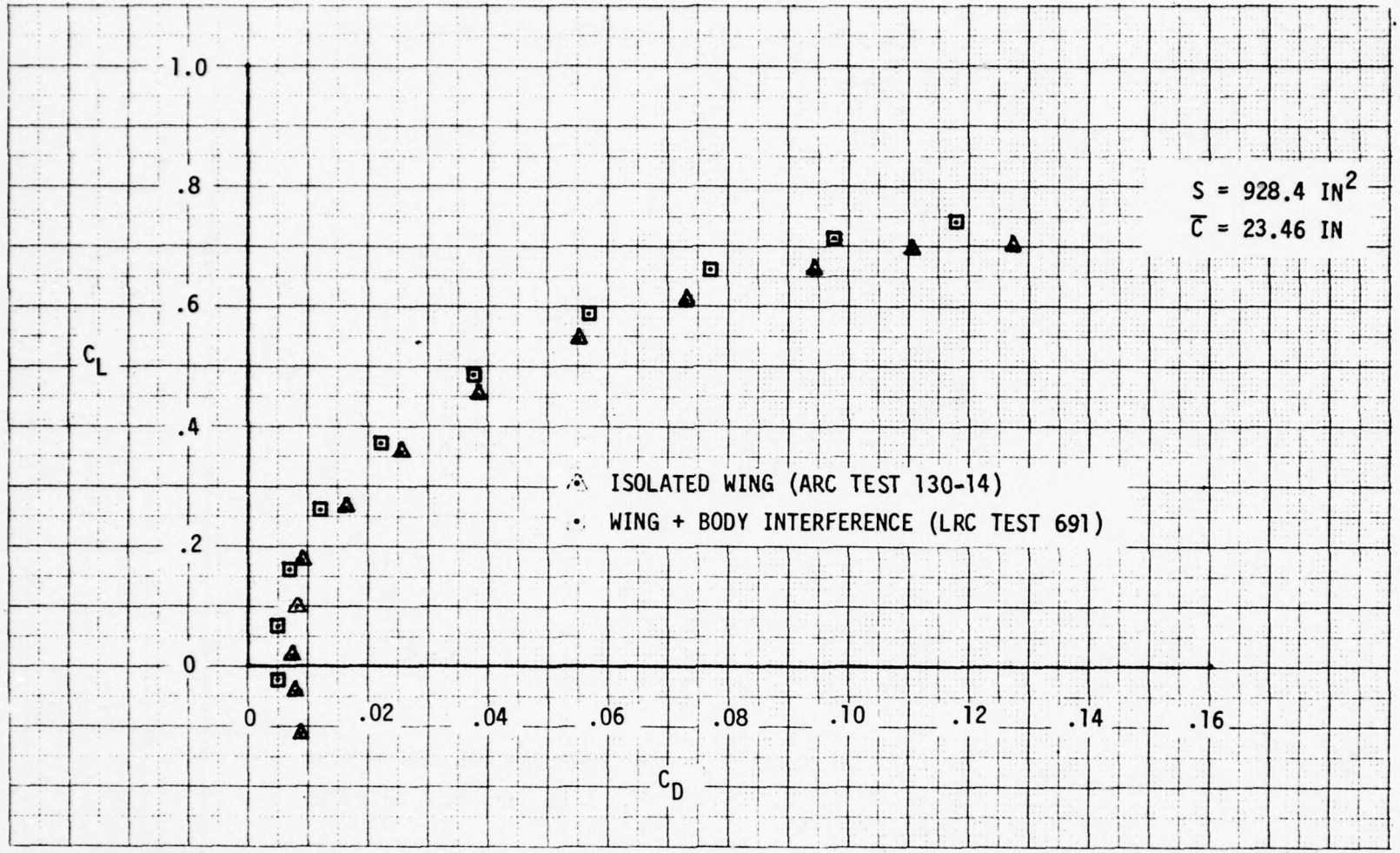

FIGURE A8 BODY INTERFERENCE EFFECT ON WING FORCE CHARACTERISTICS CONFIG. LO/TO, M = 0.9

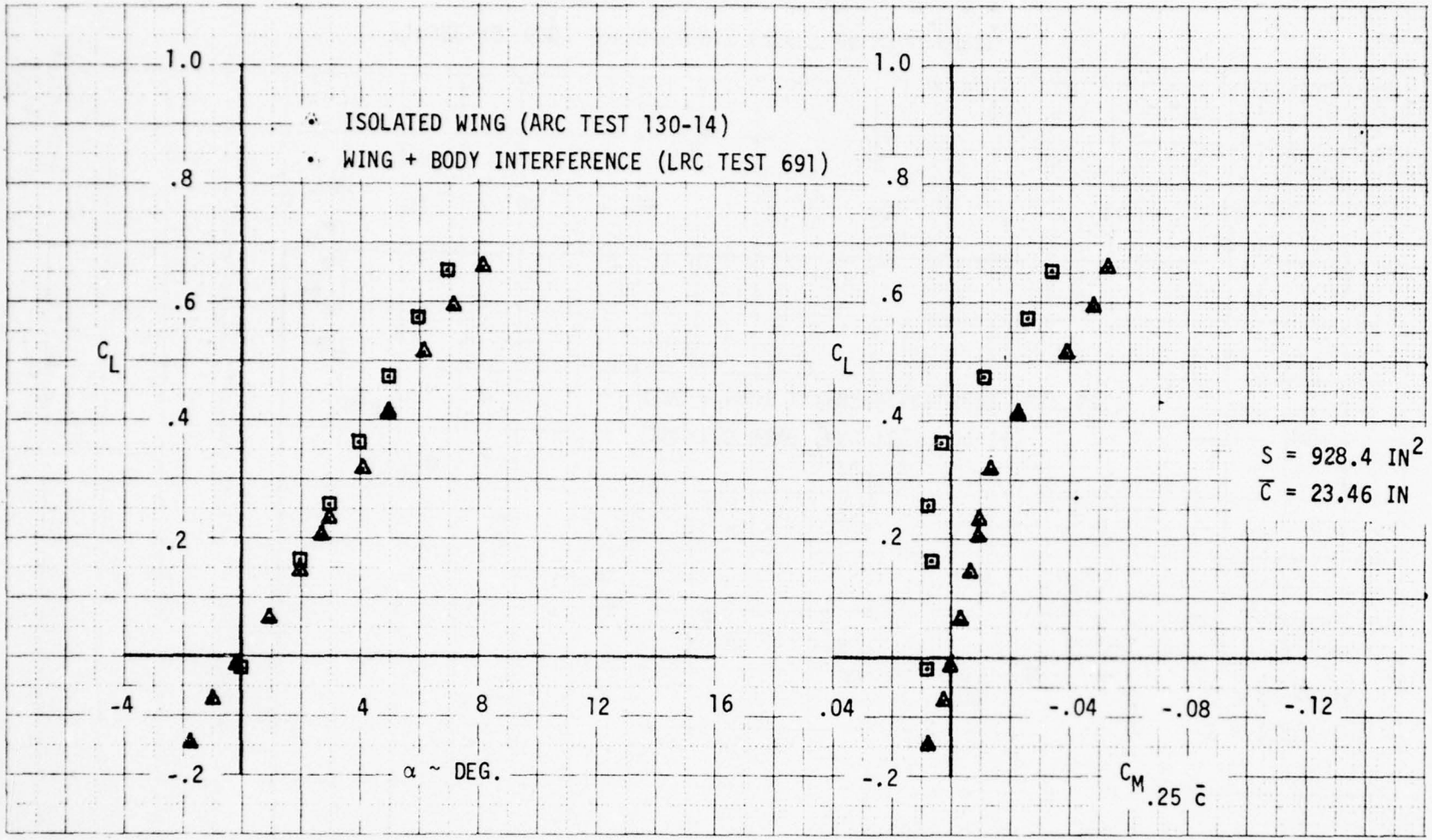

FIGURE A9 BODY INTERFERENCE EFFECT ON WING FORCE CHARACTERISTICS CONFIG. L5/TO, M = 0.9

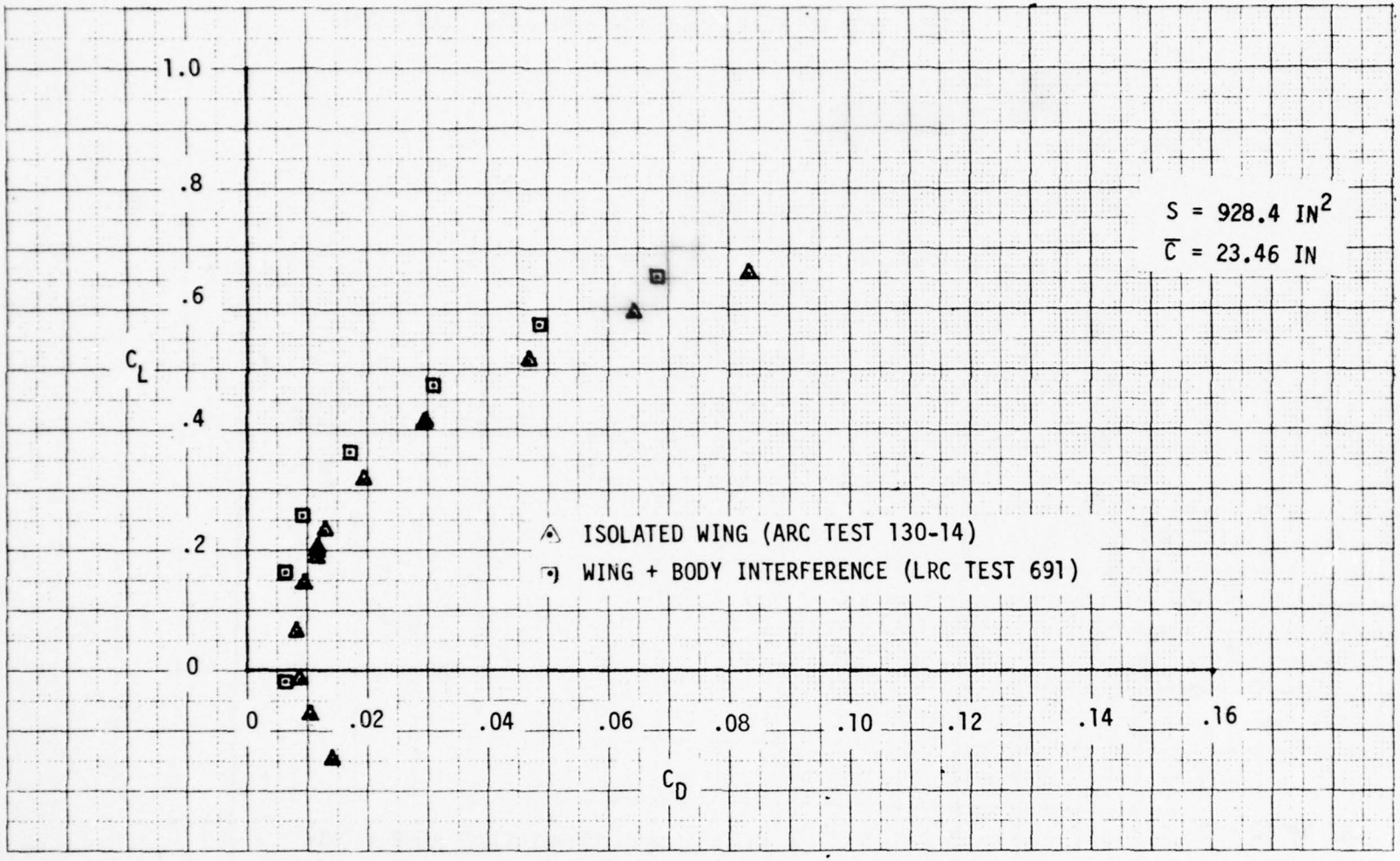

FIGURE A10 BODY INTERFERENCE EFFECT ON WING FORCE CHARACTERISTICS CONFIG. L5/TO, M = 0.9

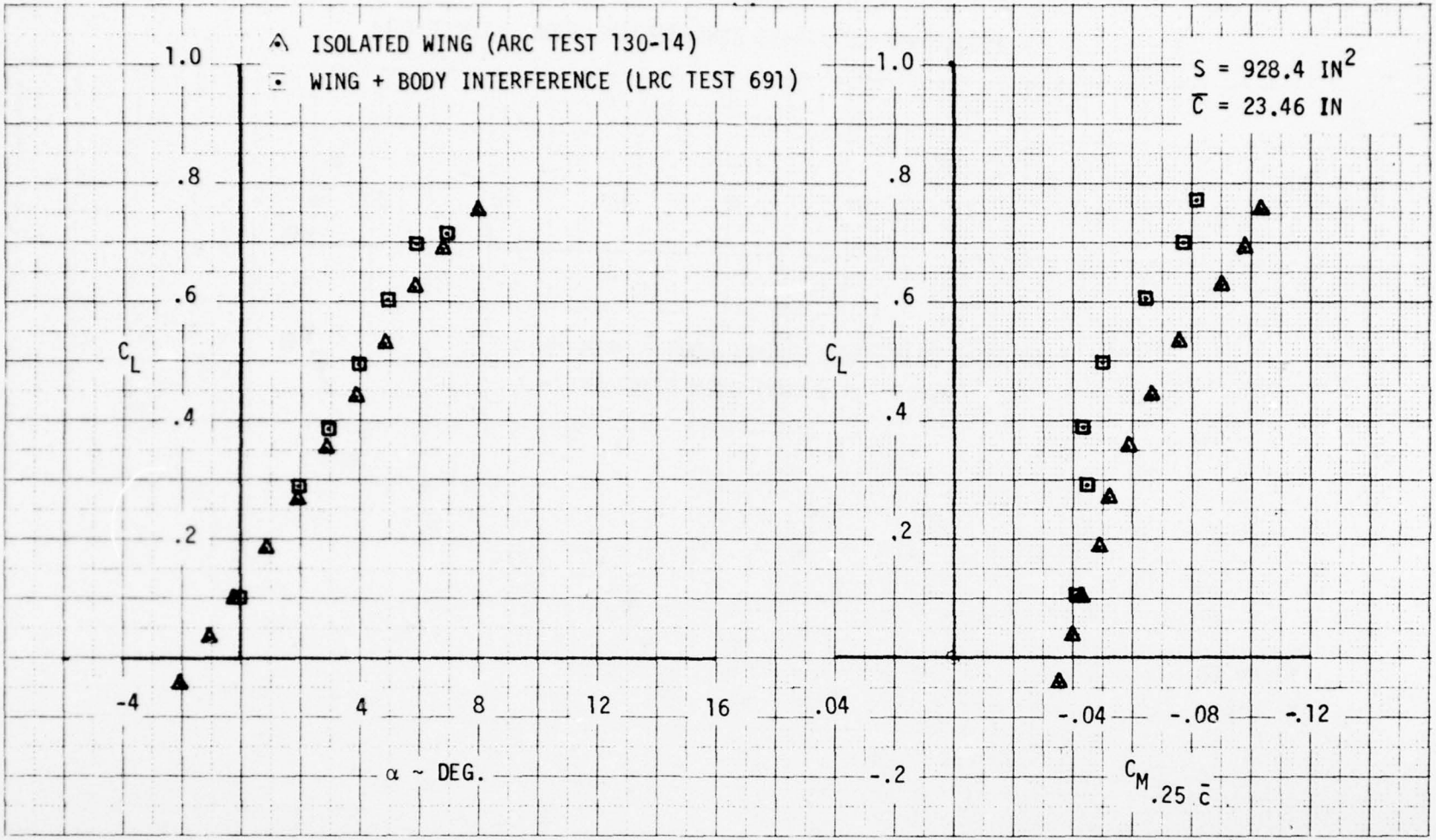

FIGURE A11 BODY INTERFERENCE EFFECT ON WING FORCE CHARACTERISTICS CONFIG. L6/T11, M = 0.9

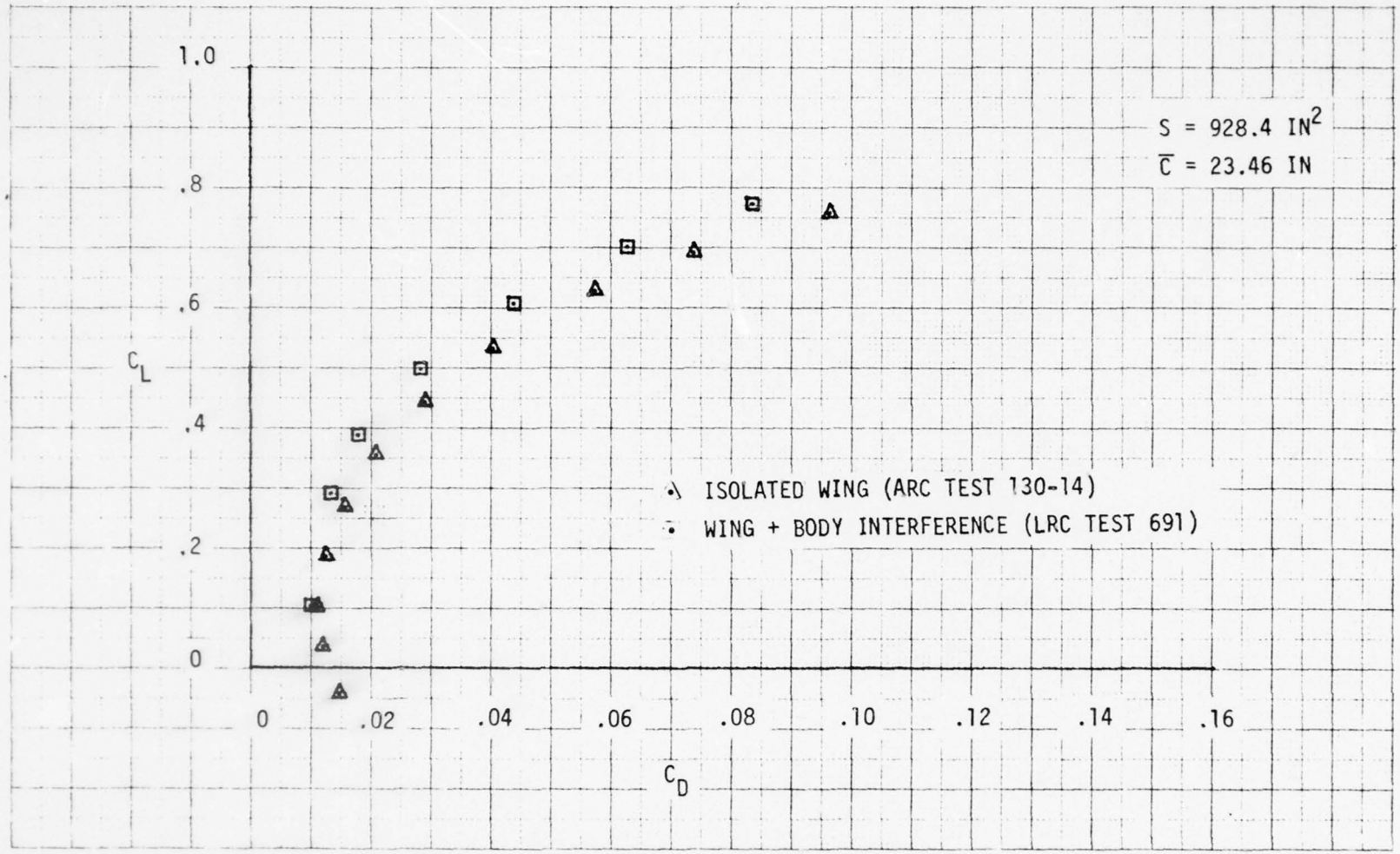

FIGURE A12 BODY INTERFERENCE EFFECT ON WING FORCE CHARACTERISTICS CONFIG. L6/T11, M = 0.9

APPENDIX B

PREDICTED AIRCRAFT LIFT AND DRAG CHARACTERISTICS

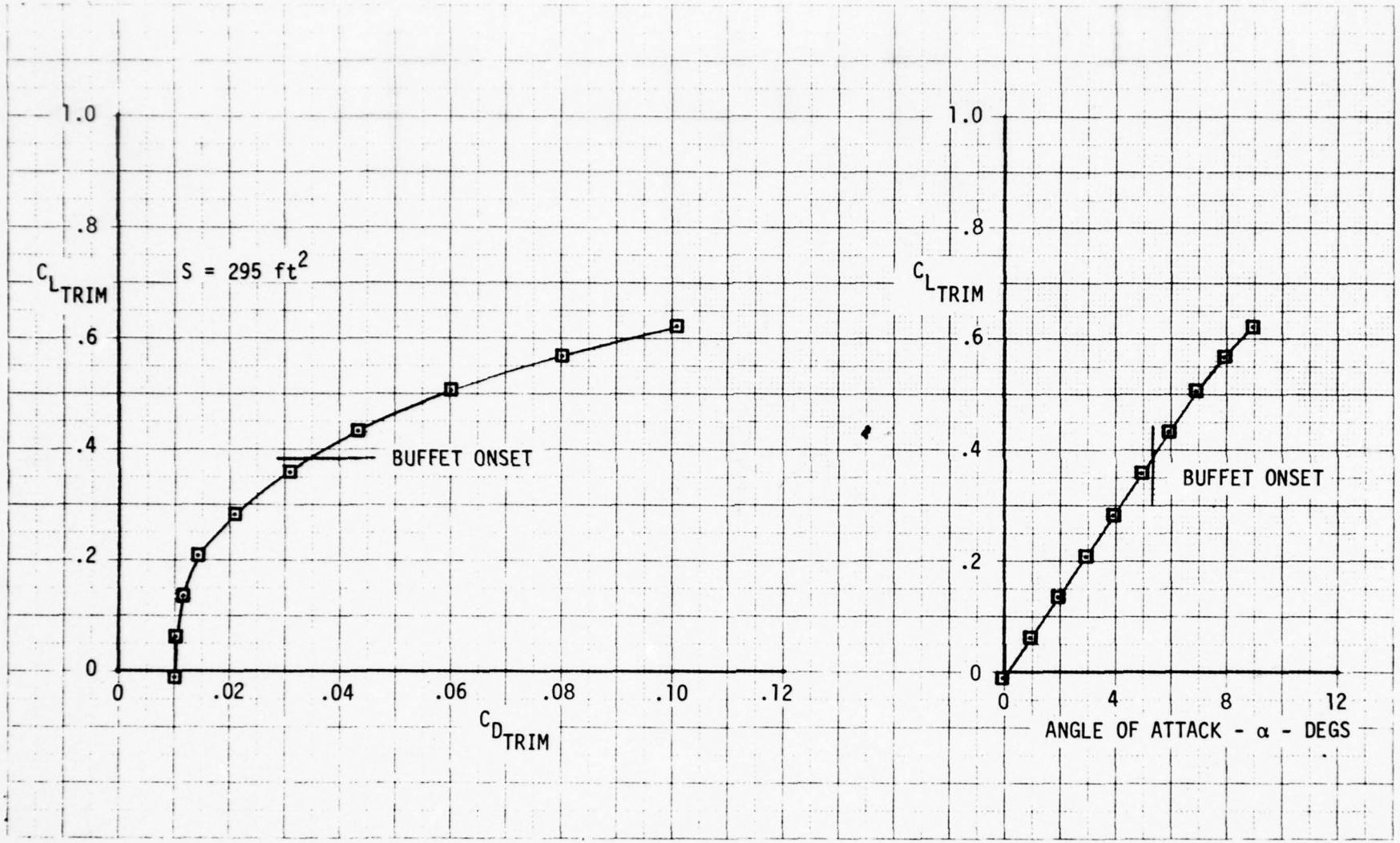

FIGURE B1 AIRCRAFT LIFT AND DRAG CHARACTERISTICS - CONFIG. LOTO, M=0.6, h=30,000 ft

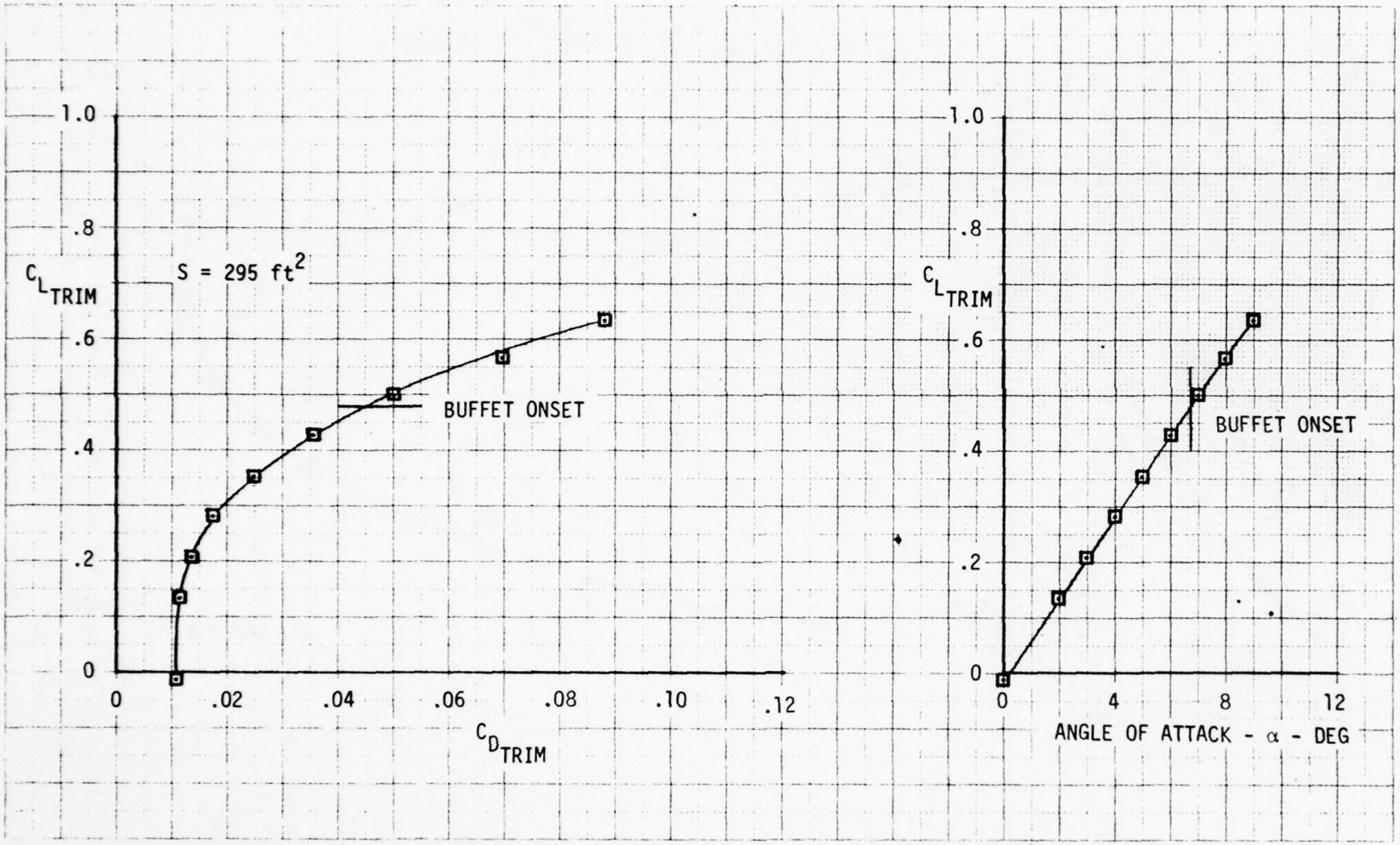

FIGURE B2 AIRCRAFT LIFT AND DRAG CHARACTERISTICS - CONFIG. L5TO, M=0.6, h=30,000 ft

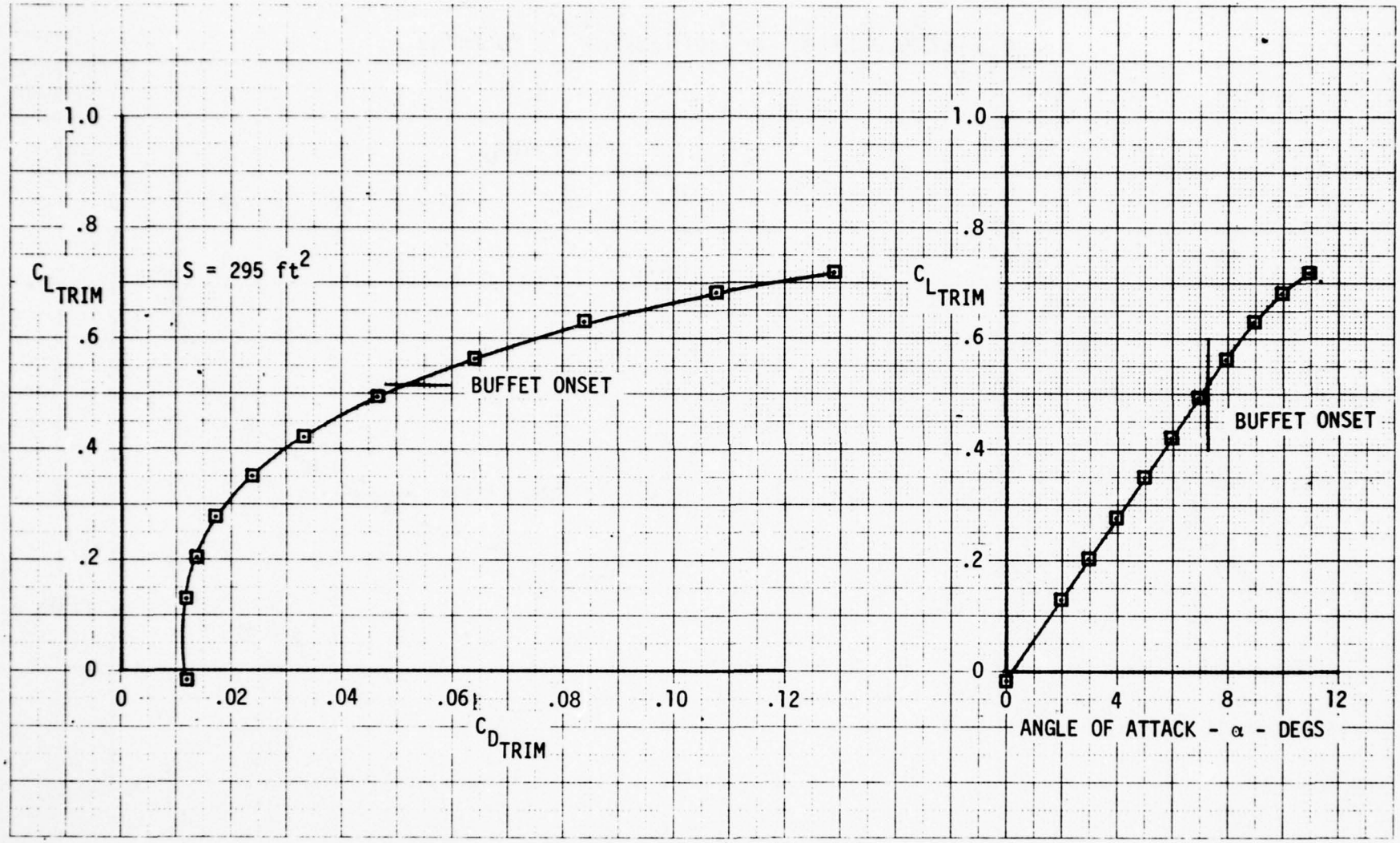

FIGURE B3 AIRCRAFT LIFT AND DRAG CHARACTERISTICS - CONFIG. L6TO, M=0.6, h=30,000 ft

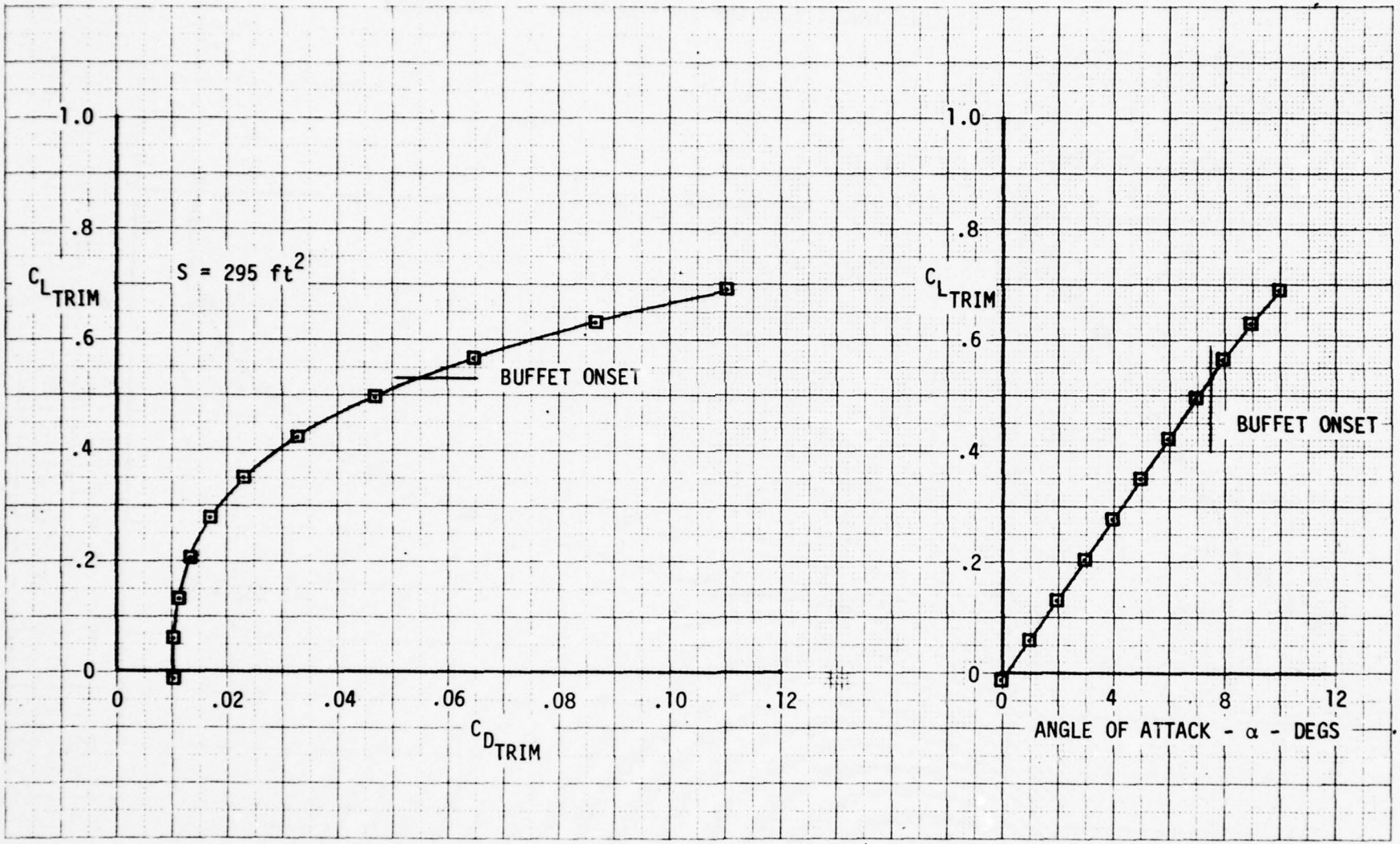

FIGURE B4 AIRCRAFT LIFT AND DRAG CHARACTERISTICS - CONFIG. L29TO, M=0.6, h=30,000 ft

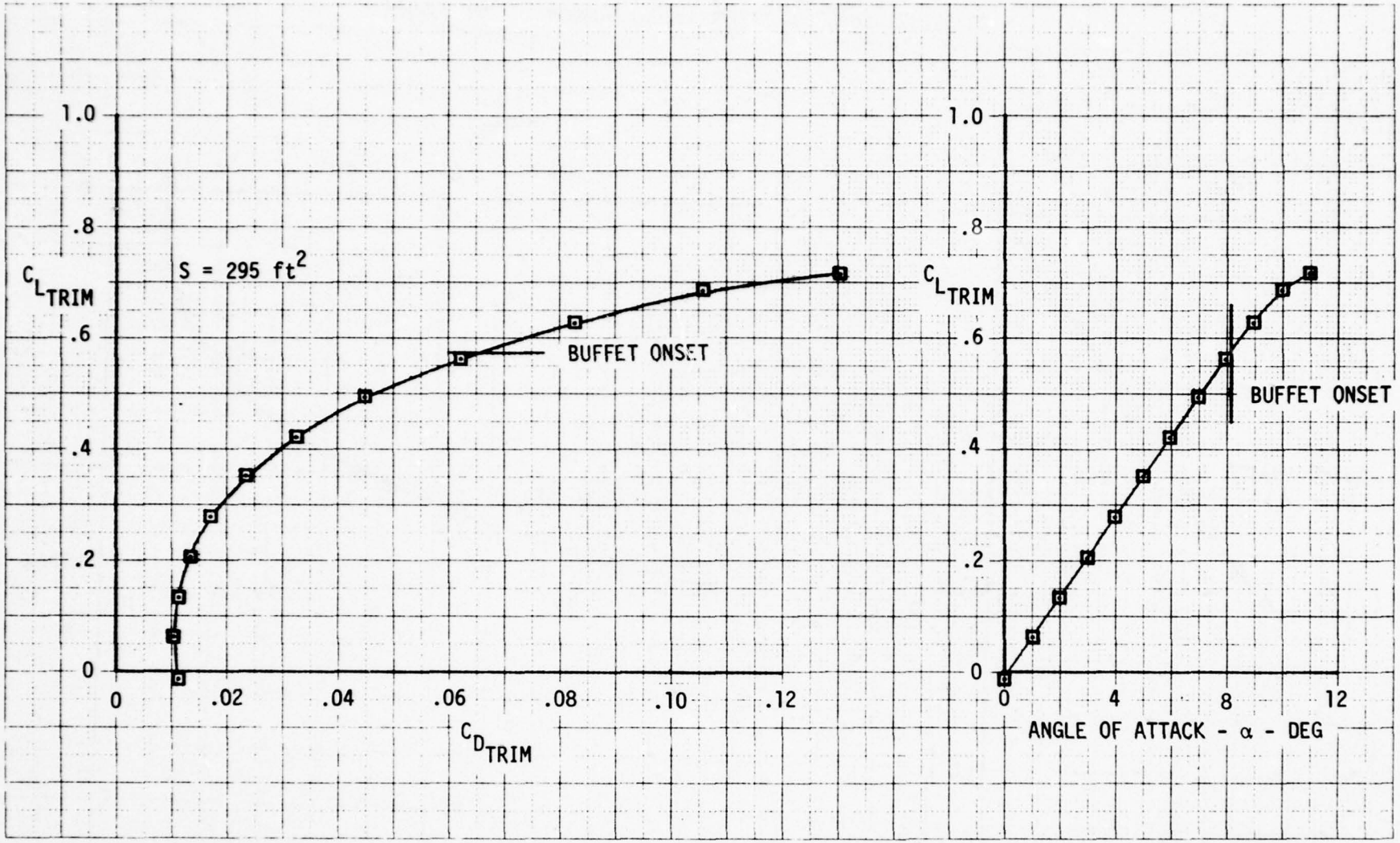

FIGURE B5 AIRCRAFT LIFT AND DRAG CHARACTERISTICS - CONFIG. L25TO, M=0.6, h=30,000 ft

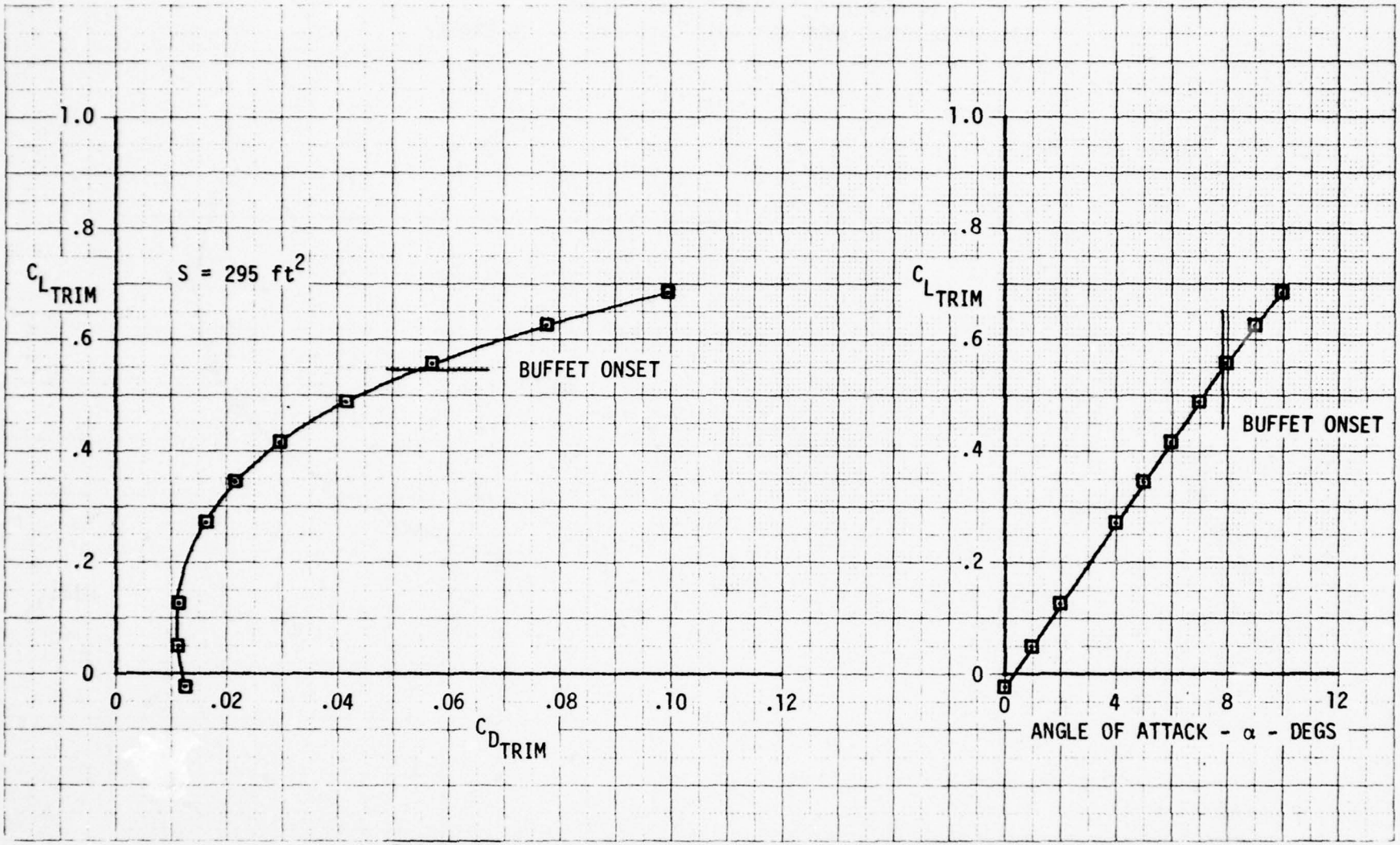

FIGURE B6 AIRCRAFT LIFT AND DRAG CHARACTERISTICS - CONFIG. L24TO, M=0.6, h=30,000 ft

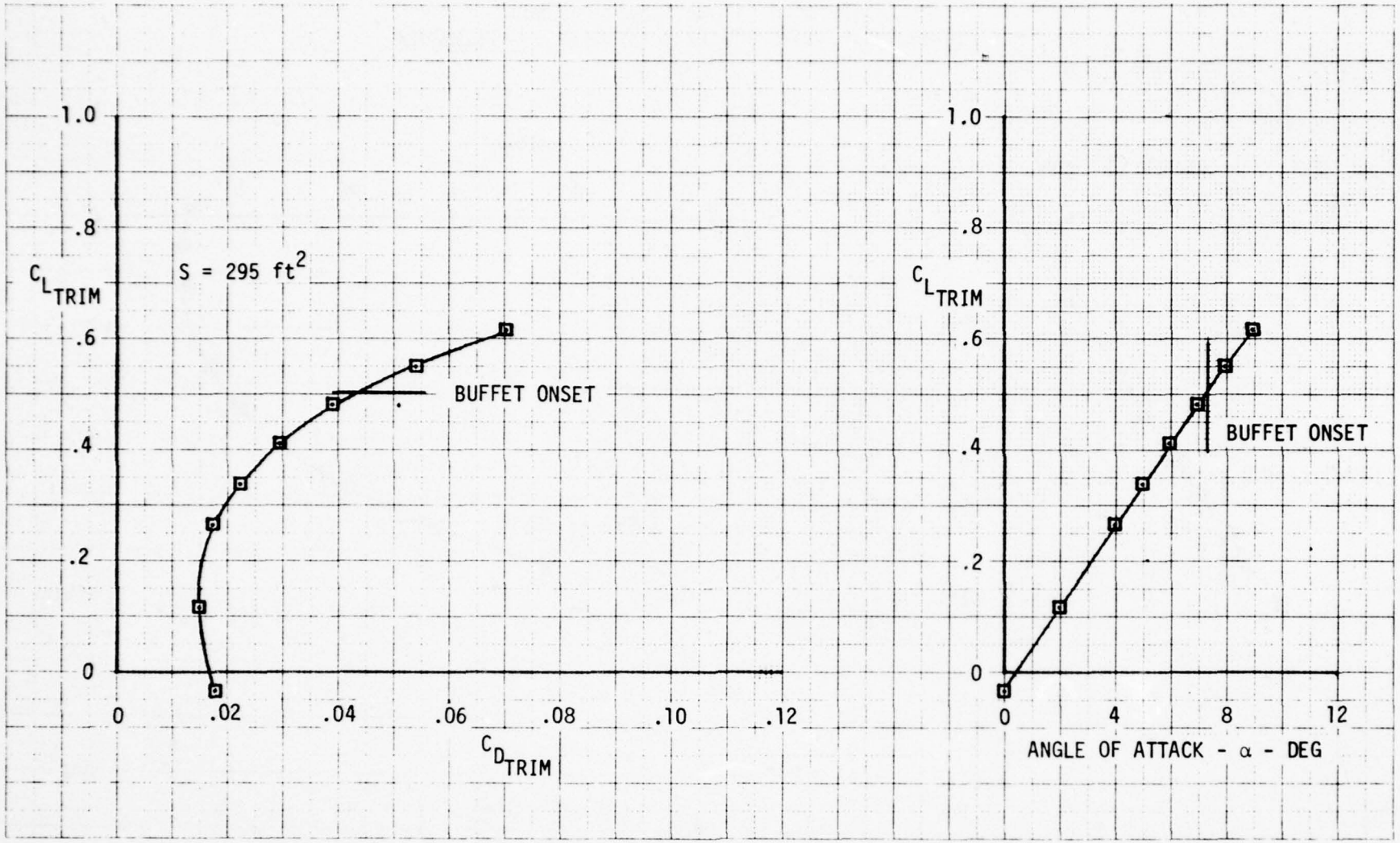

FIGURE B7 AIRCRAFT LIFT AND DRAG CHARACTERISTICS - CONFIG. L28TO, M=0.6, h=30,000 ft

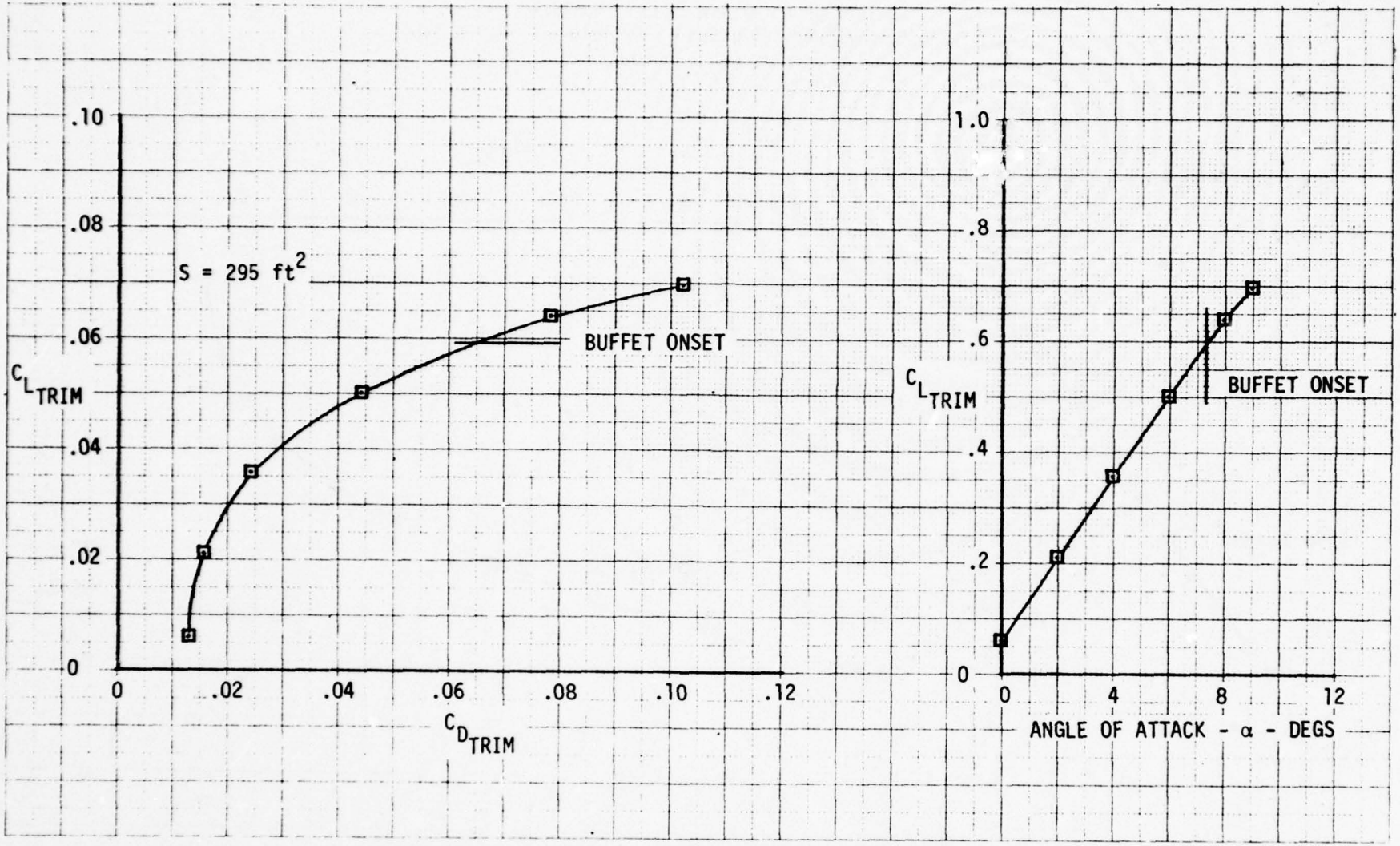

FIGURE B8 AIRCRAFT LIFT AND DRAG CHARACTERISTICS - CONFIG. L6T11, M=0.6, h=30,000 ft

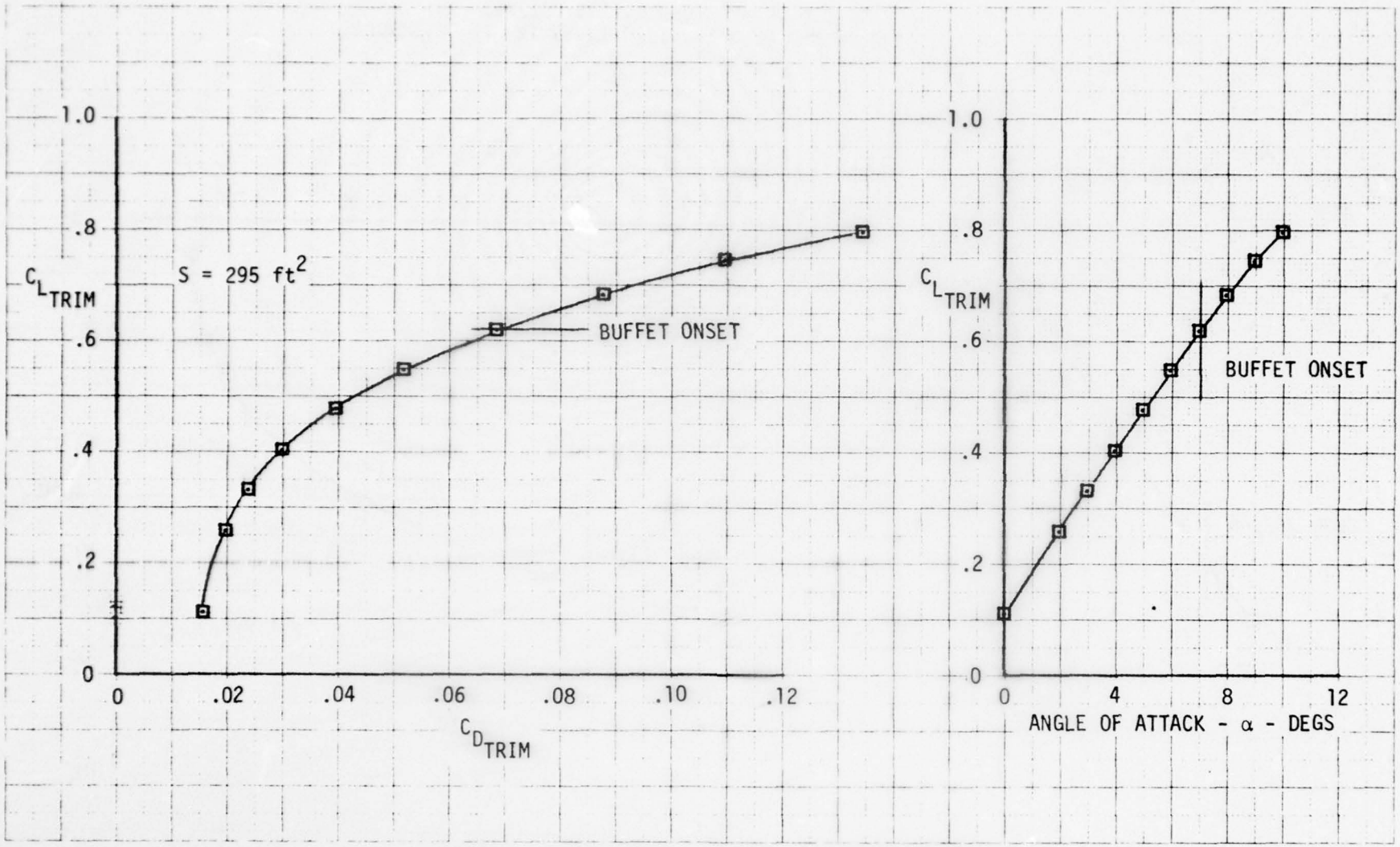

FIGURE B9 AIRCRAFT LIFT AND DRAG CHARACTERISTICS - CONFIG. L6T1, M=0.6, h=30,000 ft

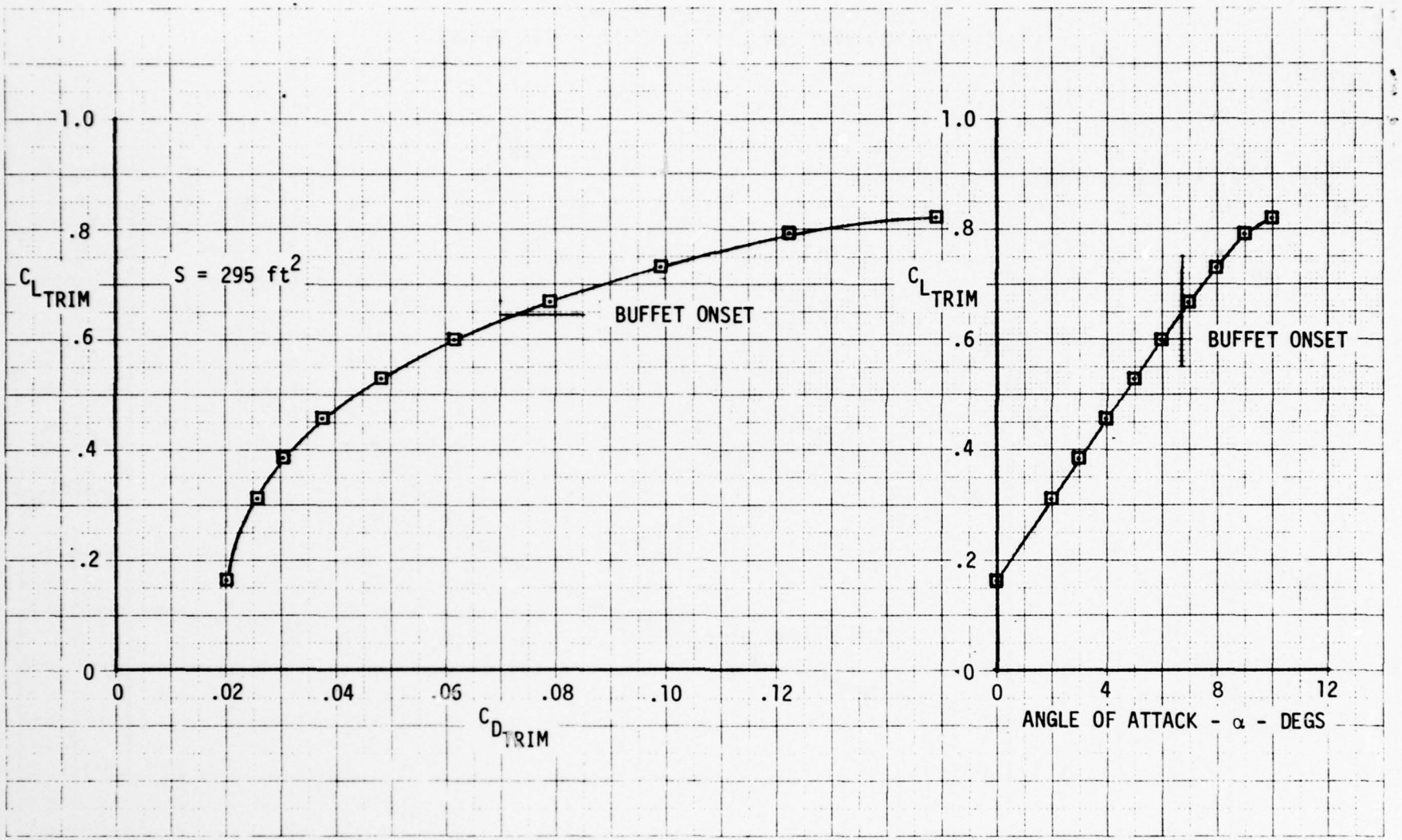

FIGURE B10 AIRCRAFT LIFT AND DRAG CHARACTERISTICS - CONFIG. L6T10, M=0.6, h=30,000 ft

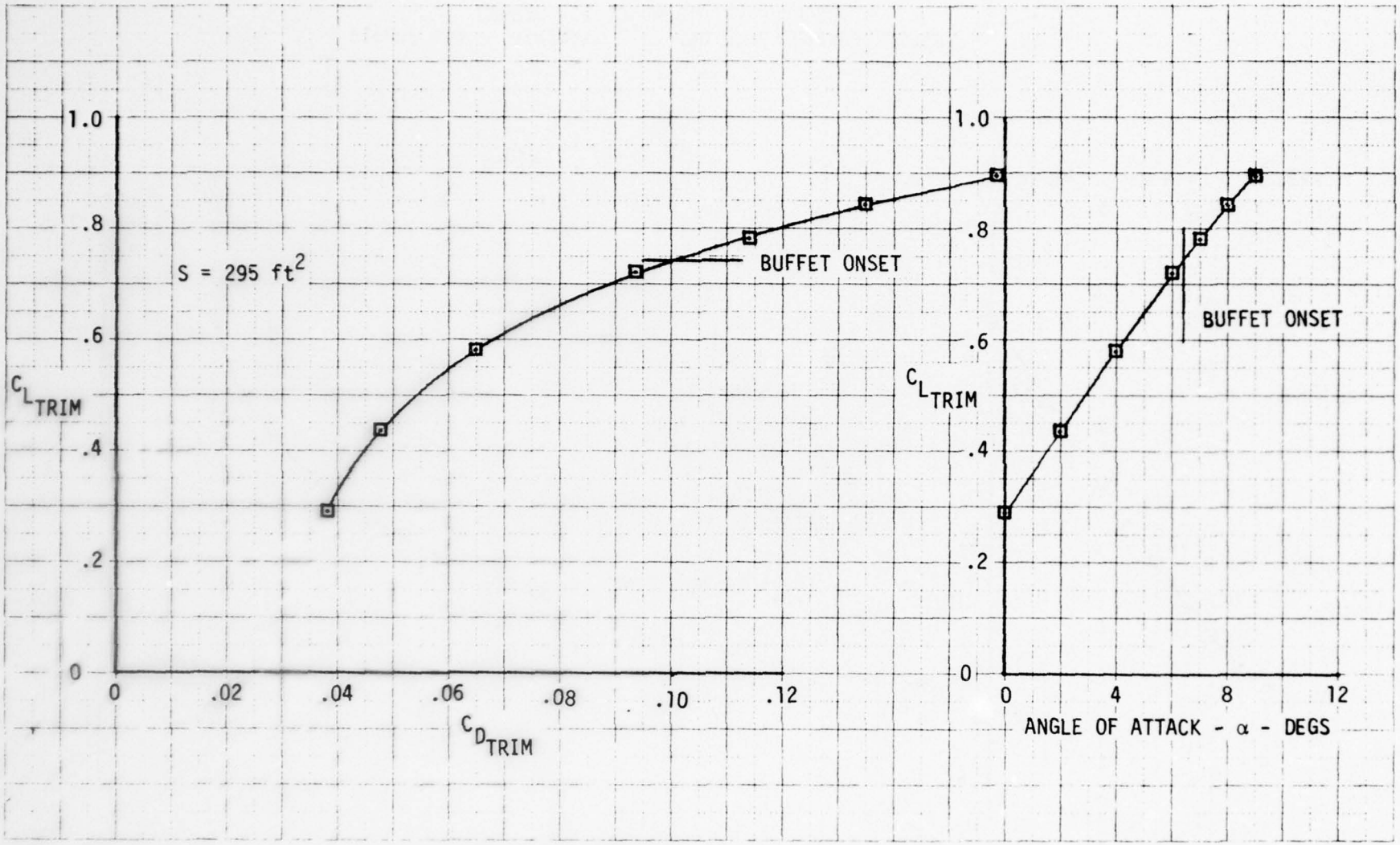

FIGURE B11 AIRCRAFT LIFT AND DRAG CHARACTERISTICS - CONFIG. L6T15, M=0.6, h=30,000 ft

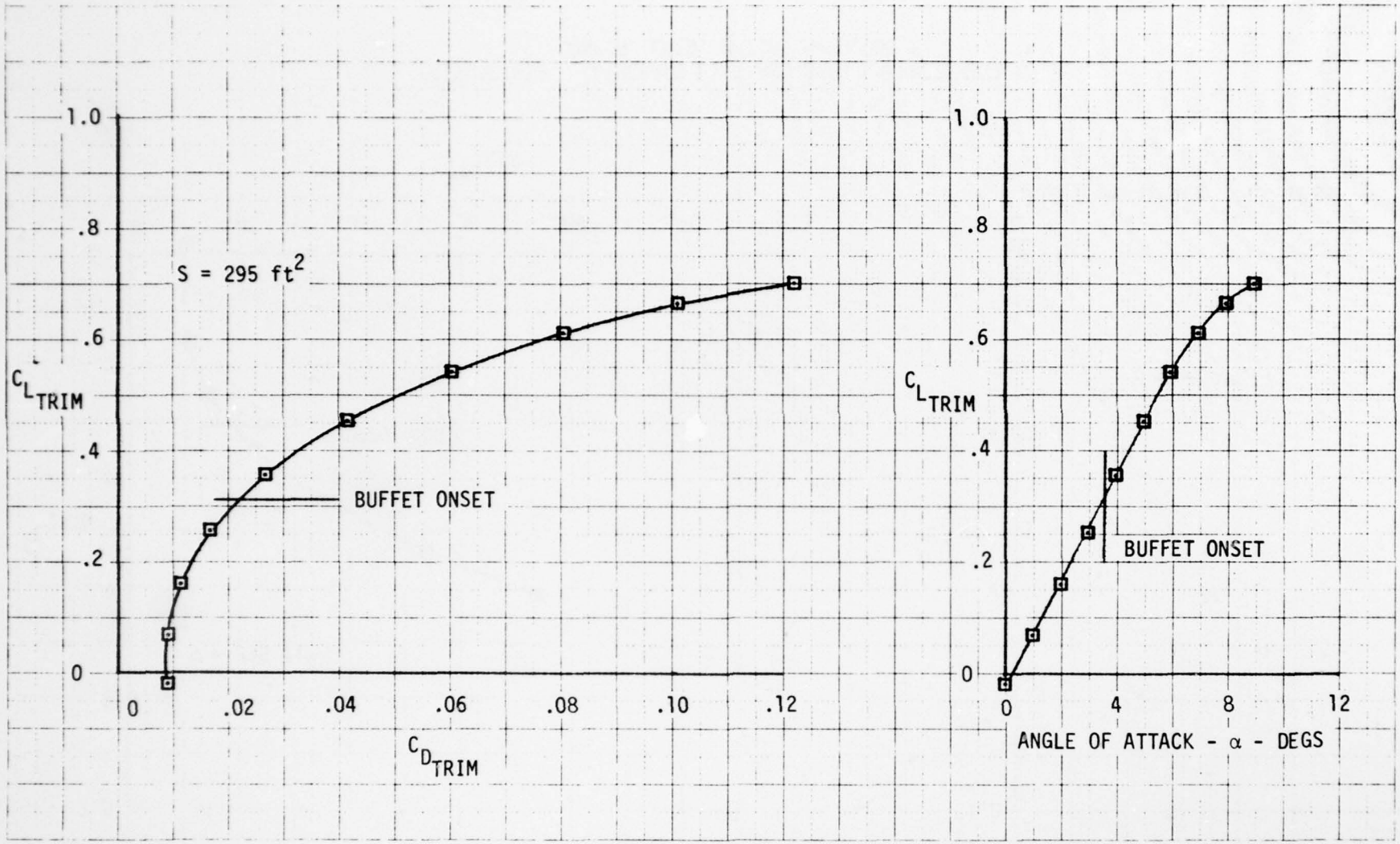

FIGURE B12 AIRCRAFT LIFT AND DRAG CHARACTERISTICS - CONFIG. LOTO, M=0.9, h=30,000 ft

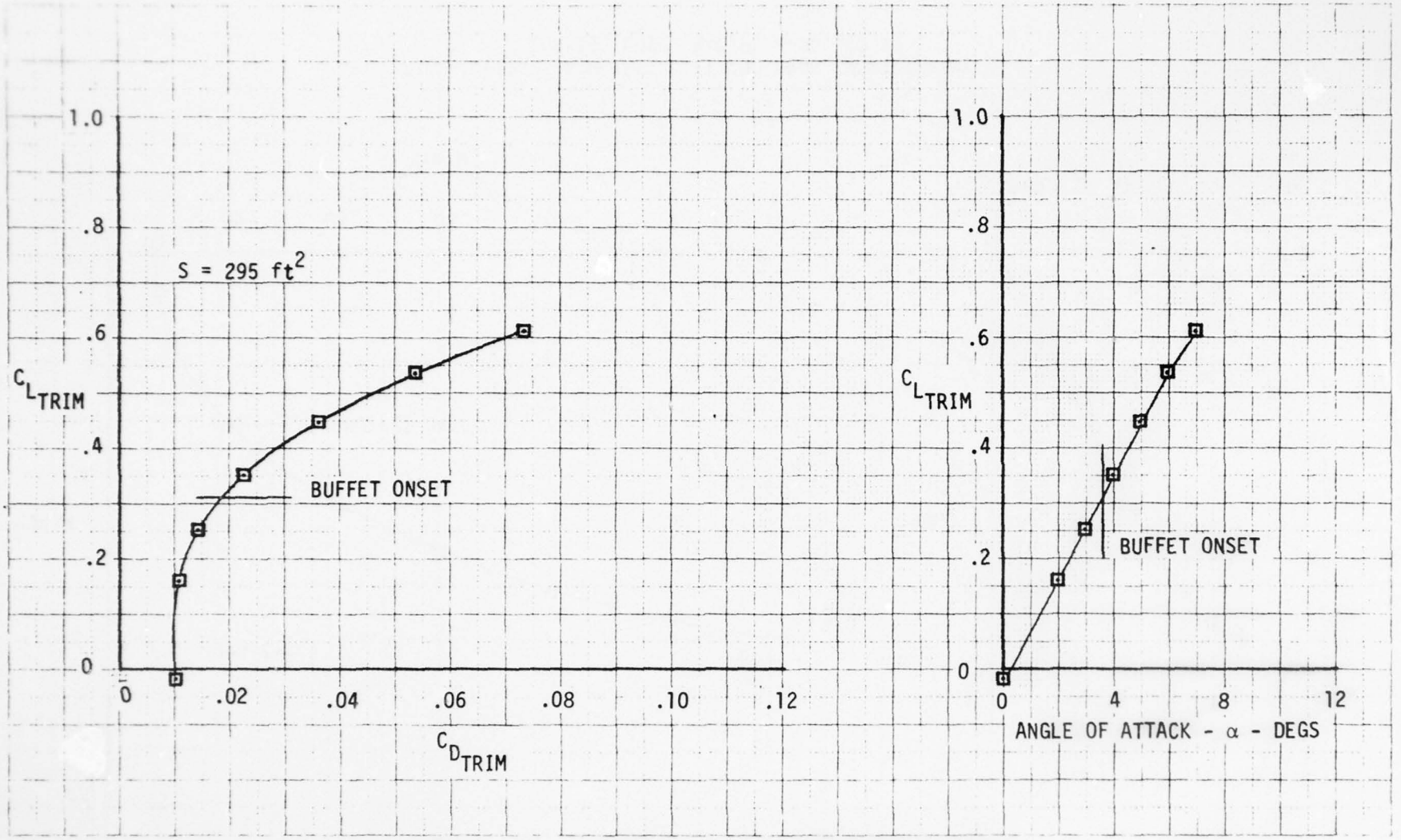

FIGURE B13 AIRCRAFT LIFT AND DRAG CHARACTERISTICS - CONFIG. L5TO, M=0.9, h=30,000 ft

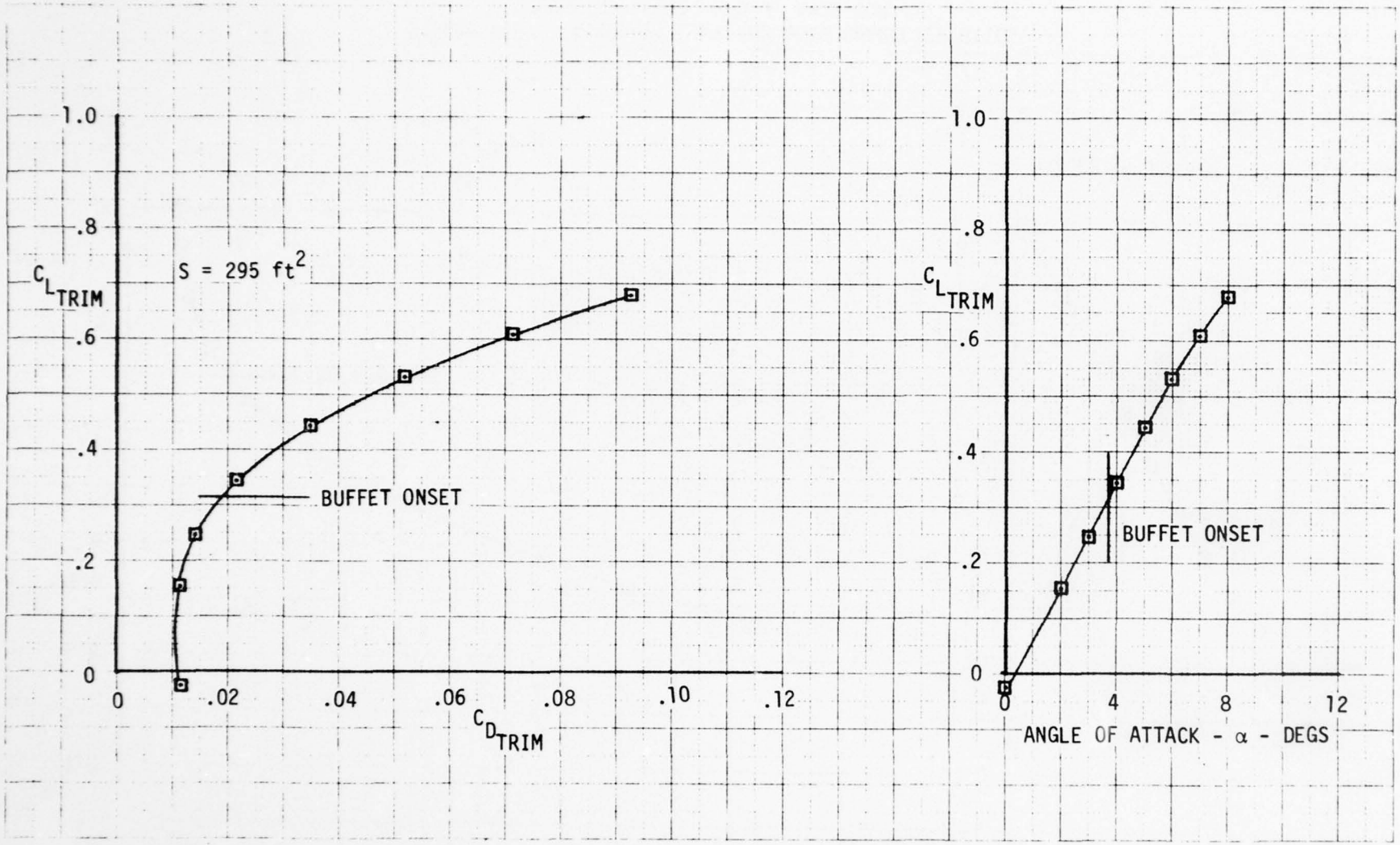

FIGURE B14 AIRCRAFT LIFT AND DRAG CHARACTERISTICS - CONFIG. L6TO, M=0.9, h=30,000 ft

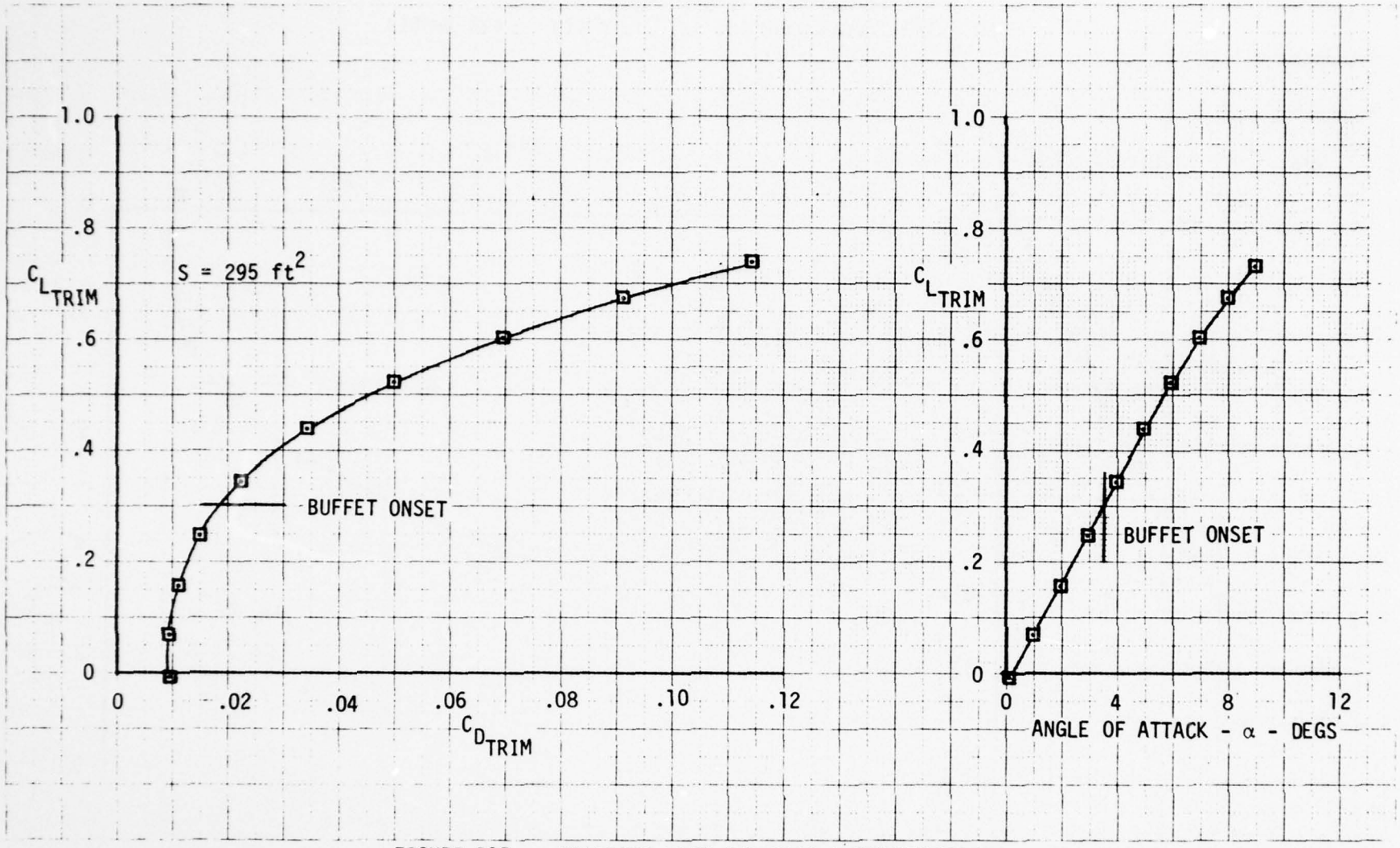

FIGURE B15 AIRCRAFT LIFT AND DRAG CHARACTERISTICS - CONFIG. L29TO, M=0.9, h=30,000 ft

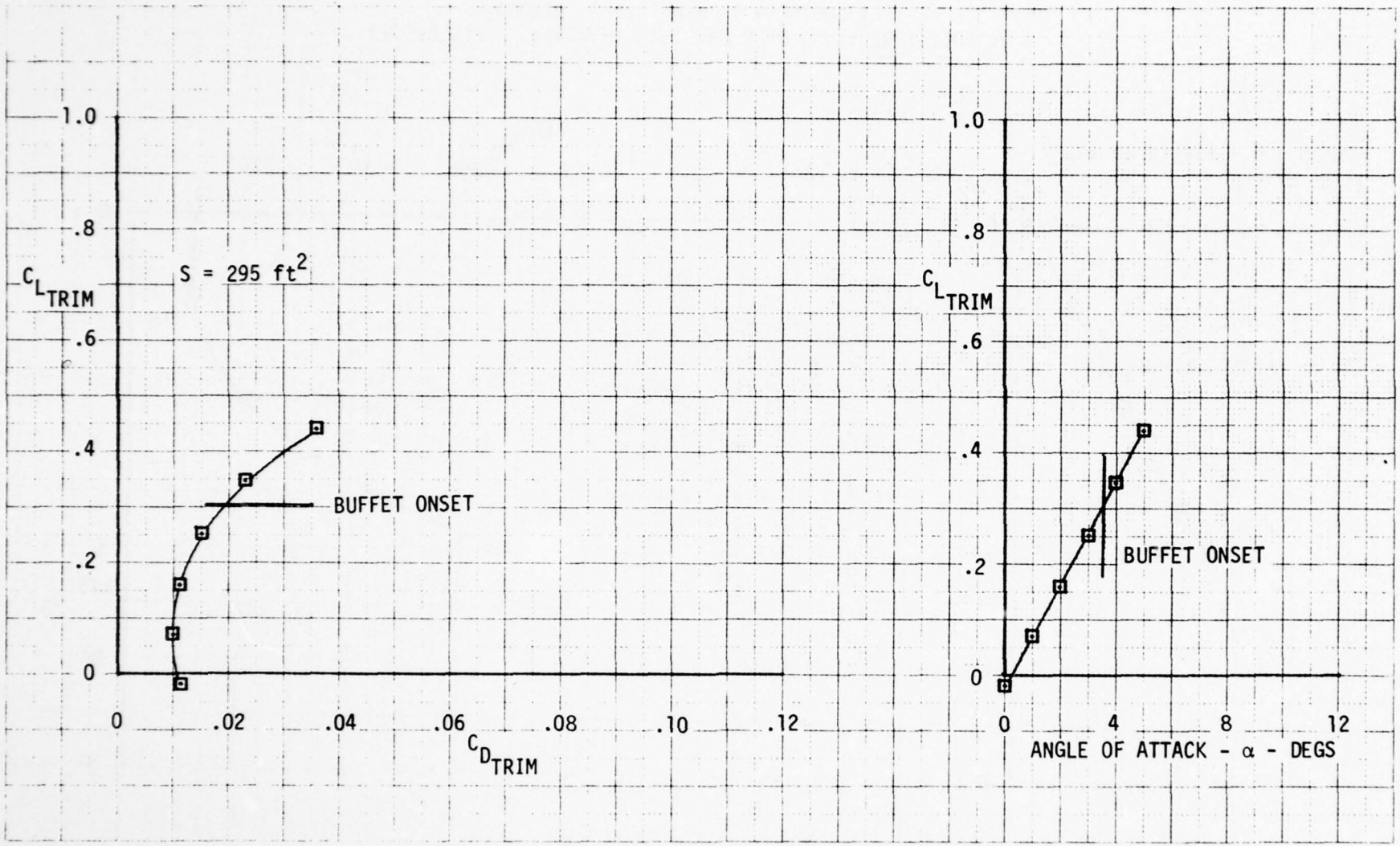

FIGURE B16 AIRCRAFT LIFT AND DRAG CHARACTERISTICS - CONFIG. L25TO, M=0.9, h=30,000 ft

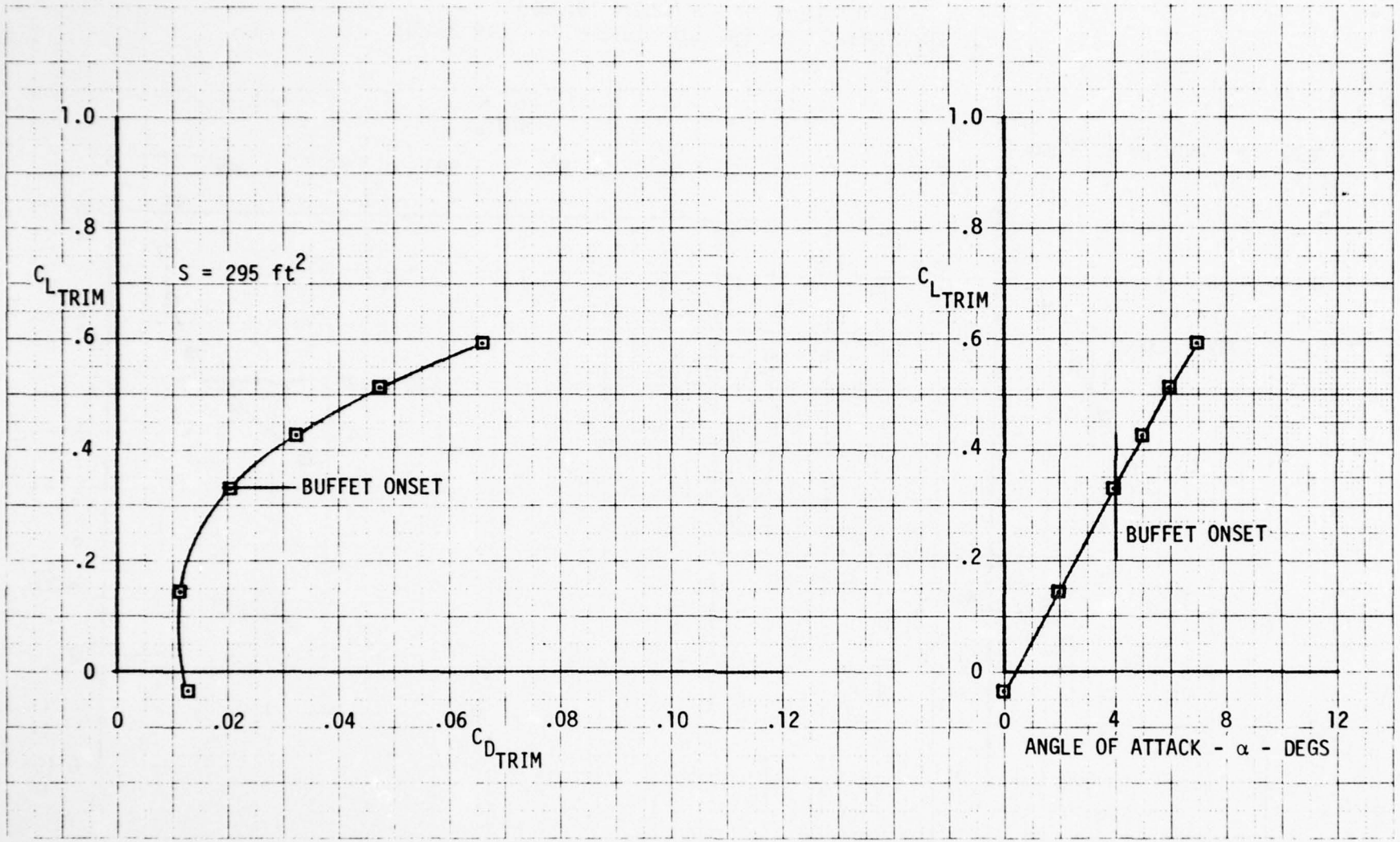

FIGURE B17 AIRCRAFT LIFT AND DRAG CHARACTERISTICS - CONFIG. L24TO, M=0.9, h=30,000 ft

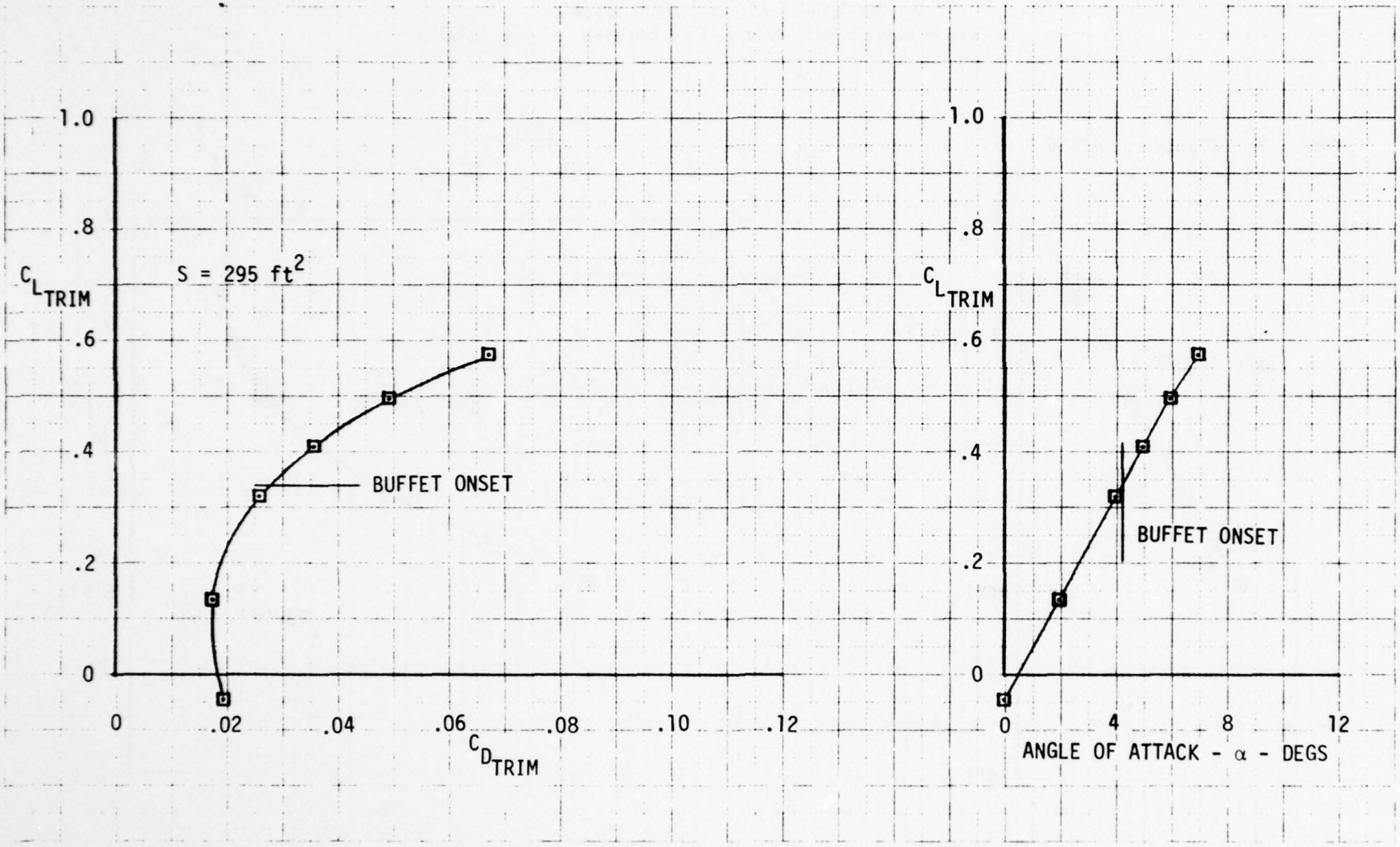

FIGURE B18 AIRCRAFT LIFT AND DRAG CHARACTERISTICS - CONFIG. L28TO, M=0.9, h=30,000 ft

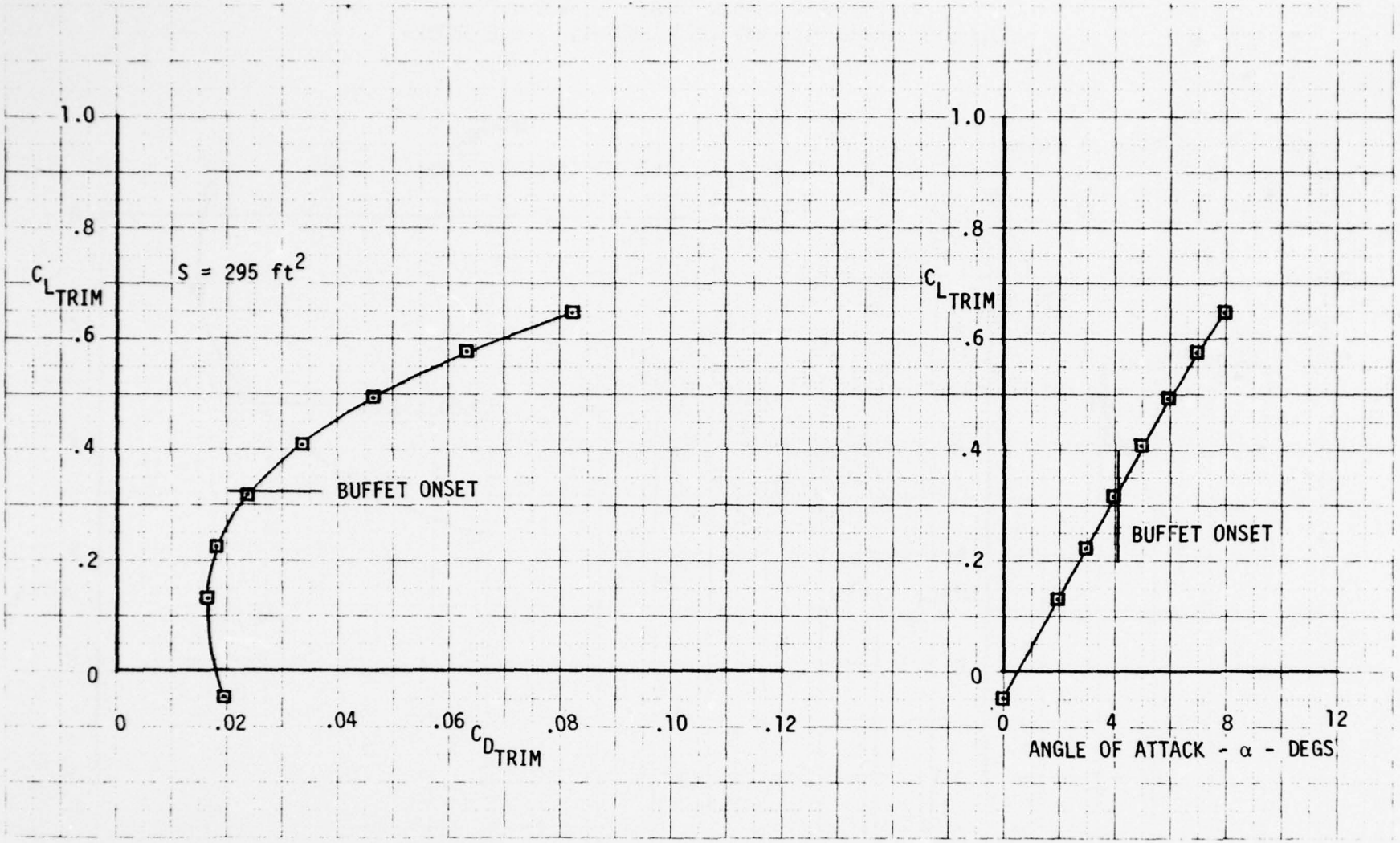

FIGURE B19 AIRCRAFT LIFT AND DRAG CHARACTERISTICS - CONFIG. L8TO, M=0.9, h=30,000 ft

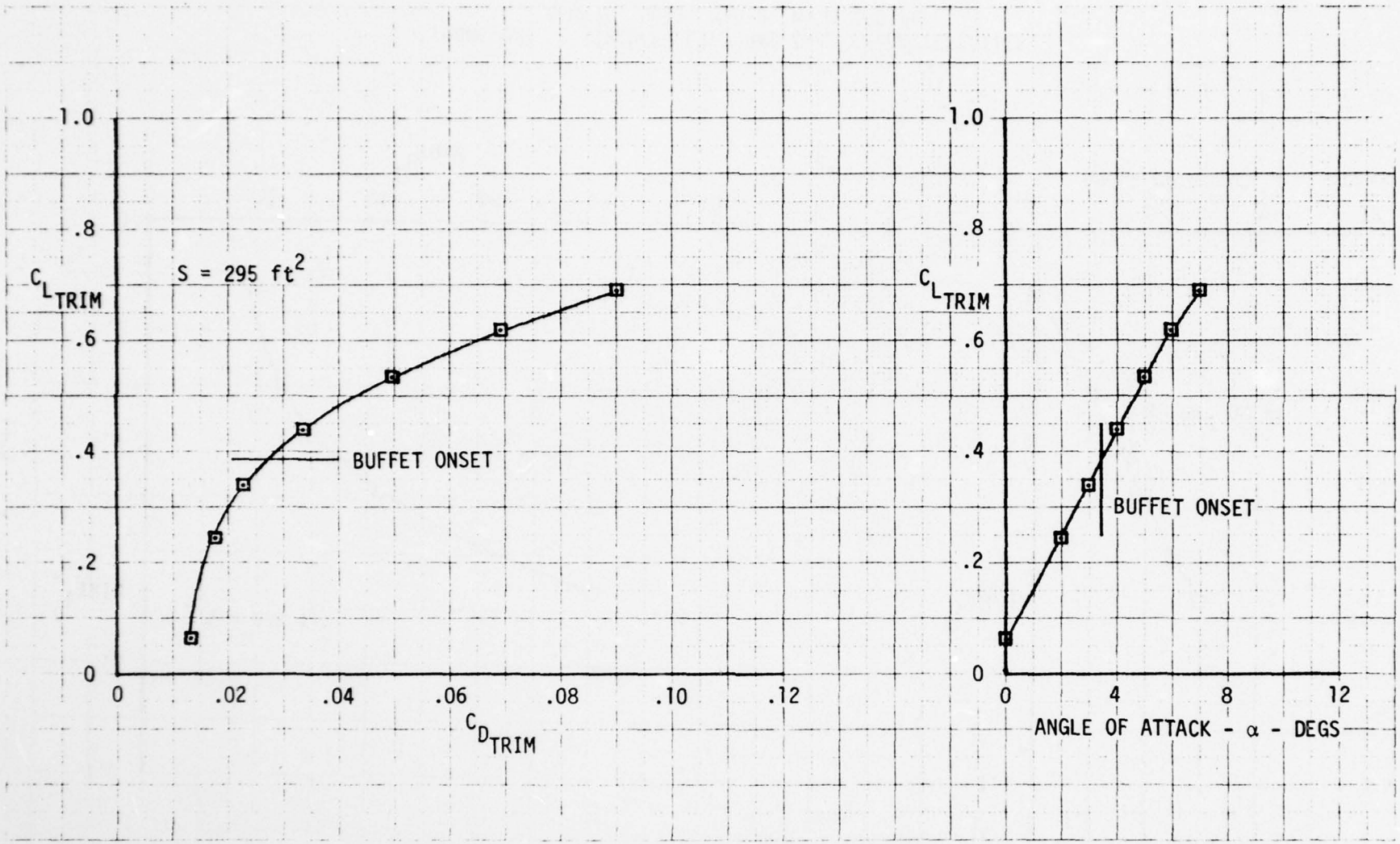

FIGURE B20 AIRCRAFT LIFT AND DRAG CHARACTERISTICS - CONFIG. L6T11, M=0.9, h=30,000 ft

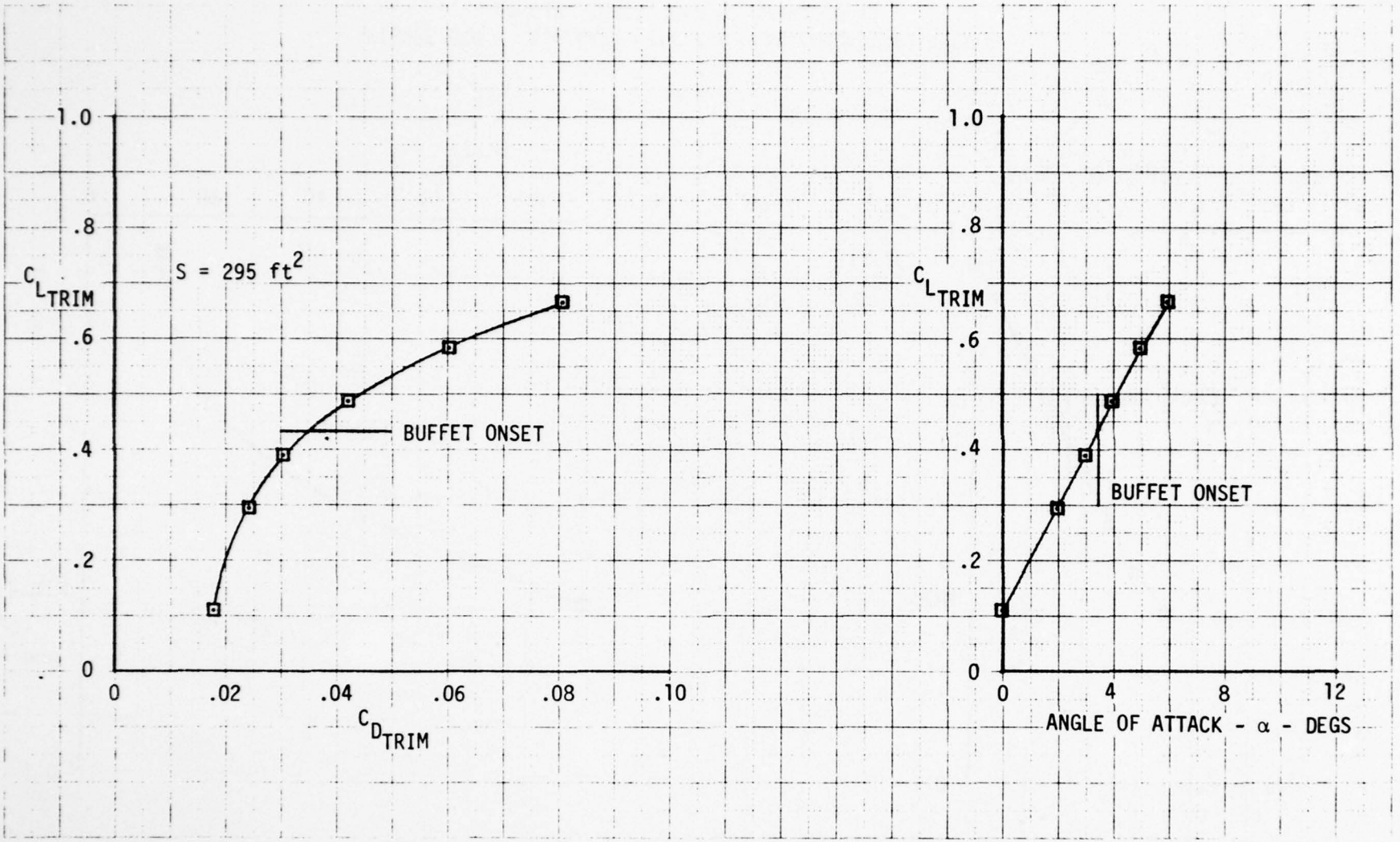

FIGURE B21 AIRCRAFT LIFT AND DRAG CHARACTERISTICS - CONFIG. L6T1, M=0.9, h=30,000 ft

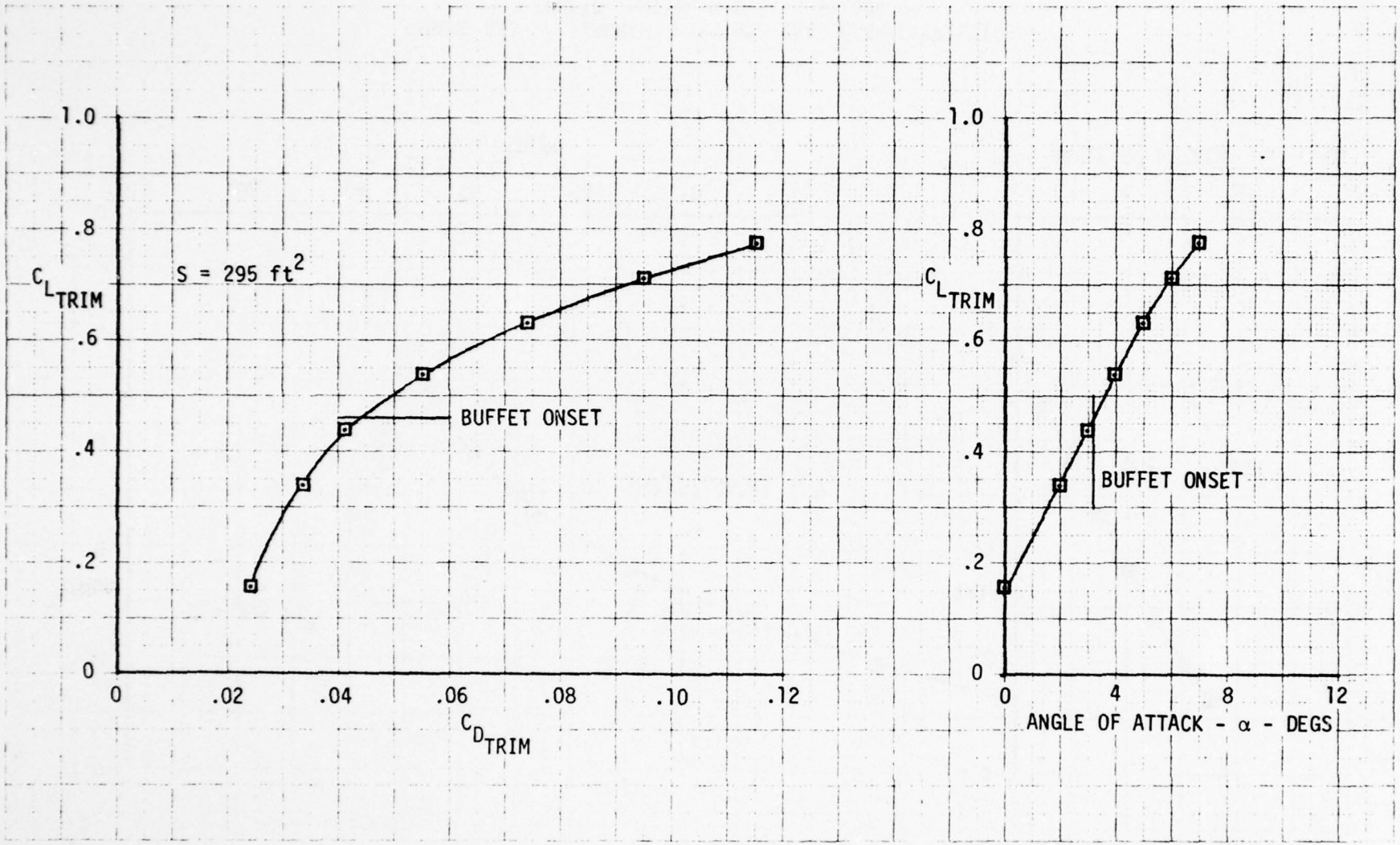

FIGURE B22 AIRCRAFT LIFT AND DRAG CHARACTERISTICS - CONFIG. L6T10, M=0.9, h=30,000 ft

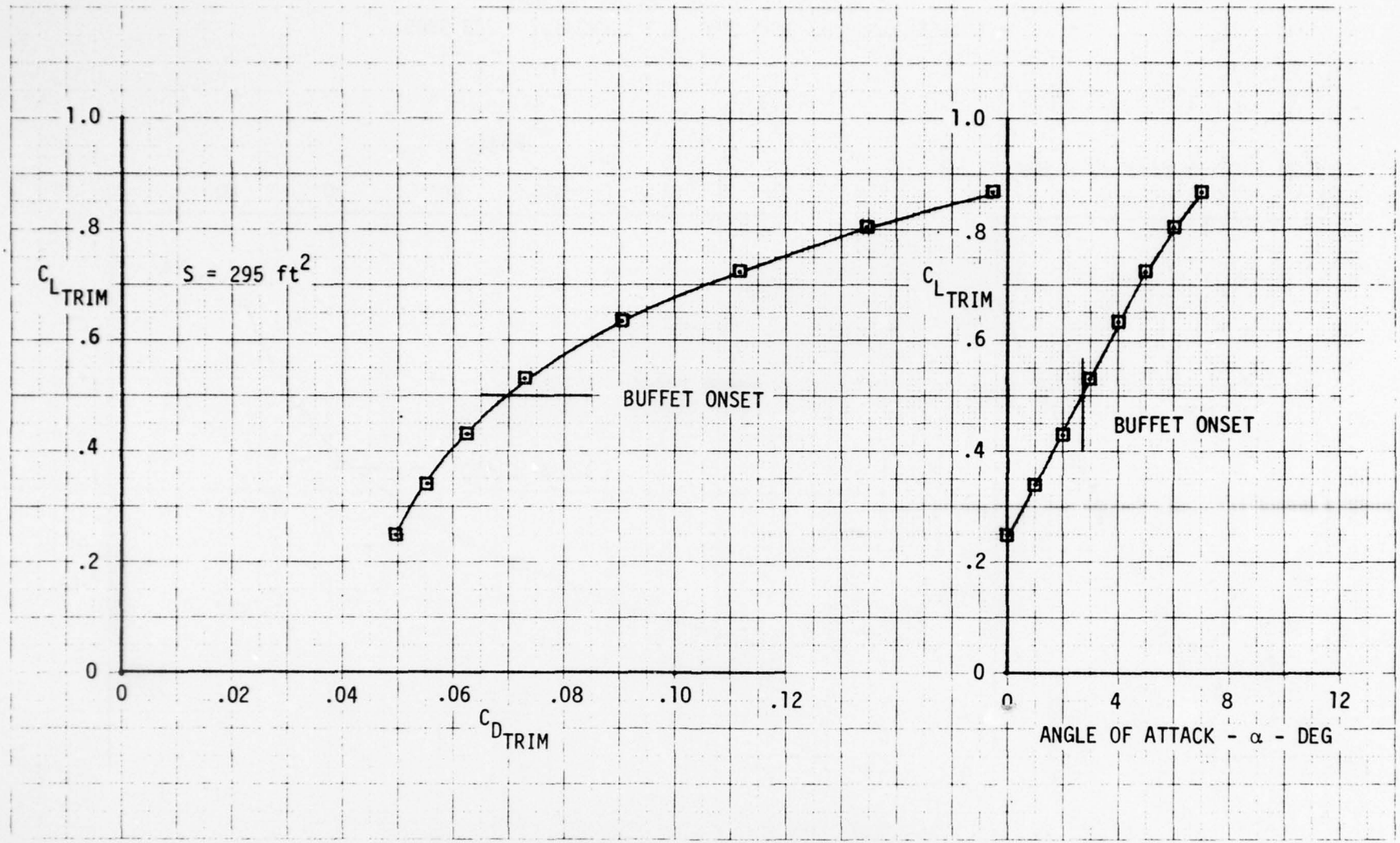

FIGURE B23 AIRCRAFT LIFT AND DRAG CHARACTERISTICS - CONFIG. L6T15, M=0.9, h=30,000 ft